University of Arkansas, Fayetteville
ScholarWorks@UARK

Theses and Dissertations

8-2019

Development of a Multimode Instrument for Remote Measurements of Unsaturated Soil Properties

Sean Elliott Salazar
University of Arkansas, Fayetteville

Follow this and additional works at: https://scholarworks.uark.edu/etd

 Part of the Civil Engineering Commons, Environmental Engineering Commons, Geotechnical Engineering Commons, and the Soil Science Commons

Recommended Citation

Salazar, Sean Elliott, "Development of a Multimode Instrument for Remote Measurements of Unsaturated Soil Properties" (2019). *Theses and Dissertations*. 3384.
https://scholarworks.uark.edu/etd/3384

This Dissertation is brought to you for free and open access by ScholarWorks@UARK. It has been accepted for inclusion in Theses and Dissertations by an authorized administrator of ScholarWorks@UARK. For more information, please contact ccmiddle@uark.edu.

Development of a Multimode Instrument for Remote Measurements of Unsaturated Soil Properties

A dissertation submitted in partial fulfillment
of the requirements for the degree of
Doctor of Philosophy in Engineering

by

Sean Elliott Salazar
University of Arkansas
Bachelor of Science in Civil Engineering, 2013
University of Arkansas
Master of Science in Civil Engineering, 2017

August 2019
University of Arkansas

This dissertation is approved for recommendation to the Graduate Council.

_____
Richard Coffman, Ph.D.
Dissertation Director

_____
Michelle Bernhardt-Barry, Ph.D.
Committee Member

_____
Thomas Oommen, Ph.D.
Committee Member

_____
Jason Tullis, Ph.D.
Committee Member

ABSTRACT

The hydromechanical behavior of soil is governed by parameters that include the moisture content, soil matric potential, texture, and the mineralogical composition of the soil. Remote characterization of these and other key properties of the soil offers advantages over conventional in situ or laboratory-based measurements: information may be acquired rapidly over large, or inaccessible areas; samples do not need to be collected; and the measurements are non-destructive. A field-deployable, ground-based remote sensor, designated the Soil Observation Laser Absorption Spectrometer (SOLAS), was developed to infer parameters of bare soils and other natural surfaces over intermediate (100 m) and long (1,000 m) ranges.

The SOLAS methodology combines hyperspectral remote sensing with differential absorption and laser ranging measurements. A transmitter propagates coherent, near-infrared light at on-line (823.20 nm) and off-line (847.00 nm) wavelengths. Backscattered light is received through a 203-mm diameter telescope aperture and is divided into two channels to enable simultaneous measurements of spectral reflectance, differential absorption, and range to the target. The spectral reflectance is measured on 2151 continuous bands that range from visible (380 nm) to shortwave infrared (2500 nm) wavelengths. A pair of photodetectors receive the laser backscatter in the 820–850 nm range. Atmospheric water vapor is inferred using a differential absorption technique in conjunction with an avalanche photodetector, while range to the target is based on a frequency-modulated, self-chirped, homodyne detection scheme.

The design, fabrication, and testing of the SOLAS is described herein. The receiver was optimized for the desired backscatter measurements and assessed through a series of trials that were conducted in both indoor and outdoor settings. Spectral reflectance measurements collected at proximal range compared well with measurements collected at intermediate ranges,

demonstrating the utility of the receiver. Additionally, the noise characteristics of the spectral measurements were determined across the full range of the detected wavelengths. Continued development of the SOLAS instrument will enable range-resolved and water vapor-corrected reflectance measurements over longer ranges. Anticipated applications for the SOLAS technology include rapid monitoring of earth construction projects, geohazard assessment, or ground-thruthing for current and future satellite-based multi- and hyperspectral data.

ACKNOWLEDGEMENTS

This material is based upon work supported by the National Science Foundation Graduate Research Fellowship Program under Grant No. DGE-1450079. Any opinions, findings, and conclusions or recommendations expressed in this material are those of the author and do not necessarily reflect the views of the National Science Foundation. The author would also like to acknowledge support from the United States Department of Transportation (USDOT) through the Office of the Assistant Secretary for Research and Technology (OST-R) under USDOT Cooperative Agreement No. OASRTRS-14-H-UARK. The views, opinions, findings and conclusions reflected in this material are solely those of the author and do not represent the official policy or position of the USDOT/OST-R, or any State or other entity. USDOT/OST-R does not endorse any third party products or services that may be included in this material.

DEDICATION

I would like to dedicate this dissertation to my mother, Betty, to my father, John, to my grandfather, (Grandpop) Joe, to my brother, Eric, to my sister, Rachel, and to my wife, Alexandra. Without their love, strength, and unending support, I could not have completed this work. I would also like to acknowledge the guidance, encouragement, and leadership, of my advisor, Dr. Rick Coffman. Finally, I would like to thank those colleagues and friends that helped me along the way, in no particular order, Adam Barnes, Johnathan Blanchard, Cyrus Garner, Brandon Rogers, Mark Kuss, Julia Loshelder, and Esteban Miranda Pinzon.

TABLE OF CONTENTS

CHAPTER 1: INTRODUCTION **1**

1.1. Chapter Overview 1
1.2. Description of the Work 1
1.3. Motivation 3
1.3.1. Limitations of Current Techniques 3
1.3.2. Significance for Geotechnical Engineering 4
1.3.3. Broader Applications 5
1.4. Document Overview 5
1.5. References 7

CHAPTER 2: BACKROUND **8**

2.1. Chapter Overview 8
2.2. Motivation 8
2.3. Optical Remote Sensing of Soils 10
2.3.1. Satellite-Based Optical Remote Sensing 10
2.3.2. Ground-Based Reflectance Spectroscopy 12
2.4. Concepts of Electronic Component Design 16
2.4.1. Tuned Laser Source 16
2.4.2. Fiber Optics 17
2.4.3. Electro-Optic Modulation 20
2.5. References 22

CHAPTER 3: DEVELOPMENT OF A MULTIMODE FIELD DEPLOYABLE LIDAR INSTRUMENT FOR TOPOGRAPHIC MEASUREMENTS OF UNSATURATED SOIL PROPERTIES: INSTRUMENT DESCRIPTION **28**

3.1. Chapter Overview 28
3.2. Limitations of the Described Study 28
3.3. Development of a Multimode Field Deployable Lidar Instrument for Topographic Measurements of Unsaturated Soil Properties: Instrument Description 29
3.4. Abstract 29
3.5. Introduction 30
3.6. Background 31
3.6.1. FMCW Lidar Altimetry 33
3.6.2. Differential Absorption Measurements 34
3.7. Development of the SOLAS Concept 36
3.8. Instrument Description 38
3.8.1. Transmitter Design 40
3.8.2. Receiver Design 42
3.8.3. Data Acquisition and Control Design 43
3.8.4. Field Ruggedization 45
3.9. Discussion 47
3.10. Conclusions 49
3.11. Acknowledgements 50
3.12. References 51

CHAPTER 4: MULTI-CHANNEL OPTICAL RECEIVER FOR GROUND-BASED TOPOGRAPHIC HYPERSPECTRAL REMOTE SENSING....59

4.1. Chapter Overview 59
4.2. Limitations of the Described Study....59
4.3. Multi-Channel Optical Receiver for Ground-Based Topographic Hyperspectral Remote Sensing....59
4.4. Abstract 60
4.5. Introduction 61
4.6. Materials and Methods 63
4.6.1. Receiver Testing....70
4.7. Results and Discussion....71
4.8. Conclusions 77
4.9. Acknowledgements 79
4.10. References 80

CHAPTER 5: VALIDATION OF A GROUND-BASED TELESCOPE-ASSISTED HYPERSPECTRAL REMOTE SENSOR 82

5.1. Chapter Overview 82
5.2. Limitations of the Described Study....82
5.3. Validation of a Ground-Based Telescope-Assisted Hyperspectral Remote Sensor....83
5.4. Abstract 83
5.5. Introduction and Background....84
5.6. Methods....85
5.6.1. Indoor and Outdoor Proximal Range Data Collection 85
5.6.2. Indoor Intermediate Range Data Collection....89
5.6.3. Outdoor Intermediate Range Data Collection 90
5.6.4. Processing Methods....93
5.7. Results and Discussion....94
5.7.1. Indoor Proximal Range Measurements 94
5.7.2. Indoor and Outdoor Intermediate Range Measurements....97
5.7.3. Noise-Equivalent-Radiance Characterization 102
5.7.4. Limitations and Future Applications....105
5.8. Conclusions 107
5.9. Acknowledgements 108
5.10. References 109

CHAPTER 6: CONCLUSIONS 111

6.1. Chapter Overview 111
6.2. Highlights 111
6.3. Limitations 112
6.4. Recommendations 113

CHAPTER 7: WORKS CITED....115

APPENDIX **126**

APPENDIX A: MISCELLANEOUS COMPONENT DESIGN AND TESTING **126**

A.1. Chapter Overview 126
A.2. Transmitter Components 126
A.2.1. Laser Tuning 127
A.2.2. Optical Isolation 128
A.2.3. Optical Amplification 130
A.2.4. Alignment of Bulk Optics 134
A.3. Receiver Components 138
A.4. References 147

APPENDIX B: SENSITIVITY TESTING AND NOISE CHARACTERIZATION **148**

B.1. Chapter Overview 148
B.2. Sensitivity Testing of the SOLAS Hyperspectral Receiver 148
B.3. Field Testing of the SOLAS Hyperspectral Receiver 158
B.4. Noise Characterization of the SOLAS Hyperspectral Receiver 163
B.5. References 168

LIST OF FIGURES

Figure 1.1. Plan view of the internal components of the SOLAS transmitter box 2

Figure 1.2. Overview of the SOLAS data acquisition and processing chain (modified from Salazar et al. 2019).....2

Figure 2.1. Wavelengths in the electromagnetic spectrum that are used for optical remote sensing techniques (Edmund Optics 2012).....10

Figure 2.2. Modeled transmittance of the Earth's atmosphere, as a function of wavelength (from Berk et al. 1989).....12

Figure 2.3. Mineralogy of soils determined using *(a)* traditional index testing (chart modified from Terzaghi et al. 1996) and scanning electron microscopy (SEM) for *(b)* Donna Fill, *(c)* Illite, and *(d)* Kaolinite soils; Particle distribution of the soils as obtained by using ASTM D422 (2007) (from Garner 2017) 15

Figure 2.4. Tunable external cavity diode laser in the Littman-Metcalf configuration (New Focus 2014). 16

Figure 2.5. Typical cross-sections for single mode fiber, step-index and graded index multimode fiber, and bow-tie and PANDA polarization-maintaining fiber (modified from Thorlabs 2018). 18

Figure 2.6. Loss of power in fiber optics due to *(a)* micro-bending and *(b)* macro-bending, and fiber optic coupling with *(c)* underfilled and *(d)* overfilled launch conditions (modified from Thorlabs 2018) 19

Figure 2.7. Numerical aperture for total internal reflection (modified from Newport 2018) 19

Figure 2.8. Characteristic curve for the Mach-Zehnder amplitude modulator (after Jenoptik 2018). 21

Figure 3.1. Absorption coefficient, as a function of wavelength, for free water and water vapor with transposed on-line (823.20 nm) and off-line (847.00 nm) laser wavelengths; raw data from Kou et al. (1993), Pope and Fry (1997), and Rothman et al. (2013).....38

Figure 3.2. Schematic of the soil observation laser absorption spectrometer (SOLAS) 39

Figure 3.3. Annotated photograph of the *(a)* front, and *(b)* rear, of the receiver (scale for reference) 43

Figure 3.4. Data acquisition and processing chain for the soil observation laser absorption spectrometer (SOLAS) instrument (note: simulated data).....44

Figure 3.5. Annotated plan view of the hermetically sealed box depicting the major components of the transmitter and the primary laser absorption spectrometer (LAS) receiver channel 46

Figure 3.6. Annotated photograph of the soil observation laser absorption spectrometer (SOLAS) instrument with major assemblies (transmitter, receiver, data acquisition and control) 47

Figure 4.1. Labeled photograph of the multi-channel optical receiver for the soil observation laser absorption spectrometer (SOLAS) 65

Figure 4.2. Schematic of the multi-channel optical receiver for the soil observation laser absorption spectrometer (SOLAS) instrument (not to scale).....66

Figure 4.3. Diameter of the field of view as a function of range for each of the soil observation laser absorption spectrometer (SOLAS) receiver channels including graphical representation of the field of view cross-sections for the three range distances (20, 35, and 60 m) tested in this paper (transmitted laser beam evolution as a function of range shown for reference).....68

Figure 4.4. Spectral reflectance as a function of wavelength for Spectralon® white reference panel, as acquired with the ASD FieldSpec 4 spectroradiometer through *(1)* receiver Channel 1 (uncoated, full-spectrum optics), and *(2)* receiver Channel 2 (NIR-optimized optics) without additional filtering, and *(3)* receiver Channel 2 with interchangeable narrowband filters (measured transmission peaks of 820 nm and 852 nm and full-width at half-maximum [FWHM] of 11 nm) 72

Figure 4.5. Relative spectral reflectance as a function of wavelength for four soil types (kaolinite, Ottawa sand, Donna Fill, and coarse river sand), as acquired with the ASD FieldSpec 4 spectrometer through receiver Channel 1, in a laboratory setting, for distances of 20, 35, and 60 m and an incidence angle of 32° 76

Figure 5.1. Labeled photograph of the laboratory setup, as used to collect proximal range spectral reflectance measurements with the ASD FieldSpec 4 Hi-Res spectroradiometer (pictured with calibrated Spectralon® reference panel as target).....86

Figure 5.2. Labeled photograph of the field setup, as used to collect intermediate range spectral reflectance measurements with the SOLAS telescope-enhanced receiver 92

Figure 5.3. Absolute reflectance spectra for dry specimens of *(a)* five soil types collected indoors at proximal ranges, *(b)* Ottawa sand, *(c)* bentonite soil, and *(d)* kaolinite soil, as compared with the USGS spectral library standards (Kokaly et al. 2017) 96

Figure 5.4. Absolute reflectance spectra for dry specimens of *(a)* kaolinite soil with a rough surface texture, and *(b)* Donna Fill with a rough surface texture, collected indoors at proximal ranges corresponding to equivalent field of view (FOV) diameters, as observed with the SOLAS at distances of 20, 35, 50, 60, and 100 m from the target 97

Figure 5.5. Reflectance spectra acquired indoors, at proximal range, and indoors at a range of 114 m for dry and wet specimens of *(a)* Ottawa sand and coarse river sand, *(b)* kaolinite soil, *(c)* bentonite soil, and *(d)* Donna Fill 99

Figure 5.6. Three independent sets of reflectance spectra acquired outdoors under solar illumination, over a period of 30 minutes, at a range of 40 m, for dry specimens of *(a)* Ottawa sand and coarse river sand, *(b)* kaolinite soil, *(c)* bentonite soil, and *(d)* Donna Fill 101

Figure 5.7. Reflectance spectra acquired indoors and outdoors, at proximal range, and outdoors at a range of 40 m for dry specimens of *(a)* Ottawa sand and coarse river sand, *(b)* kaolinite soil, *(c)* bentonite soil, and *(d)* Donna Fill 102

Figure 5.8. *(a)* Noise as a function of wavelength, as measured across the three detector ranges of the ASD FieldSpec 4 spectroradiometer (one visible near-infrared [VNIR] and two shortwave infrared [SWIR] detectors), and typical signal-to-noise ratios as functions of wavelength for *(b)* indoor and outdoor measurements acquired at proximal range, *(c)* indoor and outdoor, telescope-assisted measurements acquired at ranges of 100 m and 85 m, respectively, and *(d)* outdoor measurements acquired at proximal range and 85 m (telescope-assisted) 104

Figure A.1. Front panels of the model TLB-6800-LN tunable laser controllers displaying recommended current supply to the model TLB-6817 Vortex ECDL 127

Figure A.2. Optical isolators protecting *(a)* the 823.00 nm ECDL, *(b)* the 847.00 nm ECDL, and *(c)* the TSOA 128

Figure A.3. Plot of optical isolation and transmission as functions of wavelength for the Thorlabs IO-5-850-HP optical isolator (from Thorlabs 2019) 129

Figure A.4. Schematic of the Thorlabs TPA830P10-SP butterfly package tapered semiconductor optical amplifier with pin identification (from Thorlabs 2019).....130

Figure A.5. Dimensioned schematic of the Thorlabs TPA830P10-SP butterfly package tapered semiconductor optical amplifier (modified from Thorlabs 2019) 131

Figure A.6. View from open bottom of the butterfly package tapered amplifier mount (left) and open top of the optional fan base for additional thermal regulation (right).....132

Figure A.7. Front panel of the tapered amplifier mount with labelled DB-9 connector and DB-15 connector male plugs for cables with corresponding female sockets 132

Figure A.8. Drill pattern for the box floor and wall with cable throughputs 135

Figure A.9. Drill pattern for the box floor with additional mounting points 136

Figure A.10. Knife-edge mirror directing laser beams into a co-aligned laser path; pictured is the primary fiber-coupling stage replaced by an integrating sphere used to measure the laser power.....137

Figure A.11. Screenshots displaying integrating sphere power measurements along the laser path after co-alignment, immediately following the knife-edge mirror for *(a)* the 823.20 nm laser and *(b)* the 847.00 nm laser 137

Figure A.12. Ray diagram for *(a)* bi-convex, *(b)* best form spherical, *(c)* positive achromatic doublet, and *(d)* aspheric lens shapes (modified from Thorlabs 2019).....140

Figure A.13. Index of refraction as a function of wavelength of light for N-BK7 lens substrate (raw data from Thorlabs 2019) 141

Figure A.14. Light transmission as a function of wavelength for uncoated N-BK7 lens substrate (10 mm thick sample; raw data from Thorlabs 2019).....141

Figure A.15. Focal length shift as a function of wavelength for uncoated AL108 lens S-LAH64 substrate (raw data from Thorlabs) 142

Figure A.16. Focal length shift as a function of wavelength for uncoated AL1512 lens S-LAH64 substrate (raw data from Thorlabs) 142

Figure A.17. Light transmission as a function of wavelength for uncoated S-LAH64 lens substrate (10 mm thick sample; raw data from Thorlabs) 143

Figure A.18. Focal length shift as a function of wavelength for near-infrared coated AC080-010-B lens N-LAK22/N-SF6HT substrate (raw data from Thorlabs) 143

Figure A.19. Light transmission as a function of wavelength for NIR coated AC080-010-B lens N-LAK22/N-SF6HT substrate (raw data from Thorlabs) 144

Figure A.20. Focal length shift as a function of wavelength for NIR coated AC127-025-B lens (raw data from Thorlabs) 144

Figure A.21. Light transmission as a function of wavelength for NIR coated AC127-025-B lens N-LAK22/N-SF6HT substrate (raw data from Thorlabs) 145

Figure A.22. Light reflectance as a function of wavelength for broadband near-infrared anti-reflective coating (raw data from Thorlabs) 145

Figure A.23. Light transmission and optical density as functions of wavelength for FB820-10 narrow bandpass filter (raw data from Thorlabs) 146

Figure A.24. Light transmission and optical density as functions of wavelength for FB850-10 narrow bandpass filter (raw data from Thorlabs) 146

Figure B.1. Comparison of the effect of spectral sample size on the reflectance for the reference panel, measured at a range of 20 meters and an incidence angle of 35 degrees.....152

Figure B.2. Comparison of the effect of illumination angle (oblique = 20 degrees) on the reflectance for the reference panel, measured at a range of 20 meters and an incidence angle of 70 degrees 152

Figure B.3. Comparison of the effect of specimen orientation (in-plane rotation of 90 degrees) On the reflectance for an air-dry Ottawa sand specimen, measured at a range of 20 meters and an incidence angle of 35 degrees 153

Figure B.4. Comparison of the effect of range on the reflectance for an air-dry Ottawa sand specimen, measured at an incidence angle of 35 degrees.....153

Figure B.5. Comparison of the effect of idle time after calibration on the drift in data, Represented as reflectance over wavelength for the reference panel, measured at a range of 20 meters and an incidence angle of 35 degrees 154

Figure B.6. Comparison of the effect of idle time after calibration on the drift in data, represented as reflectance over wavelength for an air-dry Ottawa sand specimen, measured at a range of 50 meters and an incidence angle of 35 degrees.....154

Figure B.7. Comparison of the effect of incidence angle on the reflectance as a function of wavelength for the reference panel, measured at a range of 20 meters and for incidence angles of 35 and 70 degrees.....155

Figure B.8. Comparison of the effect of incidence angle on the reflectance as a function of wavelength for the reference panel, measured at a range of 50 meters and for incidence angles of 35 and 70 degrees.....155

Figure B.9. Comparison of the effect of incidence angle on the reflectance as a function of wavelength for the reference panel, measured at a range of 100 meters and for incidence angles of 35 and 70 degrees.....156

Figure B.10. Comparison of the effect of incidence angle on the reflectance as a function of wavelength for an air-dry Ottawa sand specimen, measured at a range of 20 meters and for incidence angles of 35 and 70 degrees.....156

Figure B.11. Comparison of the effect of range on the reflectance as a function of wavelength for the reference panel, measured at an incidence angles of 35 degrees 157

Figure B.12. Comparison of the effect of range on the reflectance as a function of wavelength for the reference panel, measured at an incidence angle of 70 degrees 157

Figure B.13. Comparison of the effect of indoor and outdoor environments on the spectral reflectance of a dry Ottawa sand specimen, measured at a range of 20 meters and an incidence angle of 35 degrees under artificial illumination (indoors) and 30 degrees under solar illumination (outdoors) 160

Figure B.14. Comparison of the effect of Spectralon panel referencing immediately before, or at an arbitrary time prior to measurement, on the reflectance of a dry Ottawa sand specimen, measured at a range of 20 meters and an incidence angle of 30 degrees under solar illumination 160

Figure B.15. Comparison of the effect of Spectralon® panel referencing immediately before, or at an arbitrary time prior to measurement, on the reflectance of a dry Donna Fill specimen (smooth and rough surface textures), measured at a range of 20 meters and an incidence angle of 30 degrees under solar illumination 161

Figure B.16. Comparison of the effect of Spectralon® panel referencing immediately before, or at an arbitrary time prior to measurement, on the reflectance of a dry kaolinite soil specimen (smooth and rough surface textures), measured at a range of 20 meters and an incidence angle of 30 degrees under solar illumination.....161

Figure B.17. Comparison of the effect of Spectralon® panel referencing immediately before, or at an arbitrary time prior to measurement, on the reflectance of a dry bentonite soil specimen, measured at a range of 20 meters and an incidence angle of 30 degrees under solar illumination (raw reflectance and relative reflectance values presented) 162

Figure B.18. Comparison of the spectra presented in Figure C.17 with the same spectra after a conventional splice correction procedure was applied 162

Figure B.19. Comparison of the bentonite spectrum presented in Figures 5 and 6 with the same spectrum after least-squares fit (Savitzky-Golay filter) smoothing.....163

Figure B.20. Noise-equivalent-radiance as a function of wavelength across the three detector ranges of the ASD FieldSpec 4 Hi-Res spectroradiometer (SN 18304).....165

Figure B.21. Signal-to-noise ratio as a function of wavelength for proximal measurements performed in the laboratory 166

Figure B.22. Signal-to-noise ratio as a function of wavelength for telescope-assisted measurements performed in an indoor environment (20-m range and 35-degree incidence angle, compared with 100-m range and 70-degree incidence angle).....166

Figure B.23. Signal-to-noise ratio as a function of wavelength for telescope-assisted measurements performed in an outdoor environment (20-meter range, 30-degree incidence angle, partially overcast sky, 10.5 °C air temperature, 65% humidity).....167

Figure B.24. Comparison of signal-to-noise ratios for telescope-assisted measurements performed in indoor and outdoor environments (data presented in Figures B.22 and B.23).....167

LIST OF TABLES

Table 3.1. Specifications of the soil observation laser absorption spectrometer (SOLAS) 40

Table 4.1. Specifications for the SOLAS instrument multi-channel receiver 69

Table 4.2. Statistical metrics for the baseline spectrum (Spectralon® panel) observed via Channel 1 73

Table 5.1. Summary of measurements acquired indoors, at proximal ranges, under artificial illumination 88

Table 5.2. Summary of measurements acquired outdoors, at proximal range, under solar illumination 89

Table 5.3. Summary of measurements acquired indoors, at a range of 114 m, under artificial illumination 90

Table 5.4. Summary of measurements acquired outdoors, at a range of 40 m, under solar illumination 93

Table A.1. Pin-wire-connector identification for the tapered semiconductor optical amplifier (TSOA), TSOA mount, TSOA controller, and thermoelectric-cooling 133

Table A.2. Pin identification for the TECPak DB-15 connector for thermoelectric-cooling of the TSOA mount cold plate and fan base control 133

Table A.3. Constants for the uncoated aspherical lenses 139

Table B.1. Summary of tests performed to study the influence of various factors on the data measured with the SOLAS instrument hyperspectral receiver 149

Table B.2. Summary of tests performed to study the influence of atmospheric effects on the data measured with the SOLAS instrument hyperspectral receiver 158

Table B.3. Statistical noise metrics for a typical hyperspectral baseline measurement (Salazar and Coffman 2019a) 164

LIST OF SYMBOLS AND ACRONYMS

Term	Definition
°	Degrees (angle)
°C	Degrees Celsius
%	Percent
α	Acceptance angle (fiber)
Γ	Efficiency of the inhomogeneous field distribution
δ	Sun declination
$\Delta\varphi$	Phase shift
Δt	Roundtrip time delay for atmospheric propagation
θ	Angular field of view (fore optic lens)
θ_a	Acceptance angle (fiber)
θ_c	Critical angle (fiber)
θ_s	Solar zenith angle
θ_v	Volumetric water content
λ	Wavelength (light)
λ_{on}	On-line wavelength
λ_{off}	Off-line wavelength
Λ	Voigt function
μm	Micrometer
ρ_v	Water vapor density
σ_{off}	Off-line water vapor absorption cross-section
σ_{on}	On-line water vapor absorption cross-section
σ_R	Range accuracy
τ	Chirp duration
Φ	Local latitude
ψ_m	Soil water matric potential (soil suction)
Ω	Ohm
A	Ampere
A_n	n^{th} order Aspheric coefficient (lens)
AC	Alternating Current
AFRL	Air Force Research Laboratory (USA)
AM	Amplitude Modulation
APD	Avalanche Photodetector (commonly "Avalanche Photodiode")
AR	Anti-Reflective
ASD	Analytical Spectral Devices Inc. (a Malvern Panalytical Company, Malvern, United Kingdom)
B	Signal Bandwidth
B_{RX}	Bandwidth of the receiver
BPD	Balanced Photodetector
BS	Beam Sampler
BSC	Beamsplitter Cube
c	Speed of light
cm	Centimeter
CO_2	Carbon dioxide

COTS	Commercial Off the Shelf
CSRC	Cato Springs Research Center (University of Arkansas)
CW	Continuous-Wave
CWL	Center Wavelength
CF	Clay Fraction
d	Beam diameter
dB	Decibel
dBm	Decibel milliwatt
D	Diameter of primary mirror (telescope)
D_f	Diameter of the fiber (core)
$D_{F.O.}$	Diameter of the Fore Optic lens
D_{fov}	Diameter of the field of view (appears also as D_{FOV})
DAQ	Data Acquisition
DC	Direct Current
Dia	Diameter (lens)
DIAL	Differential Absorption LIDAR
DRIFT	Diffuse Reflectance Infrared Fourier Transform
e_s	Saturation vapor pressure
e_{s0}	Saturation vapor pressure at T_0 = 273 K
E"	Lower state Energy
ECDL	External Cavity Diode Laser
EFL	Effective Focal Length
EM	Electromagnetic
EnMAP	Environmental Mapping and Analysis Program (Germany)
ENRC	Engineering Research Center (University of Arkansas)
Envisat	Environmental Satellite (ESA)
ESA	European Space Agency
FCS	Fiber-Coupling Stage
FM	Frequency Modulated
FMCW	Frequency-Modulated Continuous-Wave
FOV	Field of View (angular)
f	Focal length
$f_2 - f_1$	Chirp bandwidth
f_b	Focal length, back (lens)
f_{eff}	Focal Length, effective
f_f	Focal length, front (lens)
f_R	Beat frequency
FWHM	Full-Width at Half-Maximum
g	Electrode gap
GHz	Gigahertz
GND	Ground
GRIN	Graded-Index (multimode fiber)
h	Planck constant
h	Hour angle (local solar time)
h_1, h_2	Principal plane distances (lens)
H"	Back principal plane (lens)

HISUI	Hyperspectral Imager Suite (Japan)
HITRAN	High-resolution Transmission molecular absorption database
HyspIRI	Hyperspectral Infrared Imager (USA)
InGaAs	Indium Gallium Arsenide
IR	Infrared
IS	Integrating Sphere
ISO	Optical Isolator
k	Conic constant (lens)
k_B	Boltzmann constant
kHz	Kilohertz
km	Kilometer
$km \cdot h^{-1}$	Kilometers per hour
K	Chirp waveform-dependent constant
K	Kelvin (temperature)
KEM	Knife-Edge Mirror
L	Electrode Length
L	Latent heat of vaporization
LAS	Laser Absorption Spectrometry
LASER	Light Amplification by Stimulated Emission of Radiation (commonly "Laser")
LAST	Laser Analysis of Soil Tension
LIDAR	Light Detection and Ranging (commonly "Lidar")
$LiNbO_3$	Lithium Niobate
LL	Liquid Limit
LO	Local Oscillator
LWIR	Long-Wave Infrared
m	Meter
mm	Millimeter
mrad	Milliradian
mA	Milliampere
mW	Milliwatt
M	Dielectric Mirror
M	Number of Modes supported (multimode fiber)
M_{H2O}	Molecular weight of water
M-CRR	Multi-Channel Receiver Relay
MFD	Mode Field Diameter
MERIS	Medium Resolution Imaging Spectrometer
MHz	Megahertz
MM	Multimode (fiber)
MODTRAN	Moderate Resolution Atmospheric Transmission
MPE	Maximum Permissible Exposure
MWIR	Mid-Wave-Infrared
MZM	Mach-Zehnder Modulator
n	Index of refraction
n_3^3	Index of refraction (lithium niobate crystal)
n_{clad}	Refractive index of the cladding (fiber)

n_{core}	Refractive index of the core (fiber)
nm	Nanometer
N	F-Number
N_A	Avogadro's constant
NA	Numerical Aperture
NASA	National Aeronautics and Space Administration (USA)
NBF	Narrow Bandpass Filter
NC	No Connection
NEdL	Noise-Equivalent-Radiance
NI	National Instruments (Austin, Texas, USA)
NIR	Near-Infrared
O_2	Molecular oxygen
O_3	Trioxygen (commonly "Ozone")
OST-R	Office of the Assistant Secretary for Research and Technology
P	Optical output Power
PANDA	Polarization-maintaining and Absorption-reducing
PI	Plasticity Index
PL	Plastic Limit
PM	Polarization-Maintaining (fiber)
P_{max}	Maximum Power
P_{min}	Minimum Power
$P_{n\text{-}RX}$	Receiver Power noise
P_{off}	Received off-line backscatter signal
P_{on}	Received on-line backscatter signal
PPE	Pressure Plate Extractor
P_r	Received signal Power
PRISMA	Precursore Iperspettrale della Missione Applicativa (Italy)
P_{sig}	Detected signal Power
PXIe	PCI (Peripheral Component Interconnect) extensions for Instrumentation express
q	Electron charge
r_{33}	Electro-optic coefficient
r_{core}	Core radius (fiber)
r_{FOV}	Radius of the Field of View
r_t	Radius of the telescope lens
rad	Radian
$\Re$	Photodetector Responsivity
R	Range to target
R	Radius of curvature (lens)
R	Reflectance
R_{REF}	Reference Reflectance
R_v	Water vapor gas constant
RF	Radio Frequencies
RH	Relative Humidity
RPAS	Remotely Piloted Aircraft System
s	Second

sr	Steradian
S	Shutter
S	Temperature-dependent absorption line Strength
S_0	Absorption line Strength under standard conditions
SEM	Scanning Electron Microscope
Si	Silicon
SM	Single Mode (fiber)
SMA	SubMiniature version A
SMC	Soil Moisture Content
SNR	Signal-to-Noise Ratio
SNR_{coh}	Signal-to-Noise Ratio for shot-noise-dominant coherent detection
SOLAS	Soil Observation Laser Absorption Spectrometer
SPIE	Society of Photo-Optical Instrumentation Engineers (USA)
SSURGO	Soil Survey Geographic database
STATSGO	State Soil Geographic survey
SWCC	Soil Water Characteristic Curve
SWIR	Short-Wave Infrared
t_c	Center thickness (lens)
t_e	Edge thickness (lens)
T	Temperature
T_0	Absorption Temperature under standard conditions
TEC	Thermoelectric-Cooled
TL	Thorlabs Inc. (Newton, New Jersey, USA)
TSOA	Tapered Semiconductor Optical Amplifier
UHTC	Ultra-High Transmission Coating (Meade Instruments Corporation, Irvine, California, USA)
USDOT	United States Department of Transportation
USGS	United States Geological Survey
UV	Ultraviolet
V	Normalized frequency, V-Number (fiber)
V	Voltage
V_0	Offset Voltage (reference)
V_π	Half-wave Voltage
VBE	Variable Beam Expander
VNIR	Visible Near-Infrared
VSA	Vector Signal Analyzer
W	Watt
Y	Radial distance from optical axis (lens)
z	Sag (lens surface profile)

LIST OF PUBLISHED OR SUBMITTED PAPERS

Chapter 3: Development of a Multimode Field Deployable Lidar Instrument for Topographic Measurements of Unsaturated Soil Properties: Instrument Description. Published as: *Salazar, S.E., Garner, C.D., Coffman, R.A. (2019). "Development of a Multimode Field Deployable Lidar Instrument for Topographic Measurements of Unsaturated Soil Properties: Instrument Description." Remote Sensing, Vol. 11, No. 3, 289. doi:10.3390/rs11030289.*

Chapter 4: Multi-Channel Optical Receiver for Ground-Based Topographic Hyperspectral Remote Sensing. Published as: *Salazar, S.E., Coffman, R.A. (2019). "Multi-Channel Optical Receiver for Ground-Based Topographic Hyperspectral Remote Sensing." Remote Sensing, Vol. 11, No. 5, 578. doi:10.3390/rs11050578.*

Chapter 5: Validation of a Ground-Based Telescope-Assisted Hyperspectral Remote Sensor. Submitted as: *Salazar, S.E., Coffman, R.A. (2019). "Validation of a Ground-Based Telescope-Assisted Hyperspectral Remote Sensor." Journal of Applied Remote Sensing. Submitted for Review. Manuscript ID: JARS 190527.*

CHAPTER 1: INTRODUCTION

1.1. Chapter Overview

The development of a field-deployable lidar instrument for topographic hyperspectral measurements is described in this document. The instrument, designated the Soil Observation Laser Absorption Spectrometer (SOLAS), was designed to provide range-resolved and atmosphere-corrected hyperspectral analysis of bare soil surfaces and other targets at ranges of up to 1 km from the instrument. This document provides a detailed description of the development, fabrication, and testing of the instrument. An overview of the work that is described in this document is contained in Section 1.2. The need for the research is discussed in Section 1.3. A summary of the document in its entirety is provided in Section 1.4.

1.2. Description of the Work

The SOLAS instrument, that is described in this document, was designed to collect topographic, hyperspectral reflectance measurements that are used to infer unsaturated soil properties. The SOLAS is comprised of 1) an active transmitter (depicted in Figure 1.1) that propagates alternating laser wavelengths, and 2) a receiver that collects target backscatter. The transmitted energy is used to measure water vapor along the target-receiver path using a differential absorption technique, while simultaneously detecting the range to the target. In addition to collecting the backscatter from the transmitted lasers, the receiver measures continuous, high-resolution reflectance from the target using a hyperspectral sensor. The water vapor measurements are used to correct long-range spectral reflectance data. An overview of the SOLAS data acquisition and processing chain is included as Figure 1.2.

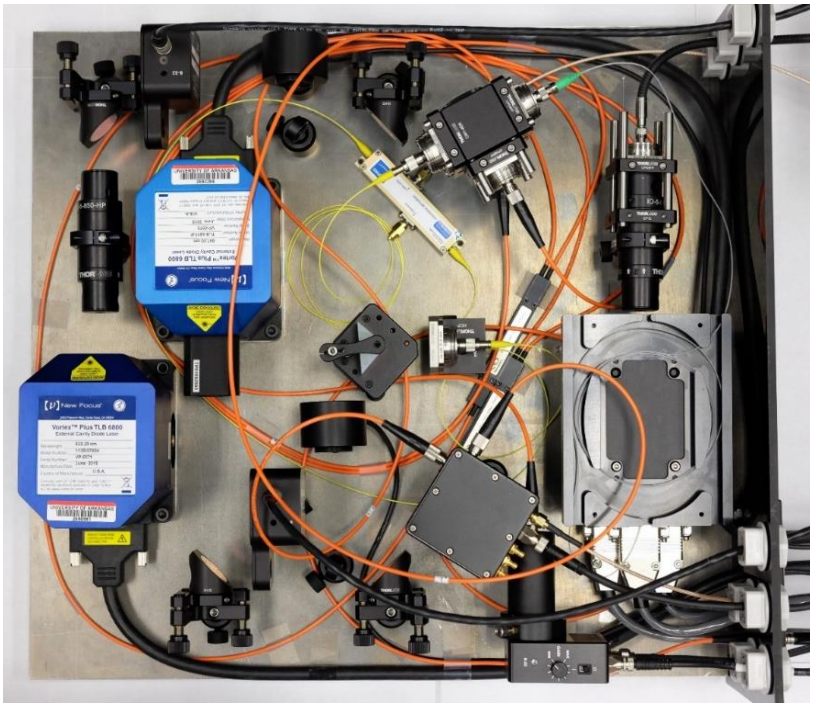

Figure 1.1. Plan view of the internal components of the SOLAS transmitter box.

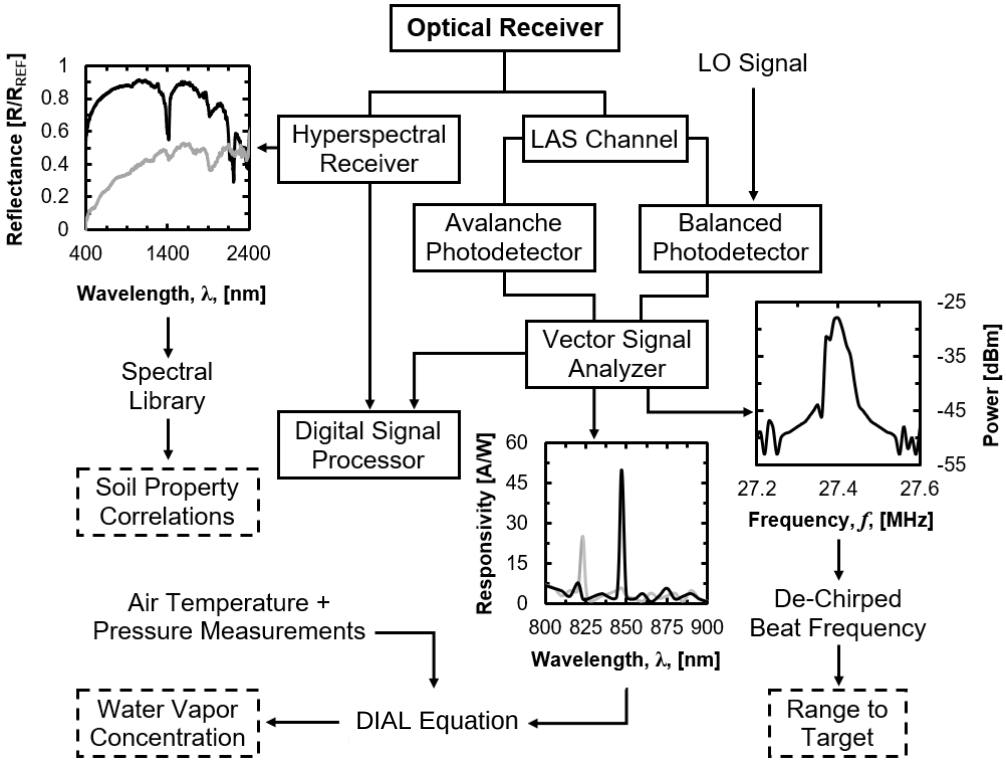

Figure 1.2. Overview of the SOLAS data acquisition and processing chain (modified from Salazar et al. 2019).

The theory behind the SOLAS was introduced and each of the instrument systems (transmitter, receiver, data acquisition) was designed and fabricated, as described in Salazar et al. (2019), presented as Chapter 3 in this document. The multi-channel optical receiver system was discussed in more detail in Salazar and Coffman (2019a), presented as Chapter 4 in this document. Hyperspectral reflectance measurements, acquired at intermediate ranges with the SOLAS receiver, were demonstrated in Salazar and Coffman (2019b), presented as Chapter 5 in this document.

1.3. Motivation

The motivation for the work is presented in this section. The limitations of current techniques of obtaining soil properties are described in Section 1.3.1. The significance of the work for the geotechnical engineering field is discussed in Section 1.3.2.

1.3.1. *Limitations of Current Techniques*

Conventional methods of obtaining properties of soils involve in situ testing using individually calibrated instruments installed into the ground, or more commonly, laboratory testing on samples recovered from the field. While these methods are essential to almost any site investigation, the data are 1) expensive to gather, 2) time-consuming to evaluate, and 3) spatially limited. Unconventional site characterization techniques, using non-destructive methods like geophysics and remote sensing, are already well established in the geosciences and other related disciplines. While geophysical methods are routinely performed as part of geotechnical site investigations, remotely sensed data, other than photography, are rarely utilized.

Remote sensing techniques are well suited for observation of vegetated and non-vegetated surfaces over vast, hazardous, or otherwise inaccessible areas. However, existing practices of collecting remotely sensed data are still limited. For example, data collected from

optical sensors aboard airborne and spaceborne platforms (i.e. multispectral imagery), suffer from low spatial, temporal, and radiometric resolution, while data collected proximally (i.e. hyperspectral measurements) are range limited, requiring personnel to spend a long time in the field collecting data. Continuous, high spectral resolution sensors have yet to overcome payload limitations aboard remotely piloted aircraft systems (RPAS) and manned aircraft missions are cost-prohibitive and require telemetry corrections. To address the need to collect high-resolution, timely, and site-specific soils information, the SOLAS was developed. The SOLAS was designed to facilitate measurements at the field scale, while keeping deployment feasibility and cost in mind.

1.3.2. *Significance for Geotechnical Engineering*

The majority of near-surface (i.e. above the water table) soil mechanics are governed by soils that are in an unsaturated (partially saturated) condition. Unsaturated soil behavior (e.g. shear strength, permeability) is controlled by parameters of the soil including volumetric water content, soil matric potential (suction), and clay mineralogy. The geotechnical engineering community has recognized the importance of unsaturated soil behavior and therefore efforts to account for and to model unsaturated soil behavior are becoming increasingly prevalent in engineering design.

The ability to infer and quantify saturated and unsaturated soil properties using a remote sensor has the potential to improve the current state of the practice of data collection. With the SOLAS technology, data may be collected from afar and on-demand from a single vantage point, all of which improve site accessibility and collection efficiency. Despite the initial buy-in costs, savings may be realized over time through the low cost-per-area application of the remote sensing technique. The disadvantage of collecting these measurements remotely is the limitation

on penetration depth. Like most other remote sensing techniques, measurements are acquired from reflected energy from the surface of the soil; values beneath the surface must be estimated through correlation to the surface measurement.

The envisioned applications for the SOLAS technology, within the realm of geotechnical engineering, include monitoring of soils on unstable slopes (e.g. shallow debris flows), and in large earth construction projects (e.g. mine faces and tailings dams). While some fields of engineering have started to incorporate remote sensing techniques to gather data, these techniques are an underutilized tool. Geotechnical and geological engineering fields stand to benefit from recent advances in remote sensing technologies like the SOLAS.

1.3.3. *Broader Applications*

The applications for the SOLAS remote sensor extend beyond the immediate scope of geotechnical engineering. The technology may ultimately be used to rapidly characterize soils, rocks, minerals or vegetation for diverse applications. Examples include agricultural science, economic geology, and ecologic research. The technology could also be used to ground truth future satellite-based multi- and hyperspectral datasets.

The SOLAS instrument was designed and assembled utilizing almost entirely commercial-off-the-shelf (COTS) parts. Although this drove up the total cost of the instrument, it eliminated the need for in-house, custom part fabrication. The use of COTS parts is an attractive attribute of the instrument because the same parts are available for future prototype iterations that wish to adapt the design of the instrument.

1.4. Document Overview

This document is comprised of six chapters. The motivation for the work and an overview of the document were provided in this chapter (Chapter 1). Background information

for the various topics encompassed within the work is provided in Chapter 2. Three consecutive, archival journal publications, presented in the order in which the manuscripts were conceived and prepared for publication, are included as Chapters 3, 4, and 5. Specifically, the concept of the SOLAS is introduced and the development of the instrument are outlined in Chapter 3. A more detailed description and first tests of the SOLAS receiver are presented in Chapter 4. Laboratory and field testing methods and results, used to validate the effectiveness of the hyperspectral receiving portion of the SOLAS, are described in Chapter 5. Concluding remarks regarding the work are presented in Chapter 6. A comprehensive list of works cited in this document is provided in Chapter 7. Finally, miscellaneous component design and testing are presented in Appendix A, while additional sensitivity testing results and noise characterization are included in Appendix B.

1.5. References

Salazar, S. E. and Coffman, R. A., 2019a, "Multi-Channel Optical Receiver for Ground-Based Topographic Hyperspectral Remote Sensing," *Remote Sens.*, Vol. 11, No. 5, 578. doi:10.3390/rs11050578.

Salazar, S. E. and Coffman, R. A., 2019b, "Preliminary Measurements from a Ground-Based Telescope-Assisted Hyperspectral Remote Sensor," *J. Appl. Remote Sens.* Submitted for Review. Manuscript Number: JARS 190527.

Salazar, S. E., Garner, C. D., and Coffman, R. A., 2019, "Development of a Multimode Field Deployable Lidar Instrument for Topographic Measurements of Unsaturated Soil Properties: Instrument Description," *Remote Sens.*, Vol. 11, No. 3, 289. doi:10.3390/rs11030289.

CHAPTER 2: BACKGROUND

2.1. Chapter Overview

An overview of the topics related to the development of the SOLAS instrument is provided in this chapter. The motivation for the work is outlined in Section 2.2. The literature was reviewed for optical remote sensing techniques that have been used to infer soil properties in Section 2.3. The concepts behind various electronic components that utilized in this work are described in Section 2.4.

2.2. Motivation

As early as 1960, Bishop et al. (1960) described the importance of understanding unsaturated soil properties for determination of the shear strength of soils. The understanding of unsaturated soil properties continues to receive scrutiny today. Soil water matric potential, also described as negative pore water pressure, or soil suction, is of particular concern to geotechnical engineers. This parameter often controls the effective stress within a soil deposit; thereby it controls the behavior of the soil. Soil suction is of particular interest in the context of slope stability. Slope failures have been attributed to the dissipation of near-surface suction within the soil deposit and a corresponding reduction in shear strength (Brackley et al. 1971, Lumb 1975, Fredlund 1981, Ho et al. 1982, Krahn et al. 1989, Blatz et al. 2004, Lu and Kaya 2014).

The unsaturated, near-surface slope failure mechanism, common to non-fire-affected areas, is also frequently observed in the form of post-wildfire debris flows in wildfire-affected areas. In the last decade, wildfires in the United States have burned an average of 26,080 km^2 of land (National Interagency Fire Center 2018). Many of these wildfires occur in mountainous areas, such as in the Intermountain West and in southern California. Following various fire events, denuded soil slopes are susceptible to debris flows, which may disrupt traffic, destroy

homes, and threaten human life. Although these debris flow events have been difficult to predict, probabilistic modeling techniques continue to improve the prediction capability (Gartner et al. 2008, Cannon et al. 2010, Negri 2016, Kern et al. 2017). The understanding of unsaturated soil properties, as associated with those predictive models, may be critical to the prediction of post-wildfire debris flows.

To date, there is a lack of data for these soil types. Information about the soil is not commonly collected. Rather, the soil properties are estimated based on existing regional databases (e.g. the State Soil Geographic Survey [STATSGO] or the Soil Survey Geographic Database [SSURGO]). The small amount of data that are available are typically too dispersed to be useful for site-specific, predictive models, because the data were collected with low spatial or low temporal resolution from airborne or spaceborne sensors, or from traditional in-situ instrumentation. Moreover, the static nature of the data does not accurately capture the time-variability, due to environmental and hydrological factors.

For the aforementioned example of post-wildfire debris flows, satellite-based remote sensing techniques are frequently used to establish the perimeter of a wildfire by assessing the remaining vegetative cover, and to estimate the burn severity after containment. Remotely sensed data, acquired from airborne and spaceborne sensors, often require ground truthing to calibrate the data. However, the proximal ground-truthing methods are often spatially limited and cannot cover large or inaccessible areas. Wildfire burn sites are well suited for the application of remote sensing techniques, due to fire-induced loss of vegetation. Therefore, there is a need to collect site-specific soils data using high spatial, temporal, and spectral-resolution remote sensing techniques.

2.3. Optical Remote Sensing of Soils

Various remote and proximal sensing techniques using wavelengths in the infrared range of the electromagnetic (EM) spectrum (presented in Figure 2.1), including the visible near-infared (VNIR), shortwave infrared (SWIR), mid-wave-infrared (MWIR), and long-wave infrared (LWIR) bands, as well as wavelengths in the microwave portion of the EM spectrum have been used to obtain soils information (Wulf et al. 2015). The information contained in the following sections is focused on multispectral and hyperspectral techniques in the VNIR and SWIR wavelength ranges.

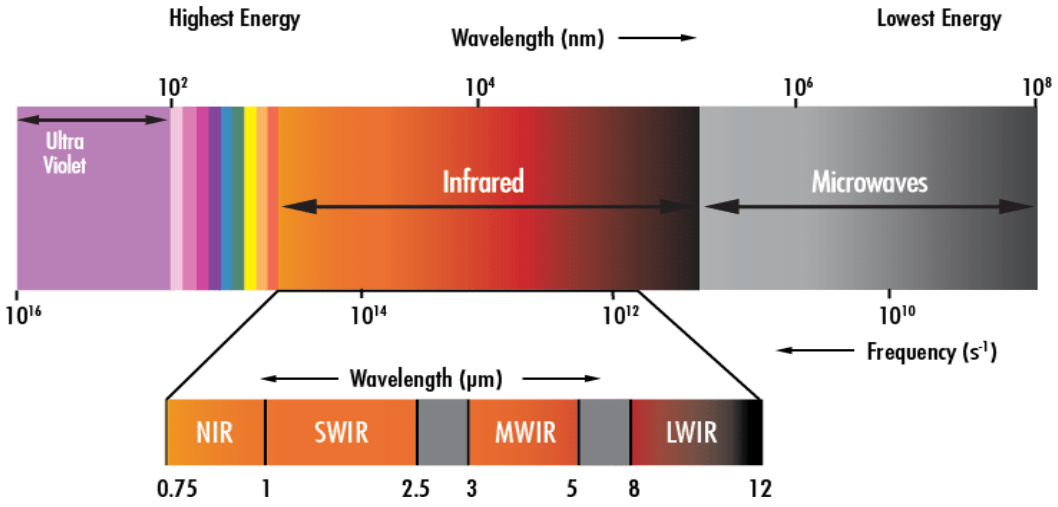

Figure 2.1. Wavelengths in the electromagnetic spectrum that are used for optical remote sensing techniques (Edmund Optics 2012).

2.3.1. *Satellite-Based Optical Remote Sensing*

Multispectral sensors aboard satellite platforms have been designed to collect radiometric information in the VNIR and SWIR wavelength ranges (e.g. the ESA Copernicus and USGS/NASA Landsat missions). The Copernicus Sentinel-2 constellation (Sentinel-2A was launched in 2015 and Sentinel-2B was launched in 2017) utilizes multispectral imagers designed for land monitoring. For example, Castaldi et al. (2019a, 2019b), used Sentinel-2 data to

estimate soil organic carbon content in cropland topsoils. The Sentinel-2 and Sentinel-3 constellations have replaced the Medium Resolution Imaging Spectrometer (MERIS) sensor aboard the ESA Envisat satellite.

There are advantages to collecting data from spaceborne platforms. Specifically, data are routinely acquired over large areas without the need for specific requests. Moreover, historic data are often available to study phenomena over long periods of time. However, there are also many disadvantages. For example, optical imagery is highly susceptible to atmospheric conditions (e.g. cloud cover) and data acquisitions are limited by the repeat pass interval. Furthermore, the Earth's atmospheric transmittance, presented as a function of wavelength in Figure 2.2, limits the spectral regions in which useful information can be derived. The majority of the scattering and absorption in the visible to near-infrared wavelengths is due to water vapor (H_2O) in the atmosphere, but also ozone (O_3), oxygen (O_2), and carbon dioxide (CO_2) gases (Clark 1999). There are numerous atmospheric transmittance and radiance models designed to correct atmospheric effects. For instance, the Moderate Resolution Atmospheric Transmission (MODTRAN) model (Berk et al. 2014, 2015) was developed through the collaboration of Spectral Sciences, Inc. and the Air Force Research Laboratory (AFRL).

The spectral resolution of sensors aboard spaceborne platforms is relatively coarse (tens of nm), while measurements are limited to discrete bands (e.g. Sentinel-2 uses 12 bands). The high spectral-resolution (< 10 nm) of continuous (hundreds of bands), hyperspectral imaging offers many advantages over multispectral imaging. Although several airborne missions (e.g. EO-1 Hyperion, HyMap, HySpex, HyspIRI) have provided limited hyperspectral datasets, there are currently no operational satellite-based hyperspectral missions. Despite the technical and operational challenges of spaceborne hyperspectral imaging, keen interest by government

agencies and research communities for a range of Earth science and applications remains (HyspIRI 2018). Forthcoming missions, for example EnMAP (Guanter et al. 2015) and PRISMA (Guarini et al. 2018), are scheduled to provide hyperspectral imaging from space.

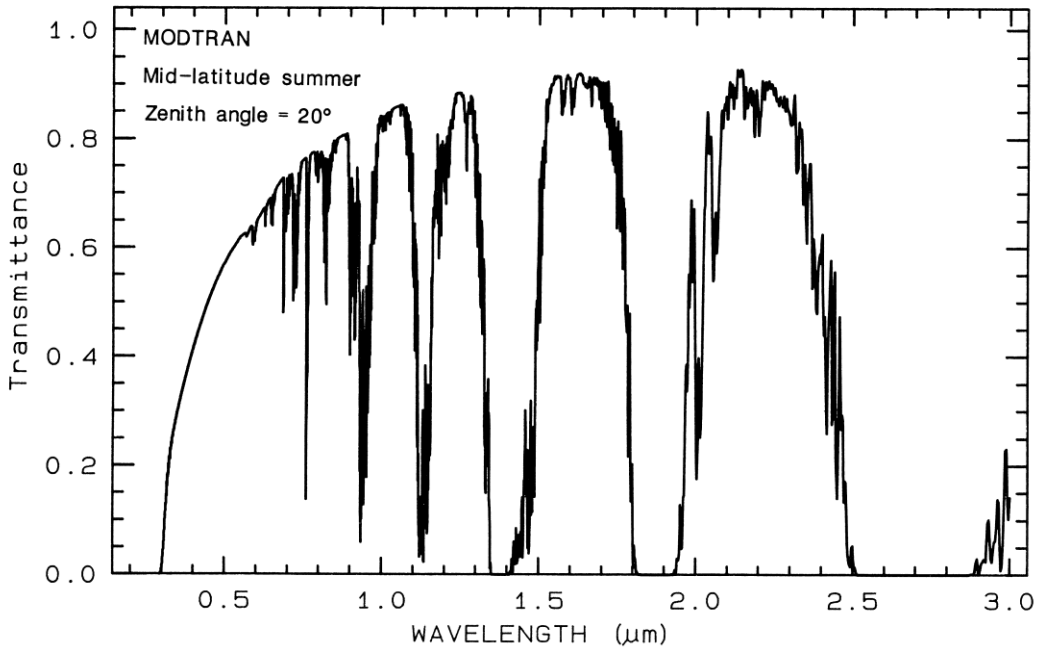

Figure 2.2. Modeled transmittance of the Earth's atmosphere, as a function of wavelength (from Berk et al. 1989).

2.3.2. *Ground-Based Reflectance Spectroscopy*

Reflectance spectroscopy, using laboratory and field-based measurement techniques, is a mature science. Spectroscopy measurements in the 380 nm to 2500 nm range are sensitive to many physical and chemical material properties, such as moisture content, crystalline structure and mineralogy, making it well suited to the study of rocks, minerals, and soils. The correlation between reflectance and soil moisture was observed as early as Ångström (1925). However, recent advances in compact and portable measurement techniques of solar irradiation reflectance spectra have enabled estimation of the soil moisture content (SMC) in the laboratory setting

(Bowers and Hanks 1965, Park 1980, Dalal and Henry 1986, Whalley et al. 1991, Bach and Mauser 1994, Ben-Dor and Banin 1995, Chang et al. 2001, Hummel et al. 2001, Liu et al. 2002, 2003, Lobell and Asner 2002, Islam et al. 2003, Whiting et al. 2004, Mouazen et al. 2006, Whiting 2009, Lesaignoux et al. 2013, Knadel et al. 2014, Nolet et al. 2014, Oltra-Carrió et al. 2015, Fabre et al. 2015, Sadeghi et al., 2015, Tian and Philpot 2015, Philpot and Tian 2016, Xu et al. 2016, Garner 2017).

For instance, a useful indicator in the determination of the SMC of a wet soil is the absorption band depth, because light in the SWIR range is heavily absorbed by water (Tian and Philpot 2015). The band depth for a given absorption feature may be estimated from the vertical distance from the reflectance spectra minima to a horizontal line between the shoulders of the feature, as described by Lobell and Asner (2002) and Morris et al. (1982) and presented in Equations 2.1 and 2.2.

$$R_{int} = \frac{R_{left} - R_{right}}{\lambda_{left} - \lambda_{right}} \cdot \left(\lambda_{center} - \lambda_{left}\right) + R_{left} \qquad \text{Equation 2.1.}$$

$$\Delta R_c = R_{int} - R_c \qquad \text{Equation 2.2.}$$

In Equation 2.1., R_{int} is the interpolated reflectance, R_{left} and R_{right} are the reflectance at the left and right shoulders, respectively, λ_{left}, λ_{right}, λ_{center} are the wavelengths at the left and right shoulders, and the center of the absorption band, respectively. In Equation 2.2., R_c is the reflectance at the band center.

The measurements in the aforementioned studies, were determined using laboratory-prepared and/or dilute soil specimens. Fewer studies have been conducted in the field setting (Mouazen et al. 2007, Haubrock et al. 2008, Xu et al. 2016). Numerous other soil reflectance correlations have been described in the literature, including grain size (Leu 1977, Chang et al. 2001, Shepherd and Walsh 2002, Cozzolino and Moron 2003, Curcio et al. 2013), clay content

(Chang et al. 2001, Walvoort and McBratney 2001, Shepherd and Walsh 2002, Cozzolino and Moron 2003, Islam et al. 2003, Knadel et al. 2013, Garner 2017), soil plasticity (Yitagesu et al. 2009, Waruru et al. 2014, Garner 2017) and matric potential (Garner 2017). Ben-Dor et al. (2009) provided a comprehensive review of the soil properties that have been derived using reflectance techniques.

Garner (2017) used a Diffuse Reflectance Infrared Fourier Transform (DRIFT) technique in conjunction with conventional laboratory testing methods to derive an empirical relationship between reflectance spectra and soil plasticity for illite and kaolinite soils and a synthetic fill material (Donna Fill). The mineralogy of the tested soils is presented in Figure 2.3. The properties for these soils were well documented through studies conducted at the University of Arkansas and have also commonly been characterized in other studies of expansive soils (e.g. Yitagesu et al. 2009).

Garner (2017) also developed a Laser Analysis of Soil Tension (LAST) technique to infer the soil-water-characteristic-curve (SWCC) for dilute soil specimens that were prepared in a pressure plate extractor (PPE). The LAST technique used two near-infrared laser diodes and reflectance measurements collected with a high radiometric-resolution spectrometer (ASD FieldSpec 4 Hi-Res; Malvern Panalytical, Longmont, Colorado, USA) to relate volumetric water content (θ_v) and soil matric potential (ψ_m) empirically through the SWCC.

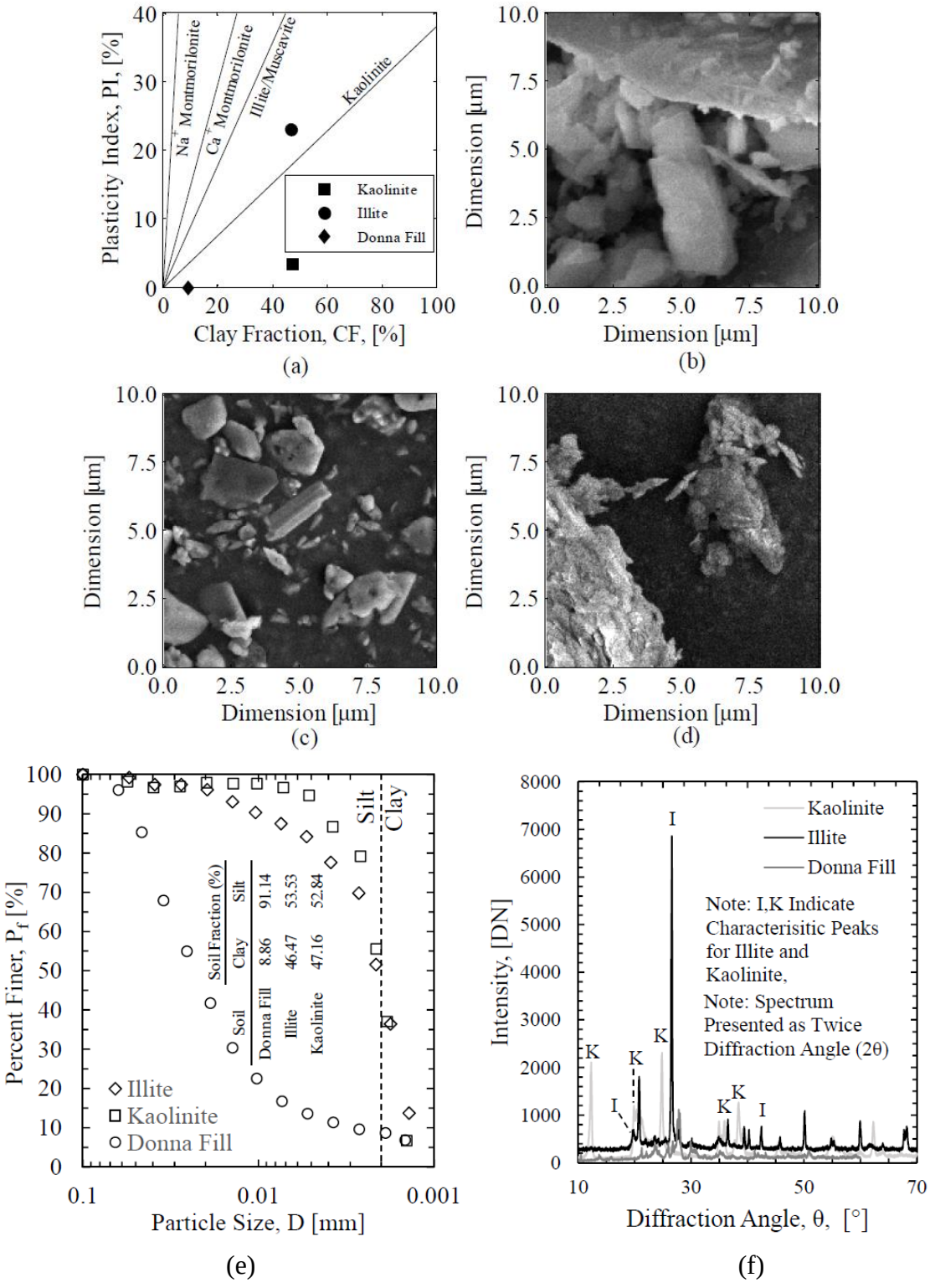

Figure 2.3. Mineralogy of soils determined using *(a)* traditional index testing (chart modified from Terzaghi et al. 1996) and scanning electron microscopy (SEM) for *(b)* Donna Fill, *(c)* Illite, and *(d)* Kaolinite soils; Particle distribution of the soils as obtained by using ASTM D422 (2007) (from Garner 2017).

2.4. Concepts of Electronic Component Design

To understand the unique properties of the electronic components that are featured in this work, the following sub-sections are dedicated to discussion of the general theory and principles of each of the major components that are included in Chapter 3. Frequency-modulated continuous-wave (FMCW) lidar theory is described in detail in Chapter 3 (Section 3.6.1.), while differential absorption lidar (DIAL) theory is also explained in Chapter 3 (Section 3.6.2.).

2.4.1. *Tuned Laser Source*

Recent advances in laser diode technology have significantly improved applications that demand high precision and tunable, single-frequency lasers, like high-resolution spectroscopy, or lidar systems. A class of lasers, called external cavity diode lasers (ECDL) provide extremely narrow linewidths (full-width at half-maximum [FWHM] of the optical spectrum). A schematic of the internal components of a Littman-Metcalf ECDL is provided in Figure 2.4.

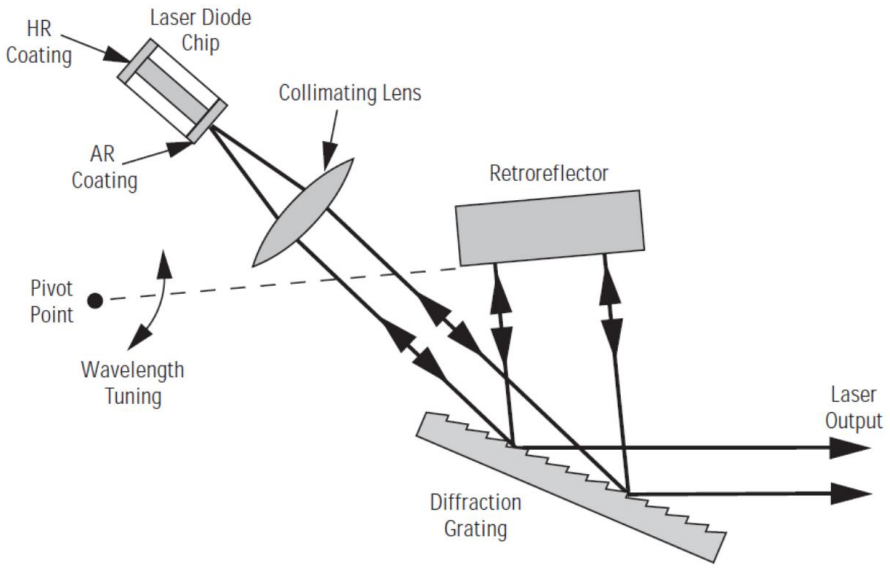

Figure 2.4. Tunable external cavity diode laser in the Littman-Metcalf configuration (New Focus 2014).

2.4.2. *Fiber Optics*

Optical fiber is commonly used to transmit information in the form of light signals that are propagated along the length of the fiber. Fiber optic cables are manufactured with various configurations, but common to all types of fiber optic cables are the core, surrounded by the cladding, and the reinforcement (such as coatings, or jackets). Depending on the desired application, the fiber material may be extruded from pure or doped silica, phosphate, fluoride, or plastic materials. For near-infrared and infrared optical waveguide applications, such as laser delivery, the core typically consists of pure fused silica, while the cladding is made of a glass with a lower refractive index, causing light to propagate entirely within the core due to total internal reflection.

Depending on the application, the fiber may be configured for single mode (SM) propagation, where light is transferred only in the transverse mode, or multimode (MM) propagation, which supports multiple propagation modes in step-index or graded-index (GRIN) formats (Figure. 2.5). A special type of SM fiber, called polarization-maintaining (PM) fiber, further limits the propagation of light to a single polarization using systematic birefringence. This birefringence is commonly attained with asymmetric fiber geometry or refractive properties, or by the inclusion of stress rods within the cladding surrounding the core (e.g. bow-tie or Polarization-maintaining AND Absorption-reducing [PANDA] designs, as presented in Figure 2.4).

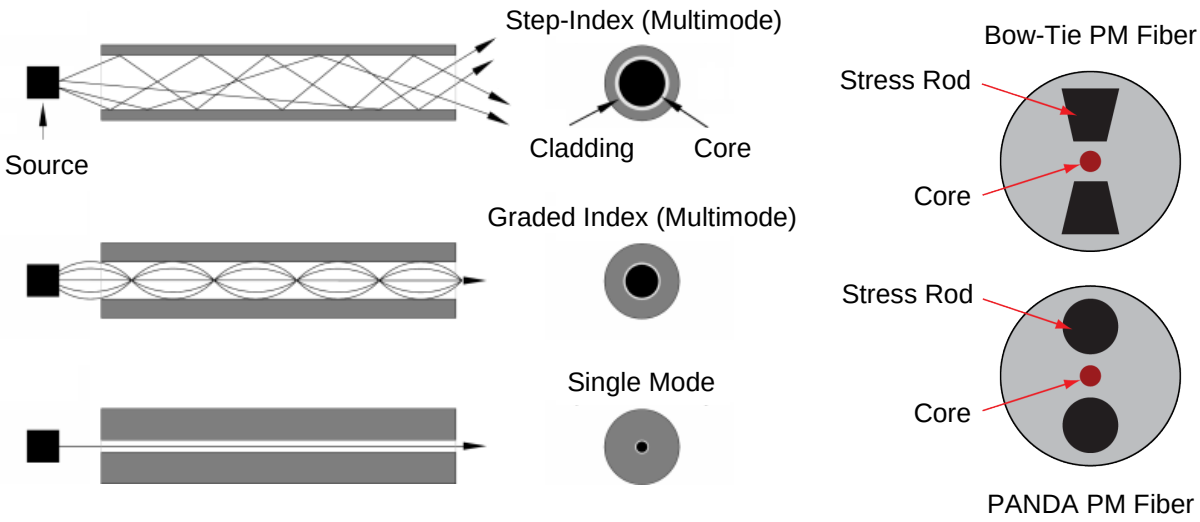

Figure 2.5. Typical cross-sections for single mode fiber, step-index and graded index (GRIN) multimode fiber, and bow-tie and PANDA polarization-maintaining fiber (modified from Thorlabs 2018).

While attenuation losses in fiber-based laser transmission are minimal over short distances (even with some losses due to scattering, micro- and macro-bending, and mode dispersion), efficiency is typically reduced in the termination at the ends of the fiber and in the connectors. Focusing and collimating lenses are utilized to couple light into and out of the fiber, respectively, where the launch conditions must be carefully considered (Figure 2.6). The acceptance angle, α (Figure 2.7) the numerical aperture (NA), the number of modes, and the mode field diameter (MFD), a measure of the distribution of the irradiance on the fiber end face, are all important parameters to consider in fiber optic design. Given properties of the fiber, the design parameters may be calculated using Equations 2.3 through 2.6 for typical step-index fibers.

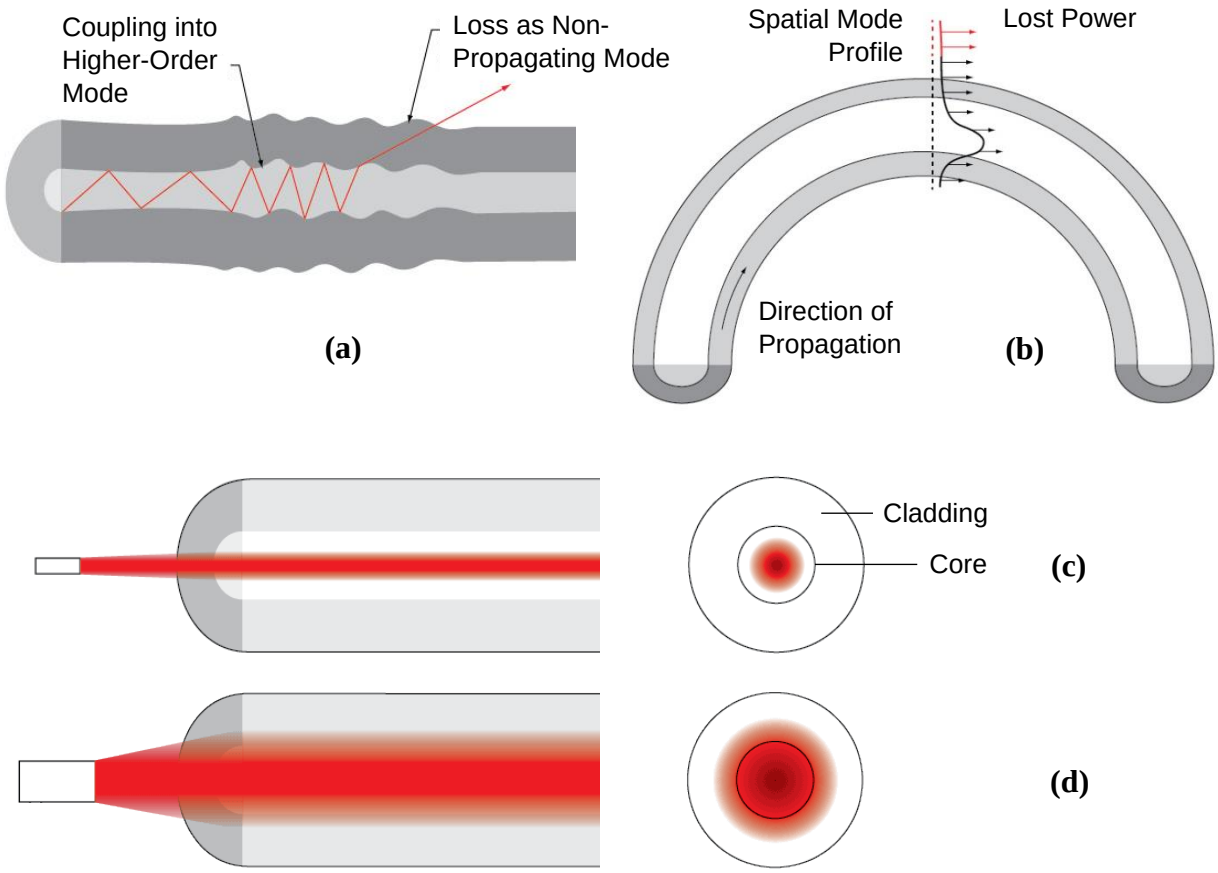

Figure 2.6. Loss of power in fiber optics due to *(a)* micro-bending and *(b)* macro-bending, and fiber optic coupling with *(c)* underfilled and *(d)* overfilled launch conditions (modified from Thorlabs 2018).

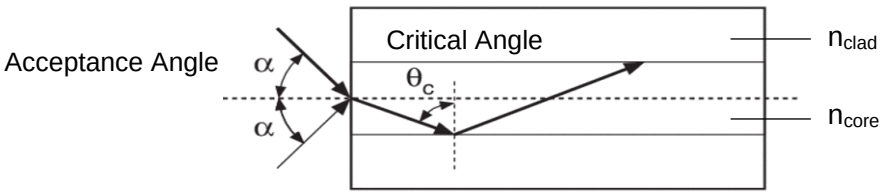

Figure 2.7. Numerical aperture for total internal reflection (modified from Newport 2018).

$$\sin\theta_c = \frac{n_{clad}}{n_{core}}$$ Equation 2.3

$$NA = n \cdot \sin\alpha = \sqrt{n_{core}^2 - n_{clad}^2}$$ Equation 2.4

$$V = \frac{2 \cdot \pi \cdot r_{core}}{\lambda} \cdot NA$$ Equation 2.5

$$M \approx \frac{V^2}{2}$$ Equation 2.6

In Equation 2.3, θ_c is the critical angle, and n_{clad} and n_{core} are the indices of refraction for the cladding and the core of the fiber, respectively. In Equation 2.4, NA is the numerical aperture, n is the index of refraction of the medium surrounding the cable (air), and α is the acceptance angle of the fiber. In Equation 2.5, V is the normalized frequency (V-number), r_{core} is the fiber core radius, and λ is the wavelength (in air). In Equation 2.6, M is the number of modes supported.

2.4.3. *Electro-Optic Modulation*

Light signals traveling through a fiber optic cable may be modulated with integrated optical waveguides, such as amplitude, phase, or polarization modulators. The underlying principle of waveguide modulators is the linear electro-optic effect (also known as the Pockels effect). The change in the refractive index of an optical material, due to the application of an external electric field, causes a modulation of the signal. Ferroelectric crystals, such as lithium niobate ($LiNbO_3$), are commonly used in electro-optic modulators, due to their polar properties. A type of modulator called a Mach-Zehnder amplitude modulator combines phase modulation (Equation 2.7) with a Mach-Zehnder interferometer. A voltage is applied to the electrodes on both branches of the modulator to interfere the signal, causing an increase in the optical output power of the linear polarized light. The output power varies periodically and may be calculated using Equations 2.7 through 2.9.

$$\Delta\varphi = -\frac{\pi \cdot L}{\lambda} \cdot n_3^3 \cdot r_{33} \cdot \frac{V}{g} \cdot \Gamma \qquad \text{Equation 2.7}$$

$$P = P_{min} + (P_{max} - P_{min}) \left(\frac{1}{2} \cdot cos \left(\frac{\pi \cdot (V - V_0)}{V_\pi} \right) + \frac{1}{2} \right) \qquad \text{Equation 2.8}$$

$$V_\pi = -\frac{\lambda \cdot g}{n_3^3 \cdot r_{33} \cdot L \cdot \Gamma} \qquad \text{Equation 2.9}$$

In Equation 2.7, $\Delta\varphi$ is the phase shift, L is the electrode length, λ is the wavelength of light, n_3^3 is the refractive index of the crystal, r_{33} is the electro-optic coefficient equal to 33 pm·V^{-1}, V is the voltage, g is the electrode gap, and Γ is the efficiency of the inhomogeneous field distribution equal to approximately 0.65 in lithium niobate ($LiNbO_3$) modulators made with x-cut crystals. In Equation 2.8, P is the optical output power, P_{min} is the minimum power, P_{max} is the maximum power, V_0 is the voltage point of operation (reference), and V_π is the half-wave voltage.

For a given half-wave voltage, V_π, used to switch from the on to off state and vice versa (phase difference of π), and the theoretical value V_0 equal to 0, the optical output power is modulated between a minimum value, P_{min}, and a maximum value, P_{max}, as illustrated in Figure 2.8. The modulation voltage is typically supplied as an RF signal. The output amplitude is therefore a function of the magnitude and shape of the supplied voltage.

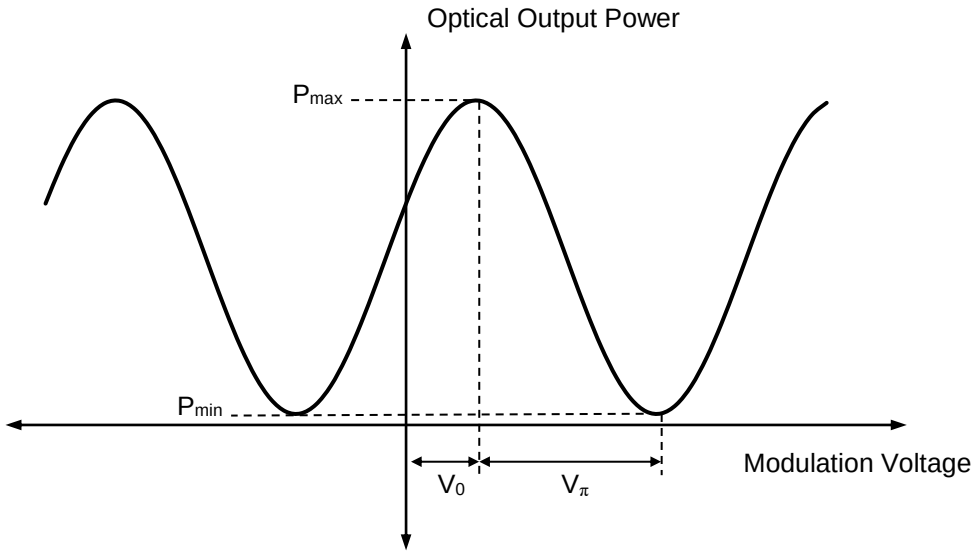

Figure 2.8. Characteristic curve for the Mach-Zehnder amplitude modulator (after Jenoptik 2018).

2.5. References

Ångström, A., 1925, “The Albedo of Various Surfaces of Ground,” *Geogr. Ann.*, Vol. 7, pp. 323-342. doi:10.2307/519495.

ASTM D422-63, 2007, “Standard Test Method for Particle-Size Analysis of Soils,” ASTM International, West Conshohocken, PA, USA, www.astm.org. doi:10.1520/DO422-63R07E02.

Bach, H. and Mauser, W., 1994, “Modelling and Model Verification of the Spectral Reflectance Of Soils Under Varying Moisture Conditions,” *Proceedings of the International Geoscience and Remote Sensing Symposium (IGARSS’94)*, Pasadena, CA, USA, August 8–12, pp. 2354-2356. doi:10.1109/IGARSS.1994.399735.

Ben-Dor, E. and Banin, A., 1995, “Near-Infrared Analysis as a Rapid Method to Simultaneously Evaluate Several Soil Properties,” *Soil Sci. Soc. Am. J.*, Vol. 59, No. 2, pp. 364-372.

Ben-Dor, E., Chabrillat, S., Demattê, J. A. M., Taylor, G. R., Hill, J., Whiting, M. L., and Sommer, S., 2009, "Using Imaging Spectroscopy to Study Soil Properties," *Remote Sens. Environ.*, Vol. 113, S. 1, pp. S38-S55. doi:10.1016/j.rse.2008.09.019.

Berk, A., Bernstein, L. S., and Robertson, D. C., 1989, “MODTRAN: A Moderate Resolution Model for LOWTRAN 7,” Final Report, GL-TR-0122, AFGL, Hanscom Air Force Base, MA, USA, 42 pgs.

Berk, A., Conforti, P. and Hawes, F., 2015, "An Accelerated Line-By-Line Option for MODTRAN Combining On-the-Fly Generation of Line Center Absorption with 0.1 cm-1 Bins and Pre-Computed Line Tails," In *Algorithms and Technologies for Multispectral, Hyperspectral, and Ultraspectral Imagery XXI*, SPIE Proceedings, Vol. 9471. doi:10.1117/12.2177444.

Berk, A., Conforti, P., Kennett, R., Perkins, T., Hawes, F., and van den Bosch, J., 2014, "MODTRAN6: A Major Upgrade of the MODTRAN Radiative Transfer Code," In *Algorithms and Technologies for Multispectral, Hyperspectral, and Ultraspectral Imagery XX*, SPIE Proceedings, Vol. 9088. doi:10.1117/12.2050433.

Bishop, A. W., Alpan, I., Blight, G. E., and Donald, I. B., 1960, “Factors Controlling the Shear Strength of Partly Saturated Cohesive Soils,” *Proc. ASCE Research Conference on Shear Strength of Cohesive Soils*, University of Colorado, Boulder, CO, USA, pp. 503-532.

Blatz, J.A., Ferreira, N.J., and Graham, J., 2004, “Effects of Near-Surface Environmental Conditions on Instability of an Unsaturated Soil Slope,” *Can. Geotech. J.*, Vol. 41, pp. 1111-1126.

Bowers, S. A. and Hanks, R. J., 1965, "Reflection of Radiant Energy from Soils," *Soil Sci.*, Vol. 100, No. 2, pp. 130-138

Brackley, I.J.A., 1971, “Partial Collapse in Unsaturated Expansive Clay,” *Proc. 5th Regional Conference on Soil Mechanics and Foundation Engineering*, South Africa, pp. 23-30.

Cannon, S. H., Gartner, J. E., Rupert, M. G., Michael, J. A., Rea, A. H., and Parrett, C., 2010, “Predicting the Probability and Volume of Post-Wildfire Debris Flows in the Intermountain West, USA." *Geol. Soc. Am. Bull.*, Vol. 122, No. 1-2, pp. 127-144.

Castaldi, F., Chabrillat, S., and van Wesemael, B., 2019a, “Sampling Strategies for Soil Property Mapping Using Multispectral Sentinel-2 and Hyperspectral EnMAP Satellite Data,” *Remote Sens.*, Vol. 11, No. 3, 309. doi:10.3390/rs11030309.

Castaldi, F., Hueni, A., Chabrillat, S., Ward, K., Buttafuoco, G., Bomans, B., Vreys, K., Brell, M., and van Wesemael, B., 2019b, “Evaluating the Capability of the Sentinel 2 Data for Soil Organic Carbon Prediction in Croplands,” *ISPRS J. Photogramm. Remote Sens.*, Vol. 147, pp. 267–282. doi:10.1016/J.ISPRSJPRS.2018.11.026

Chang, C.-W., Laird, D., Mausbach, M. J., and Hurburgh, C. R., 2001, "Near-Infrared Reflectance Spectroscopy-Principle Components Regression Analysis of Soil Properties," *Soil Sci. Soc. Am. J.*, Vol. 65, pp. 480–490.

Clark, R. N., 1999, “Chapter 1: Spectroscopy of Rocks and Minerals, and Principles of Spectroscopy,” In *Manual of Remote Sensing, Volume 3, Remote Sensing for the Earth Sciences*, 3rd ed., A.N. Rencz, Ed., John Wiley and Sons, New York, NY, USA, pp. 3–58.

Cozzolino, D. and Moron, A., 2003, "The Potential of Near-Infrared Reflectance Spectroscopy to Analyze Soil Chemical and Physical Characteristics," *J. Agr. Sci.*, Vol. 140, pp. 65–71.

Curcio, D., Ciraolo, G., D’Asaro, F., and Minacapilli, M., 2013, “Prediction of Soil Texture Distributions Using VNIR-SWIR Reflectance Spectroscopy,” *Proc. Environ. Sci.*, Vol. 19, pp. 494–503. doi:10.1016/j.proenv.2013.06.056.

Dalal, R. C. and Henry, R. J., 1986, "Simultaneous Determination of Moisture, Organic Carbon, and Total Nitrogen by Near Infrared Reflectance Spectrophotometry," *Soil Sci. Soc. Am. J.*, Vol. 50, No. 1, pp. 120–123. doi:10.2136/sssaj1986.03615995005000010023x.

Edmund Optics, 2012, “What is SWIR?,” Application Notes, Edmund Optics Inc. (Accessed 12. July, 2019).

Fabre, S., Briottet, X., and Lesaignoux, A., 2015, "Estimation of Soil Moisture Content from the Spectral Reflectance of Bare Soils in the 0.4-2.5 μm Domain," *Sensors*, Vol. 15, pp. 3262–3281. doi:10.3390/s150203262.

Fredlund, D.G., 1981, “The Shear Strength of Unsaturated Soils and its Relationship to Slope Stability Problems in Hong Kong,” *Hong Kong Eng.*, Hong Kong Institution of Engineers, April, pp. 37-45.

Garner, C. D., 2017, "Development of a Multiband Remote Sensing System for Determination of Unsaturated Soil Properties," Ph.D. dissertation, University of Arkansas, Fayetteville, AR, USA.

Gartner, J. E., Cannon, S. H., Santi, P. M., deWolfe, V. G., 2008, "Empirical Models to Predict the Volumes of Debris Flows Generated by Recently Burned Basins in the Western U.S.," *Geomorphology*, Vol. 96, pp. 339-354.

Guanter, L., Kaufmann, H., Segl, K., Foerster, S., Rogass, C., Chabrillat, S., Kuester, T., Hollstein, A., Rossner, G., Chlebek, C., et al., 2015, "The EnMAP Spaceborne Imaging Spectroscopy Mission for Earth Observation," *Remote Sens.*, Vol. 7, No. 7, pp. 8830–8857. doi:10.3390/rs70708830.

Guarini, R., Loizzo, R., Facchinetti, C., Longo, F., Ponticelli, B., Faraci, M., Dami, M., Cosi, M., Amoruso, L., de Pasquale, V., et al., 2018, "Prisma Hyperspectral Mission Products," *Proceedings of the International Geoscience and Remote Sensing Symposium (IGARSS 2018)*, Valencia, Spain, July 22–27, pp. 179–182. doi:10.1109/IGARSS.2018.8517785.

Haubrock, S. N., Chabrillat, S., Lemmnitz, C., and Kaufmann, H., 2008, "Surface Soil Moisture Quantification Models from Reflectance Data Under Field Conditions," *Int. J. Remote Sens.*, Vol. 29, No. 1, pp. 3-29. doi:10.1080/01431160701294695.

Ho, D.Y.F., Fredlund, D.G., 1982, "Increase in Strength due to Suction for Two Hong Kong Soils," *Proc. ASCE Conference on Engineering and Construction in Tropical and Residual Soils*, Honolulu, USA, pp. 263-295.

Hummel, J. W., Sudduth, K. A., and Hollinger, S. E., 2001, "Soil Moisture and Organic Matter Prediction of Surface and Subsurface Soils Using an NIR Soil Sensor," *Comput. Electron. Agr.*, Vol. 32, No. 2, pp. 149-165. doi:10.1016/S0168-1699(01)00163-6.

HyspIRI Mission Concept Team, 2018, *HyspIRI Final Report*, Jet Propulsion Laboratory, California Institute of Technology, Pasadena, CA, USA.

Islam, K., Singh, B., and McBratney, A., 2003, "Simultaneous Estimation of Various Soil Properties by Ultra-Violet, Visible, and Near-Infrared Reflectance Spectroscopy," *Aust. J. Soil Res.*, Vol. 41, No. 6, pp. 1101-1114.
pp. 422-433. doi:10.2136/sssaj2012.0401.

Jenoptik, 2018, "Jenoptik Integrated-Optical Modulators: Technical Information and Instructions for Use," Jenoptik Optical Systems GmbH (Accessed 1. December 2018).

Kern, A. N., Addison, P., Oommen, T., Salazar, S. E., Coffman, R. A., 2017, "Machine Learning Based Predictive Modeling of Debris Flow Probability Following Wildfire in the Intermountain Western United States," *Mathematical Geosciences*. doi: 10.1007/s11004-017-9681-2.

Knadel, M., Deng, F., Alinejadian, A., de Jonge, L. W., Moldrup, P., and Greve, M. H., 2014, "The Effects of Moisture Conditions – From Wet to Hyper Dry – On Visible Near Infrared Spectra of Danish Reference Soils," *Soil Sci. Soc. Am. J.*, Vol. 78, No. 2, pp. 422-433. doi:10.2136/sssaj2012.0401.

Knadel, M., Stenberg, B., Deng, F., Thomsen, A., and Greve, M. H., 2013, "Comparing Predictive Abilities of Three Visible-Near Infrared Spectrophotometers for Soil Organic Carbon and Clay Determination," *J. Near Infrared Spec.*, Vol. 21, No. 1, pp. 67-80. doi:10.1255/jnirs.1035.

Krahn, J., Fredlund, D.G., Klassen, M.J., 1989, "Effect of Soil Suction on Slope Stability at Notch Hill," *Can. Geotech. J.*, Vol. 26, pp. 269-278.

Lesaignoux, A., Fabre, S., and Briottet, X., 2013, "Influence of Soil Moisture Content on Spectral Reflectance of Bare Soils in the 0.4-14 μm Domain," *Int. J. Remote Sens.*, Vol. 34, No. 7, pp. 2268-2285. doi:10.1080/01431161.2012.743693.

Leu, D. J., 1977, "Visible and Near-Infrared Reflectance of Beach Sands: A Study on the Spectral Reflectance/Grain Size Relationship," *Remote Sens. Environ.*, Vol. 6, No. 3, pp. 169-182. doi:10.1016/0034-4257(77)90002-5.

Liu, W., Baret, F., Gu, X., Tong, Q., Zheng, L., and Zhang, B., 2002, "Relating Soil Surface Moisture to Reflectance," *Remote Sens. Environ.*, Vol. 81, pp. 238-246.

Liu, W., Baret, F., Gu, X., Zhang, B., Tong, Q., and Zheng, L., 2003, "Evaluation of Methods for Soil Surface Moisture Estimation from Reflectance Data," *Int. J. Remote Sens.*, Vol. 24, No. 10, pp. 2069-2083.

Lobell, D. B. and Asner, G. P., 2002, "Moisture Effects on Soil Reflectance," *Soil Sci. Soc. Am. J.*, Vol. 66, No. 3, pp. 722-727.

Lu, N., Kaya, M., 2014, "Power Law for Elastic Moduli of Unsaturated Soil," *J. Geotech. Geoenviron.*, Vol. 140, No. 1, pp. 46-56.

Lumb, P., 1975, "Slope Failures in Hong Kong," *Q. J. Eng. Geol.*, Vol. 8, pp. 31-65.

Machol, J., Ayers, T., Schwenz, K., Koenig, K., Hardesty, R., Senff, C., Krainak, M., Abshire, J., Bravo, H., and Sandberg, S., 2004, "Preliminary Measurements with an Automated Compact Differential Absorption LIDAR for Profiling Water Vapor," *Appl. Optics*, Vol. 43, No. 15, pp. 3110-3121.

Morris, R. V., Neely, S. C., and Mendell, W. W., 1982, "Application of Kubelka–Munk Theory of Diffuse Reflectance to Geologic Problems: The Role of Scattering," *Geophys. Res. Lett.*, Vol. 9, No. 2, pp. 113–116. doi:10.1029/GL009i002p00113.

Mouazen, A. M., Karoui, R., De Baerdemaeker, J., and Ramon, H., 2006, "Characterization of Soil Water Content Using Measured Visible and Near Infrared Spectra," *Soil Sci. Soc. Am. J.*, Vol. 70, No. 4, pp. 1295-1302. doi:10.2136/sssaj2005.0297.

Mouazen, A. M., Maleki, M. R., De Baerdemaeker, J., and Ramon, H., 2007, "On-line Measurement of Some Selected Soil Properties Using a VIS-NIR Sensor," *Soil Till. Res.*, Vol. 93, No. 1, pp. 13-27. doi:10.1016/j.still.2006.03.009.

National Interagency Fire Center, 2018, "National Fire News Year-to-Date Fires and Acres," https://www.nifc.gov/fireInfo/nfn.htm (Last accessed 18 Dec 2018).

New Focus, 2014, *TLB-6800 Vortex Plus™ Laser System User's Manual*, Rev. A, New Focus, Santa Clara, CA, USA.

Nolet, C., Poortinga, A., Roosjen, P., Bartholomeus, H., and Ruessink, G., 2014, "Measuring and Modeling the Effect of Surface Moisture on the Spectral Reflectance of Coastal Beach Sand," *PLoS One*, Vol. 9, No. 11, e112151. doi:10.1371/journal.pone.0112151

Negri, J.A., 2016, "Evaluation and Validation of Multiple Predictive Models Applied to Post-Wildfire Debris-Flow Hazards," M.S. thesis, Colorado School of Mines, Golden, CO, USA.

Oltra-Carrió, R., Baup, F., Fabre, S., Fieuzal, R., Briottet, X., 2015, "Improvement of Soil Moisture Retrieval from Hyperspectral VNIR-SWIR Data Using Clay Content Information: From Laboratory to Field Experiments," *Remote Sens.*, Vol. 7, No, 3, pp. 3184-3205. doi:10.3390/rs70303184.

Park, J. K., 1980, "A Soil Moisture Reflectance Model in Visible and Near IR Bands," *Proceedings of the International Symposium on Machine Processing of Remotely Sensed Data and Soil Information Systems and Remote Sensing and Soil Survey*, Purdue University, West Lafayette, IN, USA, June 3–6.

Philpot, W. D. and Tian, J., 2016, "The Hyperspectral Soil Line: A Preliminary Description," *Light, Energy, and the Environment*, OSA Technical Digest (Online), Optical Society of America, paper HW3E.2, 3 pgs.

Sadeghi, M., Jones, S. B., and Philpot, W. D., 2015, "A Linear Physically-Based Model for Remote Sensing of Soil Moisture Using Short Wave Infrared Bands," *Remote Sens. Environ.*, Vol. 164, pp. 66-76. doi:10.1016/j.rse.2015.04.007.

Shepherd, K. D. and Walsh, M. G., 2002, "Development of Reflectance Spectral Libraries for Characterization of Soil Properties," *Soil Sci. Soc. Am. J.*, Vol. 66, pp. 988-998.

Terzaghi, K., Peck, R., and Mesri, G., 1996, *Soil Mechanics in Engineering Practice*, 3rd ed., John Wiley and Sons, New York, NY, USA.

Tian, J. and Philpot, W. D., 2015, Relationship Between Surface Soil Water Content, Evaporation Rate, and Water Absorption Band Depths in SWIR Reflectance Spectra," *Remote Sens. Environ.*, Vol. 169, No. pp. 280-289.

Whiting, M.L., 2009, "Measuring Surface Water in Soil with Light Reflectance," *Proc. SPIE*, Vol. 7454, 74540D, 11 pgs. doi:10.1117/12.826896.

Walvoort, A. and McBratney, A., 2001, "Diffuse Reflectance Spectrometry as a Proximal Sensing Tool for Precision Agriculture," *Proceedings of the 3rd European Conference on Precision Agriculture*, Montpellier, France, June 18–20, pp. 503-508.

Waruru, B. K., Shepherd, K. D., Ndegwa, G. M., Kamoni, P. T., and Sila, A. M., 2014, "Rapid Estimation of Soil Engineering Properties Using Diffuse Reflectance Near Infrared Spectroscopy," *Biosyst. Eng.*, Vol. 121, pp. 177-185. doi:10.1016/j.biosystemseng.2014.03.003.

Whalley, W. R., Leeds-Happison, P. B., and Bowman, G. E., 1991, "Estimation of Soil Moisture Using Near Infrared Reflectance," *Hydrol. Process.*, Vol. 5, pp. 321-327.

Wulf, H., Mulder, T., Schaepman, M. E., Keller, A., and Jörg, P. C., 2015, "Remote Sensing of Soils," Report prepared by the Remote Sensing Laboratories, Dept. of Geography, University of Zurich, Switzerland, 71 pgs. doi:10.5167/uzh-109992.

Whiting, M. L., Li, L., and Ustin, S. L., 2004, "Predicting Water Content Using Gaussian Model On Soil Spectra," *Remote Sens. Environ.*, Vol. 89, No. 4, pp. 535-552.

Xu, C., Zeng, W., Huang, J., Wu, J., and van Leeuwen, W. J. D., 2016, "Prediction of Soil Moisture Content and Soil Salt Concentration from Hyperspectral Laboratory and Field Data," *Remote Sens.*, Vol. 8, No. 42, 20 pgs. doi:10.3390/rs8010042.

Yitagesu, F. A., van der Meer, F., van der Werff, H., and Zigterman, W., 2009, "Quantifying Engineering Parameters of Expansive Soils from their Reflectance Spectra," *Eng. Geol.*, Vol. 105, No. 3-4, pp. 151-160. doi:10.1016/j.enggeo.2009.01.004.

CHAPTER 3: DEVELOPMENT OF A MULTIMODE FIELD DEPLOYABLE LIDAR INSTRUMENT FOR TOPOGRAPHIC MEASUREMENTS OF UNSATURATED SOIL PROPERTIES: INSTRUMENT DESCRIPTION

3.1. Chapter Overview

A detailed description of the soil observation laser absorption spectrometer (SOLAS) is introduced in this chapter. Necessary background information is provided to place the instrument into the broader context of other remote sensors and remote sensing techniques. The development of each of the sub-systems (transmitter, receiver, data acquisition) is described and the specifications are defined. Discussion about the intended functionality and the potential future applications for the SOLAS are included.

The limitations of the Salazar et al. (2019) paper are described in Section 3.2. The full citation for the manuscript is included in Section 3.3. The abstract for the paper is contained in Section 3.4. Contained within Section 3.5 is the introduction and motivation for the paper, followed by the background information in Section 3.6. The concept of the SOLAS is described in Section 3.7. The instrument description is contained with Section 3.8. Discussion about the SOLAS and conclusions for this work are provided in Sections 3.9 and 3.10, respectively.

3.2. Limitations of the Described Study

The work presented in this chapter was focused on the provenance of the SOLAS. This was presented in the form of background information that was necessary to the development of the SOLAS and an extensive description of the instrument. While the paper included some discussion about the future applications and potential limitations of the instrument, the paper did not contain testing methods, nor results. Furthermore, the description of the optical receiver was

minimal, due to length restrictions of the manuscript, leaving opportunity to describe the receiver in more detail in subsequent work.

3.3. Development of a Multimode Field Deployable Lidar Instrument for Topographic Measurements of Unsaturated Soil Properties: Instrument Description

Reference

Salazar, Sean E., Garner, Cyrus D., and Coffman, Richard A., "Development of a Multimode Field Deployable Lidar Instrument for Topographic Measurements of Unsaturated Soil Properties: Instrument Description," Remote Sensing, Vol. 11, No. 3, 2019, 289. doi:10.3390/rs11030289.

3.4. Abstract

The hydrological and mechanical behavior of soil is determined by the moisture content, soil water (matric) potential, fines content, and plasticity. However, these parameters are often difficult or impractical to determine in the field. Remote characterization of soil parameters is a non-destructive data collection process well suited to large or otherwise inaccessible areas. A ground-based, field-deployable remote sensor, called the Soil Observation Laser Absorption Spectrometer (SOLAS), was developed to collect measurements from the surface of bare soils and to assess the in-situ condition and essential parameters of the soil. The SOLAS instrument transmits coherent light at two wavelengths using two, continuous-wave, near-infrared diode lasers and the instrument receives backscattered light through a co-axial 203-mm diameter telescope aperture. The received light is split into a hyperspectral sensing channel and a laser absorption spectrometry (LAS) channel via a multi-channel optical receiver. The hyperspectral channel detects light in the visible to shortwave infrared wavelengths, while the LAS channel filters and directs near-infrared light into a pair of photodetectors. Atmospheric water vapor is inferred using the differential absorption of the on- and off-line laser wavelengths (823.20 nm and 847.00 nm, respectively). Range measurement is determined using a frequency-modulated, self-chirped, coherent, homodyne detection scheme. The development of the instrument

(transmitter, receiver, data acquisition components) is described herein. The potential for rapid characterization of physical and hydro-mechanical soil properties, including volumetric water content, matric potential, fines content, and plasticity, using the SOLAS remote sensor is discussed. The envisioned applications for the instrument include assessing soils on unstable slopes, such as wildfire burn sites, or stacked mine tailings. Through the combination of spectroradiometry, differential absorption, and range altimetry methodologies, the SOLAS instrument is a novel approach to ground-based remote sensing of the natural environment.

Keywords: instrument development, hyperspectral, spectroradiometry, LiDAR, soil

3.5. Introduction

Remote sensing is well suited for non-intrusive observation of bare soils, especially over large, hazardous, or inaccessible areas, such as a wildfire site. For example, spaceborne remote sensing techniques are commonly used to rapidly (1) establish wildfire perimeters, (2) assess the remaining vegetative cover, and (3) determine the burn severity after containment of the fire. Collected remotely sensed data (burn severity, extent) are often calibrated with ground-truthing methods, yet these proximal ground-truthing methods are often point-wise, spatially limited, and cannot easily cover vast areas. Moreover, information about the soil is not commonly collected in these areas following a wildfire. Characterization of soil in a wildfire-affected area commonly relies on regional, typified soils data from databases like the Soil Survey Geographic Database (SSURGO) and the State Soil Geographic Survey (STATSGO). These data, however, have insufficient resolution for reliable, site-specific, predictive modeling of post-wildfire hazards (e.g. debris flows) and do not capture the time-variability associated with meteorological and hydrological action. Because burned areas are ideally suited for study with remote sensing

techniques, due to the absence of vegetation (fire-induced denudation), there is a need for methods to collect high-resolution, timely, and site-specific soils information.

To address this need, a ground-based, remote sensor, called the Soil Observation Laser Absorption Spectrometer (SOLAS), was developed to rapidly infer soil properties at the field scale. The development of the SOLAS followed laboratory-based, proof-of-concept testing that successfully derived soil water characteristic curves (SWCC) as well as index properties (liquid limit [LL], plastic limit [PL], and clay fraction [CF]) for several soil types by using only non-contact, optical techniques. By combining spectroradiometric, differential laser absorption, and range altimetry techniques, the SOLAS instrument was designed to collect range-resolved information from bare soils, including soil surface moisture (an estimation of volumetric water content, θ_v), soil matric potential (ψ_m), burn severity, LL, PL, and CF. An initial description of the SOLAS instrument is provided herein; as such, the materials and methods used in the development of the instrument are detailed and described. Additionally, supporting background information about reflectance spectroradiometry, lidar altimetry, and differential laser absorption is provided. Measurement results from field-testing will be described by the authors in later articles.

3.6. Background

A variety of remote and proximal sensing techniques for obtaining soils information have been demonstrated. These techniques include passive imaging spectroradiometry (multispectral, hyperspectral, visible near-infrared [VNIR], shortwave infrared [SWIR], and mid-wave-infrared [MWIR]), active and passive microwave systems (synthetic- and real-aperture radar, ground-penetrating radar), and gamma-ray spectrometry (Wulf et al. 2015). Although the correlation between reflectance and soil moisture was studied as early as 1925 (Ångström 1925), advances

in ground-based multispectral and hyperspectral measurement techniques of reflectance spectra, primarily in the VNIR (380–1000 nm) and SWIR (1000–2500 nm) ranges, have been utilized to estimate soil moisture content (SMC) in the laboratory setting (Bowers and Hanks 1965, Park 1980, Dalal and Henry 1986, Whalley et al. 1991, Bach and Mauser 1994, Ben-Dor and Banin 1995, Chang et al. 2001, Hummel et al. 2001, Liu et al. 2002, 2003, Lobell and Asner 2002, Islam et al. 2003, Whiting et al. 2004, Mouazen et al. 2006, Lesaignoux et al. 2013, Knadel et al. 2014, Nolet et al. 2014, Fabre et al. 2015, Sadeghi et al. 2015, Tian and Philpot 2015, Xu et al. 2016, Garner 2017). In the aforementioned studies, the laboratory measurements were collected using carefully prepared or dilute soil specimens under controlled conditions. Fewer studies were conducted under field conditions (Mouazen et al. 2007, Haubrock et al. 2008, Xu et al. 2016). Among the numerous developed soil reflectance correlations in the literature, other soil parameters of interest have included clay content (Chang et al. 2001, Walvoort and McBratney 2001, Shepherd and Walsh 2002, Cozzolino and Moron 2003, Islam et al. 2003, Knadel et al. 2013, Garner 2017), grain size (Leu 1977, Chang et al. 2001, Shepherd and Walsh 2002, Cozzolino and Moron 2003), soil plasticity (Yitagesu et al. 2009, Waruru et al. 2014, Garner 2017) and matric potential (Garner 2017).

The SOLAS instrument that is described herein was designed based on other work previously performed at the University of Arkansas. For example, Garner (2017) utilized a laboratory-based diffuse reflectance infrared Fourier transform (DRIFT) technique to develop an empirical relationship between reflectance spectra and soil plasticity for illite and kaolinite soil types, as well as for a commercial synthetic nepheline synetite material (Donna Fill Co., Little Rock, Arkansas, USA). Garner (2017) also developed a laser analysis of soil tension (LAST) technique to infer the SWCC for dilute pressure plate extractor (PPE) prepared soil specimens.

The measurement technique utilized coherent illumination from two low-power, near-infrared laser diodes and data collection using a high radiometric-resolution spectrometer (ASD FieldSpec 4 Hi-Res; Malvern Panalytical, Longmont, Colorado, USA) to relate θ_v and ψ_m through the SWCC. The empirical relationships relied upon partial least squares and principle components regression techniques (Janik and Skjemstad 1995, Chang et al. 2001, Garner 2017).

3.6.1. *FMCW Lidar Altimetry*

Among laser altimetry methods, coherent, frequency modulated continuous waveform (FMCW) lidar has been widely pursued (Karlsson and Olsson 1999, Allen et al. 2001, Pierrottet et al. 2005, 2008, Adany et al. 2009, Barber et al. 2010, Gao and Hui 2012, Mateo 2014). A pulse compression technique has been applied to FMCW lidar systems, whereby a linear frequency sweep or "chirp" with a large bandwidth is used to modulate the optical carrier signal. As documented in the aforementioned FMCW lidar literature, range accuracy was maintained, while peak output power and receiver bandwidth requirements were reduced (over direct detection or conventional, pulsed, time-of-flight systems).

Adany et al. (2009) demonstrated the advantages of a self-chirped, homodyne detection scheme for FMCW lidar. The simplified homodyne system offered significant advantages over direct detection and heterodyne detection methods through less complex receiver configuration. Furthermore, improved receiver sensitivity permitted better long-range lidar measurements. In the Adany et al. (2009) configuration, the optical signal was intensity-modulated with a linear frequency modulated (FM) sweep (from frequency f_1 to f_2) with chirp bandwidth, B, equal to $f_2 - f_1$. For the Adany et al. (2009) design, a portion of the carrier signal was used as the local oscillator (LO) in conjunction with a balanced photodetector (BPD). The range to the target was proportional to the frequency difference between the LO and the received signal (beat frequency,

f_R). For FMCW lidar with self-chirped homodyne detection, like that proposed by Adany et al. (2009), the range to target (R) should be calculated using Equations 3.1 and 3.2 (Adany et al. 2009), while the approximate range accuracy (σ_R) should be determined by using Equations 3.3 and 3.4 (Skolnik 1960, Jelalian 1992, Allen et al. 2001).

$$R = \frac{c \cdot f_R \cdot \tau}{2 \cdot (f_2 - f_1)} \quad \text{Equation 3.1}$$

$$f_R = \left(\frac{f_2 - f_1}{\tau}\right) \cdot \Delta t \quad \text{Equation 3.2}$$

$$\sigma_R = \frac{K \cdot c}{B\sqrt{SNR}} \quad \text{Equation 3.3}$$

$$SNR_{coh} = \frac{R \cdot P_r}{2 \cdot q \cdot B_{RX}} \quad \text{Equation 3.4}$$

In Equation 3.1, R is the range to target, c is the speed of light, f_R is the beat frequency, τ is the chirp duration, and $f_2 - f_1$ is the chirp bandwidth. In Equation 3.2, Δt is the time delay for roundtrip propagation through the atmosphere. In Equation 3.3, σ_R is the range accuracy, K is a chirp waveform constant, B is the signal bandwidth, and SNR is the signal to noise ratio of the receiver data. In Equation 3.4, SNR_{coh} is the signal to noise ratio for a shot-noise-dominant coherent detection process, $\Re$ is the photodetector responsivity, Pr is the received signal power, q is the electron charge (1.6×10^{-10} C), and B_{RX} is the bandwidth of the receiver.

3.6.2. *Differential Absorption Measurements*

The differential absorption lidar (DIAL) technique, sometimes also called (differential) laser absorption spectrometry (LAS), has been employed to determine the concentration of molecular species in the atmosphere by measuring the difference in light absorption between two transmitted laser wavelengths. DIAL theory was developed by Schotland (1966) but has been advanced over the last six decades (Schotland 1974, Menzies and Shumate 1976, Grant 1982, 1991, Hardesty 1984, Bösenberg 1998, Wulfmeyer and Bösenberg 1998, Wulfmeyer and

Walther 2001, Spuler et al. 2015). Moreover, during this time period, DIAL has become the most accurate measurement technique for tropospheric water vapor concentration (Ismail and Browell 1989, Bösenberg 1998, Wulfmeyer and Walther 2001, Weckwerth et al. 2016). A variety of DIAL instruments and measurement techniques have been developed to measure water vapor profiles and concentrations of other atmospheric greenhouse gases (e.g. carbon dioxide, methane). These measurements have been performed from ground-based platforms (Hardesty 1984, Prasad and Geiger 1996, Wulfmeyer 1998, Little and Papen 2001, Machol et al. 2004, Nehrir 2008, 2011, Nehrir et al. 2009, 2011, 2012, Spuler et al. 2015), airborne platforms (Remsberg and Gordley 1978, Bufton et al. 1983, Ehret et al. 1993, Bruneau et al. 2001a, 2001b, Browell et al. 2010), and proposed spaceborne platforms (Megie and Menzies 1980, Ismail and Browell 1989, Ehret et al. 2008, Wirth et al. 2009, Barrientos-Barria et al. 2014).

DIAL measurements are typically achieved by alternating the transmission of two laser wavelengths through the atmosphere along the same path to determine the water vapor concentration. The so-called on-line wavelength is tuned to correspond with a water vapor absorption feature, while the off-line wavelength is tuned to a nearby spectral region in which water vapor is not well absorbed. For accurate measurement, a spectral region of interest must be identified for which the on- and off-line wavelengths are adjacent and the temperature dependence of the DIAL measurement is minimal. Various wavelength ranges have been recommended in the literature for measurement of water vapor. For example, Grant (1991) utilized the 720–730 nm wavelength range, while Machol et al. (2004) used wavelengths near 823 nm. The water vapor density (ρ_v), averaged over distance (R), is commonly calculated using the DIAL equation proposed by Schotland (1974) and presented in the form of Equations 3.5, 3.6, and 3.7 (Machol et al. 2004). For vertical measurements of the atmospheric water vapor

concentration, the Voigt function (Λ) changes due to thermal- and pressure-broadening effects, which are typically extrapolated from ground measurements. The water vapor concentration is commonly calculated using Equations 3.8 and 3.9 (Machol et al. 2004).

$$\rho_v(R) = \frac{M_{H_2O}}{N_A} \cdot \frac{1}{2 \cdot (\sigma_{on} - \sigma_{off}) \cdot \Delta R} \cdot \left[ln \frac{P_{on} \cdot R \cdot P_{off} \cdot (R + \Delta R)}{P_{on} \cdot (R + \Delta R) \cdot P_{off} \cdot R} \right] \quad \text{Equation 3.5}$$

$$\sigma = S \cdot \Lambda \quad \text{Equation 3.6}$$

$$S(T) = S_0 \cdot \left(\frac{T_0}{T}\right)^{1.5} \cdot exp\left[-\frac{h \cdot c \cdot E''}{k_B} \left(\frac{1}{T} - \frac{1}{T_0}\right) \right] \quad \text{Equation 3.7}$$

$$\rho_v = \frac{e_s \cdot RH}{100 \cdot R_v \cdot T} \quad \text{Equation 3.8}$$

$$e_s = e_{s0} \cdot exp\left[\frac{L}{R_v} \left(\frac{1}{T_0} - \frac{1}{T}\right) \right] \quad \text{Equation 3.9}$$

In Equation 3.5, ρ_v is the water vapor density averaged over a distance ΔR at a range R, M_{H2O} is the molecular weight of water, N_A is Avogadro's constant, σ_{on} and σ_{off} are the on-line and off-line water vapor absorption cross-sections obtained from Equation 3.6, and P_{on} and P_{off} are the received on-line and off-line backscatter signals. In Equation 3.6, S is the temperature-dependent absorption line strength and Λ is the Voigt function. In Equation 3.7, S_0 and T_0 are the absorption line strength and temperature under standard conditions, T is the temperature, h is the Planck constant, c is the speed of light, E" is the lower-state energy (in cm^{-1}), and k_B is the Boltzmann constant. In Equation 3.8, e_s is the saturation vapor pressure obtained from Equation 3.9, RH is the relative humidity ($RH \approx 100 \times e/es$), where $e = \rho_v \cdot R_v \cdot T$, and R_v is the water vapor gas constant equal to 461 $J \cdot kg^{-1} \cdot K^{-1}$. In Equation 3.9, es_0 is the saturation vapor pressure at $T_0 = 273K$ and is equal to 611 Pa, and L is the latent heat of vaporization and is equal to 2.5×10^6 $J \cdot kg^{-1}$.

3.7. Development of the SOLAS Concept

The SOLAS instrument was devised to collect range-resolved hyperspectral measurements of soils while also measuring water absorption, due to water vapor, over the measurement range. Moreover, the bench-scale studies conducted by Garner (2017) indicated that under coherent illumination, empirical inference of soil matric potential (ψ_m), and volumetric water content (θ_v) was possible. The instrument therefore utilized laser transmission to achieve

these metrics while collecting passive radiometric measurements across the VNIR to SWIR range (350–2500 nm). Based on water vapor absorption spectra published by the high-resolution transmission (HITRAN) molecular absorption database (Gordon et al. 2017) and the availability of commercial off-the-shelf laser diodes, laser wavelengths of 823.20 nm (on-line) and 847.00 nm (off-line) were selected. For completeness, the on- and off-line wavelengths transmitted by the SOLAS instrument are transposed over a plot of the atmospheric absorption coefficient as a function of wavelength in Figure 3.1.

Because DIAL instruments have primarily been developed to measure vertical gas and aerosol profiles, there are limited examples of instruments operating in horizontal orientations or for topographic target returns (Grant 1982, Hardesty 1984, Sakaizawa et al. 2010, Nehrir 2011, Ishii et al. 2013). Furthermore, DIAL instruments have typically utilized pulsed, rapid spectral-switching lasers to increase the accuracy of atmospheric volume sampling, especially over long vertical ranges (vertical measurements of atmospheric water vapor are extremely sensitive to pressure- and temperature-induced gradients). To provide coherent illumination to the target, while enabling simplified topographic ranging and differential absorption measurements, a diode-laser-based FMCW laser scheme was designed to switch between the on-line and off-line laser sources over short intervals (seconds). The use of a self-chirped, homodyne detection configuration (similar to Adany et al. 2009), has enabled range-resolved measurements.

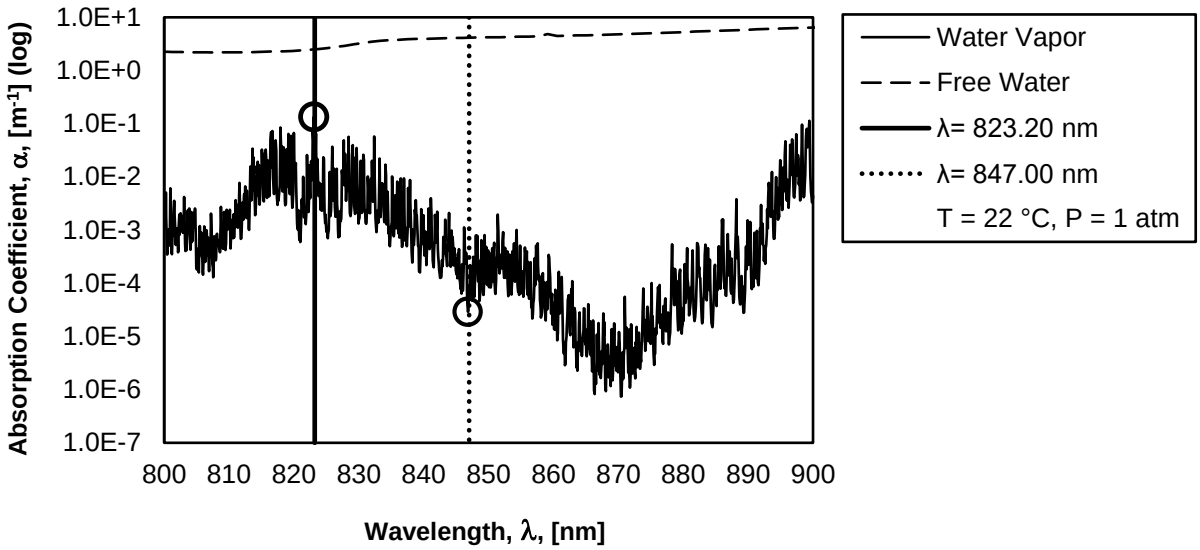

Figure 3.1. Absorption coefficient, as a function of wavelength, for free water and water vapor with transposed on-line (823.20 nm) and off-line (847.00 nm) laser wavelengths; raw data from Kou et al. (1993), Pope and Fry (1997), and Rothman et al. (2013).

3.8. Instrument Description

The SOLAS instrument combines range altimetry, differential absorption, and reflectance spectroradiometry technologies. The instrument is comprised of (1) a laser source and transmitting system, (2) a multi-channel receiving system (active LAS and passive hyperspectral sensing), and (3) a data acquisition and control system (signal processing and component control). A schematic of the major architecture of the SOLAS instrument is presented in Figure 3.2 and a table describing the technical specifications is presented as Table 3.1. Each of the instrument subsystems are further described in the following sections.

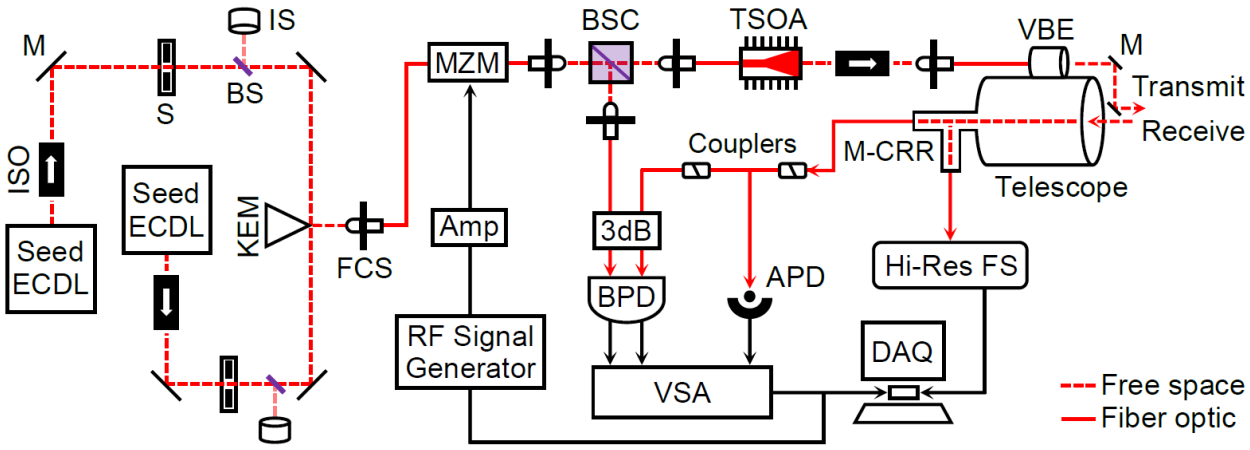

<u>Key</u>: ECDL = External Cavity Diode Laser; ISO = Optical Isolator; M = Mirror; S = Shutter; BS = Beam Sampler; IS = Integrating Sphere; KEM = Knife-Edge Mirror; FCS = Fiber-Coupling Stage; MZM = Mach-Zehnder Modulator; Amp = Amplifier; BSC = Beamsplitter Cube; TSOA = Tapered Semiconductor Optical Amplifier; VBE = Variable Beam Expander; M-CRR = Multi-Channel Receiver Relay; Hi-Res FS = High-Resolution Field Spectroradiometer; DAQ = Data Acquisition; APD = Avalanche Photodetector; 3dB = 3dB 2x2 Optical Coupler; BPD = Balanced Photodetector; VSA = Vector Signal Analyzer.

Figure 3.2. Schematic of the Soil Observation Laser Absorption Spectrometer (SOLAS).

Table 3.1. Specifications of the Soil Observation Laser Absorption Spectrometer (SOLAS).

Transmitter	Unit	Specification
Type	-	CW
On-line	[nm]	823.20
Off-line	[nm]	847.00
Linewidth	[kHz]	≤ 200
Modulation	-	Electrooptic AM
Type	-	Linear RF chirp
Frequency	[MHz]	100–500
Transmitter power	[W]	≤ 0.5 (fiber-end)
Beam diameter	[mm]	2.0–8.0
Beam divergence	[mrad]	0.29

Signal Processing	Unit	Specification
Bandwidth (instantan.)	[MHz]	50
Frequency range	[GHz]	0.01–6.6
Water vapor resolution	-	Column averaged
Range to target resolution	[cm]	10 (theoretical)

Receiver	Unit	Specification
Telescope	-	Schmidt-Cassegrain
Primary diameter (D)	[mm]	203
Focal length (*f*)	[mm]	2032
N (*f*/D)	-	10
Field of view (FOV)		
Hyperspectral channel	[mrad]	0.32–0.61
LAS channel	[mrad]	0.27
Detectors		
Hyperspectral receiver	-	ASD FieldSpec 4 Hi-Res
Type	-	Silicon, InGaAs
Spectral range	[nm]	350–2500
Number of bands	-	2151
Balanced receiver (LO sig.)	-	New Focus 1607-AC-FC
Type	-	Silicon
Bandwidth	[MHz]	650
Avalanche photodetector	-	Thorlabs APD430A
Type	-	Silicon
Bandwidth	[MHz]	400

Key: CW = Continuous-Wave; AM = Amplitude Modulation; RF = Radio Frequency; N = F-number; LAS = Laser Absorption Spectrometry; ASD = Analytical Spectral Devices; InGaAs = Indium Gallium Arsenide; LO = Local Oscillator.

3.8.1. *Transmitter Design*

The optical carrier signal is seeded by two New Focus TLB-6817 Vortex Littman–Metcalf external cavity diode lasers (ECDL) precision-tuned to center wavelengths of 823.20 nm and 847.00 nm, with fine tuning from 823.03 nm to 823.35 nm, and 846.84 nm to 847.14 nm, respectively (Newport Corporation; Irvine, California, USA). Each laser is powered with a low noise controller (New Focus TLB-6800-LN), producing 17 mW to 26 mW outputs with narrow linewidths (≤ 200 kHz). As previously presented in Figure 3.2, the laser transmission path is partially free space and partially fiber optic based. To protect each ECDL from back reflections, the laser beams pass through narrowband polarization-dependent Faraday isolators (Thorlabs IO-5-850-HP) that are tuned to match each respective wavelength (Thorlabs Inc.; Newton, New Jersey, USA). Optomechanical shutters in the free space laser paths provide a fail-safe (Thorlabs

SH05). A sequence of dielectric mirrors direct each laser beam into a polarization-maintaining fiber optic cable via a Thorlabs PAF-X-5-B fiber-coupling stage. The light energy within the fiber optic cable is then coupled into a Jenoptik AM830 Mach–Zehnder modulator (MZM) where the optical signal is intensity modulated (Jenoptik Optical Systems GmbH; Jena, Germany). The modulation is achieved by utilizing a radio frequency (RF) signal generator to encode the transmitted light with a chirp. Seventy percent of the intensity-modulated optical signal continues along the transmitter path (into the tapered semiconductor optical amplifier [TSOA]) while the remaining 30% is reflected through a free-space beamsplitting cube and fiber-coupled into a 650 MHz bandwidth New Focus 1607-AC-FC balanced photodetector (BPD) to provide the local oscillator (LO) input signal. The carrier signal is fiber-coupled and amplified through a Thorlabs TPA830P10-SP butterfly package TSOA mounted to a thermoelectric-cooled (TEC) 205 TEC Butterfly LaserMount (Arroyo Instruments LLC, San Luis Obispo, California, USA). The TSOA chip is tuned to a center wavelength (CWL) of 835 nm (centered between the 823.20 nm and 847.00 nm transmitting wavelengths). The amplified beam is subsequently shaped with a collimation package before exiting the TSOA output window in free space. The beam is then isolated (Faraday isolator tuned to a CWL of 835 nm) and coupled into a high-power, armored fiber optic cable. The laser output is transmitted into the atmosphere co-axial with the optical receiver (telescope) by means of a collimator (Thorlabs F280SMA-835), a variable beam expander (Thorlabs BE052-B), and a pair of mirrors, as depicted in Figures 3.2 and 3.3. The transmitter beam has an adjustable output diameter between 2.0 mm and 8.0 mm with an average beam divergence of 0.29 mrad (resulting in the diameter increasing to approximately 29 cm at a range of 1.0 km). The average beam diameter-dependent

power density ranges from 10–160 $mW \cdot mm^{-2}$ at the source, with the density decreasing as a function of range.

3.8.2. *Receiver Design*

The receiving aperture for the instrument is a 203-mm diameter, 2032-mm equivalent focal length, Schmidt-Cassegrain catadioptric telescope (model LX200-ACF 203 mm f/10) from Meade Instruments (Irvine, California, USA). As depicted in Figure 3.3, a custom-built, multi-channel, optical receiver relay is mounted to the rear of the telescope. The receiver was designed to gather, collimate, split, and focus the light from the telescope into two separate channels. On the primary channel (LAS channel), backscattered light is filtered (to isolate the on-line and off-line wavelengths and to reduce diffuse sunlight saturation), focused, and fiber-coupled into the SOLAS instrument. The optical signal is further divided through a multimode fiber optic coupler. Ten percent of the split light is directed into a 400 MHz bandwidth, variable gain Thorlabs APD430A silicon avalanche photodetector (APD) via a beam collimator and focuser. The remaining 90% of the light is coupled into the BPD via a 3 dB 2 × 2 fiber optic coupler. The signal is de-chirped (i.e. mixed with the LO signal) and the beat frequency is measured directly. On the secondary channel (hyperspectral channel), the light remains unfiltered and is focused and fiber-coupled into a high-resolution spectroradiometer instrument (ASD FieldSpec 4 Hi-Res). The spectral resolution of the secondary channel is 3nm in the VNIR range (350–1000 nm) and 8 nm in the SWIR range (1000–2500 nm). The sampling interval is 1.4 nm and 1.1 nm in the VNIR and SWIR ranges, respectively. The angular field of view (FOV) for the LAS channel is 0.27 mrad and the FOV for the hyperspectral channel is 0.32 mrad (VNIR range) and 0.61 mrad (SWIR range). Due to space limitations in this manuscript, the optical receiver is described in more detail in a separate publication.

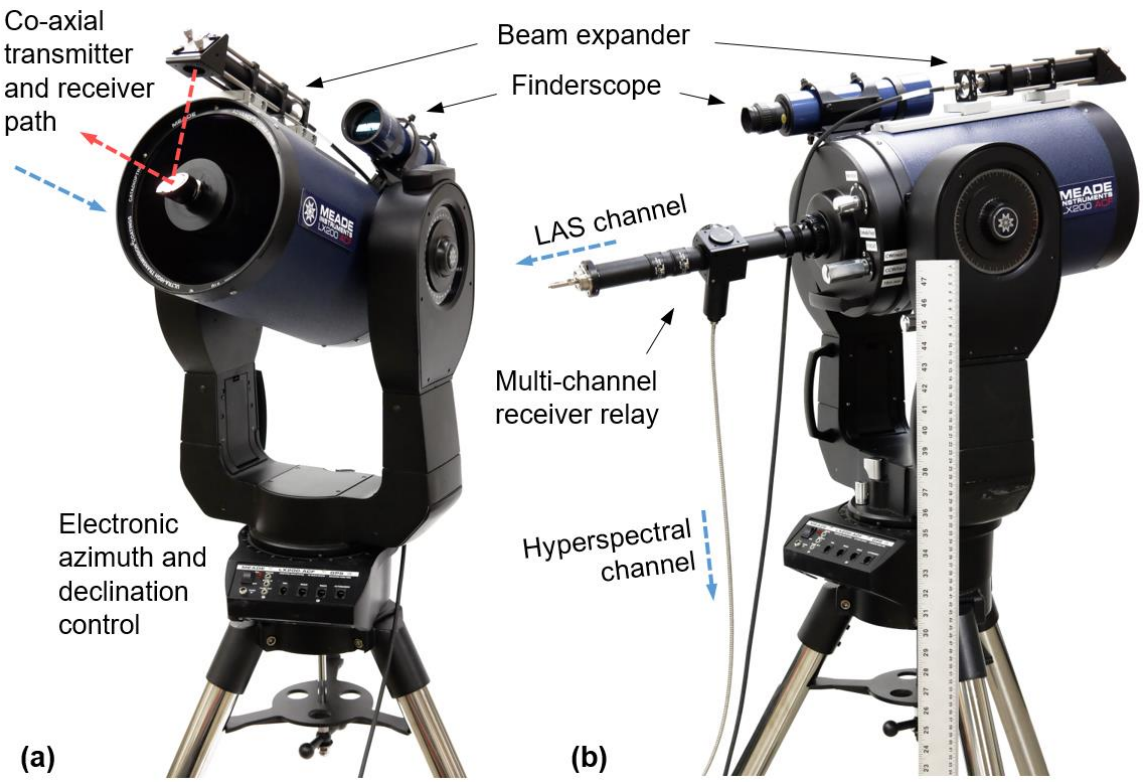

Figure 3.3. Annotated photograph of the *(a)* front, and *(b)* rear, of the receiver (scale for reference).

3.8.3. *Data Acquisition and Control Design*

Data acquisition and component control for the SOLAS are achieved via a computer that is mounted in a compact, module-based National Instruments (Austin, Texas, USA) PXIe chassis (PXIe-8135 computer, PXIe-1082 chassis) via LabVIEW software in a Windows environment. Within the chassis are (1) a high frequency RF signal generator module (PXIe-5652), (2) a wide instantaneous bandwidth vector signal analyzer (PXIe-5663E) comprised of three parallel modules (PXIe-5601, PXIe-5622, PXIe-5652), and (3) a multifunction input/output module (PXI-6238). The LabVIEW software is used to generate the chirp signal (100 MHz to 500 MHz linear ramping signal with a chirp rate of 6 MHz/μs) that is amplified and directed into the MZM. The software is also used to (1) collect and interpret the de-chirped frequency from the

BPD (to determine the range to the target), and to (2) collect and interpret data from the APD (to detect atmospheric water vapor en route to the target). The ASD RS3 software is used to collect the reflectance spectra from the spectroradiometer and the ASD ViewSpecTM Pro software is used to export the raw data for further processing. A flow diagram outlining the data acquisition and processing chain is presented in Figure 3.4.

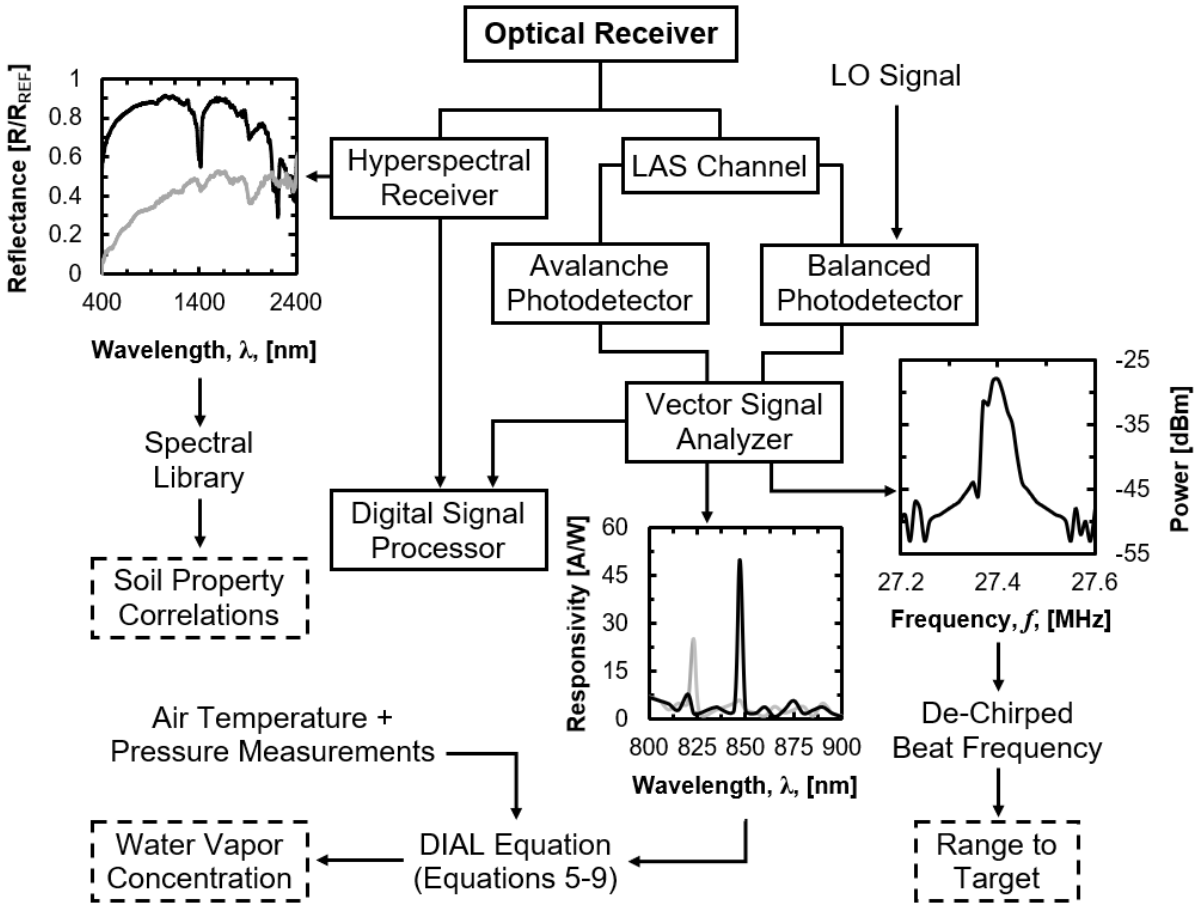

Key: DIAL = Differential Absorption Lidar; LAS = Laser Absorption Spectrometry; LO = Local Oscillator.

Figure 3.4. Data acquisition and processing chain for the Soil Observation Laser Absorption Spectrometer (SOLAS) instrument (note: simulated data).

3.8.4. *Field Ruggedization*

The majority of the components that were previously presented in Figure 3.2 are mounted within a hermetically sealed, nitrogen-purged box. The ECDL heads and MZM are mounted directly to the 12 mm thick aluminum floor of the box with thermal paste to enable the floor to act as a heat sink. The remaining power-emitting components (e.g. Thorlabs TPA830P10-SP amplifier) are actively regulated via thermoelectric cooling or are self-regulating (e.g. New Focus 1607-AC-FC and Thorlabs APD430A photodetectors). The floor of the box also acts as an optical bench for the bulk-optical components associated with the free space lasers. The transmitting and receiving fiber optic cables, RF signal cables, and component power cables are fed through one wall of the box via sealed cable glands. A plan view of the box interior is presented in Figure 3.5 and a photograph of the SOLAS instrument annotated with major assemblies is presented as Figure 3.6.

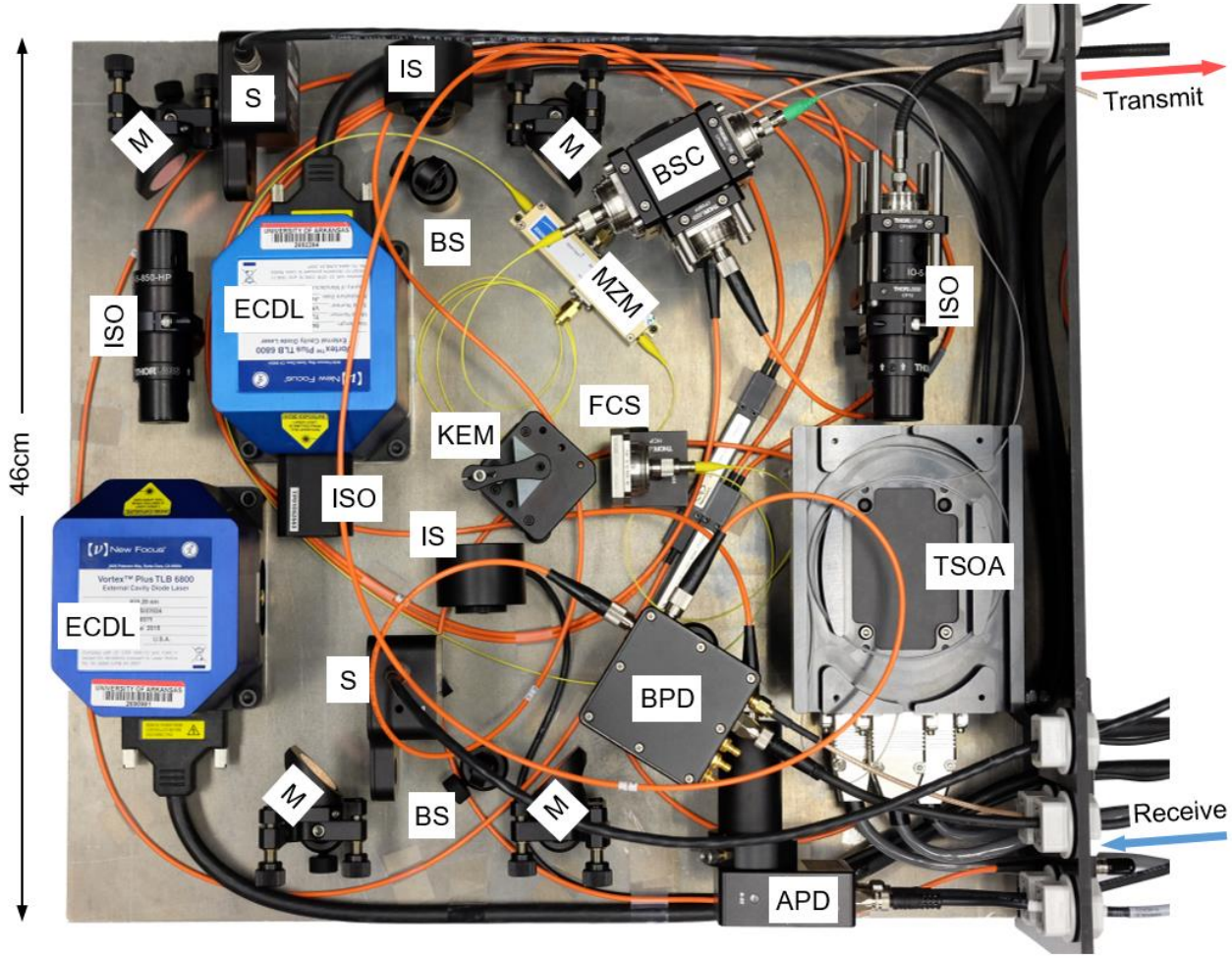

<u>Key</u>: ECDL = External Cavity Diode Laser; ISO = Optical Isolator; M = Dielectric Mirror; S = Shutter; BS = Beam Sampler; IS = Integrating Sphere; KEM = Knife-Edge Mirror; FCS = Fiber-Coupling Stage; BSC = Beamsplitter Cube; MZM = Mach-Zehnder Modulator; TSOA = Tapered Semiconductor Optical Amplifier; APD = Avalanche Photodetector; BPD = Balanced Photodetector.

Figure 3.5. Annotated plan view of the hermetically sealed box depicting the major components of the transmitter and the primary laser absorption spectrometer (LAS) receiver channel.

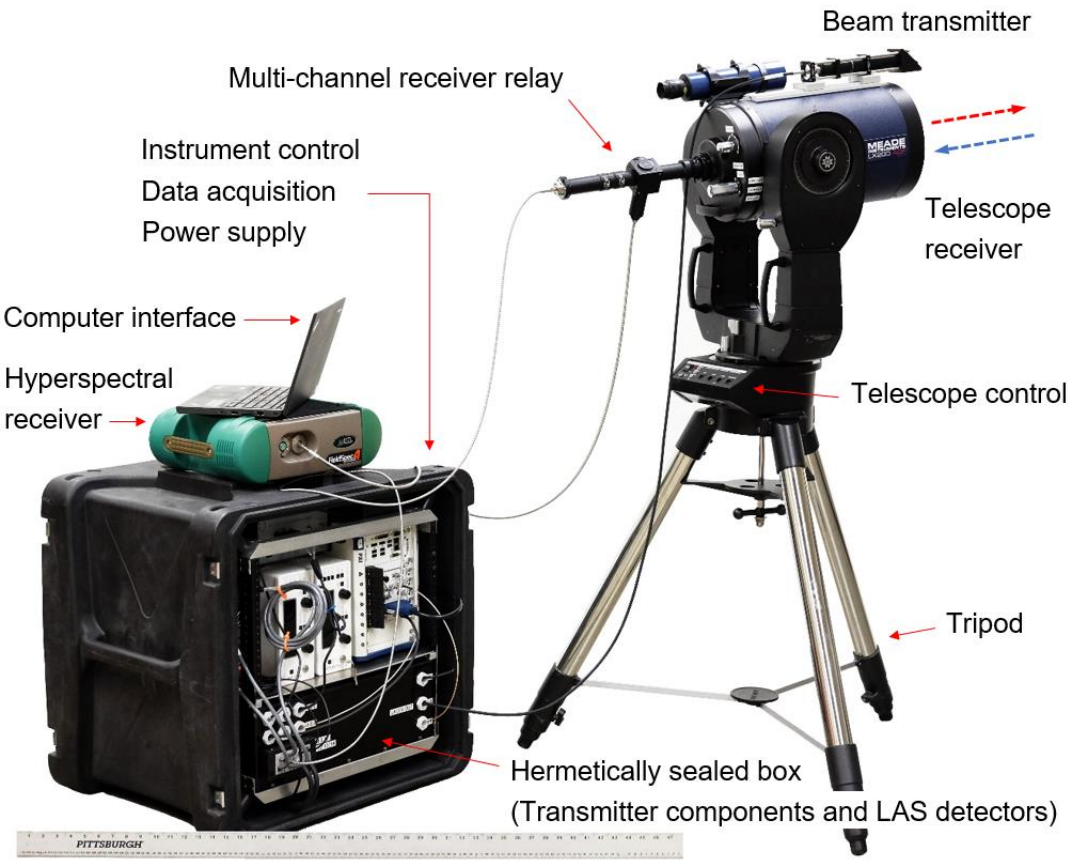

Figure 3.6. Annotated photograph of the Soil Observation Laser Absorption Spectrometer (SOLAS) instrument with major assemblies (transmitter, receiver, data acquisition and control).

3.9. Discussion

The SOLAS instrument was designed to transmit on-line and off-line wavelengths of 823.20 nm and 847.00 nm, respectively. The difference between these wavelengths combined with continuous-wave transmission, necessitated the use of two separate seed lasers (whereas some dedicated DIAL instruments have achieved on- and off-line wavelength transmission with a single, widely tunable, pulsed laser source). The two lasers were aligned into a common transmitter system using readily-available, free-space bulk optics to ease customization, calibration, and implementation. Therefore, the efficiency of the laser delivery system may be improved using an all-fiber-based design in future iterations.

The collection of measurements in the field introduces additional complexity, primarily due to (1) viewing geometry (i.e. incidence and viewing angles), (2) the sensitivity of the hyperspectral measurements to changes in light conditions (solar irradiation intensity), and (3) environmental interferences (dust, water droplets, vegetative cover). To address these issues, the instrument observation location must be carefully selected and the spectroradiometer should be calibrated using a diffuse white reference panel (e.g. Spectralon®; Labsphere Inc., North Sutton, New Hampshire, USA) positioned at approximately the same incidence angle as the intended measurements. The manufacturer of the spectroradiometer recommends frequent recalibration (referencing of the diffuse reflector panel) when collecting typical proximal (<1 m distance) measurements in the laboratory or in the field. However, it would be possible to collect remote (up to 1 km distance, or greater) measurements for an extended period of time, without frequent recalibration, if careful considerations are made. The spectroradiometer, as well as other components (e.g. laser sources, data acquisition system, and telescope), should be allowed a warm-up period (to minimize instrument noise and temperature-induced drift). Furthermore, after initial calibration of the spectroradiometer, any changes in light conditions (e.g. temporary cloud cover over target) should be observed and, if necessary, the measurements should be repeated.

The data collected by the three receivers (spectroradiometer and two LAS channel detectors) must be synthesized for meaningful interpretation of a measurement. Reflectance spectra are compiled, averaged, and compared with spectral libraries for different soil types. The measurements require post-processing (empirical calibration and statistical analysis) to extract the soil properties of interest. While reflectance data is collected using the ASD software (native to the spectroradiometer), future development of the SOLAS instrument software will enable

custom data collection and near real-time data interpretation. The reflectance measurements are susceptible to attenuation, due to atmospheric water vapor, especially at longer ranges or in conditions with higher relative humidity. To correct for the additional atmospheric absorption en route to the soil surface, the differential laser absorption measurements are used. The coherent signals also provide sub-meter range to target identification. Preliminary hyperspectral measurements have been collected for ranges greater than 100 m (laboratory setting) and 500 m field setting). Based on design calculations, measurements are possible for ranges of up to a kilometer or more (depending on atmospheric conditions), with spatial resolutions of 6 cm, 30 cm, and 60 cm (nadir) for ranges of 100 m, 500 m, and 1.0 km, respectively.

3.10. Conclusions

The development of a field-deployable, ground-based, remote sensing instrument for obtaining physical and hydro-mechanical soil properties was described herein. The Soil Observation Laser Absorption Spectrometer (SOLAS) was designed to collect range-resolved hyperspectral backscatter data from bare soil surfaces across the visible to shortwave infrared spectral ranges (350–2500 nm). The SOLAS instrument transmits two near-infrared wavelength lasers (823.20 nm and 847.00 nm) to measure atmospheric water vapor by differential absorption along the transmitter path. Self-chirped, coherent detection of the same lasers provides target range measurements. The backscattered light is received through a 203-mm diameter telescope. The combination of high-resolution reflectance spectroradiometry and lidar (ranging and differential absorption) techniques has introduced a new ground-based approach to remote sensing of the natural environment. Envisioned applications for the instrument include rapid classification of soils on unstable slopes, mine tailings, or in wildfire-affected areas. Future improvements will enable long-range measurements, increased portability (lighter instrument

components), or semi-autonomous measurements as part of a long-term monitoring installation (e.g. wildfire basin or mining operation).

3.11. Acknowledgements

This project was funded by the U.S. Department of Transportation (USDOT) through the Office of the Assistant Secretary for Research and Technology (OST-R) under USDOT Cooperative Agreement No. OASRTRS-14-H-UARK. The views, opinions, findings and conclusions reflected in this publication are solely those of the authors and do not represent the official policy or position of the USDOT/OST-R, or any State or other entity. USDOT/OST-R does not endorse any third party products or services that may be included in this publication. This material is also based upon work supported by the National Science Foundation Graduate Research Fellowship Program under Grant No. DGE-1450079. Any opinions, findings, and conclusions or recommendations expressed in this material are those of the authors and do not necessarily reflect the views of the National Science Foundation.

3.12. References

Adany, P., Allen, C., and Hui, R., 2009, "Chirped Lidar Using Simplified Homodyne Detection," *J. Lightwave Technol.*, Vol. 27, No. 16, pp. 3351-3357.

Allen, C., Cobanoglu, Y., Chong, S. K., and Gogineni, S., 2001, "Performance of a 1319 nm Laser Radar Using RF Pulse Compression," *Proceedings of the International Geoscience and Remote Sensing Symposium (IGARSS 2001)*, Sydney, Australia, July 7–13, pp. 997-999. doi:10.1109/IGARSS.2001.976726.

Ångström, A., 1925, "The Albedo of Various Surfaces of Ground," *Geogr. Ann.*, Vol. 7, pp. 323-342. doi:10.2307/519495.

Bach, H. and Mauser, W., 1994, "Modelling and Model Verification of the Spectral Reflectance Of Soils Under Varying Moisture Conditions," *Proceedings of the International Geoscience and Remote Sensing Symposium (IGARSS'94)*, Pasadena, CA, USA, August 8–12, pp. 2354-2356. doi:10.1109/IGARSS.1994.399735.

Barber, Z. W. Babbitt, W. R., Kaylor, B., Reibel, R. R., and Roos, P. A., 2010, "Accuracy of Active Chirp Linearization for Broadband Frequency Modulated Continuous Wave Ladar," *Appl. Optics*, Vol. 49, No. 2, pp. 213-219.

Barrientos-Barria, J., Mammez, D., Dherbecourt, J.-B., Raybaut, M., Melkonian, J.-M., Pelon, J., Godard, A., and Lefebvre, M., 2014, "Progress on High Energy Optical Parametric Transmitter for Multiple Greenhouse Gases DIAL," *Proceedings of the International Conference on Space Optics (ICSO 2014)*, Tenerife, Canary Islands, Spain, October 6–10, SPIE Vol. 10563. doi:10.1117/12.2304157.

Ben-Dor, E. and Banin, A., 1995, "Near-Infrared Analysis as a Rapid Method to Simultaneously Evaluate Several Soil Properties," *Soil Sci. Soc. Am. J.*, Vol. 59, No. 2, pp. 364-372.

Bösenberg, J., 1998, "Ground-Based Differential Absorption Lidar for Water-Vapor and Temperature Profiling: Methodology," *Appl. Optics*, Vol. 37, No. 18, pp. 3845-3860.

Bowers, S. A. and Hanks, R. J., 1965, "Reflection of Radiant Energy from Soils," *Soil Sci.*, Vol. 100, No. 2, pp. 130-138.

Browell, E. V., Dobler, J., Kooi, S. A., Choi, Y., Harrison, F. W., Moore, B., and Zaccheo, T. S., 2010, "Airborne Validation of Laser Remote Measurements of Atmospheric Carbon Dioxide," *Proceedings of the 25th International Laser Radar Conference (ILRC 25)*, St. Petersburg, Russia, July 5–9, pp. 779-782.

Bruneau, D., Quaglia, P., Flamant, C., Meissonnier, M., and Pelon, J., 2001a, "Airborne Lidar LEANDRE II for Water-Vapor Profiling in the Troposphere. I. System Description," *Appl. Optics*, Vol. 40, No. 21, pp. 3450-3461.

Bruneau, D., Quaglia, P., Flamant, C., and Pelon, J., 2001b, "Airborne Lidar LEANDRE II for Water-Vapor Profiling in the Troposphere. II. First Results," *Appl. Optics*, Vol. 40, No. 21, pp. 3462-3475.

Bufton, J. L., Itabe, T., and Grolemund, D. A., 1983, "Airborne Remote Sensing Measurements With a Pulsed CO_2 Dial System," *Optical and Laser Remote Sensing*, D.K. Killinger, A. Mooradian, Eds., Springer-Verlag, Berlin Heidelberg, Germany, pp. 2-9.

Chang, C.-W., Laird, D., Mausbach, M. J., and Hurburgh, C. R., 2001, "Near-Infrared Reflectance Spectroscopy-Principle Components Regression Analysis of Soil Properties," *Soil Sci. Soc. Am. J.*, Vol. 65, pp. 480-490.

Cozzolino, D. and Moron, A., 2003, "The Potential of Near-Infrared Reflectance Spectroscopy to Analyze Soil Chemical and Physical Characteristics," *J. Agr. Sci.*, Vol. 140, pp. 65-71.

Dalal, R. C. and Henry, R. J., 1986, "Simultaneous Determination of Moisture, Organic Carbon, And Total Nitrogen by Near Infrared Reflectance Spectrophotometry," *Soil Sci. Soc. Am. J.*, Vol. 50, No. 1, pp. 120-123. doi:10.2136/sssaj1986.03615995005000010023x.

Ehret, G., Kiemle, C., Renger, W., and Simmet, G., 1993, "Airborne Remote Sensing of Tropospheric Water Vapor with a Near-Infrared Differential Absorption Lidar System," *Appl. Optics*, Vol. 32, No. pp. 4534-4551.

Ehret, G., Kiemle, C., Wirth, M., Amediek, A., Fix, A., and Houweling, S., 2008, “Space-Borne Remote Sensing of CO2, CH4, and N2O by Integrated Path Differential Absorption Lidar: A Sensitivity Analysis,” *Appl. Phys. B-Lasers O.*, Vol. 90, No. 3-4, pp. 593-608.

Fabre, S., Briottet, X., and Lesaignoux, A., 2015, "Estimation of Soil Moisture Content from the Spectral Reflectance of Bare Soils in the 0.4-2.5 μm Domain," *Sensors*, Vol. 15, pp. 3262-3281. doi:10.3390/s150203262.

Gao, S. and Hui, R., 2012, "Frequency-Modulated Continuous-Wave Lidar Using I/Q Modulator For Simplified Heterodyne Detection," *Opt. Lett.*, Vol. 37, No. 11, pp. 2022-2024; doi:10.1364/OL.37.002022.

Garner, C. D., 2017, "Development of a Multiband Remote Sensing System for Determination of Unsaturated Soil Properties," Ph.D. dissertation, University of Arkansas, Fayetteville, AR, USA.

Gordon, I. E., Rothman, L. S., Hill, C., et al., 2017, "The HITRAN2016 Molecular Spectroscopic Database", *J. Quant. Spectrosc. Ra.*, Vol. 203, pp. 3-69. doi:10.1016/j.jqsrt.2017.06.038.

Grant, W. B., 1982, "Effect of Differential Spectral Reflectance on DIAL Measurements Using Topographic Targets," *Appl. Optics*, Vol. 21, No. 13, pp. 2390-2394.

Grant, W. B., 1991, "Differential Absorption and Raman Lidar for Water Vapor Profile Measurements: A Review," *Opt. Eng.*, Vol. 30, No. 1, pp. 40-48.

Hardesty, R. M., 1984, "Coherent DIAL Measurement of Range-Resolved Water Vapor Concentration," *Appl. Optics*, Vol. 23, No. 15, pp. 2545-2553.

Haubrock, S. N., Chabrillat, S., Lemmnitz, C., and Kaufmann, H., 2008, "Surface Soil Moisture Quantification Models from Reflectance Data Under Field Conditions," *Int. J. Remote Sens.*, Vol. 29, No. 1, pp. 3-29. doi:10.1080/01431160701294695.

Hummel, J. W., Sudduth, K. A., and Hollinger, S. E., 2001, "Soil Moisture and Organic Matter Prediction of Surface and Subsurface Soils Using an NIR Soil Sensor," *Comput. Electron. Agr.*, Vol. 32, No. 2, pp. 149-165. doi:10.1016/S0168-1699(01)00163-6.

Ishii, S., Koyama, M., Baron, P., Iwai, H., Mizutani, K., Itabe, T., Sato, A., and Asai, K., 2013, "Ground-Based Integrated Path Coherent Differential Absorption Lidar Measurement of CO_2: Foothill Target Return," *Atmos. Meas. Tech.*, Vol. 6, pp. 1359-1369. doi:10.5194/amt-6-1359-2013.

Islam, K., Singh, B., and McBratney, A., 2003, "Simultaneous Estimation of Various Soil Properties by Ultra-Violet, Visible, and Near-Infrared Reflectance Spectroscopy," *Aust. J. Soil Res.*, Vol. 41, No. 6, pp. 1101-1114.

Ismail, S. and Browell, E. V., 1989, "Airborne and Spaceborne Lidar Measurements of Water Vapor Profiles: A Sensitivity Analysis," *Appl. Optics*, Vol. 28, No. 17, pp. 3603-3615.

Janik, L. and Skjemstad, J., 1995, "Characterization and Analysis of Soils Using Mid-Infrared Partial Least Squares: II. Correlations with Some Laboratory Data," *Aust. J. Soil Res.*, Vol. 33, pp. 637-650.

Jelalian, A. *Laser Radar Systems*. Artech House, Norwood, MA, USA, 1992.

Karlsson, C. J. and Olsson, F. Å. A., 1999, "Linearization of the Frequency Sweep of a Frequency-Modulated Continuous-Wave Semiconductor Laser and the Resulting Ranging Performance," *Appl. Optics*, Vol. 38, No. 15, pp. 3376-3386.

Knadel, M., Deng, F., Alinejadian, A., de Jonge, L. W., Moldrup, P., and Greve, M. H., 2014, "The Effects of Moisture Conditions – From Wet to Hyper Dry – On Visible Near Infrared Spectra of Danish Reference Soils," *Soil Sci. Soc. Am. J.*, Vol. 78, No. 2, pp. 422-433. doi:10.2136/sssaj2012.0401.

Knadel, M., Stenberg, B., Deng, F., Thomsen, A., and Greve, M. H., 2013, "Comparing Predictive Abilities of Three Visible-Near Infrared Spectrophotometers for Soil Organic Carbon and Clay Determination," *J. Near Infrared Spec.*, Vol. 21, No. 1, pp. 67-80. doi:10.1255/jnirs.1035.

Kou, L., Labrie, D., and Chylek, P., 1993, "Refractive Indices of Water and Ice in the 0.65- to 2.5-μm Spectral Range," *Appl. Optics*, Vol. 32, No. 19, pp. 3531-3540.

Lesaignoux, A., Fabre, S., and Briottet, X., 2013, "Influence of Soil Moisture Content on Spectral Reflectance of Bare Soils in the 0.4-14 μm Domain," *Int. J. Remote Sens.*, Vol. 34, No. 7, pp. 2268-2285. doi:10.1080/01431161.2012.743693.

Leu, D. J., 1977, "Visible and Near-Infrared Reflectance of Beach Sands: A Study on the Spectral Reflectance/Grain Size Relationship," *Remote Sens. Environ.*, Vol. 6, No. 3, pp. 169-182. doi:10.1016/0034-4257(77)90002-5.

Little, L. M. and Papen, G. C., 2001, "Fiber-Based Lidar for Atmospheric Water-Vapor Measurements," *Appl. Optics*, Vol. 40, No. 21, pp. 3417-3427.

Liu, W., Baret, F., Gu, X., Tong, Q., Zheng, L., and Zhang, B., 2002, "Relating Soil Surface Moisture to Reflectance," *Remote Sens. Environ.*, Vol. 81, pp. 238-246.

Liu, W., Baret, F., Gu, X., Zhang, B., Tong, Q., and Zheng, L., 2003, "Evaluation of Methods for Soil Surface Moisture Estimation from Reflectance Data," *Int. J. Remote Sens.*, Vol. 24, No. 10, pp. 2069-2083.

Lobell, D. B. and Asner, G. P., 2002, "Moisture Effects on Soil Reflectance," *Soil Sci. Soc. Am. J.*, Vol. 66, No. 3, pp. 722-727.

Machol, J., Ayers, T., Schwenz, K., Koenig, K., Hardesty, R., Senff, C., Krainak, M., Abshire, J., Bravo, H., and Sandberg, S., 2004, "Preliminary Measurements with an Automated Compact Differential Absorption LIDAR for Profiling Water Vapor," *Appl. Optics*, Vol. 43, No. 15, pp. 3110-3121.

Mateo, A. B., 2014, "Applications of High Resolution and Accuracy Frequency Modulated Continuous Wave Ladar," M.S. thesis, Montana State University, Bozeman, MT, USA.

Megie, G. and Menzies, R. T., 1980, "Complementarity of UV and IR Differential Absorption Lidar for Global Measurements of Atmospheric Species," *Appl. Optics*, Vol. 19, No. 7, pp. 1173-1183.

Menzies, R. T. and Shumate, M. S., 1976, "Remote Measurements of Ambient Air Pollutants With a Bistatic Laser System," *Appl. Optics*, Vol. 15, No. 9, pp. 2080-2084.

Mouazen, A. M., Karoui, R., De Baerdemaeker, J., and Ramon, H., 2006, "Characterization of Soil Water Content Using Measured Visible and Near Infrared Spectra," *Soil Sci. Soc. Am. J.*, Vol. 70, No. 4, pp. 1295-1302. doi:10.2136/sssaj2005.0297.

Mouazen, A. M., Maleki, M. R., De Baerdemaeker, J., and Ramon, H., 2007, "On-line Measurement of Some Selected Soil Properties Using a VIS-NIR Sensor," *Soil Till. Res.*, Vol. 93, No. 1, pp. 13-27. doi:10.1016/j.still.2006.03.009.

Nehrir, A. R., 2008, "Water Vapor Profiling Using a Compact Widely Tunable Diode Laser Differential Absorption Lidar (DIAL)," M.S. thesis, Montana State University, Bozeman, MT, USA.

Nehrir, A. R., 2011, "Development of an Eye-Safe Diode-Laser-Based Micro-Pulse Differential Absorption Lidar (MP-DIAL) for Atmospheric Water-Vapor and Aerosol Studies," Ph.D. Dissertation, Montana State University, Bozeman, MT, USA.

Nehrir, A. R., Repasky, K. S., and Carlsten, J. L., 2011, "Eye-Safe Diode-Laser-Based Micropulse Differential Absorption Lidar (DIAL) for Water Vapor Profiling in the Lower Troposphere," *J. Atmos. Ocean. Tech.,* Vol. 28, pp. 131-147.

Nehrir, A. R., Repasky, K. S., and Carlsten, J. L., 2012, "Micropulse Water Vapor Differential Absorption Lidar: Transmitter Design and Performance," *Opt. Express,* Vol. 20, No. 22, pp. 25137-25151.

Nehrir, A. R., Repasky, K. S., Carlsten, J. L., Obland, M. D., and Shaw, J. A., 2009, "Water Vapor Profiling Using a Widely Tunable, Amplified Diode-Laser-Based Differential Absorption Lidar (DIAL)," *J. Atmos. Ocean. Tech.*, Vol. 26, No. 4, pp. 733-745.

Nolet, C., Poortinga, A., Roosjen, P., Bartholomeus, H., and Ruessink, G., 2014, "Measuring and Modeling the Effect of Surface Moisture on the Spectral Reflectance of Coastal Beach Sand," *PLoS One,* Vol. 9, No. 11, e112151. doi:10.1371/journal.pone.0112151.

Park, J. K., 1980, "A Soil Moisture Reflectance Model in Visible and Near IR Bands," *Proceedings of the International Symposium on Machine Processing of Remotely Sensed Data and Soil Information Systems and Remote Sensing and Soil Survey,* Purdue University, West Lafayette, IN, USA, June 3–6.

Philpot, W. D. and Tian, J., 2016, "The Hyperspectral Soil Line: A Preliminary Description," *Light, Energy, and the Environment,* OSA Technical Digest (Online), Optical Society of America, paper HW3E.2, 3 pgs.

Pierrottet, D., Amzajerdian, F., and Peri, F., 2005, "Development of an All-Fiber Coherent Laser Radar for Precision Range and Velocity Measurements," *Proceedings of the Materials Research Society Symposium,* Boston, MA, USA, November 28 – December 2005, Vol. 833. doi:10.1557/PROC-833-FF2.3

Pierrottet, D., Amzajerdian, F., Petway, L., Barnes, B., Lockard, G., and Rubio, M., 2008, "Linear FMCW Laser Radar for Precision Range and Vector Velocity Measurements," *Proceedings of the Materials Research Society Symposium,* San Francisco, CA, USA, March 24–28, Vol. 1076. doi:10.1557/PROC-1076-K04-06.

Pope, R. M. and Fry, E. S., 1997, "Absorption Spectrum (380-700 nm) of Pure Water. II. Integrating Cavity Measurements," *Appl. Optics,* Vol. 36, No. 33, pp. 8710-8723.

Prasad, N. S. and Geiger, A. R., 1996, "Remote Sensing of Propane and Methane by Means of a Differential Absorption Lidar by Topographic Reflection," *Opt. Eng.*, Vol. 35, No. 4, pp. 1105-1111.

Remsberg, E. E. and Gordley, L. L., "Analysis of Differential Absorption Lidar from the Space Shuttle," *Appl. Optics*, Vol. 17, No. 4, pp. 624-630.

Rothman, L. S., Gordon, I. E., Babikov, Y., et al., 2013, "The HITRAN2012 Molecular Spectroscopic Database," *J. Quant. Spectrosc. Ra.*, Vol. 130, pp. 4-50. doi:10.1016/j.jqsrt.2013.07.002.

Sadeghi, M., Jones, S. B., and Philpot, W. D., 2015, "A Linear Physically-Based Model for Remote Sensing of Soil Moisture Using Short Wave Infrared Bands," *Remote Sens. Environ.*, Vol. 164, pp. 66-76. doi:10.1016/j.rse.2015.04.007.

Sakaizawa, D., Kawakami, S., Nakajima, M., Sawa, Y., and Matsueda, H., 2010, "Ground-Based Demonstration of CO_2 Remote Sensor using 1.57 μm Differential Laser Absorption Spectrometer with Direct Detection," *J. Appl. Remote Sens.*, Vol. 4, No. 1, 043548. doi:10.1117/1.3507092.

Schotland, R. M., 1966, "Some Observations of the Vertical Profile of Water Vapor by a Laser Optical Radar," *Proceedings of the Fourth Symposium on Remote Sensing of the Environment*, Ann Arbor, MI, USA, April 12–14, pp. 273-283.

Schotland, R. M., 1974, "Errors in the Lidar Measurement of Atmospheric Gases by Differential Absorption," *J. Appl. Meteorol.*, Vol. 13, pp. 71-77.

Shepherd, K. D. and Walsh, M. G., 2002, "Development of Reflectance Spectral Libraries for Characterization of Soil Properties," *Soil Sci. Soc. Am. J.*, Vol. 66, pp. 988-998.

Skolnik, M. I., 1960, "Theoretical Accuracy of Radar Measurements," *IRE T. Aeron. Navig. Electr.*, pp. 123-129. doi:10.1109/TANE3.1960.4201757.

Spuler, S. M., Repasky, K. S., Morley, B., Moen, D., Hayman, M., and Nehrir, A. R., 2015, "Field Deployable Diode-Laser-Based Differential Absorption Lidar (DIAL) for Profiling Water Vapor," *Atmos. Meas. Tech.*, Vol. 8, pp. 1073-1087.

Spuler, S., Repasky, K., Morley, B., Moen, D., Weckwerth, T., Hayman, M., and Nehrir, A., 2016, "Advances in Diode-Laser-Based Water Vapor Differential Absorption Lidar," *Proceedings of the 27th International Laser Radar Conference (ILRC 27)*, New York City, NY, USA, July 5–10. doi:10.1051/epjconf/201611902003.

Tian, J. and Philpot, W. D., 2015, Relationship Between Surface Soil Water Content, Evaporation Rate, and Water Absorption Band Depths in SWIR Reflectance Spectra," *Remote Sens. Environ.*, Vol. 169, No. pp. 280-289.

Walvoort, A. and McBratney, A., 2001, "Diffuse Reflectance Spectrometry as a Proximal Sensing Tool for Precision Agriculture," *Proceedings of the 3rd European Conference on Precision Agriculture*, Montpellier, France, June 18–20, pp. 503-508.

Waruru, B. K., Shepherd, K. D., Ndegwa, G. M., Kamoni, P. T., and Sila, A. M., 2014, "Rapid Estimation of Soil Engineering Properties Using Diffuse Reflectance Near Infrared Spectroscopy," *Biosyst. Eng.*, Vol. 121, pp. 177-185. doi:10.1016/j.biosystemseng.2014.03.003.

Weckwerth, T. M., Weber, K. J., Turner, D. D., and Spuler, S. M., 2016, "Validation of a Water Vapor Micropulse Differential Absorption Lidar (DIAL)," *J. Atmos. Ocean. Tech.*, Vol. 33, No. 11, pp. 2353-2372.

Whalley, W. R., Leeds-Happison, P. B., and Bowman, G. E., 1991, "Estimation of Soil Moisture Using Near Infrared Reflectance," *Hydrol. Process.*, Vol. 5, pp. 321-327.

Whiting, M. L., Li, L., and Ustin, S. L., 2004, "Predicting Water Content Using Gaussian Model On Soil Spectra," *Remote Sens. Environ.*, Vol. 89, No. 4, pp. 535-552.

Wirth, M., Fix, A., Mahnke, P., Schwarzer, H., Schrandt, F., and Ehret, G., 2009, "The Airborne Multi-Wavelength Water Vapor Differential Absorption Lidar WALES: System Design And Performance," *Appl. Phys. B-Lasers O.*, Vol. 96, pp. 201-213. doi:10.1007/s00340-009-3365-7.

Wulf, H., Mulder, T., Schaepman, M. E., Keller, A., and Jörg, P. C., 2015, "Remote Sensing of Soils," Report prepared by the Remote Sensing Laboratories, Dept. of Geography, University of Zurich, Switzerland, 71 pgs. doi:10.5167/uzh-109992.

Wulfmeyer, V., 1998, "Ground-Based Differential Absorption Lidar for Water-Vapor and Temperature Profiling: Development and Specifications of a High-Performance Laser Transmitter," *Appl. Optics*, Vol. 37, No. 18, pp. 3804-3824.

Wulfmeyer, V. and Bösenberg, J., 1998, "Ground-Based Differential Absorption Lidar for Water-Vapor Profiling: Assessment of Accuracy, Resolution, and Meteorological Applications," *Appl. Optics*, Vol. 37, No. 18, pp. 3825-3844.

Wulfmeyer, V. and Walther, C., 2001, "Future Performance of Ground-Based and Airborne Water-Vapor Differential Absorption Lidar. I. Overview and Theory," *Appl. Optics*, Vol. 40, No. 30, pp. 5304-5320.

Xu, C., Zeng, W., Huang, J., Wu, J., and van Leeuwen, W. J. D., 2016, "Prediction of Soil Moisture Content and Soil Salt Concentration from Hyperspectral Laboratory and Field Data," *Remote Sens.*, Vol. 8, No. 42, 20 pgs. doi:10.3390/rs8010042.

Yitagesu, F. A., van der Meer, F., van der Werff, H., and Zigterman, W., 2009, "Quantifying Engineering Parameters of Expansive Soils from their Reflectance Spectra," *Eng. Geol.*, Vol. 105, No. 3-4, pp. 151-160. doi:10.1016/j.enggeo.2009.01.004.

CHAPTER 4: MULTI-CHANNEL OPTICAL RECEIVER FOR GROUND-BASED TOPOGRAPHIC HYPERSPECTRAL REMOTE SENSING

4.1. Chapter Overview

A detailed description of the SOLAS multi-channel optical receiver is contained in this chapter. The design and specifications of the receiver are described and short-range tests, that were conducted to verify the functionality of the design, are presented. Discussion about the utility of the SOLAS for remote sensing of soils, rocks, and vegetation is provided.

The limitations of the Salazar and Coffman (2019a) paper are outlined in Section 4.2. The full citation for the manuscript is included in Section 4.3, followed by the abstract in Section 4.4. Contained within Section 4.5 are the introduction and motivation for the paper. The materials and methods used to develop and test the receiver are described in Section 4.6. The results are discussed in Section 4.7 and concluding remarks are contained in Section 4.8.

4.2. Limitations of the Described Study

The focus of the work presented in this chapter was the design and preliminary testing of the SOLAS optical receiver. The results presented were therefore limited in scope. Moreover, the testing took place indoors, using artificially-illuminated targets, and was not subject to the same environmental factors that are present in outdoor testing under solar illumination. The paper included some discussion about the aforementioned limitations in Section 4.7; opportunity to conduct more extensive testing of the SOLAS was presented.

4.3. Multi-Channel Optical Receiver for Ground-Based Topographic Hyperspectral Remote Sensing

Reference

Salazar, Sean E. and Coffman, Richard A., "Multi-Channel Optical Receiver for Ground-Based Topographic Hyperspectral Remote Sensing," Remote Sensing, Vol. 11, No. 5, 2019, 578. doi:10.3390/rs11050578.

4.4. Abstract

Receiver design is integral to the development of a new remote sensor. An effective receiver delivers backscattered light to the detector while optimizing the signal-to-noise ratio at the desired wavelengths. Towards the goal of effective receiver design, a multi-channel optical receiver was developed to collect range-resolved, backscattered energy for simultaneous hyperspectral and differential absorption spectrometry (LAS) measurements. The receiver is part of a new, ground-based, multi-mode lidar instrument for remote characterization of soil properties. The instrument, referred to as the Soil Observation Laser Absorption Spectrometer (SOLAS), was described previously in the literature. A detailed description of the multi-channel receiver of the SOLAS is presented herein. The hyperspectral channel receives light across the visible near-infrared (VNIR) to shortwave infrared (SWIR) spectrum (350–2500 nm), while the LAS channel was optimized for detection in a narrower portion of the near-infrared range (820–850 nm). The range-dependent field of view for each channel is presented and compared with the beam evolution of the SOLAS instrument transmitter. Laboratory-based testing of each of the receiver channels was performed to determine the effectiveness of the receiver. Based on reflectance spectra collected for four soil types, at distances of 20, 35, and 60 m from the receiver, reliable hyperspectral measurements were gathered, independent of the range to the target. Increased levels of noise were observed at the edges of the VNIR and SWIR detector ranges, which were attributed to the lack of sensitivity of the instrument in these regions. The suitability of the receiver design, for the collection of both hyperspectral and LAS measurements at close-ranges, is documented herein. Future development of the instrument will enable the combination of long-range, ground-based hyperspectral measurements with the LAS measurements to correct for absorption, due to atmospheric water vapor. The envisioned

application for the instrument includes the rapid characterization of bare or vegetated soils and minerals, such as are present in mine faces and tailings, or unstable slopes.

Keywords: instrument development, hyperspectral, spectroradiometry, telescope, receiver, soil

4.5. Introduction

All remote sensors, including various types of lidar instruments, employ receivers to collect backscattered energy. The receiver design is commonly dependent on the sensor type and the instrument application. While some lidar receivers use one or more lenses to focus and collimate incoming light, others utilize custom, large-aperture optical arrays to maximize, split, or otherwise manipulate the received energy. Ground-based, atmosphere-focused laser absorption spectrometry (LAS) instruments, commonly identified as differential absorption lidars (DIAL), have often employed a telescope as the primary aperture of the receiver (Hardesty 1984, Little and Papen 2001, Machol et al. 2004, Spuler et al. 2015). Compact, large-diameter telescopes have been favored because the relative light grasp of a telescope is directly proportional to the square of the aperture area, aiding in long-range atmospheric measurements.

While most examples in the literature utilize simple, single-channel, configurations to receive light, some researchers have designed multi-channel optical receivers, placed between the primary aperture (telescope) and the data acquisition system. For example, Moore et al. (1996) split light into separate channels to allow for simultaneous low-gain/high-gain detection and laser-to-telescope alignment. Likewise, Repasky (2016) and Moen (2016) split light into near-field and far-field receiver channels to provide atmospheric measurements over short (1 km) and long (up to 12 km) ranges, respectively. In another iteration of the Moen (2016) two-

channel DIAL receiver, a shared telescope for transmission and receiving enabled stable alignment and eye-safe beam expansion (Spuler et al. 2015).

As DIAL instruments have historically been developed to collect atmospheric backscatter from water vapor and aerosols in the troposphere, there are limited examples of DIAL instruments operating in horizontal orientations to collect backscatter from a topographic (hard) target (Grant 1982, Hardesty 1984, Nehrir 2011, Ishii et al. 2013). In the aforementioned instances, the topographic targets served as a test for bias, due to differential spectral reflectance (Grant 1982, Ishii et al. 2013), or as a measurement of spectral purity (Nehrir 2011). Typical DIAL configurations provide information for two wavelengths (one wavelength centered on a molecular species absorption line, λ_{on}, while the second, nearby wavelength, λ_{off}, serves as a reference).

In this paper, a multi-channel optical receiver is described. The receiver was developed to enable simultaneous range-resolved hyperspectral measurements of hard targets and differential laser absorption measurements for atmospheric corrections of the hyperspectral measurements. The receiver is part of a new ground-based remote sensing instrument, called the Soil Observation Laser Absorption Spectrometer (SOLAS), previously described in the literature by Salazar et al. (2019). The instrument was developed for rapid characterization of bare soil, rock surfaces, and/or vegetation. There is also potential for cross-platform calibration and validation (ground-truth) of airborne or upcoming spaceborne hyperspectral missions, such as PRISMA, EnMAP, HISUI, and HyspIRI (Loizzo et al. 2016, Guanter et al. 2015, Tanii et al. 2017, JPL 2018). The SOLAS instrument transmits two amplitude-modulated continuous-wave (AM-CW) near-infrared (NIR) lasers with wavelengths of 823.20 nm and 847.00 nm. The SOLAS receives backscattered light with a hyperspectral sensor and a pair of near-infrared

photodetectors. The hyperspectral receiver detects light continuously across the visible to shortwave infrared (SWIR) range (350–2500 nm). A balanced photodetector is used to determine the range to the target using a frequency-modulated continuous-wave (FMCW) lidar, while an avalanche photodetector is used to determine the horizontal concentration of atmospheric water vapor en route to the target via a differential laser absorption measurement technique. The atmospheric measurements will be used in the future to correct the hyperspectral reflectance from long-range targets. Although the SOLAS instrument was described previously (Salazar et al. 2019), a more detailed discussion of the development and testing of the multi-channel receiver portion of the instrument, as used to collect the backscattered energy, is discussed in the following sections.

4.6. Materials and Methods

The primary aperture of the SOLAS instrument receiver consists of a Meade LX200-ACF Schmidt-Cassegrain catadioptric telescope (Meade Instruments; Irvine, California, USA). The surfaces of the telescope optics are coated with a proprietary Ultra High Transmission Coating (UHTC). The UHTC is designed to reduce reflections while maximizing light transmission. Various compounds are used in the coating (aluminum and titanium oxides on the front and back of the corrector lens; titanium and silicon dioxides on the reflecting surface of the primary and secondary mirrors). The telescope has a diameter of 203 mm and an effective focal length of 2032 mm that focuses light into a multi-channel, polarization insensitive, optical relay mounted to the rear port of the telescope. An uncoated Thorlabs LB1471 field lens (Thorlabs Inc.; Newton, New Jersey, USA), positioned at the focal plane of the telescope, gathers the received light from the rear port. Positioned behind the field lens is a 0.8–25.0 mm diameter adjustable Thorlabs SM1D25 iris and an uncoated Thorlabs LBF254-050 spherical singlet collimator lens.

A Thorlabs BPD254-G Polka-Dot 50:50 beamsplitter positioned at 45° splits the collimated light evenly into two separate channels; one hyperspectral channel and one LAS channel.

The hyperspectral channel, referred to in this paper as Channel 1, is reserved for hyperspectral backscatter measurements. For this channel, light is focused with two uncoated aspheric lenses (Thorlabs AL1512 and AL108) and coupled into a high radiometric-resolution spectroradiometer (Analytical Spectral Devices [ASD] FieldSpec 4 Hi-Res; Malvern Panalytical, Longmont, Colorado, USA) via a multimode fiber bundle. The ASD FieldSpec 4 instrument detects light continuously over the visible to SWIR wavelengths using 2151 bands. The visible near-infrared (VNIR) bands, ranging in wavelength from 350 to 1000 nm, use a silicon detector to provide a spectral resolution of 3 nm and a sampling interval of 1.4 nm. Two sets of SWIR bands, ranging in wavelength from 1001 to 1800 nm and 1801 to 2500 nm, each using a thermoelectric-cooled indium gallium arsenide (InGaAs) detector, provide a spectral resolution of 8 nm and a sampling interval of 1.1 nm. The wavelength reproducibility is 0.1 nm and the wavelength accuracy is 0.5 nm.

The LAS channel, referred to in this paper as Channel 2, focuses light via two, coated, positive achromatic doublet lenses (Thorlabs AC127-050-B and AC080-10-B) and optionally filters the light using one of two interchangeable narrow bandpass filters, centered at 820 nm or 850 nm (Thorlabs FB820-10 and FB850-10, respectively), each with full-width at half-maximum (FWHM) filtering of 10 ± 2nm. After focusing and filtering, the light in Channel 2 is collimated into a 50-µm core diameter, anti-reflective-coated, step-index multimode, fiber optic cable (Thorlabs M50L02S-B) via a Thorlabs PAF-SMA-5-B aspheric lens fiber-coupling stage. The aforementioned light on Channel 2 is delivered to a pair of near-infrared photodetectors as part of a topographic LAS measurement system. The LAS measurement system is described in

further detail in Salazar et al. (2019). A labeled photograph of the receiver is presented in Figure 4.1 and a schematic of the receiver is presented in Figure 4.2.

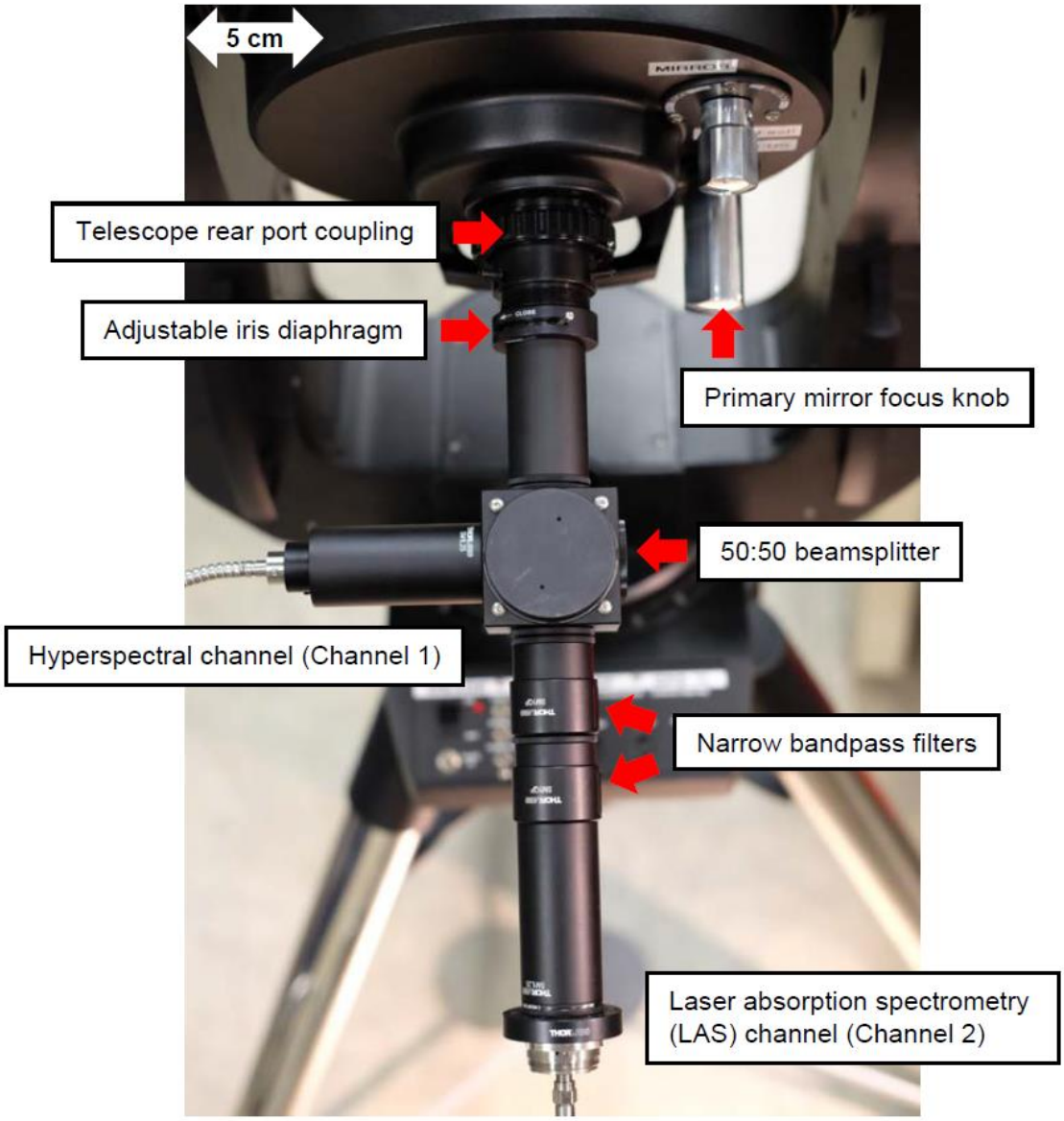

Figure 4.1. Labeled photograph of the multi-channel optical receiver for the Soil Observation Laser Absorption Spectrometer (SOLAS).

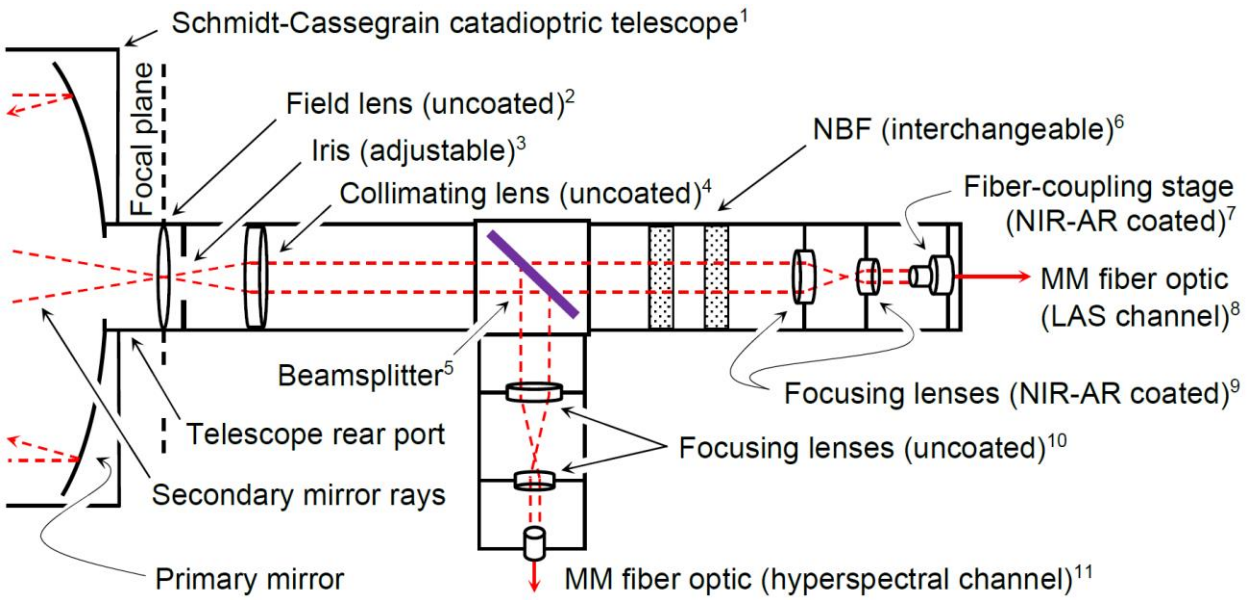

Key: [1]Primary aperture (Meade Instruments LX200-ACF telescope), Ø 203 mm, f_{eff} = 2032 mm, f/10; [2]Uncoated biconvex lens (Thorlabs (TL) LB1471), f = 50 mm; [3]Adjustable iris diaphragm (TL SM1D25), Ø 0.8–25 mm; [4]Uncoated spherical singlet lens (TL LBF254-050), f = 50 mm; [5]Uncoated broad transmission 50:50 polka-dot beamsplitter (TL BPD254-G); [6]Narrow bandpass filters (NBF): 820 nm (TL FB820-10) or 850 nm (TL FB850-10); [7]Near-infrared anti-reflective (NIR-AR) coated aspheric lens fiber-coupling stage (TL PAF-SMA-5-B), 4.9 mm clear aperture, f = 4.6 mm; [8]AR coated multi-mode (MM) fiber optic cable (TL M50L02S-B), Ø 50 µm, numerical aperture = 0.22; [9]NIR-AR coated achromatic doublet lenses, f = 25 mm (TL AC127-050-B), f = 10 mm (TL AC080-10-B); [10]Uncoated aspheric lenses, f = 12 mm (TL AL1512), f = 8 mm (TL AL108); [11]MM fiber optic bundle to ASD FieldSpec 4 Hi-Res spectroradiometer.

Figure 4.2. Schematic of the multi-channel optical receiver for the Soil Observation Laser Absorption Spectrometer (SOLAS) instrument (not to scale).

The field of view (FOV) for each of the receiver channels was determined using Equation 4.1 (Chourdakis et al. 2002). The diameter of the fiber core, D_f, and the focal length, f, of the primary mirror of the telescope were used to determine the FOV.

$$FOV = \frac{D_f}{f} \qquad \text{Equation 4.1}$$

The placement of the optical components (focusing and collimating lenses) between the telescope and the fiber for each channel of the receiver magnifies the image onto the core of the fiber, thereby increasing the FOV of the channel (Nehrir 2011). Thus, the image is magnified by

factors of 50/12 and 12/8 for Channel 1 (hyperspectral channel), where light is focused onto the bare end of the fiber bundle. The 105 μm core diameter for the VNIR bands and 200 μm core for the SWIR bands resulted in a FOV of 0.321 mrad and 0.612 mrad for the VNIR and SWIR bands, respectively. For Channel 2 (LAS channel), where light is focused into 50μm fiber using a fiber-coupling stage, the image is magnified by factors of 50/25, 25/10, and 10/4.6, resulting in a FOV of 0.267 mrad. As part of the LAS functionality of the SOLAS instrument, the actively transmitted laser has a variable beam diameter of 2.0 mm up to a maximum of 8.0 mm and a beam divergence of 0.285 mrad. A plot of the FOV diameter as a function of range, for each of the receiver channels, is presented in Figure 4.3. For comparison, the laser beam evolution is included, though the relationship between the FOV and the laser beam diameter is only important for the LAS measurements, which are not presented in this paper. For completeness, the specifications for each of the receiver channels are summarized in Table 4.1.

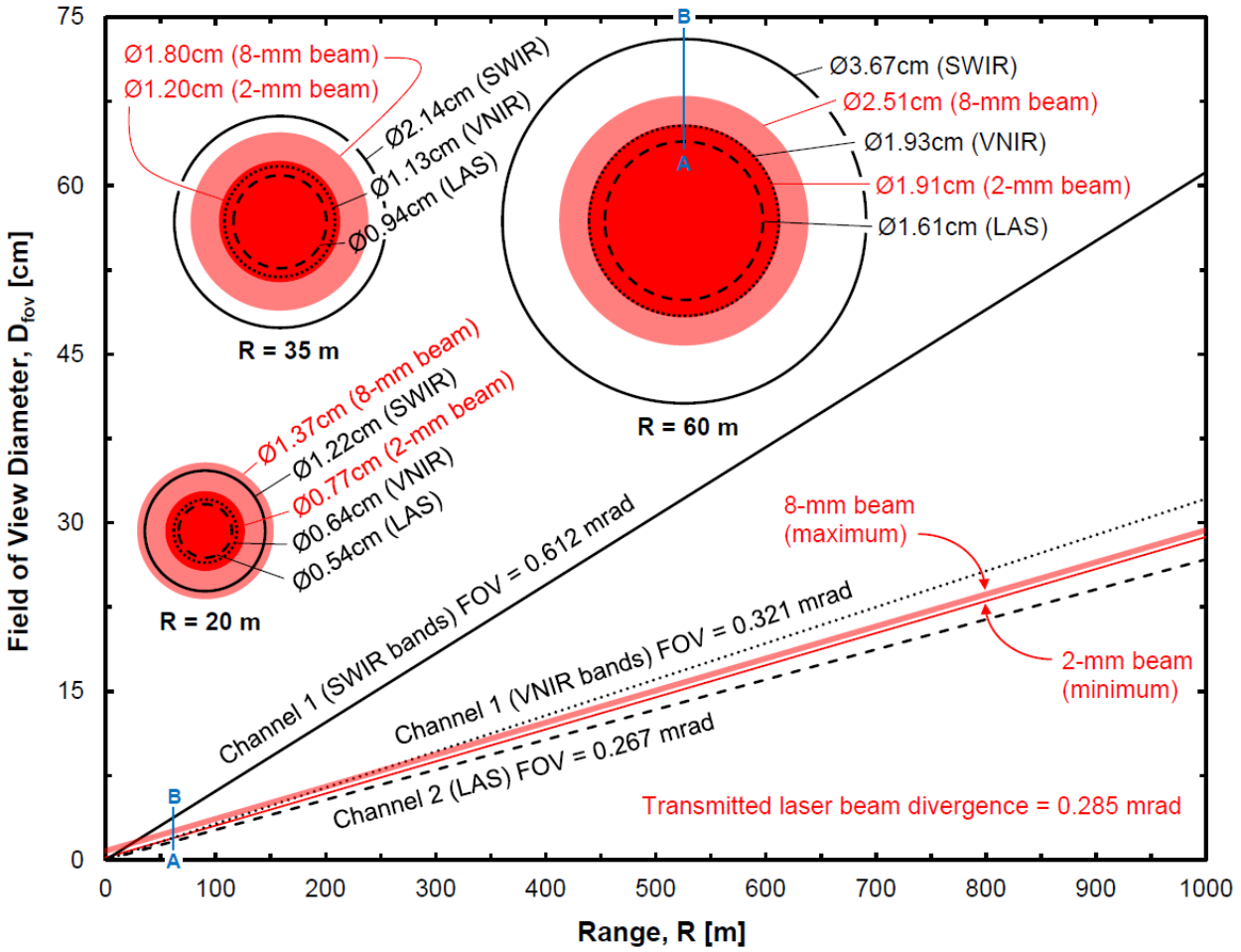

Key: SWIR = Shortwave Infrared (1001–2500 nm); VNIR = Visible Near-Infrared (350–1000 nm); LAS = Laser Absorption Spectrometry; R = Range; FOV = Field of View.

Figure 4.3. Diameter of the field of view as a function of range for each of the Soil Observation Laser Absorption Spectrometer (SOLAS) receiver channels including graphical representation of the field of view cross-sections for the three range distances (20, 35, and 60 m) tested in this paper (transmitted laser beam evolution as a function of range shown for reference).

Table 4.1. Specifications for the SOLAS instrument multi-channel receiver.

Primary aperture	**Unit**	**Specification**
Telescope	-	Schmidt-Cassegrain
Diameter (D)	(mm)	203
Focal length (f)	(mm)	2032
N (f/D)	-	10
Common channel	**Unit**	**Specification**
Field lens (uncoated)	-	Thorlabs LB1471
Iris (adjustable)	-	Thorlabs SM1D25
Diaphraghm diameter	(mm)	0.8–25.0
Collimating lens (uncoated)	-	Thorlabs LBF254-050
f (at λ = 835 nm)	(mm)	50.4
Beamsplitter	-	Thorlabs BPD254-G
Type	-	50:50 Polka-Dot, B270 glass
Hyperspectral channel (Channel 1)	**Unit**	**Specification**
Field of view (FOV)	(mrad)	0.32 (VNIR); 0.61 (SWIR)
Focusing lenses (uncoated)	-	Thorlabs AL1512 and AL108
f (at λ = 1425 nm)	(mm)	12.2 and 8.2
Fiber optic cable	-	Multimode bundle (57 fibers)
Core diameter (D_f)	(μm)	105 (VNIR); 200 (SWIR)
Acceptance angle (θ_a)	(rad)	0.22
LAS channel (Channel 2)	**Unit**	**Specification**
FOV	(mrad)	0.27
Focusing lenses (NIR-AR coated)	-	Thorlabs AC127-025-B and AC080-010-B
f (at λ = 835 nm)	(mm)	25.0 and 10.0
Narrow bandpass filters	-	Thorlabs FB820-10 and FB850-10
CWL	(nm)	820 and 852 (tested)
FWHM	(nm)	11.0 and 10.7 (tested)
Fiber-coupling stage (NIR-AR coated)	-	Thorlabs PAF-SMA-5-B
f (at λ = 835 nm)	(mm)	4.6
Fiber optic cable	-	Thorlabs M50L02S-B
Type	-	Step-index multimode (AR-coated)
Core diameter (D_f)	(μm)	50
Acceptance angle (θ_a)	(rad)	0.22

Key: N = F-number; VNIR = Visible Near-Infrared (350–1000 nm); SWIR = Shortwave Infrared (1001–2500 nm); ASD = Analytical Spectral Devices; InGaAs = Indium Gallium Arsenide; LAS = Laser Absorption Spectrometry; NIR = Near-Infrared; AR = Anti-Reflective; CWL = Center Wavelength; FWHM = Full-Width at Half-Maximum.

4.6.1. *Receiver Testing*

The receiver was tested, in a laboratory setting, to verify the transmission of the wavelengths of interest through each channel. A 25 by 25 cm, calibrated Spectralon® (Labsphere Inc., North Sutton, New Hampshire, USA) diffuse reflectance reference panel was positioned with an incidence angle of 32° relative to the receiver and the receiver was focused on the center of the panel at a range of 5 m. To achieve focus, the primary mirror of the telescope was adjusted until the focal plane aligned with the receiver optics. The correct alignment was verified by observing the maximum amplitude response, as measured with the ASD FieldSpec 4 instrument. An ASD "Illuminator" direct-current powered tungsten quartz halogen lamp provided full-spectrum illumination across the reference panel. The ASD FieldSpec 4 instrument collected 10 reflectance spectra of the panel through each of the receiver channels. The reflectance measurement from the panel, as observed through Channel 1, provided a reference (baseline) for the measurements observed through Channel 2.

Four specimens, consisting of different types of soil, were prepared for observation with the receiver. The soil types included: (i) KaoWhite-S, a commercial kaolinite soil (Thiele Kaolin Co., Sandersville, Georgia, USA); (ii) Ottawa sand, a pure silica (O_2Si) sand (Humboldt Mfg. Co., Elgin, Illinois, USA); (iii) coarse, quartzitic, Arkansas River sand (Arkhola, Van Buren, Arkansas, USA); and (iv) Donna Fill, a synthetic nepheline synetite material (Donna Fill Co., Little Rock, Arkansas, USA). Each specimen was 25 cm in diameter and 0.5 cm thick. The aforementioned Spectralon® reference panel was placed in view of the receiver at a distance of 20 m, with an effective incidence angle of 32°, and the panel was illuminated with the full-spectrum halogen lamp shining perpendicular to the surface of the panel. Baseline reflectance values were recorded for the panel, followed by the collection of reflectance spectra for each of

the soil specimens placed in view of the receiver at the same range and incidence angle as the reference panel. Ten spectra were gathered for each specimen via Channel 1. This procedure was repeated for distances of 35 and 60 m (maximum distance available within the laboratory).

For the data that were collected for the Spectralon® panel and the soil specimens, each set of spectra were averaged, normalized with respect to the reference panel, and plotted as a function of wavelength. A splice correction procedure (Danner et al. 2015) was applied to the reflectance values for $\lambda > 1000$ nm to eliminate offsets that occurred at the transition wavelengths (1000 nm, 1800 nm) between the VNIR and two SWIR channel bands. A Savitzky-Golay (1964) filter was also applied to smooth the spectra.

4.7. Results and Discussion

The spectral reflectance of the reference panel, as acquired via each of the receiver channels, is presented as a function of wavelength in Figure 4.4. The reflectance spectrum collected via Channel 1 was characteristic of a Lambertian reflector across the range of wavelengths (reflectance values close to 1.0). Although Channel 2 was designed to deliver light to a pair of near-infrared photodetectors used for the LAS measurements, as discussed previously in this paper and in Salazar et al. (2019), the specifications of the ASD FieldSpec 4 instrument were well suited for also assessing the functionality of the Channel 2 optical design across the near-infrared wavelength range. This also enabled direct comparison between receiver channels. Analysis of the spectrum collected via Channel 2 revealed that transmission was significantly reduced outside of the VNIR range. These findings were explained by the inclusion of the broadband NIR-AR coatings, optimized for the 650–1050 nm range, that exist on the optical elements within Channel 2; Channel 1 delivers light without any additional optical coatings. The spectra collected via Channel 2, with the addition of each of the interchangeable narrow

bandpass filter (820 or 850 nm), indicated the effectiveness of the filters, allowing only collection around the wavelengths of interest (λ_{on} = 823.20 nm or λ_{off} = 847.00 nm) for the LAS measurements. The filters may be employed to isolate the λ_{on} or λ_{off} backscatter in cases where sunlight saturates the returns.

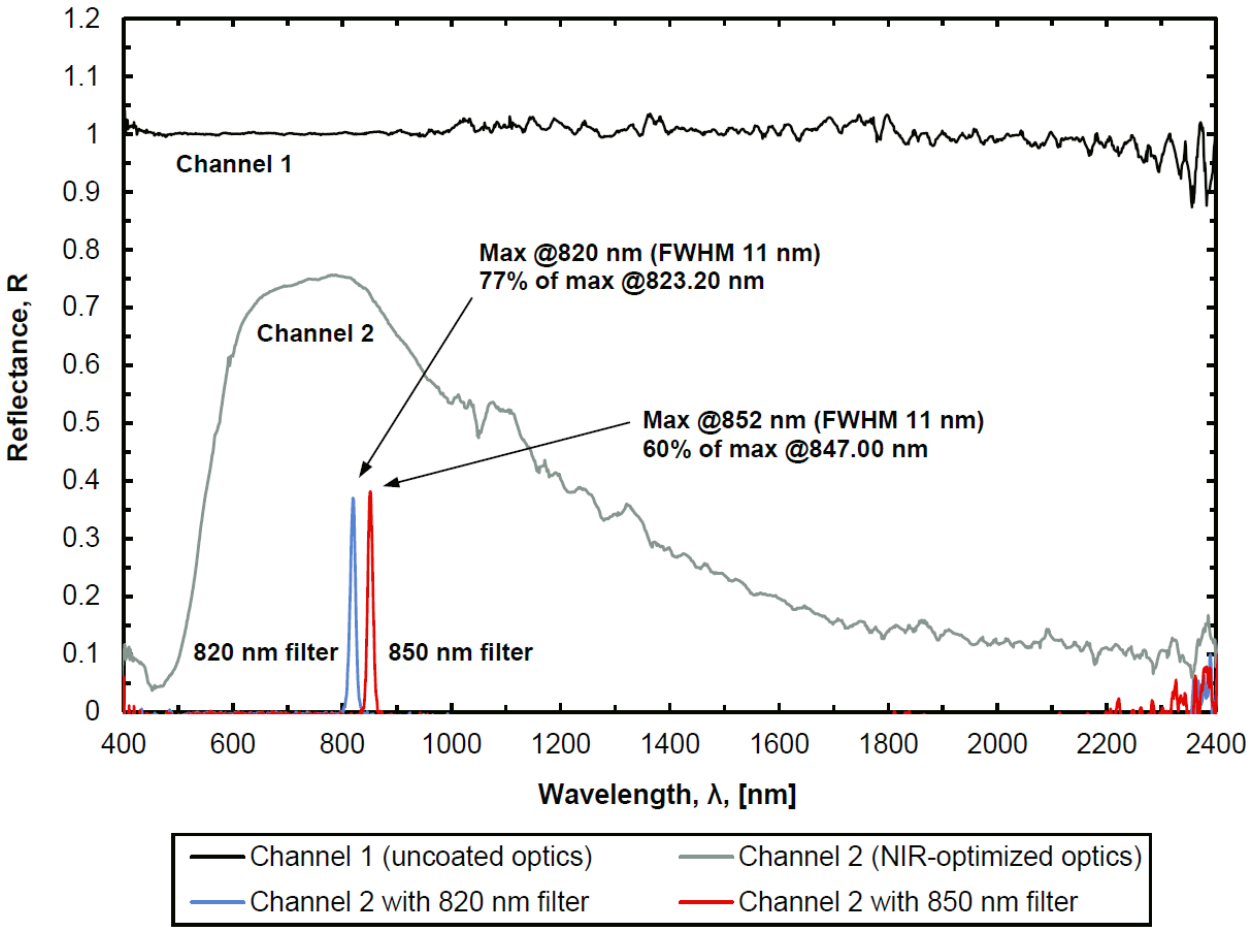

Figure 4.4. Spectral reflectance as a function of wavelength for Spectralon® white reference panel, as acquired with the ASD FieldSpec 4 spectroradiometer through *(1)* receiver Channel 1 (uncoated, full-spectrum optics), and *(2)* receiver Channel 2 (NIR-optimized optics) without additional filtering, and *(3)* receiver Channel 2 with interchangeable narrowband filters (measured transmission peaks of 820 nm and 852 nm and full-width at half-maximum [FWHM] of 11 nm).

For each of the spectra, increased levels of noise were observed for the wavelengths near the edges of each detector range. The noise was primarily attributed to the lack of sensitivity of

the silicon and InGaAs detectors at the edges of the ranges (ASD 1999, Hueni and Bialek 2017). The statistical metrics for each of the three detector ranges of a typical baseline spectrum, as observed via Channel 1 (presented previously in Figure 4.4), are summarized in Table 4.2. The SWIR 1 range (1001–1800 nm) was the most stable, followed by the VNIR range (350–1000 nm), and then the SWIR 2 range (1801–2500 nm). The measured signal-to-noise ratio (SNR) was greatest for the VNIR range. These findings matched other findings in the literature (ASD 1999, Hueni and Bialek 2017). Furthermore, it is hypothesized that the mismatch in the FOV between the VNIR and SWIR bands, as illustrated previously in Figure 4.3, may be a factor in the spectral noise, due to inconsistent specimen uniformity (surface roughness) between different FOV. Although the maximum range tested was 60 m (Figure 4.5), the effect that the difference in the FOV between the VNIR and SWIR bands has on the SNR is hypothesized to increase at longer distances. This hypothesis will continue to be tested in future work, especially when performing field measurements at long ranges.

Table 4.2. Statistical metrics for the baseline spectrum (Spectralon® panel) observed via Channel 1.

Statistical Metric (Reflectance Units)	**VNIR Range*** (350–1000 nm)	**SWIR 1 Range** (1001–1800 nm)	**SWIR 2 Range*** (1801–2500 nm)
Mean	1.00	1.01	0.976
Variance	1.11×10^{-3}	2.00×10^{-4}	4.10×10^{-3}
Sum of Squares of Deviations	7.07×10^{-1}	1.60×10^{-1}	2.83
Standard Deviation	3.34×10^{-2}	1.41×10^{-2}	6.40×10^{-2}
Noise Equivalent Radiance ($W \cdot cm^{-2} \cdot nm^{-1} \cdot sr^{-1}$)†	9.2×10^{-10}	1.7×10^{-9}	7.5×10^{-10}
Signal-to-Noise Ratio (Radiance Units)†	42	25	26

*Erroneous reflectance values greater than 1.2 at the near (350 nm) and far (2500 nm) edges of the wavelength range were excluded from the statistical summary (approximately 1% of the 2151 individual wavelength bands). †Typical values for the midpoint of each wavelength range (measured at 700, 1400, and 2100 nm).

Both receiver channels shared common optical elements ("coated" and "uncoated"), namely the UHTC-coated telescope, and the uncoated field lens, collimating lens, and beamsplitter (see Table 4.1 for specifications). Although the UHTC was optimized by the telescope manufacturer for wavelengths in the visible range (450–700 nm) for astronomic observations, there was no evidence that the UHTC adversely affected transmission of light outside of this range. To maximize the transmission of full-spectrum light through the hyperspectral channel (Channel 1), the remaining optical elements (common field lens, common collimating lens, common beamsplitter, and the focusing lenses within Channel 1) were uncoated. However, the lens substrates reduced transmission efficiency at longer wavelengths. For example, according to data provided by Thorlabs, transmission of light at 2200 nm was reduced by 10.7% and 9.7% from maximum for the common lenses and the Channel 1 lenses, respectively. Furthermore, due to the wavelength-dependent focal length of the lenses, defocusing of the light most likely occurred at the shortest and longest wavelengths in the spectrum. To optimize detection of the λ_{on} and λ_{off} backscattered signals for the LAS measurements, the design wavelength of the common lenses, after the light was collected by the telescope, was 835 nm (mean wavelength between absorption lines). Similarly, the focal lengths of the lens pair within Channel 2 were optimized for 835 nm. However, the design wavelength of the hyperspectral channel was 1425 nm (mean wavelength of receiver bandwidth). According to data provided by Thorlabs, the sum of the focal length shifts for the pair of uncoated lenses in the hyperspectral channel was +0.79 mm at 2200 nm and −0.52 mm at 500 nm. The effects of transmission losses and defocusing were noted for completeness, but were considered to have an insignificant impact on the measurements, based on the observed SNR.

The relative reflectance spectra of the four tested soil specimens, as acquired via the uncoated optical elements on Channel 1 (hyperspectral channel), are presented as a function of wavelength in Figure 4.5. The kaolinite soil was the most reflective, followed by the Ottawa sand, while the coarse river sand was less reflective than the Donna Fill at wavelengths below 1000 nm and more reflective than the Donna Fill at wavelengths above 1000 nm. The kaolinite soil spectra exhibited water absorption features around the 970 nm, 1400 nm and 1900 nm wavelength bands with characteristic doublets in the 1400 nm and 2200 nm regions. The Ottawa sand, coarse river sand, and the Donna Fill spectra exhibited absorption features around the 1900 nm wavelength band, with otherwise milder or non-distinguishable features. Although the specimens tested in this study were dry, the hygroscopic moisture content likely affected the fine-grained kaolinite soil more than the other specimens. Typical hygroscopic moisture contents (gravimetric) were determined to be ~1% for the kaolinite soil, <0.2% for the Donna Fill, ~0.1% for the Ottawa sand, and <0.1% for the coarse river sand.

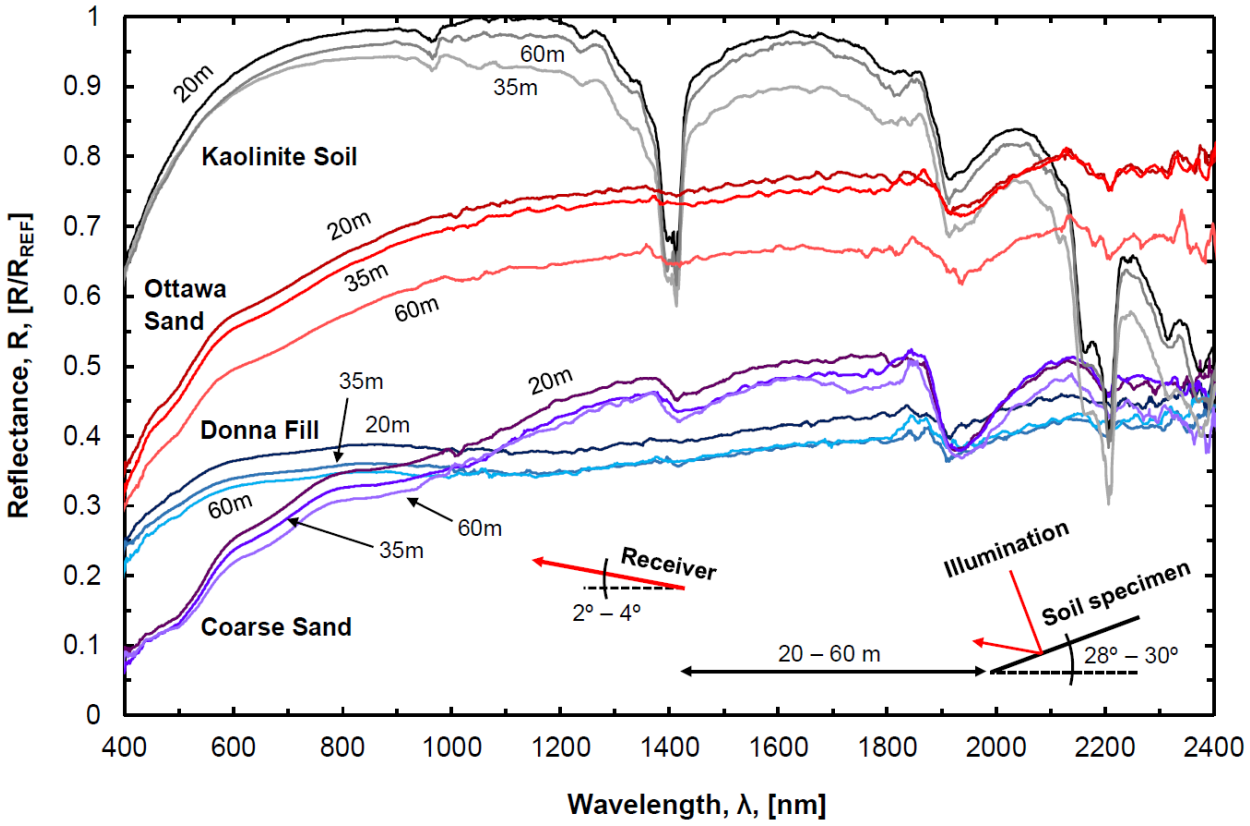

Figure 4.5. Relative spectral reflectance as a function of wavelength for four soil types (kaolinite, Ottawa sand, Donna Fill, and coarse river sand), as acquired with the ASD FieldSpec 4 spectrometer through receiver Channel 1, in a laboratory setting, for distances of 20, 35, and 60 m and an incidence angle of 32°.

As the observation distance increased, the magnitude of the reflectance for each of the tested specimens generally decreased across the range of wavelengths. However, the shape of each of the spectra was consistent, regardless of distance from the receiver, indicating collection of reliable measurements, independent of the range to target, was possible. The relatively large drop in reflectance, observed for the Ottawa sand specimen at a distance of 60 m, was attributed to the specimen sliding gently due to gravity (resulting in a slightly shallower incidence angle for this measurement). As the specimens were tested in an indoor laboratory environment and under direct illumination of an artificial full-spectrum lamp, no long-path atmospheric absorption or solar absorption features were observed (ASD 1999). Thus, the presence of absorption features

indicated that even under laboratory conditions (low relative humidity), the measurements were sensitive to absorption and scattering en route to the receiver. The general decrease in reflectance with an increase in range is believed to be attributed to the absorption and scattering, while the increase in the FOV diameter may also be a factor. Future experimental verification is required to verify these hypotheses.

The stable environmental conditions of the laboratory setting minimized the temperature-induced radiometric errors (Hueni and Bialek 2017) that are typical of the spectroradiometer instrument. A 1-hour warm-up period, before measurements were collected, further minimized these errors. Although frequent referencing of the Spectralon® standard to establish a baseline for subsequent measurements is recommended by the manufacturer, only one reference was collected for each range (20, 35, and 60 m). Future measurements performed in an outdoor field setting will be more sensitive to changes in temperature and illumination conditions (solar irradiation) and may require more frequent referencing of the Spectralon® panel or a companion spectrometer to measure a reference simultaneously. Atmospheric attenuation, due to absorption and scattering by water vapor and other aerosols along the receiver path, will necessitate corrections to derive exact reflectance measurements. These corrections will be achieved using the LAS measurement system of the SOLAS instrument, as described previously (Salazar et al. 2019), and will be addressed in future work.

4.8. Conclusions

A multi-channel optical receiver was designed and tested for inclusion within a new ground-based, topographic, hyperspectral lidar instrument, called the soil observation laser absorption spectrometer (SOLAS). The primary aperture of the receiver is a 203-mm diameter telescope that focuses backscattered light into an optical beamsplitting array to enable

simultaneous data collection via two channels. One of the channels collects hyperspectral radiometric measurements across the visible near-infrared (VNIR) and shortwave infrared (SWIR) ranges (350–2500 nm), while the other channel directs light into a pair of near-infrared photodetectors for range-resolved, laser absorption spectrometry (LAS) measurements in the 820–850 nm region. Testing of each of the channels, in a laboratory setting, demonstrated the suitability of the receiver design for measurements of the wavelengths of interest. Specifically, the hyperspectral channel was optimized to collect light from 350 nm to 2500 nm, while the LAS channel was optimized to detect backscattered energy from transmitted laser absorption lines of 823.20 nm and 847.00 nm.

Testing of four different soil specimens (kaolinite, Ottawa sand, Donna Fill, and coarse river sand), at various distances from the receiver (20, 35, and 60 m), indicated that reliable hyperspectral measurements could be collected, independent of the range to target. Increased noise was observed in the VNIR and SWIR bands, particularly for the wavelengths near the edges of each detector measurement range (350, 1000, 1800, and 2500 nm), which was attributed to lack of instrument sensitivity in these bands. Some of the observed noise was also attributed to diverging fields of view for the VNIR and SWIR bands and wavelength-dependent transmission losses and defocusing of the received light. Future development of the LAS channel will enable atmospheric corrections for long-range hyperspectral measurements (up to 1 km or greater) and has the potential to improve ground-based optical remote sensing practices. Envisioned applications for the receiver, as part of the SOLAS instrument, include rapid classification of soils, rocks and minerals, and vegetation for ecological or agronomic research, forensic investigations of natural hazards (e.g., wildfire-induced erosion and debris flows), or monitoring of earth construction sites (e.g., mine tailings). Future measurements from the

terrestrial platform of the SOLAS may provide ground-truth data for airborne or forthcoming spaceborne missions, such as PRISMA, EnMAP, HISUI, and HyspIRI (Loizzo et al. 2016, Guanter et al. 2015, Tanii et al. 2017, JPL 2018). More information on the complete SOLAS instrument is available in Salazar et al. (2019).

4.9. Acknowledgements

This project was funded by the U.S. Department of Transportation (USDOT) through the Office of the Assistant Secretary for Research and Technology (OST-R) under USDOT Cooperative Agreement No. OASRTRS-14-H-UARK. The views, opinions, findings and conclusions reflected in this publication are solely those of the authors and do not represent the official policy or position of the USDOT/OST-R, or any State or other entity. USDOT/OST-R does not endorse any third party products or services that may be included in this publication. This material is also based upon work supported by the National Science Foundation Graduate Research Fellowship Program under Grant No. DGE-1450079. Any opinions, findings, and conclusions or recommendations expressed in this material are those of the authors and do not necessarily reflect the views of the National Science Foundation.

4.10. References

Analytical Spectral Devices, 1999, *ASD Technical Guide*, 3rd ed., Hatchell, D. C., Ed., Analytical Spectral Devices, Inc., Boulder, CO, USA.

Chourdakis, G., Papayannis, A., and Porteneuve, J., 2002, "Analysis of the Receiver Response For a Noncoaxial Lidar System with Fiber-Optic Output," *Appl. Opt.*, Vol. 41, pp. 2715–2723. doi:10.1364/ao.41.002715.

Danner, M., Locherer, M., Hank, T., and Richter, K., 2015, "Spectral Sampling with the ASD FieldSpec 4—Theory, Measurement, Problems, Interpretation," EnMAP Field Guides Technical Report, GFZ Data Services, Potsdam, Germany.

Grant, W. B., 1982, "Effect of Differential Spectral Reflectance on DIAL Measurements Using Topographic Targets," *Appl. Optics*, Vol. 21, No. 13, pp. 2390-2394.

Guanter, L., Kaufmann, H., Segl, K., Foerster, S., Rogass, C., Chabrillat, S., Kuester, T., Hollstein, A., Rossner, G., Chlebek, C., et al., 2015, "The EnMAP Spaceborne Imaging Spectroscopy Mission for Earth Observation," *Remote Sens.*, Vol. 7, No. 7, pp. 8830–8857. doi:10.3390/rs70708830.

Hardesty, R. M., 1984, "Coherent DIAL Measurement of Range-Resolved Water Vapor Concentration," *Appl. Optics*, Vol. 23, No. 15, pp. 2545-2553.

Hueni, A. and Bialek, A., 2017, "Cause, Effect, and Correction of Field Spectroradiometer Interchannel Radiometric Steps," *IEEE J. Sel. Top. Appl. Earth Obs. Remote Sens.*, Vol. 10, pp. 1542–1551. doi:10.1109/JSTARS.2016.2625043.

HyspIRI Mission Concept Team, 2018, *HyspIRI Final Report*, Jet Propulsion Laboratory, California Institute of Technology, Pasadena, CA, USA.

Ishii, S., Koyama, M., Baron, P., Iwai, H., Mizutani, K., Itabe, T., Sato, A., and Asai, K., 2013, "Ground-Based Integrated Path Coherent Differential Absorption Lidar Measurement of CO_2: Foothill Target Return," *Atmos. Meas. Tech.*, Vol. 6, pp. 1359-1369. doi:10.5194/amt-6-1359-2013.

Little, L. M. and Papen, G. C., 2001, "Fiber-Based Lidar for Atmospheric Water-Vapor Measurements," *Appl. Optics*, Vol. 40, No. 21, pp. 3417-3427.

Loizzo, R., Ananasso, C., Guarini, R., Lopinto, E., Candela, L., and Pisani, A. R., 2016, "The PRISMA Hyperspectral Mission," *Proceedings of the Living Planet Symposium 2016*, Prague, Czech Republic, May 9–13.

Machol, J., Ayers, T., Schwenz, K., Koenig, K., Hardesty, R., Senff, C., Krainak, M., Abshire, J., Bravo, H., and Sandberg, S., 2004, "Preliminary Measurements with an Automated Compact Differential Absorption LIDAR for Profiling Water Vapor," *Appl. Optics*, Vol. 43, No. 15, pp. 3110-3121.

Moen, D. R., 2016, "Two Channel Receiver Design and Implementation for a Ground Based Micro-Pulse Differential Absorption Lidar (DIAL) Instrument," M.S. thesis, Montana State University, Bozeman, MT, USA.

Moore, A. S., Brown, K. E., Hall, W. M., Barnes, J. C., Edwards, W. C., Petway, L. B., Little, A. D., Luck, W. S., Jones, I. W., Antill, C. W., et al., 1996, "Development of the Lidar Atmospheric Sensing Experiment (LASE) – An Advanced Airborne DIAL Instrument," In *Advances in Atmospheric Remote Sensing with Lidar: Selected Papers of the 18th International Laser Radar Conference (ILRC)*, Berlin, Germany, July 22–26; A. Ansmann, R. Neuber, P. Rairoux, and U. Wandinger, Eds., Springer-Verlag, Berlin/Heidelberg, Germany, pp. 281–288. ISBN 9783540618874.

Nehrir, A. R., 2011, "Development of an Eye-Safe Diode-Laser-Based Micro-Pulse Differential Absorption Lidar (MP-DIAL) for Atmospheric Water-Vapor and Aerosol Studies," Ph.D. Dissertation, Montana State University, Bozeman, MT, USA.

Repasky, K. S. (Montana State University, Bozeman, Montana, USA). Personal Correspondence, July 19, 2016.

Salazar, S. E., Garner, C. D., and Coffman, R. A., 2019, "Development of a Multimode Field Deployable Lidar Instrument for Topographic Measurements of Unsaturated Soil Properties: Instrument Description," *Remote Sens.*, Vol. 11, No. 3, 289. doi:10.3390/rs11030289.

Savitzky, A. and Golay, M. J. E., 1964, "Smoothing and Differentiation of Data by Simplified Least Squares Procedures," *Anal. Chem.*, Vol. 36, pp. 1627–1639. doi:10.1021/ac60214a047.

Spuler, S. M., Repasky, K. S., Morley, B., Moen, D., Hayman, M., and Nehrir, A. R., 2015, "Field Deployable Diode-Laser-Based Differential Absorption Lidar (DIAL) for Profiling Water Vapor," *Atmos. Meas. Tech.*, Vol. 8, pp. 1073-1087.

Tanii, J., Kashimura, O., Ito, Y., and Iwasaki, A., 2017, "Flight Model of HISUI Hyperspectral Sensor Onboard ISS (International Space Station)," In *Sensors, Systems, and Next-Generation Satellites XXI,* SPIE Proceedings, Vol. 10423. doi:10.1117/12.2278169.

CHAPTER 5: VALIDATION OF A GROUND-BASED TELESCOPE-ASSISTED HYPERSPECTRAL REMOTE SENSOR

5.1. Chapter Overview

A description of various indoor and outdoor trials that were conducted with the SOLAS hyperspectral receiver are presented in this chapter. The results were compared with conventional reflectance spectroscopy measurements that were acquired at proximal range 1) in the laboratory under artificial illumination, and 2) outdoors under solar illumination conditions. Additionally, the signal noise was characterized and compared for each of the tests.

The limitations of the Salazar and Coffman (2019b) paper are outlined in Section 5.2. The full citation for the manuscript is included in Section 5.3, followed by the abstract in Section 5.4. Contained within Section 5.5 are the introduction and motivation for the paper. The methods that were employed to test the SOLAS under various conditions are described in Section 5.6 and the results from the tests are discussed in Section 5.7. Section 5.8 contains concluding remarks.

5.2. Limitations of the Described Study

The focus of the work described in this chapter was the testing of the SOLAS hyperspectral receiver, including the first outdoor measurements collected with the instrument. Although many trials were conducted as part of the development of the SOLAS, the manuscript contains only selected results from trials that were used to quantify the utility of the measurement technique. Moreover, the study did not incorporate the active laser transmitting portion of the instrument, nor the associated laser absorption spectrometry (LAS) measurements. While the paper included some discussion about envisioned applications of the technique, further testing is required to validate the full functionality of the SOLAS, especially at longer ranges.

5.3. Validation of a Ground-Based Telescope-Assisted Hyperspectral Remote Sensor

Reference

Salazar, Sean E. and Coffman, Richard A., "Validation of a Ground-Based Telescope-Assisted Hyperspectral Remote Sensor," Journal of Applied Remote Sensing. Submitted for Review. Manuscript Number: JARS 190527.

5.4. Abstract

The utility of the ground-based soil observation laser absorption spectrometer (SOLAS) was demonstrated through spectral reflectance measurements of five soil types during laboratory- and field-based collection. The SOLAS telescope-assisted measurements, acquired under solar and artificial illumination, from ranges of 40 to 144 meters, respectively, were compared with proximal measurements. The spectra acquired at range compared well with the spectra acquired proximally. Specimen type, range-dependent spatial resolution, and environmental conditions are discussed herein. The signal-to-noise ratio (SNR) was assessed and is presented as a function of wavelength for the spectral range of the receiver for each measurement condition. The proximal measurements performed outdoors, under solar illumination, had the greatest SNR, while the remote measurements performed indoors, under artificial illumination, had the lowest SNR. For the outdoor measurements, loss of signal was observed around the 1400 nm and 1900 nm bands, due to long-path atmospheric water vapor absorption. Future improvements to the SOLAS remote sensor, discussed herein, will enable measurements of reflectance over longer ranges. Envisioned applications include remote characterization of surface materials for large earth construction projects (e.g. surface mines, tailings), for geohazard investigations, or for ground truthing of current and future multi- and hyperspectral satellite data.

Keywords: instrument development, hyperspectral, reflectance, spectroradiometry, telescope, soil

5.5. Introduction and Background

Hyperspectral sensing, primarily in the visible near-infrared (VNIR) and shortwave infrared (SWIR) ranges, has become increasingly utilized for ecologic (Adam et al. 2010), geologic (van der Meer et al. 2012), civil engineering (Waruru et al. 2014), and agronomic (Pasolli et al. 2018) applications. While high spectral resolution (≤ 10 nm) sensing for rapid characterization of rocks, minerals, soils and vegetation is commonly performed at the proximal range (< 1 meter), remote measurements with increasingly higher spectral and spatial resolutions have been demonstrated (Goetz 2009, Schaepman et al. 2009). The proliferation of compact sensors has enabled portable and accurate measurements of spectral reflectance from ground-based, manned- and unmanned aircraft, and even from spaceborne platforms. The prototype soil observation laser absorption spectrometer (SOLAS), that is discussed in this paper, enabled high resolution measurements at ranges greater than conventional proximal measurements, while maintaining cost and deployment feasibility. This type of device is needed because previous airborne missions have been cost prohibitive, and continuous, full-spectrum sensors have not overcome payload limitations for unmanned platforms.

The development of the SOLAS was described previously in the literature (Salazar et al. 2019, Salazar and Coffman 2019). The SOLAS utilizes a portable, tripod-mounted telescope that collimates reflected light through an optical receiver into a high radiometric-resolution spectroradiometer (Analytical Spectral Devices [ASD] FieldSpec 4 Hi-Res; Malvern Panalytical Ltd., Malvern, United Kingdom). Light is detected on 2151 continuous bands from the ultraviolet to SWIR wavelengths. The FieldSpec instrument utilizes a silicon detector for the VNIR wavelength range (350 – 1000 nm) with a spectral resolution of 3 nm and a sampling interval of 1.4 nm. A pair of thermoelectric-cooled indium gallium arsenide (InGaAs) detectors

provide a spectral resolution of 8 nm and a sampling interval of 1.1 nm for the SWIR wavelength ranges including 1001 – 1800 nm and 1801 – 2500 nm, respectively.

The motivation for this paper was to demonstrate the utility of the telescope-assisted hyperspectral measurements through indoor (laboratory) and outdoor (field) collection using different soil specimens as targets. Presented in this paper are 1) the methods used to collect data, 2) the collected data, and 3) an accompanying discussion of the results. Additionally, the signal noise of the measurements is characterized as a function of wavelength across the entire receiver spectrum and future improvements to the SOLAS receiving system are suggested.

5.6. Methods

The SOLAS receiver was tested in an indoor and an outdoor environment, at various ranges from the target. Proximal range measurements, performed both indoors and outdoors, were also collected to provide comparisons for the telescope-assisted measurements. The methods that were used to collect the hyperspectral data are described herein.

5.6.1. *Indoor and Outdoor Proximal Range Data Collection*

Specimens consisting of five different soil materials (Ottawa sand, coarse river sand, Donna Fill, bentonite soil, and kaolinite soil) were characterized in the laboratory using a benchtop setup. An 8-degree field-of-view (FOV) fore optic was attached to the end of the fiber-optic bundle leading to the ASD FieldSpec 4 spectroradiometer. The setup, depicted in Figure 5.1, was similar to that used by other researchers (Garner 2017), and as recommended by ASD for conventional measurements in the laboratory or field. A 25 cm by 25 cm, calibrated reference panel (Spectralon®; Labsphere Inc., North Sutton, New Hampshire, USA) was placed in the field of view of the fore optic. For proximal, near-field range (< 1 meter) measurements, the perpendicular diameter of the field of view, D_{FOV}, was determined using Equation 5.1,

$$D_{FOV} = D_{F.O.} + 2 \cdot R \cdot tan\left(\frac{\theta}{2}\right), \quad \text{Equation 5.1}$$

where $D_{F.O.}$ was the diameter of the fore optic lens, R was the range, and θ was the angular field-of-view in degrees. The perpendicular D_{FOV} for the aforementioned laboratory setup corresponded with the perpendicular D_{FOV} for the SOLAS receiver for ranges of 20, 35, 50, 60, and 100 m. The distance between the fore optic and the target surface, equivalent to the D_{FOV} at a given range in the field, was determined using the relationship presented in Equation 5.1.

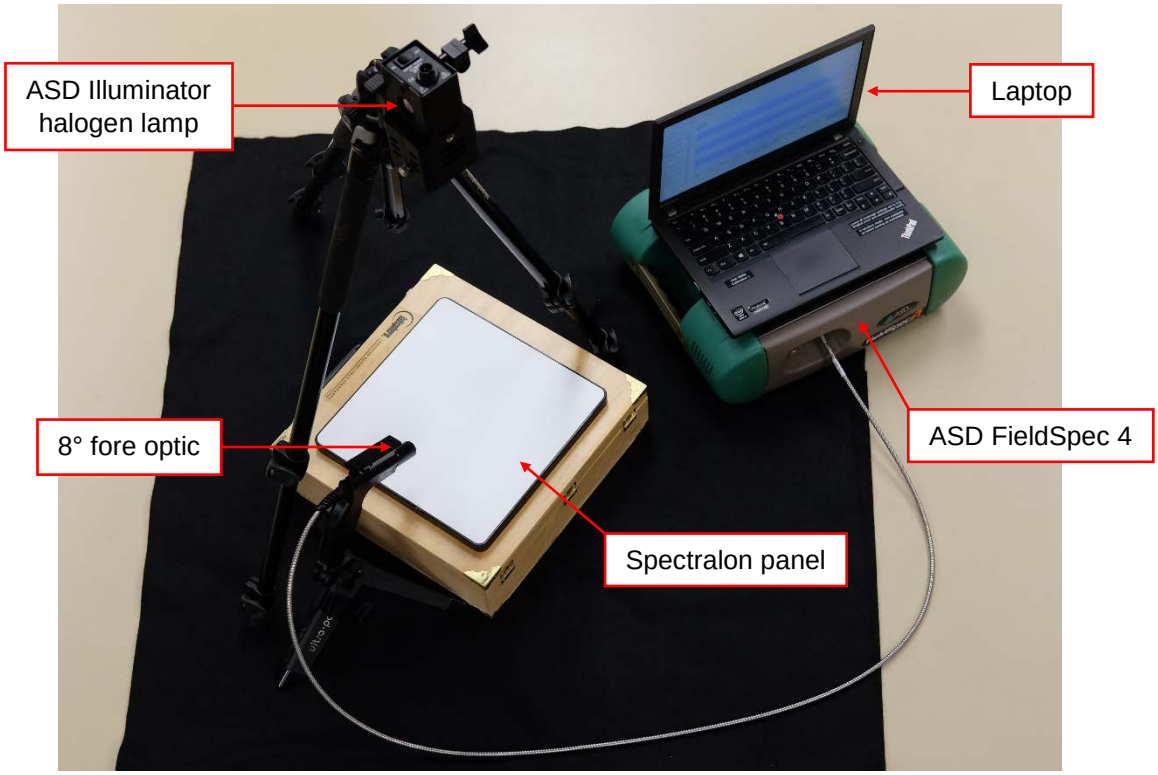

Figure 5.1. Labeled photograph of the laboratory setup, as used to collect proximal range spectral reflectance measurements with the ASD FieldSpec 4 Hi-Res spectroradiometer (pictured with calibrated Spectralon® reference panel as target).

The incidence angle of the fore optic, relative to the target surface, was set to 30 degrees to match typical field scale measurements performed using the SOLAS. A tungsten quartz, full-spectrum, halogen lamp (ASD "Illuminator") was directed perpendicular to the target surface.

The FieldSpec 4 instrument and Illuminator lamp were allowed to warm up for one hour before any spectra were acquired to minimize temperature-induced radiometric errors. The following procedure was used for a set of measurements, provided each D_{FOV} equivalent range. The fore optic was centered on the Spectralon panel, the instrument settings were optimized within the ASD RS^3 software, and ten reference spectra were collected for a given acquisition. After referencing of the Spectralon panel, the panel was successively replaced with one of seven 25-cm diameter, dry soil specimens (Ottawa sand, coarse river sand, Donna Fill with smooth and rough surface textures, bentonite soil, or kaolinite soil with smooth and rough surface textures). Like with the reference panel, ten spectra were collected for each specimen. A summary of the baseline measurements acquired for the soil specimens, as collected from proximal range distances while indoors, is presented in Table 5.1.

The five soil types were also tested outdoors, under solar illumination. The aforementioned procedures were repeated to collect reflectance spectra at a proximal range of 12 cm with an incidence angle of 44 degrees and an illumination angle of approximately 60 degrees relative to the target surface. The D_{FOV} was 2.4 cm, equivalent to a SOLAS measurement at 40 m from the target. The resulting spectra served as a comparison for the SOLAS measurements that are described in Section 5.6.3. A summary of the measurements acquired for the soil specimens, as collected from proximal range while outdoors, is presented in Table 5.2.

The specimens that were tested were selected because of previous studies in which benchmark characteristics were determined for the soils (Garner 2017). A brief description of each of the soil types follows. The Ottawa sand (Humboldt Mfg. Co., Elgin, Illinois, USA) was a pure silica (SiO_2) sand. The coarse, quartzitic river sand was sourced from the Arkansas River (Arkhola, Van Buren, Arkansas, USA). The Donna Fill (Donna Fill Co., Little Rock, Arkansas,

USA) was a synthetic nepheline synetite material that was dark gray in color. The bentonite soil was a tan-colored Smectitic clay (PondSeal^{TM}) that was sourced from Wyoming, USA. The kaolinite soil was a commercial KaoWhite-S product (Thiele Kaolin Co., Sandersville, Georgia, USA).

Table 5.1. Summary of measurements acquired indoors, at proximal ranges, under artificial illumination.

Acquisition Number	Target	Incidence Angle (°)	Illumination Angle (°)	Range (cm)	Corresponding Range (m)	D_{FOV} (cm)
1, 9, 17, 25, 33	Spectralon®	30	90	3	20	1.2
				10	35	2.1
2, 10, 18, 26, 34	Ottawa sand			16	50	3.1
				21	60	3.7
3, 11, 19, 27, 35	Coarse sand			38	100	6.1
4, 12, 20, 28, 36	Donna Fill (smooth)					
5, 13, 21, 29, 37	Donna Fill (rough)					
6, 14, 22, 30, 38	Bentonite					
7, 15, 23, 31, 39	Kaolinite (smooth)					
8, 16, 24, 32, 40	Kaolinite (rough)					

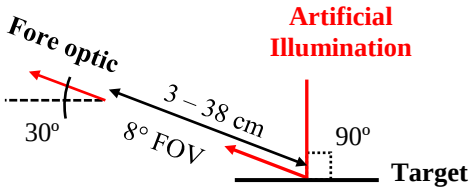

Table 5.2. Summary of measurements acquired outdoors, at proximal range, under solar illumination.

Acquisition Number	Target	Incidence Angle (°)	Illumination Angle (°)	Range (cm)	D_{FOV} (cm)
1	Spectralon®	44	~ 60	12	2.4
2	Ottawa sand				
3	Coarse sand				
4	Donna Fill				
5	Bentonite				
6	Kaolinite				

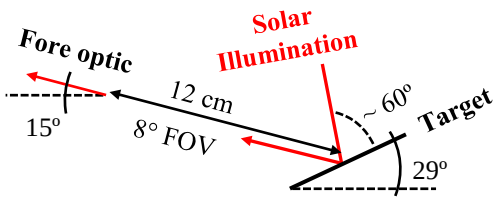

5.6.2. *Indoor Intermediate Range Data Collection*

The five soil types that were tested in the laboratory at proximal range distances were also tested indoors along the length of a 120-m long interior hallway, located within the University of Arkansas Engineering Research Center (ENRC). The specimens were tested at a range of 114 m (maximum available distance while indoors within ENRC) using the SOLAS receiver. Each specimen was 25 cm in diameter and was prepared dry or as a wet mixture (at various water contents close to saturation of the pore space). The target was inclined at an angle of 29 degrees relative to the ground surface and the SOLAS receiver was declined at 1 degree relative to the ground surface. Therefore, the effective incidence angle relative to the target was 30 degrees. The Illuminator lamp was directed perpendicular to the target surface. The angular FOV of the SOLAS receiver was 3.5×10^{-2} degrees; the range-dependent D_{FOV} of the SOLAS receiver was previously described in more detail (Salazar and Coffman 2019). After referencing the Spectralon panel, each of the ten specimens was placed within the field of view of the receiver and ten reflectance spectra were collected for each of the specimens. A summary of the

intermediate range measurements, as acquired indoors at a range of 114 m, is presented in Table 5.3.

Table 5.3. Summary of measurements acquired indoors, at a range of 114 m, under artificial illumination.

Acquisition Number	Target	Incidence Angle (°)	Illumination Angle (°)	Range (m)	D_{FOV} (cm)
1	Spectralon®	30	90	114	7.0
2	Ottawa sand (dry)				
3	Ottawa sand (wet)				
4	Coarse sand (dry)				
5	Coarse sand (wet)				
6	Donna Fill (dry)				
7	Donna Fill (wet)				
8	Bentonite (dry)				
9	Bentonite (wet)				
10	Kaolinite (dry)				
11	Kaolinite (wet)				

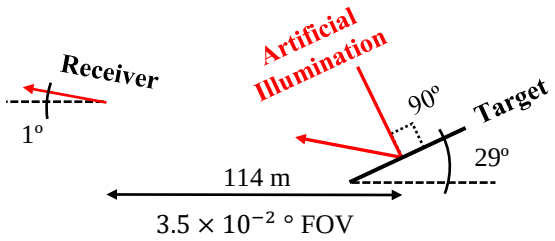

5.6.3. Outdoor Intermediate Range Data Collection

The SOLAS receiver was tested in an outdoor environment at the Cato Springs Research Center (CSRC) that is located south of the University of Arkansas campus. The same five soil types that were tested indoors (dry condition only) were tested outdoors at a range of 40 m. The SOLAS device was set up on the rooftop of the CSRC, as depicted in Figure 5.2, to allow for a better vantage point and a greater incidence angle relative to the target. Similar to the indoor trials, the target was inclined 29 degrees relative to the ground, while the SOLAS receiver was declined 15 degrees for an effective incidence angle of 44 degrees relative to the target. The

illumination angle from the sun was approximated based on the time of year and time of day using the spherical trigonometric relationship presented in Equation 5.2,

$$\cos(\theta_s) = \sin(\Phi) \cdot \sin(\delta) + \cos(\Phi) \cdot \cos(\delta) \cdot \cos(h)\,, \qquad \text{Equation 5.2}$$

where θ_s is the solar zenith angle, Φ is the local latitude, δ is the sun declination, and h is the hour angle (local solar time). During the readings, the sky was clear (no cloud coverage) at the time of the measurements and the air temperature was 22°C with a humidity of 43% and a wind speed of 20 $km \cdot h^{-1}$.

To determine the repeatability of the measurements under outdoor conditions and solar illumination, the set of measurements was repeated twice within the span of 30 minutes. As described in Section 5.6.1, the set of specimens was also tested at the proximal range (12 cm), with the aforementioned 8-degree fore optic, under the same solar illumination conditions. These proximal measurements provided a comparison to the outdoor measurements collected at a range of 40 m. A summary of the intermediate range measurements, as acquired outdoors at a range of 40 m, is presented in Table 5.4.

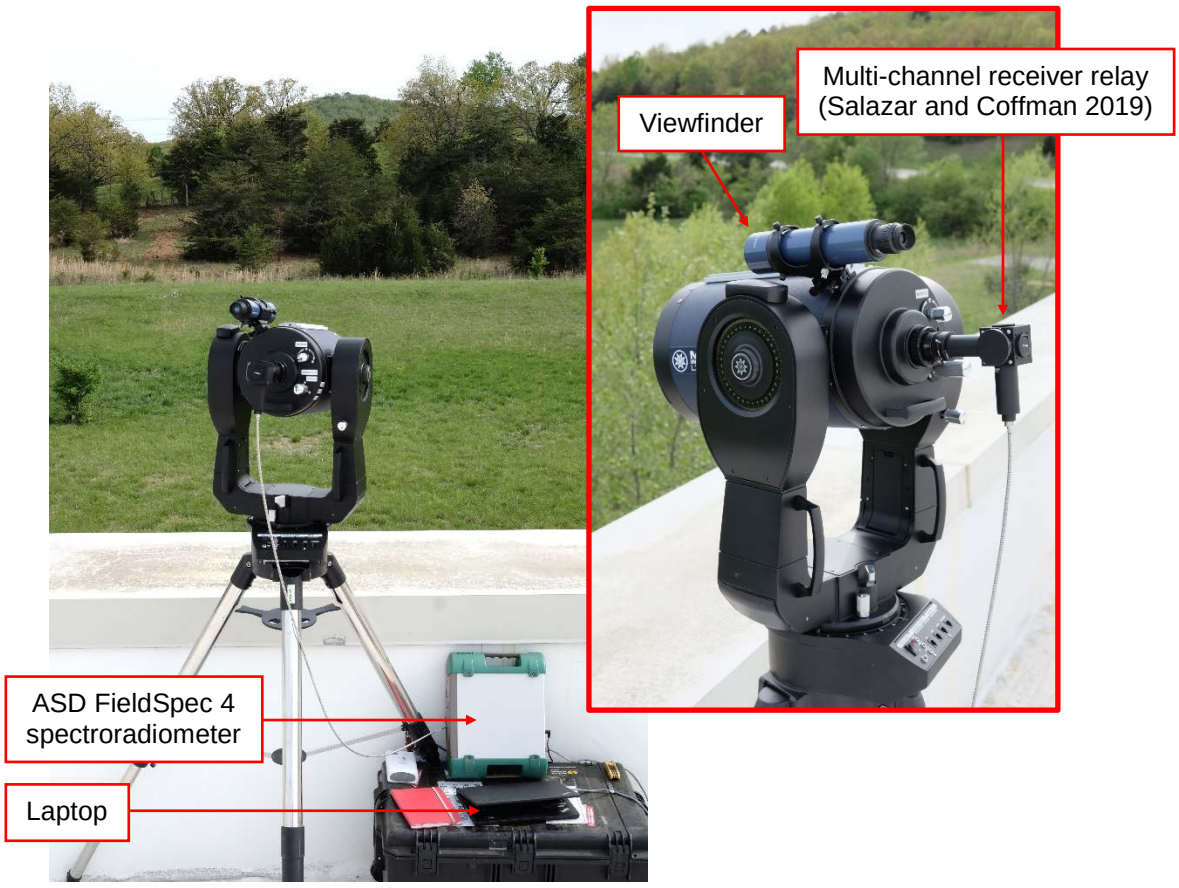

Figure 5.2. Labeled photograph of the field setup, as used to collect intermediate range spectral reflectance measurements with the SOLAS telescope-enhanced receiver.

Table 5.4. Summary of measurements acquired outdoors, at a range of 40 m, under solar illumination.

Acquisition Number	Target	Incidence Angle (°)	Illumination Angle (°)	Range (m)	D_{FOV} (cm)
1, 7, 13	Spectralon®	44	~ 60	40	2.4
2, 8, 14	Ottawa sand				
3, 9, 15	Coarse sand				
4, 10, 16	Donna Fill				
5, 11, 17	Bentonite				
6, 12, 18	Kaolinite				

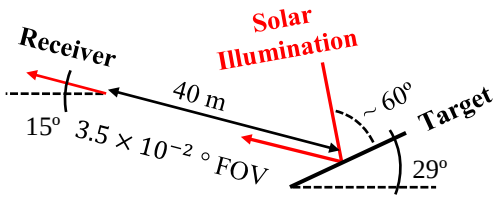

5.6.4. *Processing Methods*

For each set of measurements, of a given specimen, the raw reflectance values were averaged and normalized with respect to the Spectralon reference panel. The resulting reflectance values were then plotted as a function of wavelength. While the proximal range measurements did not require additional corrections, the SOLAS telescope-assisted measurements, collected indoors, under artificial illumination, were splice corrected (Danner et al. 2015) if an offset was observed at the transition wavelengths between the three instrument detector ranges (VNIR, SWIR 1, and SWIR 2). For the measurements collected outdoors, under solar illumination, the 1900-nm long-path water vapor absorption band interfered with the aforementioned splice correction procedure at the 1800-nm detector transition. The spectra collected outdoors were therefore not corrected. A Savitzky-Golay filter (Savitzky and Golay 1964) was applied to smooth all of the collected spectra, except for the indoor proximal range measurements, which did not require filtering.

For each of the aforementioned sets of measurements, the noise was characterized. A procedure outlined by ASD (ASD 1999, Fager 2019) was followed to determine the baseline

noise of the detectors within the FieldSpec 4 instrument. The noise-equivalent radiance was determined indoors at a proximal range using the Spectralon reference panel as the target, due to the Lambertian reflectance properties of the panel across the 350–2500 nm range. The noise-equivalent radiance was used to derive the signal-to-noise ratio (SNR) across the range of wavelengths for typical measurements 1) performed at proximal ranges using the 8-degree fore optic indoors and outdoors, and 2) collected at various intermediate ranges using the SOLAS telescope-enhanced receiver indoors and outdoors.

5.7. Results and Discussion

5.7.1. *Indoor Proximal Range Measurements*

The baseline spectra for each of the five materials that were tested in this study are presented in Figure 5.3(a). Because the measurements were collected indoors, at proximal ranges, and under artificial illumination, as described in Section 5.6.1, the resulting spectra were expected to be smooth and to contain minimal noise. The spectra are presented in terms of absolute reflectance with respect to wavelength to allow for comparison with United States Geological Survey (USGS) Spectral Library data (Kokaly et al. 2017). The spectra for the Ottawa sand [Figure 5.3(b)], bentonite soil [Figure 5.3(c)], and kaolinite soil [Figure 5.3(d)] specimens generally matched the USGS standards. the USGS spectral library did not contain a material named “bentonite”. The closest match within the database was a Montmorillonite clay soil. Although both soils are in the Smectite group and share mineralogical properties, it is likely that the color of the soil and perhaps the particle size distribution differed. Moreover, the USGS reflectance spectra were collected with similar, though different, ASD spectroradiometers and with a perpendicular incidence angle.

As presented in Figure 5.3(d), the surface roughness had an influence on the amplitude of the reflectance values, while the general trends, including absorption features, were well preserved. The kaolinite soil specimen that was prepared with a smooth surface texture reflected more light across the entire VNIR and SWIR wavelength range than the kaolinite soil specimen that was prepared with a rough surface texture. A similar, though less pronounced, effect was observed for the darker Donna Fill specimens that were prepared with smooth and rough surface textures.

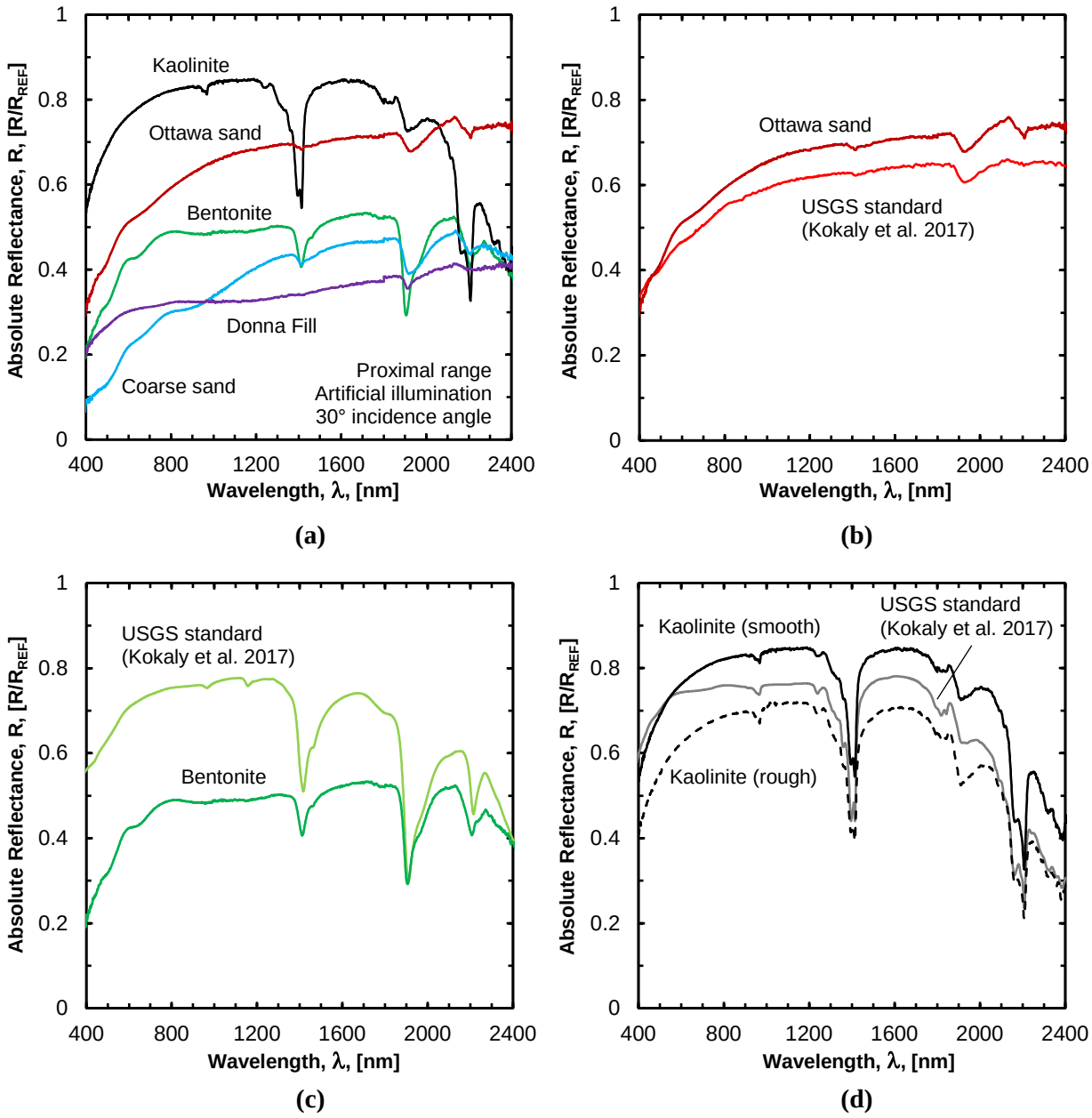

Figure 5.3. Absolute reflectance spectra for dry specimens of *(a)* five soil types collected indoors at proximal ranges, *(b)* Ottawa sand, *(c)* bentonite soil, and *(d)* kaolinite soil, as compared with the USGS spectral library standards (Kokaly et al. 2017).

Another factor that affected the spectral amplitude was the range-dependent field of view diameter, D_{FOV} or spatial resolution, of the measurements. An increase in D_{FOV} generally resulted in an increase in the reflectance values across the wavelength range, as presented in

Figure 5.4 for the rough-textured kaolinite soil and Donna Fill specimens. This was likely due to more light being reflected into the fore optic, given an increase in the distance between the fore optic and the target surface. For D_{FOV} greater than 6 cm, the effect of range on the spectral amplitude was negligible. Likewise, the effect was insignificant for the other soil specimens, including the smooth-textured kaolinite and Donna Fill specimens (not presented in Figure 5.4).

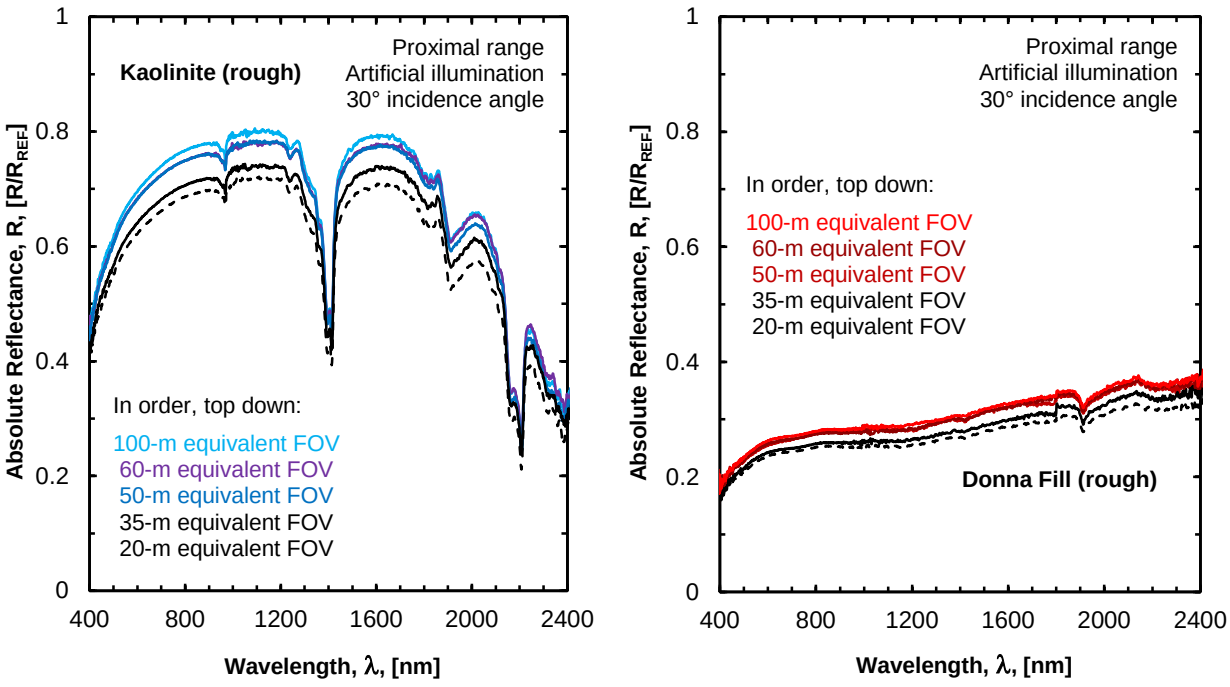

Figure 5.4. Absolute reflectance spectra for dry specimens of *(a)* kaolinite soil with a rough surface texture, and *(b)* Donna Fill with a rough surface texture, collected indoors at proximal ranges corresponding to equivalent field of view (FOV) diameters, as observed with the SOLAS at distances of 20, 35, 50, 60, and 100 m from the target.

5.7.2. *Indoor and Outdoor Intermediate Range Measurements*

The results from the indoor intermediate range measurements that were described in Section 5.6.2, collected at a range of 114 meters, are presented in Figure 5.5 along with the aforementioned proximal range measurements for comparison. Although other indoor measurements were presented by the authors previously (Salazar and Coffman 2019), the

measurements were limited to a range of 60 meters. The telescope-assisted measurements contained increased levels of noise over those presented previously (Salazar and Coffman 2019), especially in the SWIR wavelength range ($\lambda > 1000$ nm). It is hypothesized that this was due to the SOLAS receiver not being properly centered on the target, which affected the SWIR wavelengths more than the VNIR wavelengths, due to the range-dependent divergence in the field of view. This was a topic discussed previously by the authors (Salazar and Coffman 2019). It is also possible that the primary mirror of the telescope was not finely focused before measurements were acquired. In addition to the dry soil specimens that were tested indoors at proximal and intermediate ranges, the spectra for the wet soil specimens, tested indoors at the intermediate range, are presented in Figure 5.5.

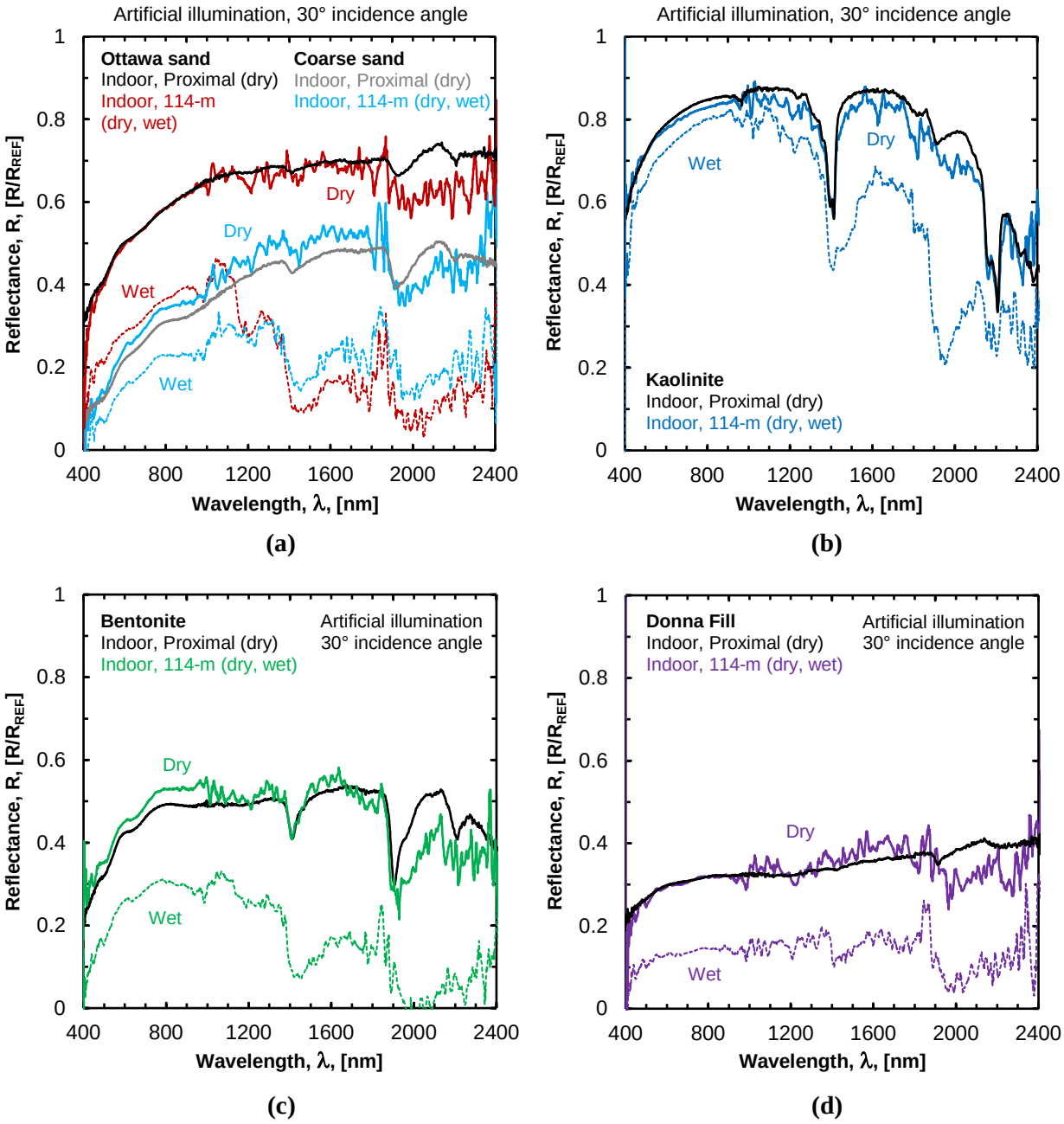

Figure 5.5. Reflectance spectra acquired indoors, at proximal range, and indoors at a range of 114 m for dry and wet specimens of *(a)* Ottawa sand and coarse river sand, *(b)* kaolinite soil, *(c)* bentonite soil, and *(d)* Donna Fill.

The results for the outdoor intermediate range measurements that were described in Section 5.6.3 are presented in Figures 5.6 and 5.7. The repeatability of the measurements is demonstrated in Figure 5.6. The average of the three measurements, acquired for each specimen

using the SOLAS receiver at a range of 40 meters, is presented in Figure 5.7, alongside the indoor and outdoor proximal measurements. When comparing the telescope-assisted measurements to the spectra collected proximally, the D_{FOV} was matched as closely as possible, though the range-dependent D_{FOV} effect was small, as discussed in Section 5.7.1. The indoor and outdoor measurements compared well, generally; however, the outdoor measurements, acquired under solar illumination, were dominated by the loss in signal-to-noise ratio (SNR) around the 1400 nm and 1900 nm bands, due to long-path water vapor absorption. The erroneous reflectance values around these bands were preserved to illustrate the effect on the signal; however, they are commonly removed in post-processing. As described in Section 5.6.4, the transition between adjacent detectors in the FieldSpec instrument sometimes resulted in an offset that was addressed with a simple splice correction procedure during processing. However, this procedure was not applicable to the transition between the two SWIR detectors because of the interference of the long-path water vapor absorption band.

Spectral signatures outside of the long-path absorption bands were identifiable. For example, the kaolinite spectra contained the characteristic doublet feature in the 2200 nm region and the bentonite spectra retained the signature in the 2200–2300 nm region. The Ottawa and river sands contained weak features with signature peaks at 2140 nm followed by troughs at 2200 nm. As expected, the Donna Fill spectra contained no distinguishable features.

The spectra for all of the specimens, collected with the SOLAS receiver, contained a feature around the 970 nm water absorption band; however, the absorption feature was only discernible for the kaolinite spectra. An inverted artifact with increased reflectivity was observed for the sand, bentonite, and Donna Fill specimens. It is hypothesized that the decreased sensitivity at the upper range of the VNIR detector and the lower range of the SWIR 1 detector, as discussed in

Section 5.7.3, contributed to the artifact, with the possibility of the telescope amplifying the effect.

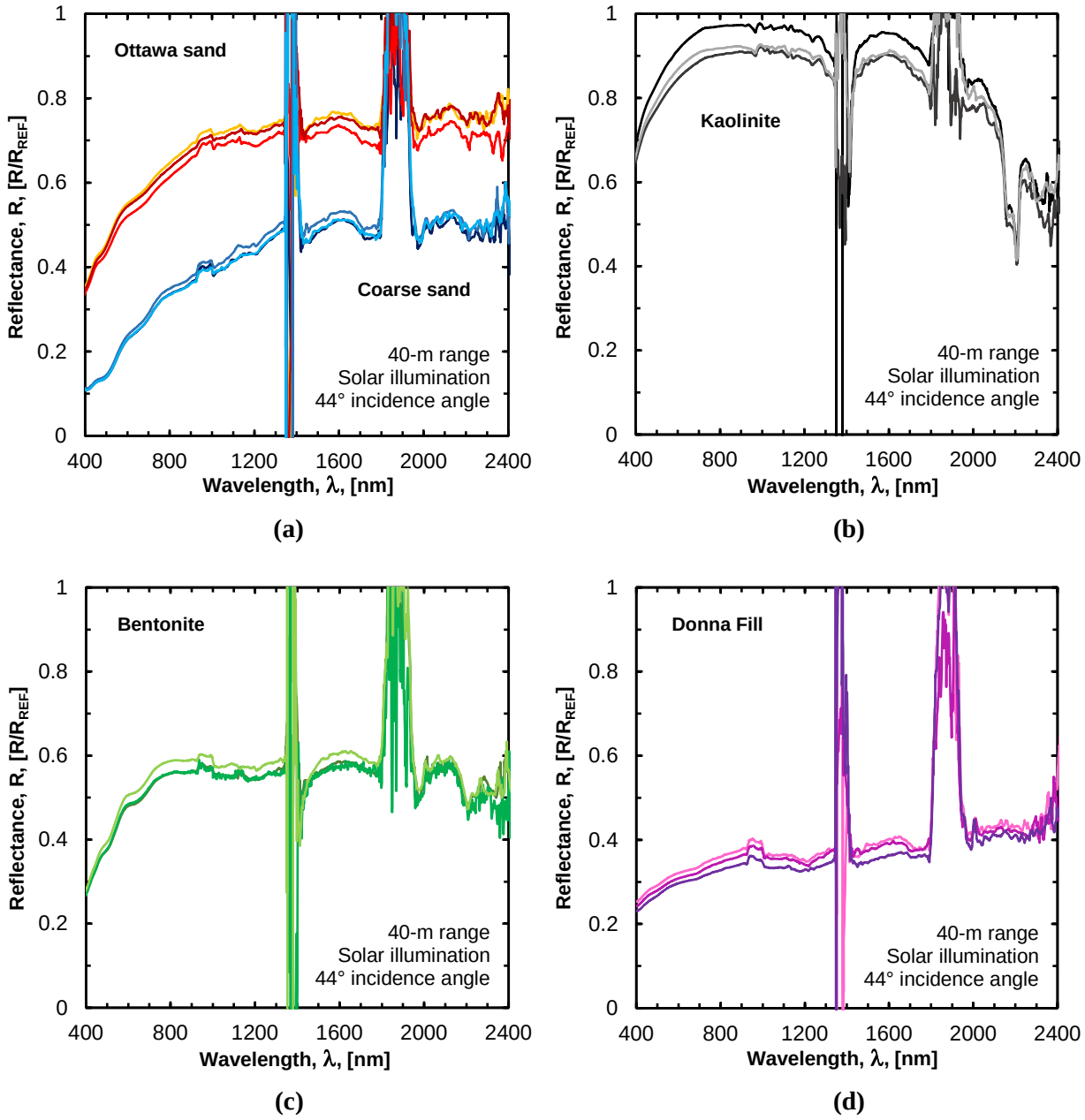

Figure 5.6. Three independent sets of reflectance spectra acquired outdoors under solar illumination, over a period of 30 minutes, at a range of 40 m, for each dry specimen of *(a)* Ottawa sand and coarse river sand, *(b)* kaolinite soil, *(c)* bentonite soil, and *(d)* Donna Fill.

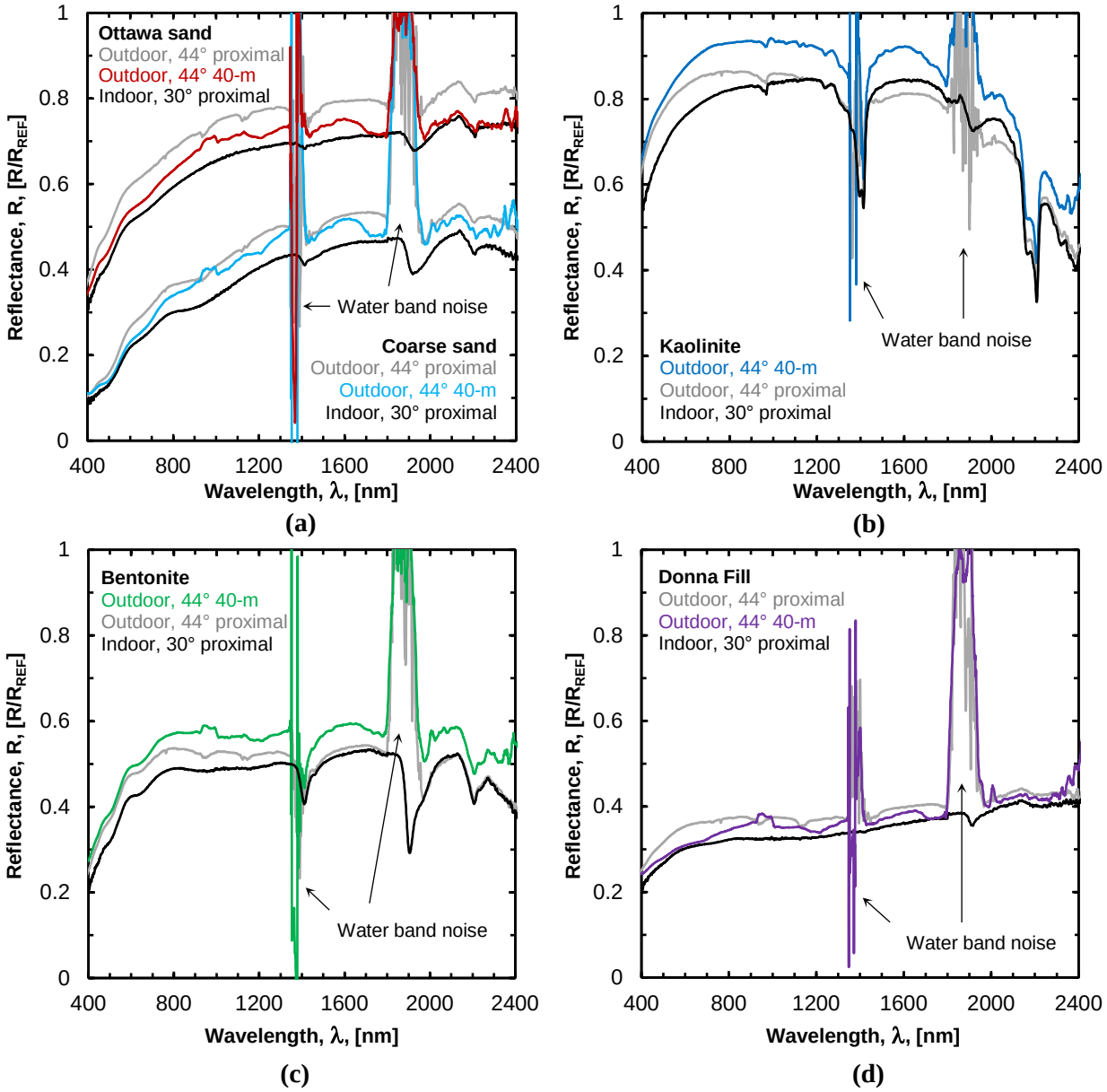

Figure 5.7. Reflectance spectra acquired indoors and outdoors, at proximal range, and outdoors at a range of 40 m for dry specimens of *(a)* Ottawa sand and coarse river sand, *(b)* kaolinite soil, *(c)* bentonite soil, and *(d)* Donna Fill.

5.7.3. *Noise-Equivalent Radiance Characterization*

The noise statistics for typical telescope-assisted measurements were presented previously (Salazar and Coffman 2019); however, the noise was not previously characterized across the entire VNIR to SWIR wavelength range. Therefore, for completeness, the noise-

equivalent radiance for the ASD FieldSpec 4 instrument is plotted as a function of wavelength in Figure 5.8(a). For each of the three detectors, the measured noise was greatest near the edges of each detector range, which is attributed to reduced sensitivity of the silicon and InGaAs detectors at these wavelengths (ASD 1999, Hueni and Bialek 2017). While the SWIR 1 range (1001–1800 nm) was the most stable range statistically, it also contained the greatest noise-equivalent-radiance value (7.5×10^{-9} $W\cdot cm^{-2}\cdot nm^{-1}\cdot sr^{-1}$ at 1001 nm).

As described in Section 5.6.4, the noise-equivalent radiance was used to derive the SNR across the entire range of collected wavelengths. A plot of the SNR for typical indoor and outdoor measurements, as acquired at proximal range, is presented in Figure 5.8(b). The measurements acquired under solar illumination had a greater SNR than the measurements acquired under artificial illumination, except for where the sunlight was absorbed by the atmosphere. Similarly, as presented in Figure 5.8(c), a comparison of the SNR for telescope-assisted, remote measurements performed indoors and outdoors, indicated that the SNR was greater for the outdoor measurements. A comparison of proximal and remote measurements, acquired outdoors under solar illumination, revealed far greater SNR for the proximal measurements, as presented in Figure 5.8(d).

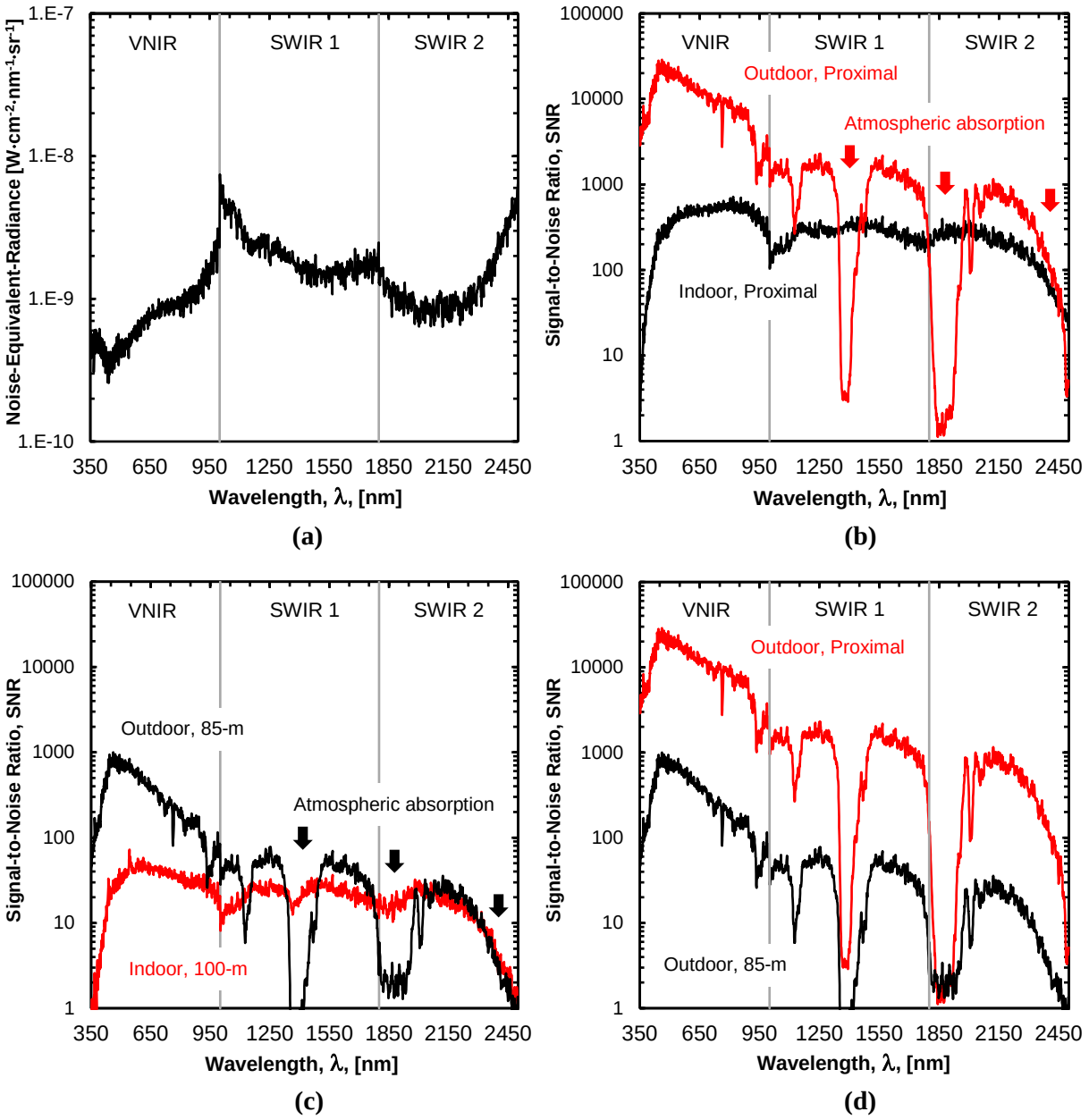

Figure 5.8. ***(a)*** **Noise as a function of wavelength, as measured across the three detector ranges of the ASD FieldSpec 4 spectroradiometer (one visible near-infrared [VNIR] and two shortwave infrared [SWIR] detectors), and typical signal-to-noise ratios as functions of wavelength for** ***(b)*** **indoor and outdoor measurements acquired at proximal range,** ***(c)*** **indoor and outdoor, telescope-assisted measurements acquired at ranges of 100 m and 85 m, respectively, and** ***(d)*** **outdoor measurements acquired at proximal range and 85 m (telescope-assisted).**

According to previous studies using ASD FieldSpec 4 instrument (Hueni and Bialek 2017), increased levels of noise were observed due to ambient temperature fluctuations and at-sensor radiance levels. The noise manifested itself at the edges of each of the three detector wavelength ranges in the form of radiometric 'jumps' between detectors; however, the noise was always greatest at the far edges of the instrument range (near 350 nm and 2500 nm). The ambient temperature-induced noise was minimized once the instrument had achieved internal thermal equilibrium, requiring a one hour (minimum) warmup period. Ambient temperature fluctuations of 5 °C or more also required time to achieve thermal equilibrium within the instrument. It is recommended that future measurements are collected in radiance mode (as opposed to reflectance mode). This will allow for the application of a parabolic correction algorithm (available in the ASD software) before calculating reflectance factors for further analysis. Corrections that were applied directly to the reflectance data, did not fully address the thermal noise, nor were the corrections applicable to measurements that were affected by long-path water vapor absorption near the 1900 nm water band (as discussed previously in Section 5.7.2).

5.7.4. *Limitations and Future Applications*

The measurements that were collected for this study were limited by several factors. For example, the maximum incidence angle of the reflectance measurements was limited primarily by the angle of repose of the dry granular soil specimens (Ottawa and coarse river sands). Despite this constraint, it was demonstrated that the SOLAS receiver could be utilized to collect measurements from oblique targets that mimicked soil slopes and other natural surfaces. Another major limitation for testing the maximum range of the SOLAS receiver was the size of the Spectralon reference panel used in this study. Specifically, the range-dependent D_{FOV} (spot

size) of the receiver could not exceed the elevation (effective height) of the target, which was significantly reduced by the shallow incidence angles tested in this study. Conversely, the azimuthal dimension of the field of view was not affected by the incidence angle.

A solution to the target size limitation is the incorporation of a companion spectrometer that measures a reference simultaneous to the sample target (e.g. ASD FieldSpec Dual methodology). This would eliminate the need for placing a reference panel downrange, making long-range measurements more practical. An added benefit of near simultaneous referencing of the Spectralon panel is the reduction of error associated with rapid changes in atmospheric conditions (cloud cover, wind etc.). Although the outdoor measurements presented in this study were collected under relatively stable atmospheric conditions, even small variations in the solar irradiance or illumination angle resulted in changes in the amplitude of the reflectance spectra and the SNR.

In the future, the SOLAS will incorporate differential laser absorption measurements (Salazar et al. 2019). These measurements of atmospheric attenuation, due to absorption and scattering by water vapor along the receiver path, will enable corrections to determine exact reflectance measurements. Deployment of the SOLAS will enable remote classification of surface materials over large areas that are hazardous or otherwise difficult-to-access. Examples of the applications of the SOLAS include rapid characterization of rocks, minerals, soils, or vegetation on slopes or outcroppings for economic geology, agriculture or forestry research, monitoring earth construction projects (e.g. mining operations, tailings dams), or forensic investigation of geohazards (e.g. landslides, debris flows). The SOLAS could also provide high spatial, spectral, and temporal resolution ground truth data for current multispectral (e.g. Sentinel-2; Drusch et al. 2012) or future hyperspectral (e.g. EnMAP; Guanter et al. 2015,

HyspIRI; HyspIRI MCT 2018) satellite missions. More information about the SOLAS instrument is available in the literature (Salazar et al. 2019, Salazar and Coffman 2019).

5.8. Conclusions

Hyperspectral reflectance measurements were acquired for five different soil types (Ottawa sand, coarse river sand, Donna Fill, bentonite soil, and kaolinite soil) under artificial illumination (indoors) and under solar illumination (outdoors). Telescope-assisted measurements, acquired using the soil observation laser absorption spectrometer (SOLAS) device, were demonstrated for intermediate ranges of 40 meters and 114 meters from the target. Reflectance spectra, acquired at proximal range in the laboratory and in the field, were provided for comparison. The spectra matched well, with distinguishable absorption and reflectance features, characteristic of soil mineralogy. Additionally, the effect of specimen type, range-dependent spatial resolution, and environment on the measured reflectance was presented and discussed.

The SNR of the measurements was determined as a function of wavelength for the full spectral range of the receiver. The greatest overall SNR was observed for the proximal measurements that were performed outdoors, followed by the proximal measurements that were performed indoors, the remote measurements that were performed outside, and finally, the remote measurements that were performed indoors. Signal loss around the 1400 nm and 1900 nm bands, due to long-path atmospheric water vapor absorption, was observed for the outdoor measurements. Increased levels of noise, inherent to the design of the spectoradiometer, were observed for the wavelengths near the edges of each detector range (350, 1000, 1800, and 2500 nm). Proper instrument warmup practices minimized the radiometric noise present in the signal,

particularly at the transition from one detector to the next. Future development of the SOLAS remote sensor will allow for derivation of exact reflectance measurements over longer ranges.

5.9. Acknowledgements

This project was funded by the U.S. Department of Transportation (USDOT) through the Office of the Assistant Secretary for Research and Technology (OST-R) under USDOT Cooperative Agreement No. OASRTRS-14-H-UARK. The views, opinions, findings and conclusions reflected in this publication are solely those of the authors and do not represent the official policy or position of the USDOT/OST-R, or any State or other entity. USDOT/OST-R does not endorse any third party products or services that may be included in this publication. This material is also based upon work supported by the National Science Foundation Graduate Research Fellowship Program under Grant No. DGE-1450079. Any opinions, findings, and conclusions or recommendations expressed in this material are those of the authors and do not necessarily reflect the views of the National Science Foundation.

5.10. References

Adam, E., Mutanga, O., and Rugege, D., 2010, "Multispectral and Hyperspectral Remote Sensing for Identification and Mapping of Wetland Vegetation: A Review," *Wetlands Ecol. Manage.*, Vol. 18, pp. 281–296. doi:10.1007/s11273-009-9169-z.

Analytical Spectral Devices, 1999, *ASD Technical Guide*, 3rd ed., Hatchell, D. C., Ed., Analytical Spectral Devices, Inc., Boulder, CO, USA.

Danner, M., Locherer, M., Hank, T., and Richter, K., 2015, "Spectral Sampling with the ASD FieldSpec 4—Theory, Measurement, Problems, Interpretation," EnMAP Field Guides Technical Report, GFZ Data Services, Potsdam, Germany.

Drusch, M., Del Bello, U., Carlier, S., Colin, O., Fernandez, V., Gascon, F., Hoersch, B., Isola, C., Laberinti, P., Martimort, P., Meygret, A., Spoto, F., Sy, O., Marchese, F., and Bargellini, P., 2012, "Sentinel-2: ESA's Optical High-Resolution Mission for GMES Operational Services," *Remote Sens. Environ.*, Vol. 120, pp. 25–36. doi:10.1016/j.rse.2011.11.026.

Fager, G. (Analytical Spectral Devices, Longmont, CO, USA). Personal Correspondence, February 26, 2019.

Garner, C. D., 2017, "Development of a Multiband Remote Sensing System for Determination of Unsaturated Soil Properties," Ph.D. dissertation, University of Arkansas, Fayetteville, AR, USA.

Goetz, A. F. H., 2009, "Three Decades of Hyperspectral Remote Sensing of the Earth: A Personal Review," *Remote Sens. Environ.*, Vol. 113, pp. S5–S16. doi:10.1016/j.rse.2007.12.014.

Hueni, A. and Bialek, A., 2017, "Cause, Effect, and Correction of Field Spectroradiometer Interchannel Radiometric Steps," *IEEE J. Sel. Top. Appl. Earth Obs. Remote Sens.*, Vol. 10, pp. 1542–1551. doi:10.1109/JSTARS.2016.2625043.

HyspIRI Mission Concept Team, 2018, *HyspIRI Final Report*, Jet Propulsion Laboratory, California Institute of Technology, Pasadena, CA, USA.

Kokaly, R. F., Clark, R. N., Swayze, G. A., Livo, K. E., Hoefen, T. M., Pearson, N. C., Wise, R. A., Benzel, W. M., Lowers, H. A., Driscoll, R. L., and Klein, A. J., 2017, *USGS Spectral Library Version 7: U.S. Geological Survey Data Series 1035*, United States Geological Survey, Reston, VA, USA, pp. 1–61. doi:10.3133/ds1035.

Loizzo, R., Ananasso, C., Guarini, R., Lopinto, E., Candela, L., and Pisani, A. R., 2016, "The PRISMA Hyperspectral Mission," *Proceedings of the Living Planet Symposium 2016*, Prague, Czech Republic, May 9–13.

Pasolli, E., Prasad, S., Crawford, M. M., and Tilton, J. C., 2018, "Advances in Hyperspectral Image Classification Methods for Vegetation and Agricultural Cropland Studies," In *Hyperspectral Indices and Image Classifications for Agriculture and Vegetation*, P. S. Thenkabail, J. G. Lyon, and A. Huete, Eds., CRC Press, Boca Raton, FL, USA, pp. 67–104. doi:10.1201/9781315159331.

Salazar, S. E. and Coffman, R. A., 2019, "Multi-Channel Optical Receiver for Ground-Based Topographic Hyperspectral Remote Sensing," *Remote Sens.*, Vol. 11, No. 5, 578. doi:10.3390/rs11050578.

Salazar, S. E., Garner, C. D., and Coffman, R. A., 2019, "Development of a Multimode Field Deployable Lidar Instrument for Topographic Measurements of Unsaturated Soil Properties: Instrument Description," *Remote Sens.*, Vol. 11, No. 3, 289. doi:10.3390/rs11030289.

Savitzky, A. and Golay, M. J. E., 1964, "Smoothing and Differentiation of Data by Simplified Least Squares Procedures," *Anal. Chem.*, Vol. 36, pp. 1627–1639. doi:10.1021/ac60214a047.

Schaepman, M. E., Ustin, S. L., Plaza, A. J., Painter, T. H., Verrelst, J., and Liang, S., 2009, "Earth System Science Related Imaging Spectroscopy – An Assessment," *Remote Sens. Environ.*, Vol. 113, pp. S123–S137. doi:10.1016/j.rse.2009.03.001.

Van der Meer, F. D., van der Werff, H. M. A., van Ruitenbeek, F. J. A., Hecker, C. A., Bakker, W. H., Noomen, M. F., van der Meijde, M., Carranza, E. J. M., Boudewijn de Smeth, J., and Woldai, T., 2012, "Multi- and Hyperspectral Geologic Remote Sensing: A Review," *Int. J. Appl. Earth Obs. Geoinf.*, Vol. 14, pp. 112–128. doi:10.1016/j.jag.2011.08.002.

Waruru, B. K., Shepherd, K. D., Ndegwa, G. M., Kamoni, P. T., and Sila, A. M., 2014, "Rapid Estimation of Soil Engineering Properties Using Diffuse Reflectance Near Infrared Spectroscopy," *Biosyst. Eng.*, Vol. 121, pp. 177-185. doi:10.1016/j.biosystemseng.2014.03.003.

CHAPTER 6: CONCLUSIONS

6.1. Chapter Overview

Outlined in this chapter are the conclusions that were drawn from this work. Some of the highlights of the work are listed in Section 6.2. The major limitations of the work are described in Section 6.3. Recommendations are provided in Section 6.4.

6.2. Highlights

The SOLAS technology that was developed in this work was designed, components were procured, and a field-ruggedized and rapidly deployable instrument was fabricated and assembled. The SOLAS receiver was successfully implemented to collect hyperspectral reflectance measurements from soil targets at ranges of up to 114 meters from the instrument, as documented in Chapter 5. Additional testing, not included in this work, indicated that measurements could be collected at a range of 175 meters from the instrument. The SOLAS therefore significantly extended the range of high spectral resolution reflectance measurements beyond conventional field spectroscopy techniques at proximal distances. The range limitations are further discussed in Section 6.3 and suggestions for increasing the range are provided in Section 6.4.

While adoption of the ASD FieldSpec 4 spectroradiometer instrument into the SOLAS platform reduced the typical signal-to-noise ratio (SNR) of measurements performed at proximal range, an acceptable SNR was maintained for the telescope-assisted, intermediate range measurements. For example, the typical peak SNR was approximately 16,000:1 for proximal range measurements of the Spectralon reference panel, while the corresponding peak SNR was 1000:1 for a typical measurement at 85 m from the target under the same conditions. Because

the SNR was heavily wavelength-dependent, these values were provided for illustration purposes only. The average ratio of the proximal range SNR to the intermediate range SNR was 16:1.

The SOLAS transmitter was assembled and individual components were tested. However, measurements with the active portion of the instrument were not collected, as discussed in Section 6.3. Future improvements to the transmitter will enable integration of the active measurements, as outlined in Section 6.4.

6.3. Limitations

Chapters 3, 4, and 5 contained discussions about the limitations of the SOLAS technology. For reference, the limitations included:

- low coupling efficiency between the free-space and fiber-based transmitting laser path(s) (Section 3.9);
- separate software used to acquire different sets of data (Section 3.9);
- the range-dependent divergence in the field-of-view between the VNIR and SWIR channels of the receiver (Section 4.6);
- the oblique (shallow) incidence angles of the targets that were measured (Section 5.7.4);
- the size of the targets that were measured in relation to the spot size of the SOLAS, given the incidence angles (Section 5.7.4);
- the need for a downrange reference panel for calibrated reflectance measurements (Sections 3.9, 4.7, and 5.7.4);
- the need for frequent referencing of the panel, even under clear sky conditions (Sections 3.9, 4.7, and 5.7.4);

- the sensitivity of the spectroradiometer to temperature-induced noise, when collecting data over long periods of time or in fluctuating weather conditions, e.g. strong solar irradiation or wind (Sections 4.7 and 5.7.3);

Additionally, the following limitations, not described in the preceding chapters, are noted.

- The output polarization of the free-space laser beams, following optical isolation, did not correspond with the input polarization of the fiber.
- The 23.8 nm difference between the 823.2 nm on-line and 847.0 nm off-line wavelengths required careful consideration for wavelength optimization. For components along the common transmitter path (e.g. Mach-Zehnder modulator, tapered amplifier), the design wavelength was selected as close to the middle of the on- and off-line wavelengths (i.e. 835 nm) as possible. The availability of off-the-shelf designs were limited, while custom components were cost-prohibitive.
- Soil properties, other than general classification of soil type, were not derived from spectral reflectance measurements.

6.4. Recommendations

In accordance with the aforementioned limitations, the following recommendations will facilitate future improvements to the SOLAS technology.

- The efficiency of the SOLAS transmitter design could be improved with an all fiber design, eliminating most of the losses that are due to coupling.
- Custom software should be developed to provide a more cohesive data acquisition scheme.

- A companion spectrometer should be utilized to enable simultaneous measurements of the reference panel and the target. This will also make measurements more practical by eliminating the need to place a reference downrange of the instrument.
- To minimize the temperature-induced noise, a one-hour warmup period should precede any data acquisition. Measurements should be collected in radiance mode, as opposed to reflectance mode, to allow for radiometric corrections during data processing.
- A waveplate (or set of waveplates) should be placed into the free-space laser beam path(s) before the lasers enter the first fiber-coupling stage. This will ensure that the input polarization of the laser beams matches the orientation of the polarization-maintaining fiber optic cable of the Mach-Zehnder modulator.
- The on-line and off-line wavelengths of the transmitting lasers that were selected are suited to differential absorption measurements, but a simpler design that utilizes a single, more widely tunable laser source is possible. This would simplify the design of the bulk optics that are utilized to direct, shape, and modulate the transmitted light signal. Alternatively, two lasers that are closer in wavelength would improve the efficiency of the transmitter, due to component optimization over a narrower wavelength range.
- Laser safety must be considered when using the SOLAS transmitter. Maximum permissible exposure (MPE) limits must be observed when not wearing protective eyewear. For more information about the MPE, refer to the University of Arkansas Office of Environmental Health and Safety.
- Future miniaturization of the SOLAS prototype will improve the instrument's portability. It is recommended that a low fidelity prototype is developed and tested for inclusion aboard a small RPAS.

CHAPTER 7: WORKS CITED

Adam, E., Mutanga, O., and Rugege, D., 2010, "Multispectral and Hyperspectral Remote Sensing for Identification and Mapping of Wetland Vegetation: A Review," *Wetlands Ecol. Manage.*, Vol. 18, pp. 281–296. doi:10.1007/s11273-009-9169-z.

Adany, P., Allen, C., and Hui, R., 2009, "Chirped Lidar Using Simplified Homodyne Detection," *J. Lightwave Technol.*, Vol. 27, No. 16, pp. 3351-3357.

Allen, C., Cobanoglu, Y., Chong, S. K., and Gogineni, S., 2001, "Performance of a 1319 nm Laser Radar Using RF Pulse Compression," *Proceedings of the International Geoscience and Remote Sensing Symposium (IGARSS 2001)*, Sydney, Australia, July 7–13, pp. 997-999. doi:10.1109/IGARSS.2001.976726.

Ångström, A., 1925, "The Albedo of Various Surfaces of Ground," *Geogr. Ann.*, Vol. 7, pp. 323-342. doi:10.2307/519495.

Analytical Spectral Devices, 1999, *ASD Technical Guide*, 3rd ed., Hatchell, D. C., Ed., Analytical Spectral Devices, Inc., Boulder, CO, USA.

ASTM D422-63, 2007, "Standard Test Method for Particle-Size Analysis of Soils," ASTM International, West Conshohocken, PA, USA, www.astm.org. doi:10.1520/DO422-63R07E02.

Bach, H. and Mauser, W., 1994, "Modelling and Model Verification of the Spectral Reflectance Of Soils Under Varying Moisture Conditions," *Proceedings of the International Geoscience and Remote Sensing Symposium (IGARSS'94)*, Pasadena, CA, USA, August 8–12, pp. 2354-2356. doi:10.1109/IGARSS.1994.399735.

Barber, Z. W. Babbitt, W. R., Kaylor, B., Reibel, R. R., and Roos, P. A., 2010, "Accuracy of Active Chirp Linearization for Broadband Frequency Modulated Continuous Wave Ladar," *Appl. Optics*, Vol. 49, No. 2, pp. 213-219.

Barrientos-Barria, J., Mammez, D., Dherbecourt, J.-B., Raybaut, M., Melkonian, J.-M., Pelon, J., Godard, A., and Lefebvre, M., 2014, "Progress on High Energy Optical Parametric Transmitter for Multiple Greenhouse Gases DIAL," *Proceedings of the International Conference on Space Optics (ICSO 2014)*, Tenerife, Canary Islands, Spain, October 6–10, SPIE Vol. 10563. doi:10.1117/12.2304157.

Ben-Dor, E. and Banin, A., 1995, "Near-Infrared Analysis as a Rapid Method to Simultaneously Evaluate Several Soil Properties," *Soil Sci. Soc. Am. J.*, Vol. 59, No. 2, pp. 364-372.

Ben-Dor, E., Chabrillat, S., Demattê, J. A. M., Taylor, G. R., Hill, J., Whiting, M. L., and Sommer, S., 2009, "Using Imaging Spectroscopy to Study Soil Properties," *Remote Sens. Environ.*, Vol. 113, S. 1, pp. S38-S55. doi:10.1016/j.rse.2008.09.019.

Berk, A., Bernstein, L. S., and Robertson, D. C., 1989, “MODTRAN: A Moderate Resolution Model for LOWTRAN 7,” Final Report, GL-TR-0122, AFGL, Hanscom Air Force Base, MA, USA, 42 pgs.

Berk, A., Conforti, P. and Hawes, F., 2015, "An Accelerated Line-By-Line Option for MODTRAN Combining On-the-Fly Generation of Line Center Absorption with 0.1 cm-1 Bins and Pre-Computed Line Tails," In *Algorithms and Technologies for Multispectral, Hyperspectral, and Ultraspectral Imagery XXI*, SPIE Proceedings, Vol. 9471. doi:10.1117/12.2177444.

Berk, A., Conforti, P., Kennett, R., Perkins, T., Hawes, F., and van den Bosch, J., 2014, "MODTRAN6: A Major Upgrade of the MODTRAN Radiative Transfer Code," In *Algorithms and Technologies for Multispectral, Hyperspectral, and Ultraspectral Imagery XX*, SPIE Proceedings, Vol. 9088. doi:10.1117/12.2050433.

Bösenberg, J., 1998, "Ground-Based Differential Absorption Lidar for Water-Vapor and Temperature Profiling: Methodology," *Appl. Optics*, Vol. 37, No. 18, pp. 3845-3860.

Bowers, S. A. and Hanks, R. J., 1965, "Reflection of Radiant Energy from Soils," *Soil Sci.*, Vol. 100, No. 2, pp. 130-138.

Browell, E. V., Dobler, J., Kooi, S. A., Choi, Y., Harrison, F. W., Moore, B., and Zaccheo, T. S., 2010, “Airborne Validation of Laser Remote Measurements of Atmospheric Carbon Dioxide,” *Proceedings of the 25th International Laser Radar Conference (ILRC 25)*, St. Petersburg, Russia, July 5–9, pp. 779-782.

Bruneau, D., Quaglia, P., Flamant, C., Meissonnier, M., and Pelon, J., 2001a, "Airborne Lidar LEANDRE II for Water-Vapor Profiling in the Troposphere. I. System Description," *Appl. Optics*, Vol. 40, No. 21, pp. 3450-3461.

Bruneau, D., Quaglia, P., Flamant, C., and Pelon, J., 2001b, "Airborne Lidar LEANDRE II for Water-Vapor Profiling in the Troposphere. II. First Results," *Appl. Optics*, Vol. 40, No. 21, pp. 3462-3475.

Bufton, J. L., Itabe, T., and Grolemund, D. A., 1983, "Airborne Remote Sensing Measurements With a Pulsed CO_2 Dial System," In *Optical and Laser Remote Sensing*, D.K. Killinger, A. Mooradian, Eds., Springer-Verlag, Berlin Heidelberg, Germany, pp. 2-9.

Castaldi, F., Chabrillat, S., and van Wesemael, B., 2019a, “Sampling Strategies for Soil Property Mapping Using Multispectral Sentinel-2 and Hyperspectral EnMAP Satellite Data,” *Remote Sens.*, Vol. 11, No. 3, 309. doi:10.3390/rs11030309.

Castaldi, F., Hueni, A., Chabrillat, S., Ward, K., Buttafuoco, G., Bomans, B., Vreys, K., Brell, M., and van Wesemael, B., 2019b, “Evaluating the Capability of the Sentinel 2 Data for Soil Organic Carbon Prediction in Croplands,” *ISPRS J. Photogramm. Remote Sens.*, Vol. 147, pp. 267–282. doi:10.1016/J.ISPRSJPRS.2018.11.026.

Chang, C.-W., Laird, D., Mausbach, M. J., and Hurburgh, C. R., 2001, "Near-Infrared Reflectance Spectroscopy-Principle Components Regression Analysis of Soil Properties," *Soil Sci. Soc. Am. J.*, Vol. 65, pp. 480-490.

Chourdakis, G., Papayannis, A., and Porteneuve, J., 2002, "Analysis of the Receiver Response For a Noncoaxial Lidar System with Fiber-Optic Output," *Appl. Opt.*, Vol. 41, pp. 2715–2723. doi:10.1364/ao.41.002715.

Clark, R. N., 1999, "Chapter 1: Spectroscopy of Rocks and Minerals, and Principles of Spectroscopy," In *Manual of Remote Sensing, Volume 3, Remote Sensing for the Earth Sciences*, 3rd ed., A.N. Rencz, Ed., John Wiley and Sons, New York, NY, USA, pp. 3–58.

Cozzolino, D. and Moron, A., 2003, "The Potential of Near-Infrared Reflectance Spectroscopy to Analyze Soil Chemical and Physical Characteristics," *J. Agr. Sci.*, Vol. 140, pp. 65-71.

Curcio, D., Ciraolo, G., D'Asaro, F., and Minacapilli, M., 2013, "Prediction of Soil Texture Distributions Using VNIR-SWIR Reflectance Spectroscopy," *Proc. Environ. Sci.*, Vol. 19, pp. 494–503. doi:10.1016/j.proenv.2013.06.056.

Dalal, R. C. and Henry, R. J., 1986, "Simultaneous Determination of Moisture, Organic Carbon, And Total Nitrogen by Near Infrared Reflectance Spectrophotometry," *Soil Sci. Soc. Am. J.*, Vol. 50, No. 1, pp. 120-123. doi:10.2136/sssaj1986.03615995005000010023x.

Danner, M., Locherer, M., Hank, T., and Richter, K., 2015, "Spectral Sampling with the ASD FieldSpec 4—Theory, Measurement, Problems, Interpretation," EnMAP Field Guides Technical Report, GFZ Data Services, Potsdam, Germany.

Drusch, M., Del Bello, U., Carlier, S., Colin, O., Fernandez, V., Gascon, F., Hoersch, B., Isola, C., Laberinti, P., Martimort, P., Meygret, A., Spoto, F., Sy, O., Marchese, F., and Bargellini, P., 2012, "Sentinel-2: ESA's Optical High-Resolution Mission for GMES Operational Services," *Remote Sens. Environ.*, Vol. 120, pp. 25–36. doi:10.1016/j.rse.2011.11.026.

Ehret, G., Kiemle, C., Renger, W., and Simmet, G., 1993, "Airborne Remote Sensing of Tropospheric Water Vapor with a Near-Infrared Differential Absorption Lidar System," *Appl. Optics*, Vol. 32, No. pp. 4534-4551.

Ehret, G., Kiemle, C., Wirth, M., Amediek, A., Fix, A., and Houweling, S., 2008, "Space-Borne Remote Sensing of CO2, CH4, and N2O by Integrated Path Differential Absorption Lidar: A Sensitivity Analysis," *Appl. Phys. B-Lasers O.*, Vol. 90, No. 3-4, pp. 593-608.

Fabre, S., Briottet, X., and Lesaignoux, A., 2015, "Estimation of Soil Moisture Content from the Spectral Reflectance of Bare Soils in the 0.4-2.5 μm Domain," *Sensors*, Vol. 15, pp. 3262-3281. doi:10.3390/s150203262.

Fager, G. (Analytical Spectral Devices, Longmont, CO, USA). Personal Correspondence, February 26, 2019.

Gao, S. and Hui, R., 2012, "Frequency-Modulated Continuous-Wave Lidar Using I/Q Modulator For Simplified Heterodyne Detection," *Opt. Lett.*, Vol. 37, No. 11, pp. 2022-2024; doi:10.1364/OL.37.002022.

Garner, C. D., 2017, "Development of a Multiband Remote Sensing System for Determination of Unsaturated Soil Properties," Ph.D. dissertation, University of Arkansas, Fayetteville, AR, USA.

Goetz, A. F. H., 2009, "Three Decades of Hyperspectral Remote Sensing of the Earth: A Personal Review," *Remote Sens. Environ.*, Vol. 113, pp. S5–S16. doi:10.1016/j.rse.2007.12.014.

Gordon, I. E., Rothman, L. S., Hill, C., et al., 2017, "The HITRAN2016 Molecular Spectroscopic Database", *J. Quant. Spectrosc. Ra.*, Vol. 203, pp. 3-69. doi:10.1016/j.jqsrt.2017.06.038.

Grant, W. B., 1982, "Effect of Differential Spectral Reflectance on DIAL Measurements Using Topographic Targets," *Appl. Optics*, Vol. 21, No. 13, pp. 2390-2394.

Grant, W. B., 1991, "Differential Absorption and Raman Lidar for Water Vapor Profile Measurements: A Review," *Opt. Eng.*, Vol. 30, No. 1, pp. 40-48.

Guanter, L., Kaufmann, H., Segl, K., Foerster, S., Rogass, C., Chabrillat, S., Kuester, T., Hollstein, A., Rossner, G., Chlebek, C., et al., 2015, "The EnMAP Spaceborne Imaging Spectroscopy Mission for Earth Observation," *Remote Sens.*, Vol. 7, No. 7, pp. 8830–8857. doi:10.3390/rs70708830.

Guarini, R., Loizzo, R., Facchinetti, C., Longo, F., Ponticelli, B., Faraci, M., Dami, M., Cosi, M., Amoruso, L., de Pasquale, V., et al., 2018, "Prisma Hyperspectral Mission Products," *Proceedings of the International Geoscience and Remote Sensing Symposium (IGARSS 2018)*, Valencia, Spain, July 22–27, pp. 179–182. doi:10.1109/IGARSS.2018.8517785.

Hardesty, R. M., 1984, "Coherent DIAL Measurement of Range-Resolved Water Vapor Concentration," *Appl. Optics*, Vol. 23, No. 15, pp. 2545-2553.

Haubrock, S. N., Chabrillat, S., Lemmnitz, C., and Kaufmann, H., 2008, "Surface Soil Moisture Quantification Models from Reflectance Data Under Field Conditions," *Int. J. Remote Sens.*, Vol. 29, No. 1, pp. 3-29. doi:10.1080/01431160701294695.

Hueni, A. and Bialek, A., 2017, "Cause, Effect, and Correction of Field Spectroradiometer Interchannel Radiometric Steps," *IEEE J. Sel. Top. Appl. Earth Obs. Remote Sens.*, Vol. 10, pp. 1542–1551. doi:10.1109/JSTARS.2016.2625043.

Hummel, J. W., Sudduth, K. A., and Hollinger, S. E., 2001, "Soil Moisture and Organic Matter Prediction of Surface and Subsurface Soils Using an NIR Soil Sensor," *Comput. Electron. Agr.*, Vol. 32, No. 2, pp. 149-165. doi:10.1016/S0168-1699(01)00163-6.

HyspIRI Mission Concept Team, 2018, *HyspIRI Final Report*, Jet Propulsion Laboratory, California Institute of Technology, Pasadena, CA, USA.

Ishii, S., Koyama, M., Baron, P., Iwai, H., Mizutani, K., Itabe, T., Sato, A., and Asai, K., 2013, "Ground-Based Integrated Path Coherent Differential Absorption Lidar Measurement of CO_2: Foothill Target Return," *Atmos. Meas. Tech.*, Vol. 6, pp. 1359-1369. doi:10.5194/amt-6-1359-2013.

Islam, K., Singh, B., and McBratney, A., 2003, "Simultaneous Estimation of Various Soil Properties by Ultra-Violet, Visible, and Near-Infrared Reflectance Spectroscopy," *Aust. J. Soil Res.*, Vol. 41, No. 6, pp. 1101-1114.

Ismail, S. and Browell, E. V., 1989, "Airborne and Spaceborne Lidar Measurements of Water Vapor Profiles: A Sensitivity Analysis," *Appl. Optics*, Vol. 28, No. 17, pp. 3603-3615.

Janik, L. and Skjemstad, J., 1995, "Characterization and Analysis of Soils Using Mid-Infrared Partial Least Squares: II. Correlations with Some Laboratory Data," *Aust. J. Soil Res.*, Vol. 33, pp. 637-650.

Jelalian, A. *Laser Radar Systems*. Artech House, Norwood, MA, USA, 1992.

Karlsson, C. J. and Olsson, F. Å. A., 1999, "Linearization of the Frequency Sweep of a Frequency-Modulated Continuous-Wave Semiconductor Laser and the Resulting Ranging Performance," *Appl. Optics*, Vol. 38, No. 15, pp. 3376-3386.

Knadel, M., Deng, F., Alinejadian, A., de Jonge, L. W., Moldrup, P., and Greve, M. H., 2014, "The Effects of Moisture Conditions – From Wet to Hyper Dry – On Visible Near Infrared Spectra of Danish Reference Soils," *Soil Sci. Soc. Am. J.*, Vol. 78, No. 2, pp. 422-433. doi:10.2136/sssaj2012.0401.

Knadel, M., Stenberg, B., Deng, F., Thomsen, A., and Greve, M. H., 2013, "Comparing Predictive Abilities of Three Visible-Near Infrared Spectrophotometers for Soil Organic Carbon and Clay Determination," *J. Near Infrared Spec.*, Vol. 21, No. 1, pp. 67-80. doi:10.1255/jnirs.1035.

Kokaly, R. F., Clark, R. N., Swayze, G. A., Livo, K. E., Hoefen, T. M., Pearson, N. C., Wise, R. A., Benzel, W. M., Lowers, H. A., Driscoll, R. L., and Klein, A. J., 2017, *USGS Spectral Library Version 7: U.S. Geological Survey Data Series 1035*, United States Geological Survey, Reston, VA, USA, pp. 1–61. doi:10.3133/ds1035.

Kou, L., Labrie, D., and Chylek, P., 1993, "Refractive Indices of Water and Ice in the 0.65- to 2.5-μm Spectral Range," *Appl. Optics*, Vol. 32, No. 19, pp. 3531-3540.

Lesaignoux, A., Fabre, S., and Briottet, X., 2013, "Influence of Soil Moisture Content on Spectral Reflectance of Bare Soils in the 0.4-14 μm Domain," *Int. J. Remote Sens.*, Vol. 34, No. 7, pp. 2268-2285. doi:10.1080/01431161.2012.743693.

Leu, D. J., 1977, "Visible and Near-Infrared Reflectance of Beach Sands: A Study on the Spectral Reflectance/Grain Size Relationship," *Remote Sens. Environ.*, Vol. 6, No. 3, pp. 169-182. doi:10.1016/0034-4257(77)90002-5.

Little, L. M. and Papen, G. C., 2001, "Fiber-Based Lidar for Atmospheric Water-Vapor Measurements," *Appl. Optics*, Vol. 40, No. 21, pp. 3417-3427.

Liu, W., Baret, F., Gu, X., Tong, Q., Zheng, L., and Zhang, B., 2002, "Relating Soil Surface Moisture to Reflectance," *Remote Sens. Environ.*, Vol. 81, pp. 238-246.

Liu, W., Baret, F., Gu, X., Zhang, B., Tong, Q., and Zheng, L., 2003, "Evaluation of Methods for Soil Surface Moisture Estimation from Reflectance Data," *Int. J. Remote Sens.*, Vol. 24, No. 10, pp. 2069-2083.

Lobell, D. B. and Asner, G. P., 2002, "Moisture Effects on Soil Reflectance," *Soil Sci. Soc. Am. J.*, Vol. 66, No. 3, pp. 722-727.

Loizzo, R., Ananasso, C., Guarini, R., Lopinto, E., Candela, L., and Pisani, A. R., 2016, "The PRISMA Hyperspectral Mission," *Proceedings of the Living Planet Symposium 2016*, Prague, Czech Republic, May 9–13.

Machol, J., Ayers, T., Schwenz, K., Koenig, K., Hardesty, R., Senff, C., Krainak, M., Abshire, J., Bravo, H., and Sandberg, S., 2004, "Preliminary Measurements with an Automated Compact Differential Absorption LIDAR for Profiling Water Vapor," *Appl. Optics*, Vol. 43, No. 15, pp. 3110-3121.

Mateo, A. B., 2014, "Applications of High Resolution and Accuracy Frequency Modulated Continuous Wave Ladar," M.S. thesis, Montana State University, Bozeman, MT, USA.

Megie, G. and Menzies, R. T., 1980, "Complementarity of UV and IR Differential Absorption Lidar for Global Measurements of Atmospheric Species," *Appl. Optics*, Vol. 19, No. 7, pp. 1173-1183.

Menzies, R. T. and Shumate, M. S., 1976, "Remote Measurements of Ambient Air Pollutants With a Bistatic Laser System," *Appl. Optics*, Vol. 15, No. 9, pp. 2080-2084.

Moen, D. R., 2016, "Two Channel Receiver Design and Implementation for a Ground Based Micro-Pulse Differential Absorption Lidar (DIAL) Instrument," M.S. thesis, Montana State University, Bozeman, MT, USA.

Moore, A. S., Brown, K. E., Hall, W. M., Barnes, J. C., Edwards, W. C., Petway, L. B., Little, A. D., Luck, W. S., Jones, I. W., Antill, C. W., et al., 1996, "Development of the Lidar Atmospheric Sensing Experiment (LASE) – An Advanced Airborne DIAL Instrument," In *Advances in Atmospheric Remote Sensing with Lidar: Selected Papers of the 18th International Laser Radar Conference (ILRC)*, Berlin, Germany, July 22–26; A. Ansmann, R. Neuber, P. Rairoux, and U. Wandinger, Eds., Springer-Verlag, Berlin/Heidelberg, Germany, pp. 281–288. ISBN 9783540618874.

Morgan, J., 1953, *Introduction to Geometrical and Physical Optics*, 1st ed., McGraw-Hill, New York, NY, USA.

Morris, R. V., Neely, S. C., and Mendell, W. W., 1982, "Application of Kubelka–Munk Theory of Diffuse Reflectance to Geologic Problems: The Role of Scattering," *Geophys. Res. Lett.*, Vol. 9, No. 2, pp. 113–116. doi:10.1029/GL009i002p00113.

Mouazen, A. M., Karoui, R., De Baerdemaeker, J., and Ramon, H., 2006, "Characterization of Soil Water Content Using Measured Visible and Near Infrared Spectra," *Soil Sci. Soc. Am. J.*, Vol. 70, No. 4, pp. 1295-1302. doi:10.2136/sssaj2005.0297.

Mouazen, A. M., Maleki, M. R., De Baerdemaeker, J., and Ramon, H., 2007, "On-line Measurement of Some Selected Soil Properties Using a VIS-NIR Sensor," *Soil Till. Res.*, Vol. 93, No. 1, pp. 13-27. doi:10.1016/j.still.2006.03.009.

Nehrir, A. R., 2008, "Water Vapor Profiling Using a Compact Widely Tunable Diode Laser Differential Absorption Lidar (DIAL)," M.S. thesis, Montana State University, Bozeman, MT, USA.

Nehrir, A. R., 2011, "Development of an Eye-Safe Diode-Laser-Based Micro-Pulse Differential Absorption Lidar (MP-DIAL) for Atmospheric Water-Vapor and Aerosol Studies," Ph.D. Dissertation, Montana State University, Bozeman, MT, USA.

Nehrir, A. R., Repasky, K. S., and Carlsten, J. L., 2011, "Eye-Safe Diode-Laser-Based Micropulse Differential Absorption Lidar (DIAL) for Water Vapor Profiling in the Lower Troposphere," *J. Atmos. Ocean. Tech.*, Vol. 28, pp. 131-147.

Nehrir, A. R., Repasky, K. S., and Carlsten, J. L., 2012, "Micropulse Water Vapor Differential Absorption Lidar: Transmitter Design and Performance," *Opt. Express*, Vol. 20, No. 22, pp. 25137-25151.

Nehrir, A. R., Repasky, K. S., Carlsten, J. L., Obland, M. D., and Shaw, J. A., 2009, "Water Vapor Profiling Using a Widely Tunable, Amplified Diode-Laser-Based Differential Absorption Lidar (DIAL)," *J. Atmos. Ocean. Tech.*, Vol. 26, No. 4, pp. 733-745.

New Focus, 2014, *TLB-6800 Vortex Plus™ Laser System User's Manual*, Rev. A, New Focus, Santa Clara, CA, USA.

Nolet, C., Poortinga, A., Roosjen, P., Bartholomeus, H., and Ruessink, G., 2014, "Measuring and Modeling the Effect of Surface Moisture on the Spectral Reflectance of Coastal Beach Sand," *PLoS One*, Vol. 9, No. 11, e112151. doi:10.1371/journal.pone.0112151.

Park, J. K., 1980, "A Soil Moisture Reflectance Model in Visible and Near IR Bands," *Proceedings of the International Symposium on Machine Processing of Remotely Sensed Data and Soil Information Systems and Remote Sensing and Soil Survey*, Purdue University, West Lafayette, IN, USA, June 3–6.

Pasolli, E., Prasad, S., Crawford, M. M., and Tilton, J. C., 2018, "Advances in Hyperspectral Image Classification Methods for Vegetation and Agricultural Cropland Studies," In *Hyperspectral Indices and Image Classifications for Agriculture and Vegetation*, P. S. Thenkabail, J. G. Lyon, and A. Huete, Eds., CRC Press, Boca Raton, FL, USA, pp. 67–104. doi:10.1201/9781315159331.

Philpot, W. D. and Tian, J., 2016, "The Hyperspectral Soil Line: A Preliminary Description," *Light, Energy, and the Environment*, OSA Technical Digest (Online), Optical Society of America, paper HW3E.2, 3 pgs.

Pierrottet, D., Amzajerdian, F., and Peri, F., 2005, "Development of an All-Fiber Coherent Laser Radar for Precision Range and Velocity Measurements," *Proceedings of the Materials Research Society Symposium*, Boston, MA, USA, November 28 – December 2005, Vol. 833. doi:10.1557/PROC-833-FF2.3

Pierrottet, D., Amzajerdian, F., Petway, L., Barnes, B., Lockard, G., and Rubio, M., 2008, "Linear FMCW Laser Radar for Precision Range and Vector Velocity Measurements," *Proceedings of the Materials Research Society Symposium*, San Francisco, CA, USA, March 24–28, Vol. 1076. doi:10.1557/PROC-1076-K04-06.

Pope, R. M. and Fry, E. S., 1997, "Absorption Spectrum (380-700 nm) of Pure Water. II. Integrating Cavity Measurements," *Appl. Optics*, Vol. 36, No. 33, pp. 8710-8723.

Prasad, N. S. and Geiger, A. R., 1996, "Remote Sensing of Propane and Methane by Means of a Differential Absorption Lidar by Topographic Reflection," *Opt. Eng.*, Vol. 35, No. 4, pp. 1105-1111.

Remsberg, E. E. and Gordley, L. L., "Analysis of Differential Absorption Lidar from the Space Shuttle," *Appl. Optics*, Vol. 17, No. 4, pp. 624-630.

Repasky, K. S. (Montana State University, Bozeman, Montana, USA). Personal Correspondence, July 19, 2016.

Rothman, L. S., Gordon, I. E., Babikov, Y., et al., 2013, "The HITRAN2012 Molecular Spectroscopic Database," *J. Quant. Spectrosc. Ra.*, Vol. 130, pp. 4-50. doi:10.1016/j.jqsrt.2013.07.002.

Sadeghi, M., Jones, S. B., and Philpot, W. D., 2015, "A Linear Physically-Based Model for Remote Sensing of Soil Moisture Using Short Wave Infrared Bands," *Remote Sens. Environ.*, Vol. 164, pp. 66-76. doi:10.1016/j.rse.2015.04.007.

Sakaizawa, D., Kawakami, S., Nakajima, M., Sawa, Y., and Matsueda, H., 2010, "Ground-Based Demonstration of CO_2 Remote Sensor using 1.57 μm Differential Laser Absorption Spectrometer with Direct Detection," *J. Appl. Remote Sens.*, Vol. 4, No. 1, 043548. doi:10.1117/1.3507092.

Salazar, S. E. and Coffman, R. A., 2019a, "Multi-Channel Optical Receiver for Ground-Based Topographic Hyperspectral Remote Sensing," *Remote Sens.*, Vol. 11, No. 5, 578. doi:10.3390/rs11050578.

Salazar, S. E. and Coffman, R. A., 2019b, "Preliminary Measurements from a Ground-Based Telescope-Assisted Hyperspectral Remote Sensor," *J. Appl. Remote Sens.* Submitted for Review. Manuscript Number: JARS 190527.

Salazar, S. E., Garner, C. D., and Coffman, R. A., 2019, "Development of a Multimode Field Deployable Lidar Instrument for Topographic Measurements of Unsaturated Soil Properties: Instrument Description," *Remote Sens.*, Vol. 11, No. 3, 289. doi:10.3390/rs11030289.

Savitzky, A. and Golay, M. J. E., 1964, "Smoothing and Differentiation of Data by Simplified Least Squares Procedures," *Anal. Chem.*, Vol. 36, pp. 1627–1639. doi:10.1021/ac60214a047.

Schaepman, M. E., Ustin, S. L., Plaza, A. J., Painter, T. H., Verrelst, J., and Liang, S., 2009, "Earth System Science Related Imaging Spectroscopy – An Assessment," *Remote Sens. Environ.*, Vol. 113, pp. S123–S137. doi:10.1016/j.rse.2009.03.001.

Schotland, R. M., 1966, "Some Observations of the Vertical Profile of Water Vapor by a Laser Optical Radar," *Proceedings of the Fourth Symposium on Remote Sensing of the Environment*, Ann Arbor, MI, USA, April 12–14, pp. 273-283.

Schotland, R. M., 1974, "Errors in the Lidar Measurement of Atmospheric Gases by Differential Absorption," *J. Appl. Meteorol.*, Vol. 13, pp. 71-77.

Shepherd, K. D. and Walsh, M. G., 2002, "Development of Reflectance Spectral Libraries for Characterization of Soil Properties," *Soil Sci. Soc. Am. J.*, Vol. 66, pp. 988-998.

Skolnik, M. I., 1960, "Theoretical Accuracy of Radar Measurements," *IRE T. Aeron. Navig. Electr.*, pp. 123-129. doi:10.1109/TANE3.1960.4201757.

Spuler, S. M., Repasky, K. S., Morley, B., Moen, D., Hayman, M., and Nehrir, A. R., 2015, "Field Deployable Diode-Laser-Based Differential Absorption Lidar (DIAL) for Profiling Water Vapor," *Atmos. Meas. Tech.*, Vol. 8, pp. 1073-1087.

Spuler, S., Repasky, K., Morley, B., Moen, D., Weckwerth, T., Hayman, M., and Nehrir, A., 2016, "Advances in Diode-Laser-Based Water Vapor Differential Absorption Lidar," *Proceedings of the 27th International Laser Radar Conference (ILRC 27)*, New York City, NY, USA, July 5–10. doi:10.1051/epjconf/201611902003.

Tanii, J., Kashimura, O., Ito, Y., and Iwasaki, A., 2017, "Flight Model of HISUI Hyperspectral Sensor Onboard ISS (International Space Station)," In *Sensors, Systems, and Next-Generation Satellites XXI*, SPIE Proceedings, Vol. 10423. doi:10.1117/12.2278169.

Thorlabs, 2014, *IO-5-850-HP Free-Space Isolator User Guide*, Rev. A, Thorlabs, Inc., Newton, NJ, USA.

Terzaghi, K., Peck, R., and Mesri, G., 1996, *Soil Mechanics in Engineering Practice*, 3rd ed., John Wiley and Sons, New York, NY, USA.

Tian, J. and Philpot, W. D., 2015, Relationship Between Surface Soil Water Content, Evaporation Rate, and Water Absorption Band Depths in SWIR Reflectance Spectra," *Remote Sens. Environ.*, Vol. 169, No. pp. 280-289.

Van der Meer, F. D., van der Werff, H. M. A., van Ruitenbeek, F. J. A., Hecker, C. A., Bakker, W. H., Noomen, M. F., van der Meijde, M., Carranza, E. J. M., Boudewijn de Smeth, J., and Woldai, T., 2012, "Multi- and Hyperspectral Geologic Remote Sensing: A Review," *Int. J. Appl. Earth Obs. Geoinf.*, Vol. 14, pp. 112–128. doi:10.1016/j.jag.2011.08.002.

Walvoort, A. and McBratney, A., 2001, "Diffuse Reflectance Spectrometry as a Proximal Sensing Tool for Precision Agriculture," *Proceedings of the 3rd European Conference on Precision Agriculture*, Montpellier, France, June 18–20, pp. 503-508.

Waruru, B. K., Shepherd, K. D., Ndegwa, G. M., Kamoni, P. T., and Sila, A. M., 2014, "Rapid Estimation of Soil Engineering Properties Using Diffuse Reflectance Near Infrared Spectroscopy," *Biosyst. Eng.*, Vol. 121, pp. 177-185. doi:10.1016/j.biosystemseng.2014.03.003.

Weckwerth, T. M., Weber, K. J., Turner, D. D., and Spuler, S. M., 2016, "Validation of a Water Vapor Micropulse Differential Absorption Lidar (DIAL)," *J. Atmos. Ocean. Tech.*, Vol. 33, No. 11, pp. 2353-2372.

Whalley, W. R., Leeds-Happison, P. B., and Bowman, G. E., 1991, "Estimation of Soil Moisture Using Near Infrared Reflectance," *Hydrol. Process.*, Vol. 5, pp. 321-327.

Whiting, M.L., 2009, "Measuring Surface Water in Soil with Light Reflectance," *Proc. SPIE*, Vol. 7454, 74540D, 11 pgs. doi:10.1117/12.826896.

Whiting, M. L., Li, L., and Ustin, S. L., 2004, "Predicting Water Content Using Gaussian Model On Soil Spectra," *Remote Sens. Environ.*, Vol. 89, No. 4, pp. 535-552.

Wirth, M., Fix, A., Mahnke, P., Schwarzer, H., Schrandt, F., and Ehret, G., 2009, “The Airborne Multi-Wavelength Water Vapor Differential Absorption Lidar WALES: System Design And Performance,” *Appl. Phys. B-Lasers O.*, Vol. 96, pp. 201-213. doi:10.1007/s00340-009-3365-7.

Wulf, H., Mulder, T., Schaepman, M. E., Keller, A., and Jörg, P. C., 2015, "Remote Sensing of Soils," Report prepared by the Remote Sensing Laboratories, Dept. of Geography, University of Zurich, Switzerland, 71 pgs. doi:10.5167/uzh-109992.

Wulfmeyer, V., 1998, "Ground-Based Differential Absorption Lidar for Water-Vapor and Temperature Profiling: Development and Specifications of a High-Performance Laser Transmitter," *Appl. Optics*, Vol. 37, No. 18, pp. 3804-3824.

Wulfmeyer, V. and Bösenberg, J., 1998, "Ground-Based Differential Absorption Lidar for Water-Vapor Profiling: Assessment of Accuracy, Resolution, and Meteorological Applications," *Appl. Optics*, Vol. 37, No. 18, pp. 3825-3844.

Wulfmeyer, V. and Walther, C., 2001, "Future Performance of Ground-Based and Airborne Water-Vapor Differential Absorption Lidar. I. Overview and Theory," *Appl. Optics*, Vol. 40, No. 30, pp. 5304-5320.

Xu, C., Zeng, W., Huang, J., Wu, J., and van Leeuwen, W. J. D., 2016, "Prediction of Soil Moisture Content and Soil Salt Concentration from Hyperspectral Laboratory and Field Data," *Remote Sens.*, Vol. 8, No. 42, 20 pgs. doi:10.3390/rs8010042.

Yitagesu, F. A., van der Meer, F., van der Werff, H., and Zigterman, W., 2009, “Quantifying Engineering Parameters of Expansive Soils from their Reflectance Spectra,” *Eng. Geol.*, Vol. 105, No. 3-4, pp. 151-160. doi:10.1016/j.enggeo.2009.01.004.

APPENDIX

APPENDIX A: MISCELLANEOUS COMPONENT DESIGN AND TESTING

A.1. Chapter Overview

Additional component design and testing methods, that were not provided in the preceding chapters, are presented herein. The transmitter components are discussed in Section A.2 and the receiver components are discussed in Section A.3. In addition to the information provided in this chapter, reference should be made to manufacturers' user manuals for each component for full specifications and safe handling and operation.

A.2. Transmitter Components

Details about the installation, calibration, and implementation of several of the key transmitter components is discussed in this section. Reference to manufacturer user manuals is made where appropriate. Furthermore, reference to additional data not explicitly contained within this chapter, or contained in the Appendices, is made where appropriate. In the following sections, laser safety precautions are paramount. Always wear protective goggles when working with equipment that has the potential to emit laser radiation.

Class 3B and 4 Lasers

Hazardous to eye and skin from direct viewing, specular, and diffuse reflections. Avoid direct eye or skin exposure. Laser eyewear protection required at all times. Maximum Permissible Exposure (MPE) depends on power, wavelength and exposure period.

Refer to the University of Arkansas Office of Environmental Health and Safety (EH&S) Laser Safety Manual. EH&S determines the MPE.

See also: ANSI Z136.1 - *Safe Use of Lasers (2014);* ANSI Z136.5 - *Safe Use of Lasers in Educational Institutions (2009);* ANSI Z136.6 - *Safe Use of Lasers Outdoors (2005)*.

A.2.1. *Laser Tuning*

The pair of New Focus TLB-6817 Vortex external cavity diode lasers (ECDL) were tuned to wavelength ranges centered at the desired on-line and off-line wavelengths by the manufacturer (Newport Corporation; Irvine, California, USA). Specifically, the on-line wavelength was tuned to 823.03nm to 823.35nm with a center wavelength (CWL) of 823.20nm, while the off-line wavelength was tuned to 846.84nm to 847.14nm with a CWL of 847.00nm. Fine-tuning of the lasing wavelength and of the output power was achieved by adjusting the current and the voltage supplied to the laser heads via the laser controllers, as depicted in Figure A.1. The full instructions for operation of the ECDL can be found in the *TLB-6800 Vortex Plus™ Laser System User's Manual* (New Focus 2014).

Figure A.1. Front panels of the model TLB-6800-LN tunable laser controllers displaying recommended current supply to the model TLB-6817 Vortex ECDL.

A.2.2. *Optical Isolation*

The free space laser beams required optical isolation to prevent back-reflections from entering and damaging each ECDL. Isolators were placed in the beam path immediately following transmission from each of the ECDL and the tapered optical semiconductor amplifier (TSOA). The isolators were Thorlabs IO-5-850-HP free-space, adjustable, narrowband, polarization-dependent Faraday isolators, except for the isolator following the 847.00 nm wavelength ECDL (Model Number TLB-6817-P) which already had a similar, factory-installed optical isolator mounted to the cavity output. All three isolators are depicted in Figure A.2.

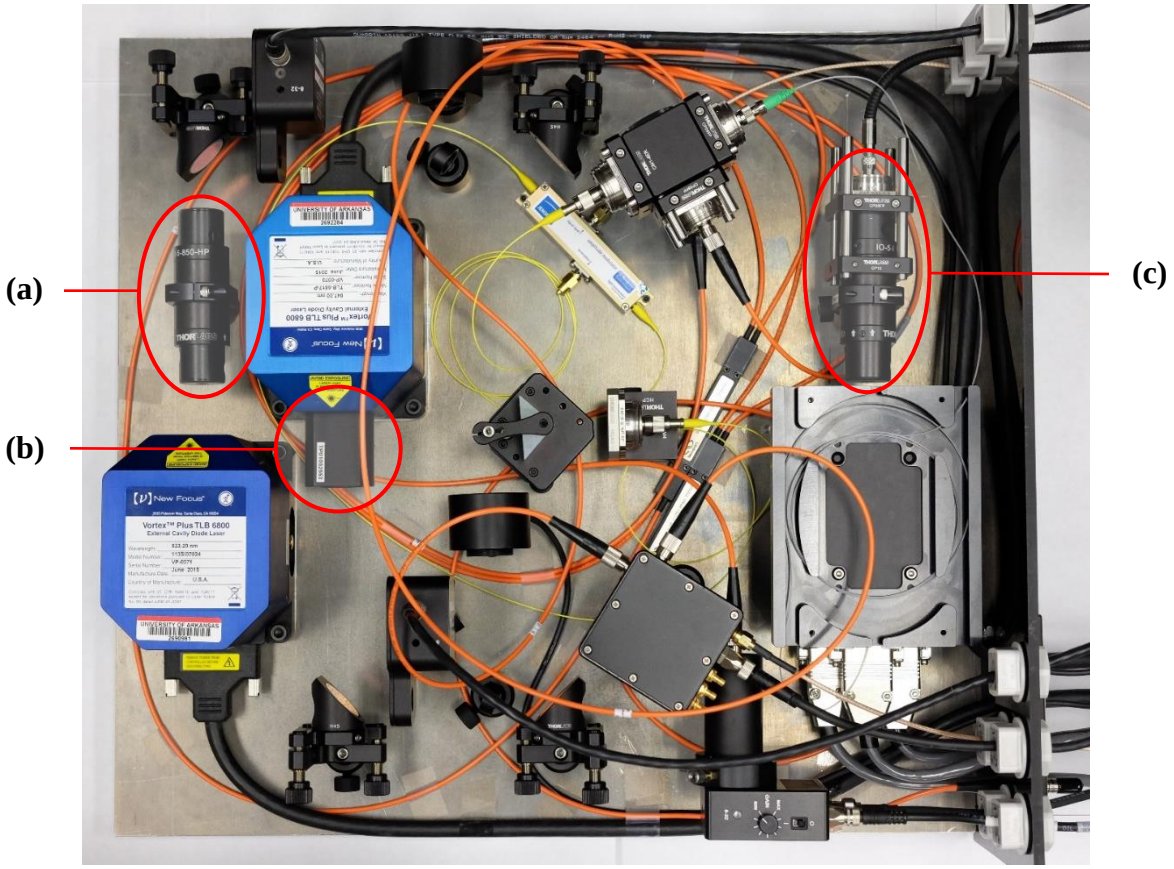

Figure A.2. Optical isolators protecting *(a)* the 823.00 nm ECDL, *(b)* the 847.00 nm ECDL, and *(c)* the TSOA.

The isolators were rated for operation in the 810 – 890 nm wavelength range (as presented in Figure A.3), but were tunable for center wavelengths between 835 nm and 865 nm. Each isolator was initially aligned (height and orientation) so that the free-space laser beams were centered through the 5-mm diameter aperture of each isolator. A Thorlabs S144C integrating sphere indium gallium arsenide (InGaAs) photodiode was used in conjunction with a Thorlabs PM100USB power meter to measure the transmission of the lasers through the isolators operating in the forward mode. For each isolator, the slip ring cap screw was loosened and the isolator was rotated until the power transmission was maximized, thereby aligning the input polarizer to the laser's plane of polarization. The screw was then tightened to lock the isolator position in place. Each isolator was then operated in the reverse mode for fine-tuning. The output polarizer setscrew was loosened and the polarizer was adjusted to minimize the transmission through the isolator.

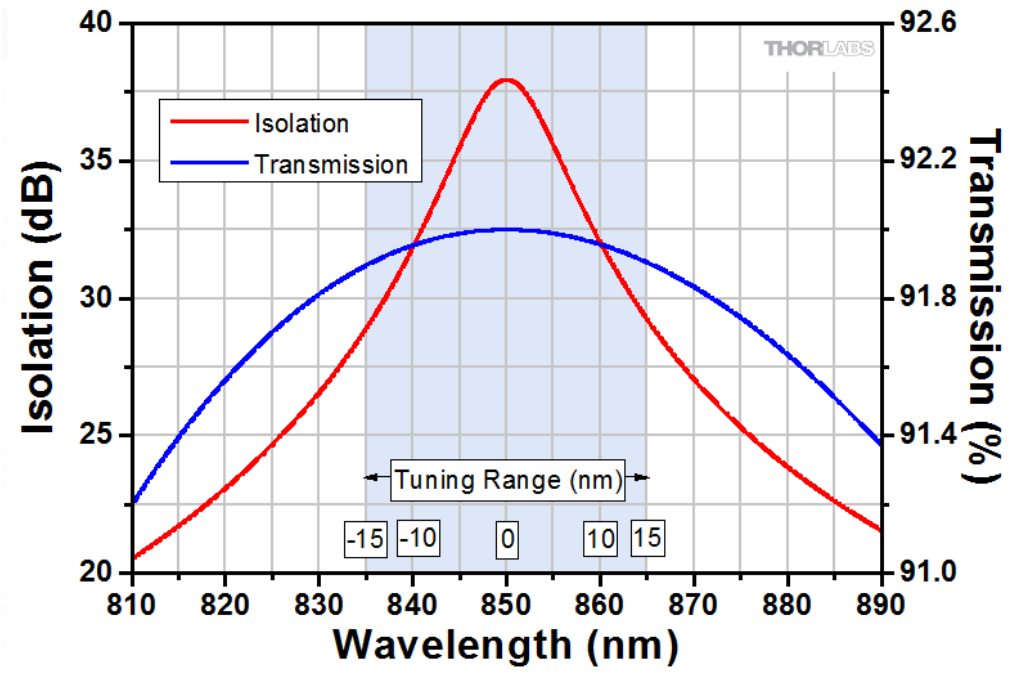

Figure A.3. Plot of optical isolation and transmission as functions of wavelength for the Thorlabs IO-5-850-HP optical isolator (from Thorlabs 2019).

The full instructions for optimization of the isolators are available in the *IO-5-850-HP Free-Space Isolator User Guide* (Thorlabs 2014). The factory-installed isolator for the 847.00 nm laser, depicted previously in Figure A.2(b), was fine-tuned by the manufacturer and was not further adjustable.

A.2.3 *Optical Amplification*

The transmitting laser wavelengths were amplified to enable detection for long-range targets. The modulated light was amplified with a Thorlabs TPA830P10-SP 14-pin butterfly package TSOA. A schematic of the TSOA is presented as Figure A.4. A larger, fully-dimensioned schematic of the amplifier is presented as Figure A.5.

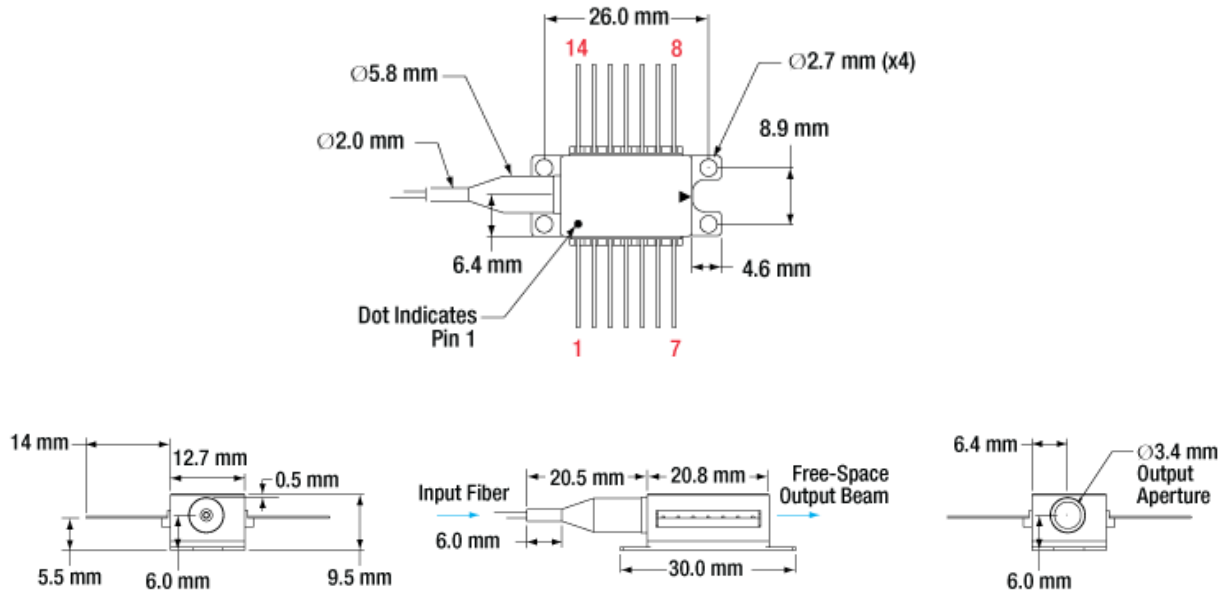

Figure A.4. Schematic of the Thorlabs TPA830P10-SP butterfly package tapered semiconductor optical amplifier with pin identification (from Thorlabs 2019).

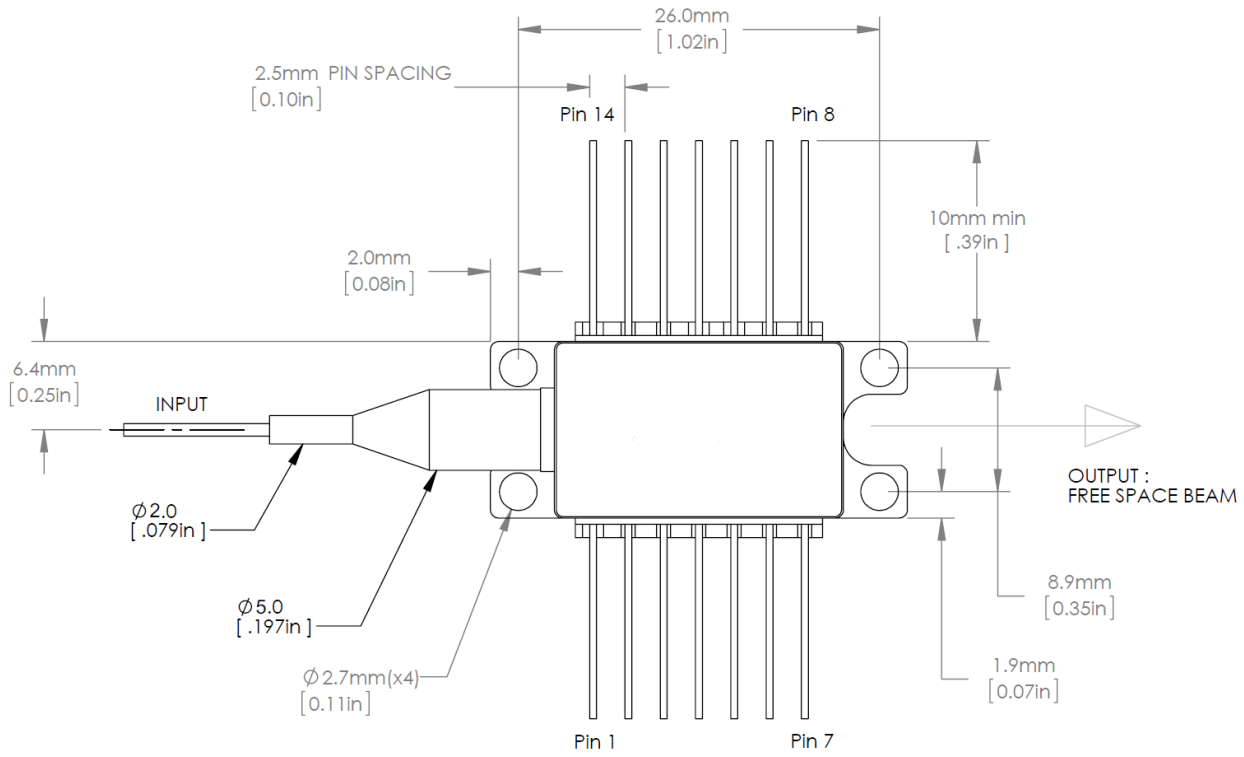

Figure A.5. Dimensioned schematic of the Thorlabs TPA830P10-SP butterfly package tapered semiconductor optical amplifier (modified from Thorlabs 2019).

The TSOA was mounted to a thermoelectric-cooled (TEC) Arroyo Instruments (San Luis Obispo, CA, USA) 205 TEC Butterfly LaserMount with the optional Fan Base for additional thermal regulation. The pins of the TSOA were mapped to correspond with the mount's internal wiring (as depicted in Figure A.6), laser controller, and TEC controllers, as presented in Tables A.1 and A.2. A photograph of the male plug and female socket for each connector type is presented in Figure A.7. Additionally, a fiber management tray and cover were installed to protect the TSOA during operation.

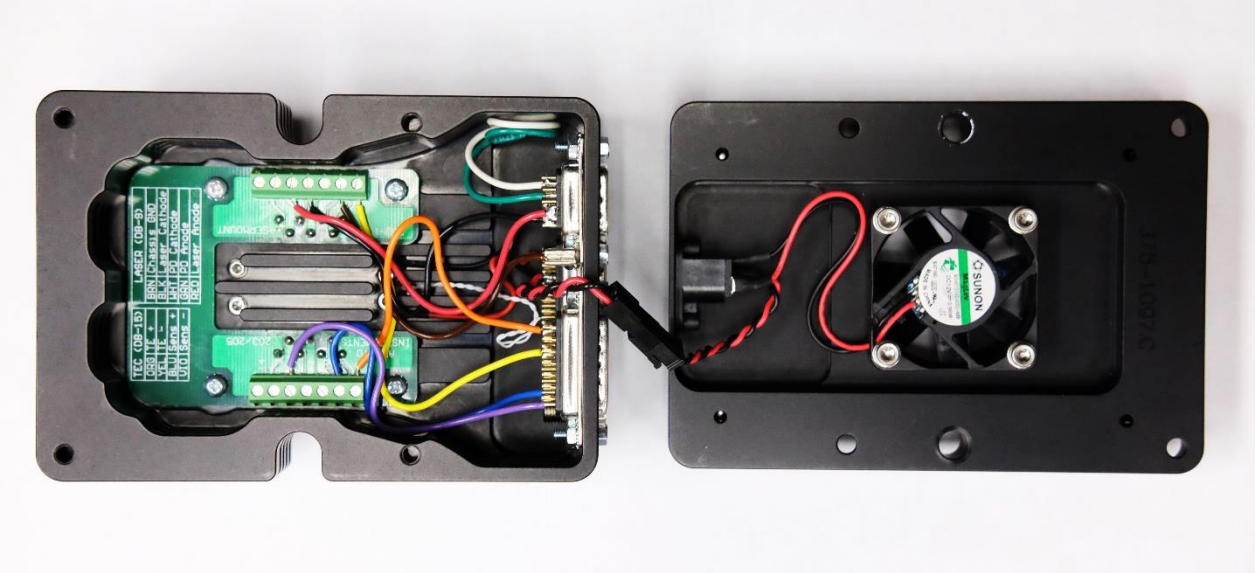

Figure A.6. View from open bottom of the butterfly package tapered amplifier mount (left) and open top of the optional fan base for additional thermal regulation (right).

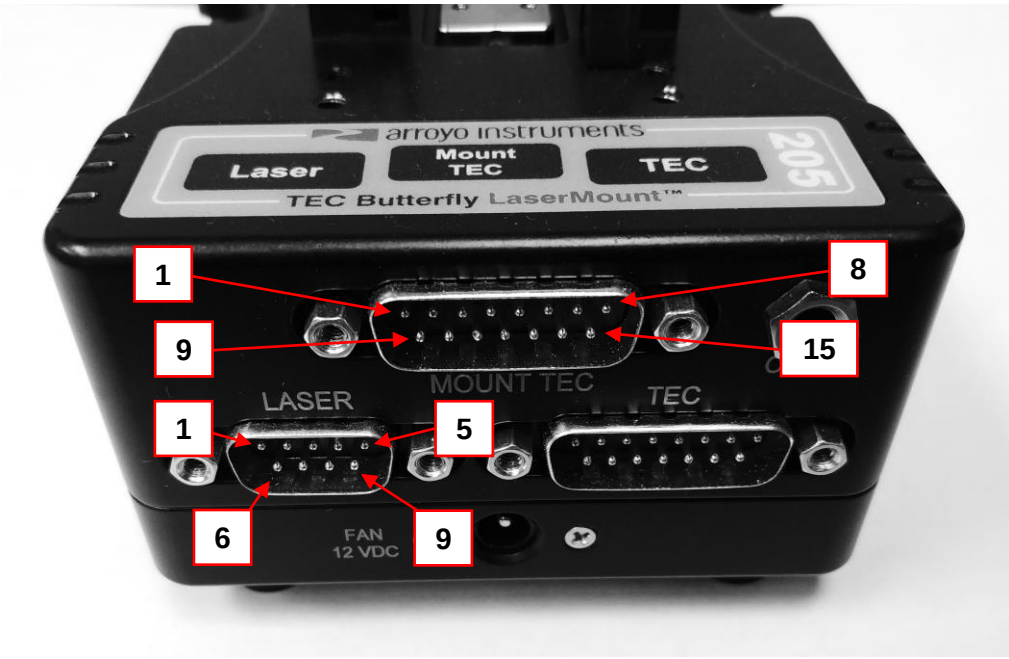

Figure A.7. Front panel of the tapered amplifier mount with labelled DB-9 connector and DB-15 connector male plugs for cables with corresponding female sockets.

Table A.1. Pin-wire-connector identification for the tapered semiconductor optical amplifier (TSOA), TSOA mount, TSOA controller, and thermoelectric-cooling (TEC).

TSOA Pin Identification	Corresponding Mount Pin-Outs	Wire Color	Description	LaserPak DB-9 Pin Identification	TECPak DB-15 Pin Identification
1	8	Orange	TEC +	-	1,2
2	9	Blue	Thermistor (Chip)	-	7
3	10	-	NC*	-	-
4	11	-	NC	-	-
5	12	Purple	Thermistor (Chip)	-	8
6	13	-	NC	-	-
7	14	-	NC	-	-
8	1	-	NC	-	-
9	2	-	NC	-	-
10	3	Red	TSOA Anode	8,9	-
11	4	Black	TSOA Cathode	4,5	-
12	5	-	NC	-	-
13	6	Brown	Case (Chassis Ground)	Shell	-
14	7	Yellow	TEC -	-	3,4
-	-	White	NC	6	-
-	-	Green	NC	7	-

Table A.2. Pin identification for the TECPak DB-15 connector for thermoelectric-cooling of the TSOA mount cold plate and fan base control.

Pin Identification	Wire Color	Description	Element
1,2	Red	TEC +	Cold Plate
3,4	Black	TEC -	
5,6	-	NC*	
7	White	Thermistor	Cold Plate
8	White	Thermistor	
9	-	NC	
10	-	NC	
11	Red	Fan +	Fan Base
12	Black	Fan -	
13	-	NC	
14	-	NC	
15	-	NC	

*NC = No Connection

A.2.4. *Alignment of the Bulk Optics*

The aluminum floor of the sealed transmitter box served as the optical bench for the components housed within the box as well as the heat sink for the ECDL and the Mach-Zehnder modulator. All components were mounted to the floor using tapped holes and screws and the majority of components were additionally mounted to height- and rotation-adjustable posts and post-holders. The bottom of each ECDL head was intimately affixed to the floor with thermal paste to enable the transfer of heat into the sink. Schematics of the drill patterns are presented in Figures A.8 and A.9.

The height-above-floor of each of the seed laser beams was 50.82mm. Accordingly, the posts, kinematic mirror mounts, and knife-edge mirror were adjusted in height and in rotation to direct the paths of each of the beams into the first fiber-coupling stage located near the center of the box, as depicted previously in Figure A.2. The optical isolator and fiber-coupling stage immediately following the TSOA were adjusted to match the amplified beam height of 66.40mm.

The free space path of each laser was directed into the fiber optic path using the bulk optical components. The free-space optical isolators (discussed previously in Section A.2.2) were placed in the laser path immediately following the ECDL to eliminate potentially damaging back-reflections. The dielectric mirrors were mounted to kinematic, 45-degree angled mirror mounts. The optomechanical shutters (Thorlabs SH05) and beam samplers (Thorlabs BSF05-B) were placed in the laser paths. The shutters provided a mechanical fail-safe for each of the beams, while the samplers picked off 1–10 percent of the beam to enable instantaneous laser power measurements with the pair of integrating spheres. To aid in co-alignment of the laser beams, one of the integrating spheres was used to measure the power before entering the first fiber-coupling stage, as depicted in Figures A.10 and A.11.

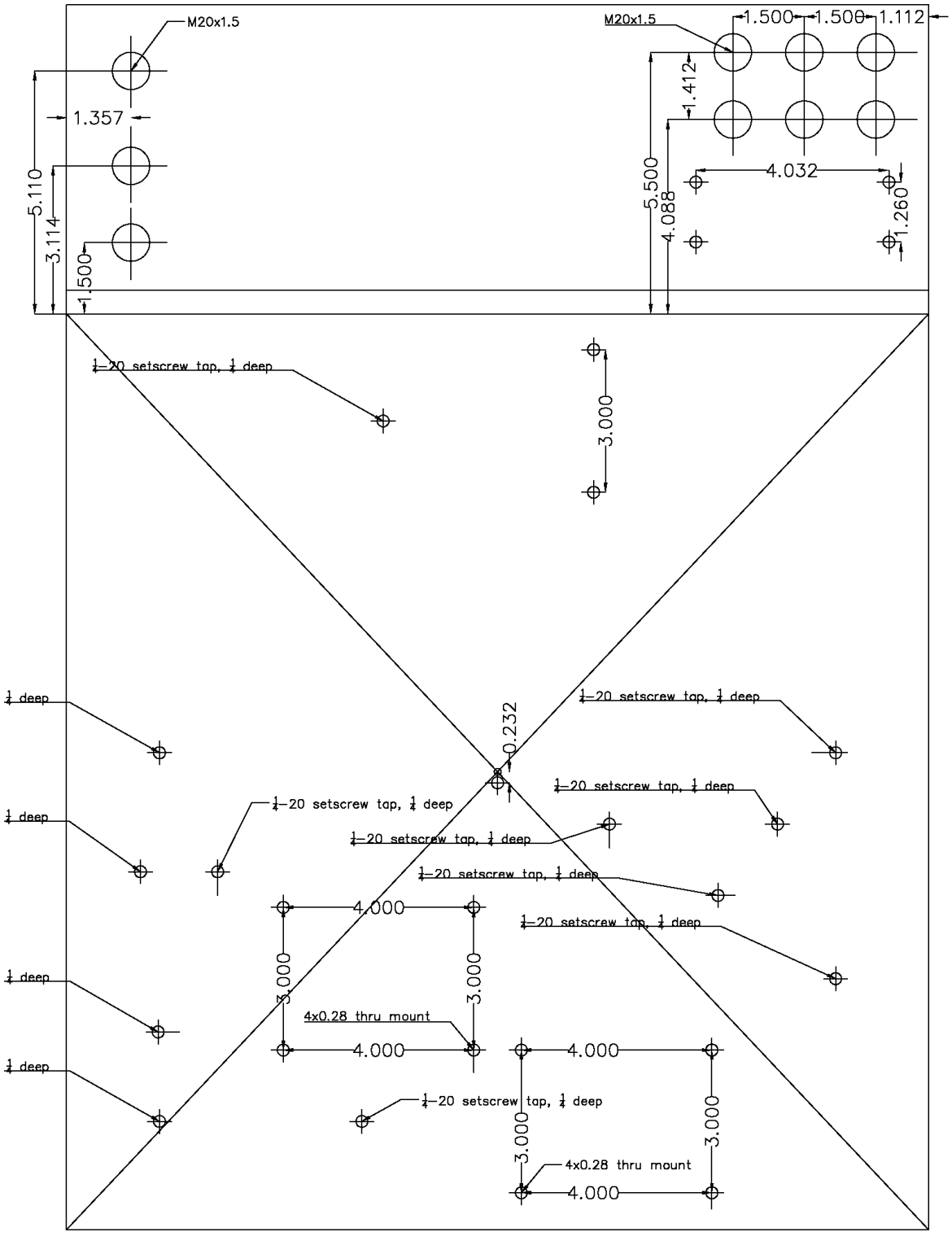

Figure A.8. Drill pattern for the box floor and wall with cable throughputs.

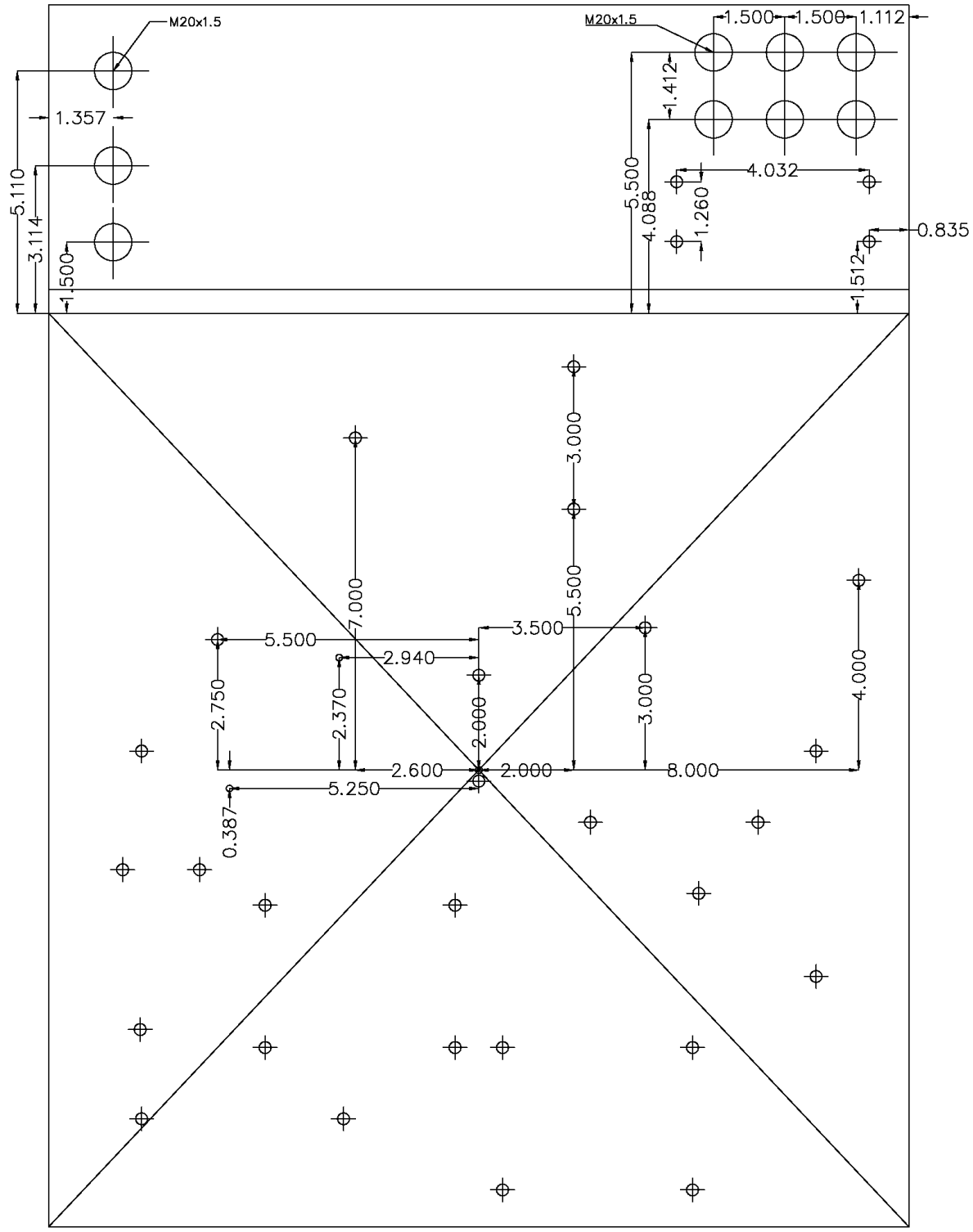

Figure A.9. Drill pattern for the box floor with additional mounting points.

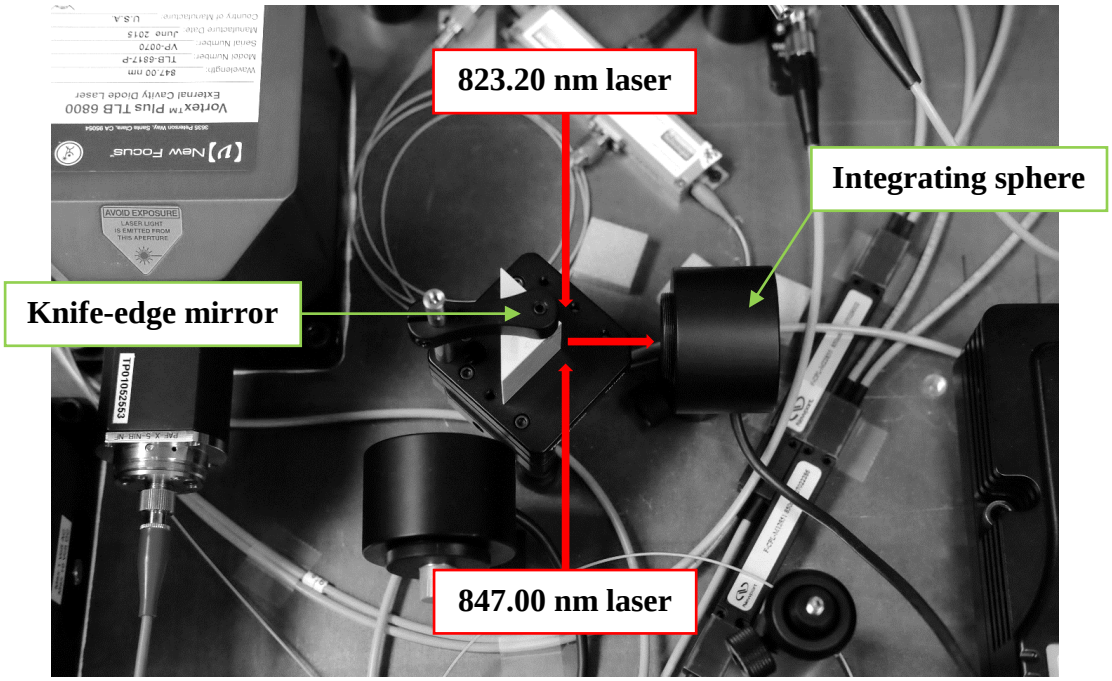

Figure A.10. Knife-edge mirror directing laser beams into a co-aligned laser path; pictured is the primary fiber-coupling stage replaced by an integrating sphere used to measure the laser power.

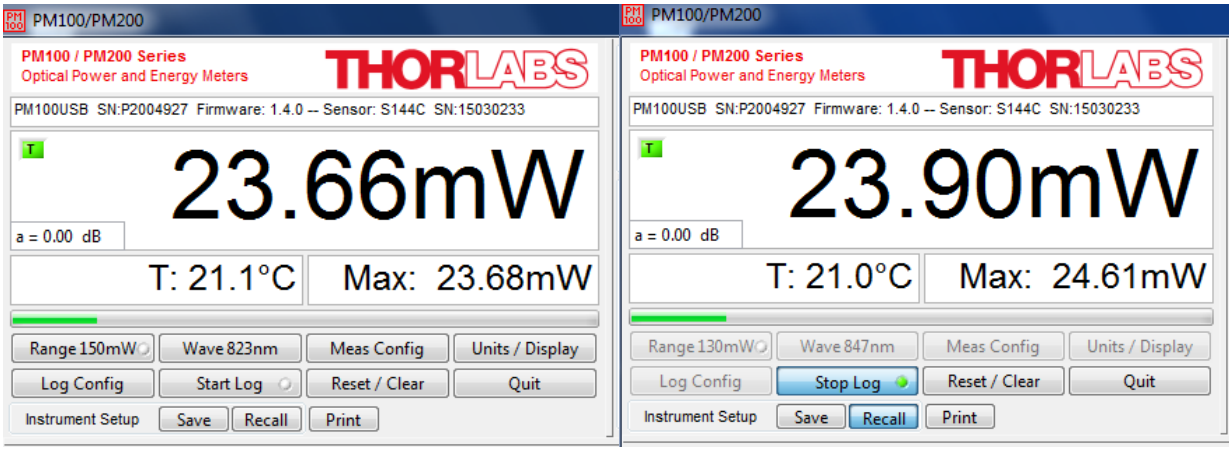

(a) **(b)**

Figure A.11. Screenshots displaying integrating sphere power measurements along the laser path after co-alignment, immediately following the knife-edge mirror for *(a)* the 823.20 nm laser and *(b)* the 847.00 nm laser.

A.3. Receiver Components

The multichannel optical receiver was designed to collect light from the receiving aperture (telescope) and direct the light into two separate receiving channels (the hyperspectral channel and the laser absorption spectrometry [LAS] measurements channel). The lenses mounted within the receiver were selected based on the form type (shape), focal length, and transmittance characteristics (coating type). To optimize detection of the online (823.20 nm) and offline (847.00 nm) backscattered signals, the common lenses (Thorlabs LB1471 field lens and Thorlabs LBF254-050 collimating lens) were optomechanically aligned for a CWL of 835 nm (mean wavelength between absorption lines). The field lens and the collimating lens were uncoated to allow maximum optical transmission from the ultraviolet to shortwave infrared range (350 – 2500 nm). Similarly, the focusing lenses in the hyperspectral channel were uncoated. The focal lengths were aligned for a CWL of 1425 nm (mean wavelength of receiver bandwidth). The focusing lenses in the LAS channel were coated for optimal light transmission in the spectral region of 650 – 1050 nm. Like the common lenses, the focal lengths were aligned to 835 nm.

The thick lens formula (Equation A.1 and Equation A.2) was utilized to calculate the focal lengths for the field and collimating lenses (bi-convex and best form spherical lens shapes, respectively) and for the focusing lenses for the LAS receiver channel (achromatic doublet lenses). The aspheric lens equation (Equation A.3) was used in conjunction with the values presented in Table A.3 for the uncoated aspheres used for the hyperspectral channel. Each of the lens shapes are represented by schematics in Figure A.12.

$$\frac{1}{f} = (n-1)\cdot\left[\frac{1}{R_1} - \frac{1}{R_2} + \frac{t_c\cdot(n-1)}{n\cdot R_1\cdot R_2}\right] \qquad \text{Morgan (1953)} \qquad \text{Equation A.1}$$

$$h_1 = -\frac{t_c \cdot f \cdot (n-1)}{R_2 \cdot n} \qquad h_2 = -\frac{t_c \cdot f \cdot (n-1)}{R_1 \cdot n}$$ Morgan (1953) Equation A.2

$$z = \frac{Y^2}{R \cdot \left(1 + \sqrt{1-(1+k)\cdot \frac{Y^2}{R^2}}\right)} + A_4 \cdot Y^4 + A_6 \cdot Y^6 + \cdots + A_n \cdot Y^n + \cdots + A_{16} \cdot Y^{16}$$ Equation A.3

In Equation A.1, f is the focal length of the lens, n is the index of refraction of the lens material, R_1 and R_2 are the radii of curvature of the first and second surfaces of the lens, respectively, and t_c is the center thickness of the lens. In Equation A.2, h_1 and h_2 are the principal plane distances. In Equation A.3, z is the sag (surface profile), Y is the radial distance from the optical axis, k is the conic constant, and A_n is the n^{th} order aspheric coefficient. Lens data from Thorlabs (2019).

Table A.3. Constants for the uncoated aspherical lenses.

	Thorlabs AL108*		**Thorlabs AL1512†**	
Constant	Side 1	Side 2	Side 1	Side 2
R	6.215 mm	Plano	9.32 mm	Plano
k	-1	-	-1	-
A_4	2.0059414×10^{-4}	-	5.7598697×10^{-5}	-
A_6	$-1.0498431 \times 10^{-7}$	-	-2.503422×10^{-8}	-
A_8	$-1.1263556 \times 10^{-8}$	-	$-6.7519988 \times 10^{-10}$	-
A_{10}	$-1.0201221 \times 10^{-10}$	-	$-2.0018474 \times 10^{-12}$	-
A_{12}	$8.4002262 \times 10^{-13}$	-	$3.8684828 \times 10^{-15}$	-
A_{14}	$4.6362363 \times 10^{-15}$	-	$1.2447477 \times 10^{-16}$	-
A_{16}	$1.2062946 \times 10^{-16}$	-	$-3.659331 \times 10^{-19}$	-

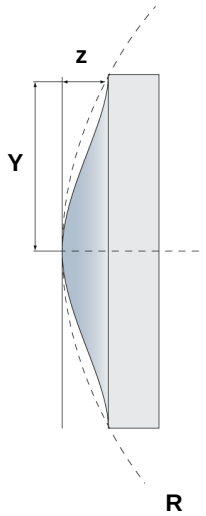

** **AL108** – Precision asphere: 10mm diameter; uncoated S-LAH64 substrate; EFL = 8mm; NA = 0.55; clear aperture (collimation, aspheric side = 9mm; focusing, plano side = 7.7mm).*
*† **AL1512** – Precision asphere: 15mm diameter; uncoated S-LAH64 substrate; EFL = 12mm; NA =0.55; clear aperture (collimation, aspheric side =13.5mm; focusing, plano side = 11.7mm).*

The index of refraction of the N-BK7 lens material (used in the lens equation) was calculated based on the design wavelengths (Figure A.13). The transmission efficiency of the light that was focused through the lenses was calculated based on data presented in Figure A.14. The remaining aspheric (Thorlabs AL108 and Thorlabs AL1512) and achromatic doublet lenses

(Thorlabs AC080-10-B and AC127-050-B) were designed using data presented in Figures A.15 through Figure A.24. An adjustable iris diaphragm (Thorlabs SM1D25) functioned as the field stop for the receiver aperture and was located immediately behind the field lens. The aperture diameter range was manually adjustable from 0.8 mm to 25.0 mm.

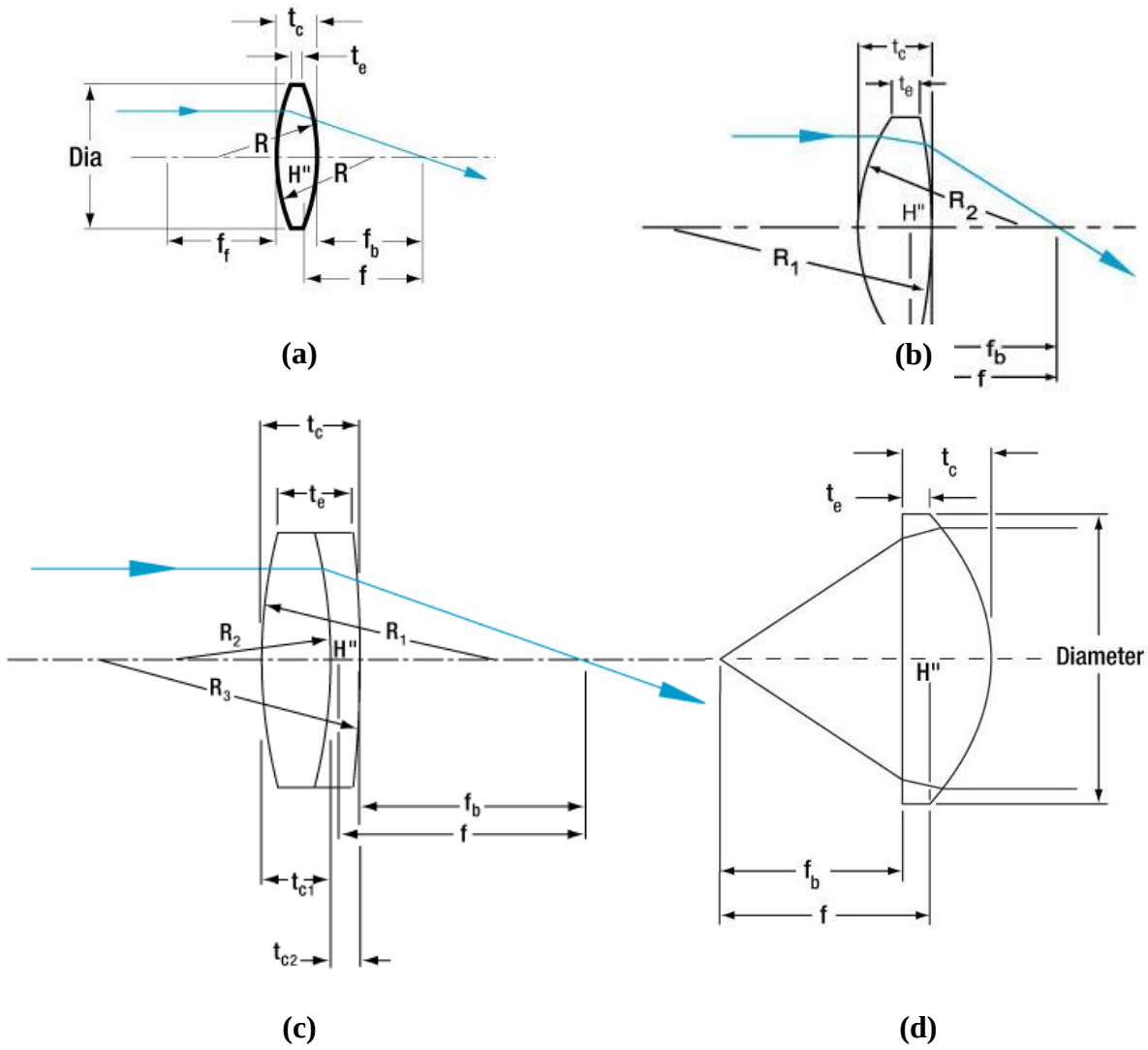

Key: Dia = Diameter; t_c = Center Thickness; t_e = Edge Thickness; R = Radius of Curvature; H'' = Back Principal Plane; f = Focal Length; f_f = Front Focal Length; f_b = Back Focal Length; z = Sag (Surface Profile); Y = Radial Distance from Optical Axis. **Note:** All figures assume Cartesian sign convention.

Figure A.12. Ray diagram for *(a)* bi-convex, *(b)* best form spherical, *(c)* positive achromatic doublet, and *(d)* aspheric lens shapes (modified from Thorlabs 2019).

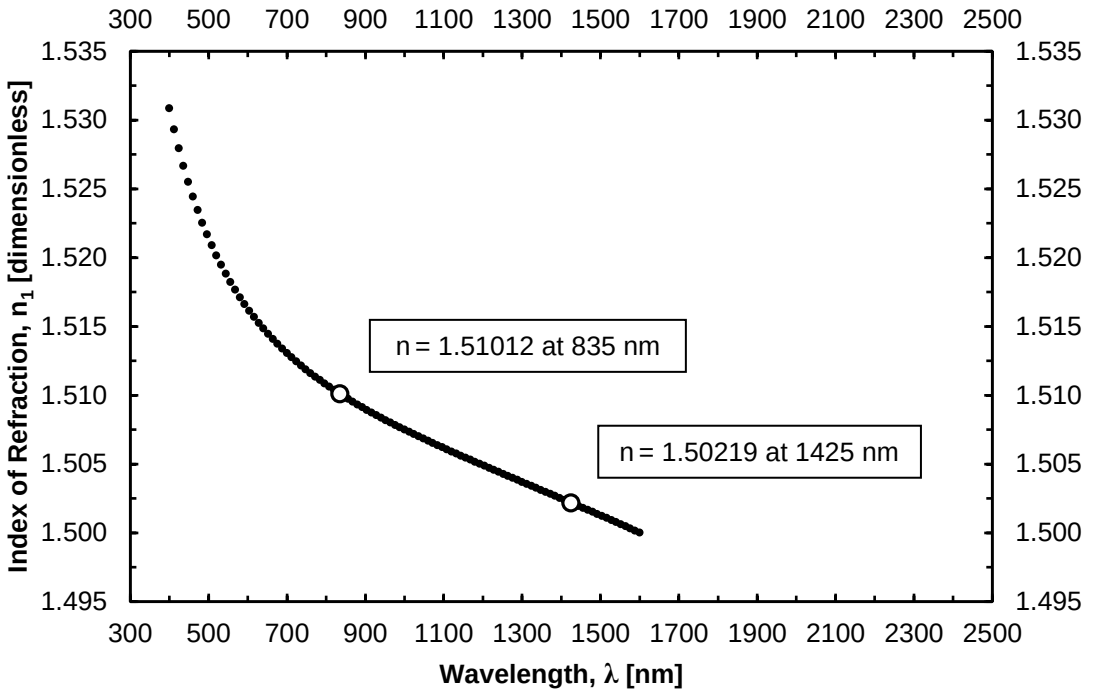

Figure A.13. Index of refraction as a function of wavelength of light for N-BK7 lens substrate (raw data from Thorlabs 2019).

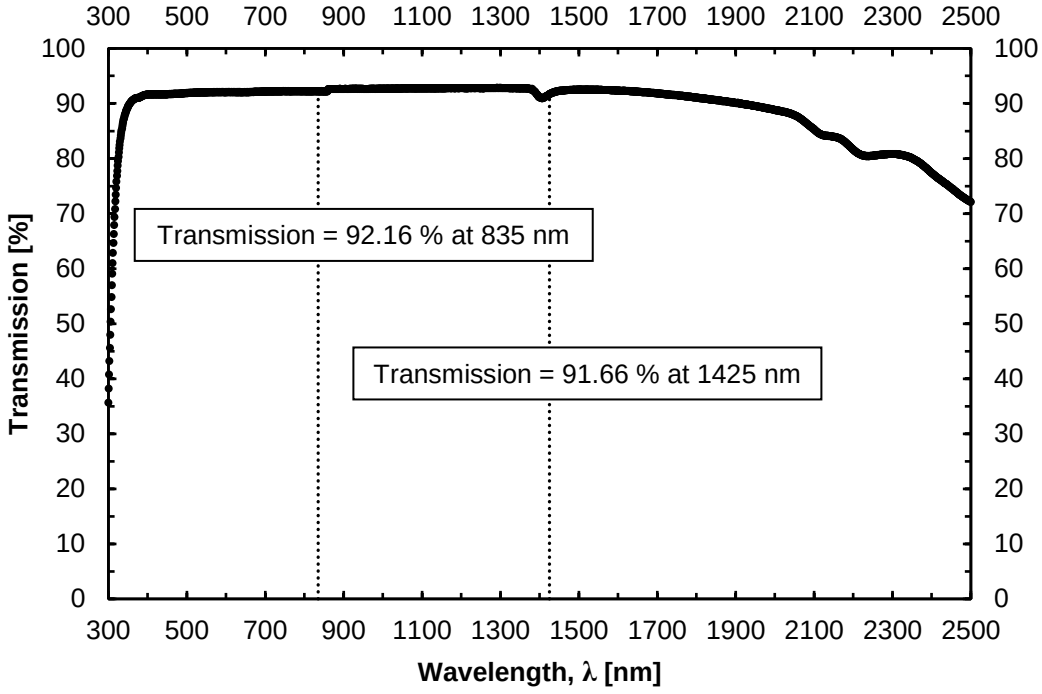

Figure A.14. Light transmission as a function of wavelength for uncoated N-BK7 lens substrate (10 mm thick sample; raw data from Thorlabs 2019).

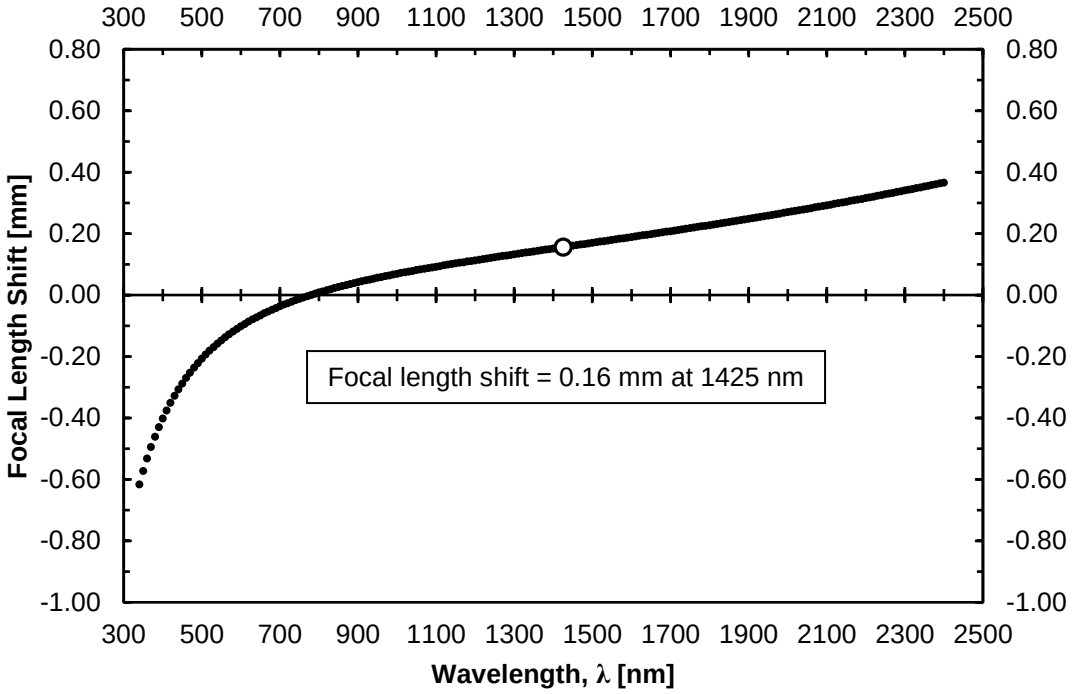

Figure A.15. Focal length shift as a function of wavelength for uncoated AL108 lens S-LAH64 substrate (raw data from Thorlabs).

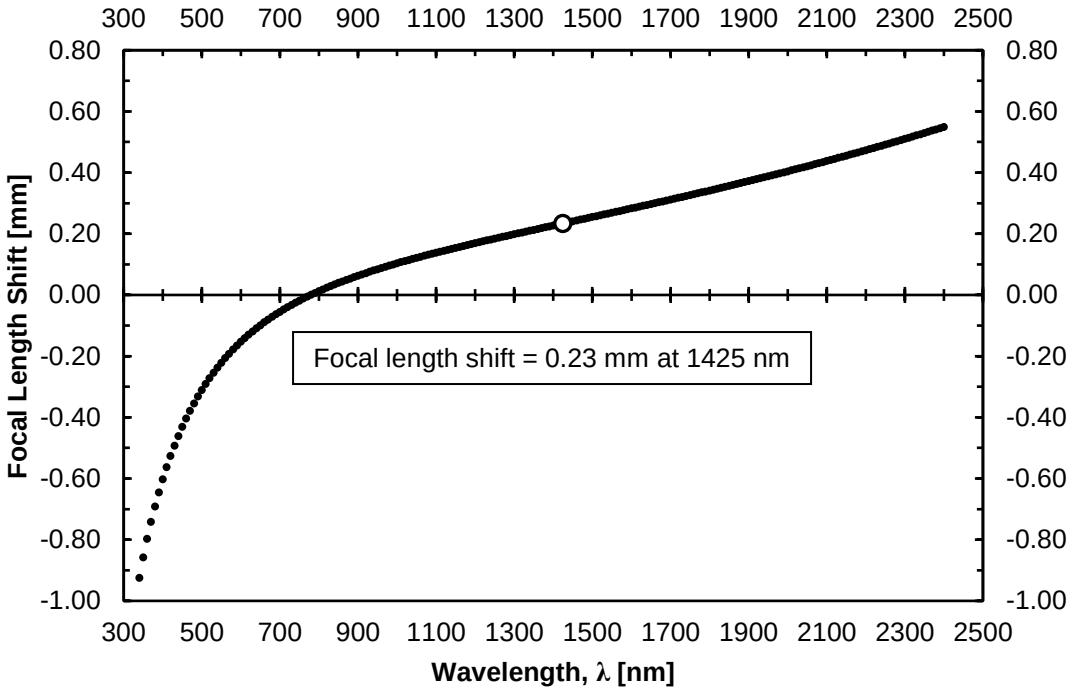

Figure A.16. Focal length shift as a function of wavelength for uncoated AL1512 lens S-LAH64 substrate (raw data from Thorlabs).

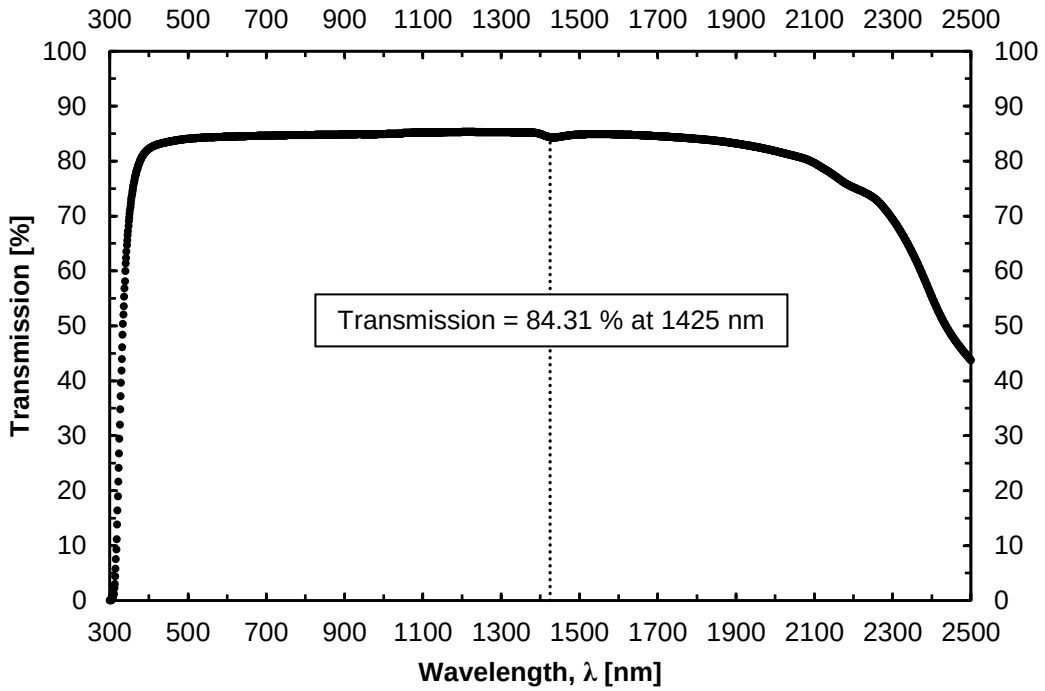

Figure A.17. Light transmission as a function of wavelength for uncoated S-LAH64 lens substrate (10 mm thick sample; raw data from Thorlabs).

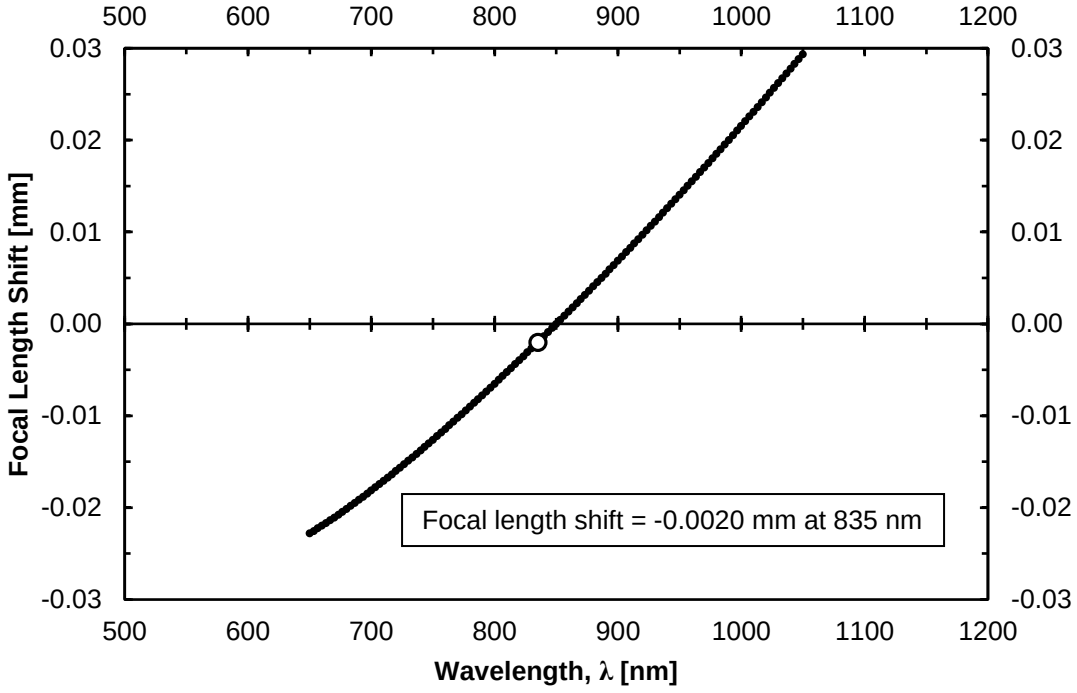

Figure A.18. Focal length shift as a function of wavelength for near-infrared coated AC080-010-B lens N-LAK22/N-SF6HT substrate (raw data from Thorlabs).

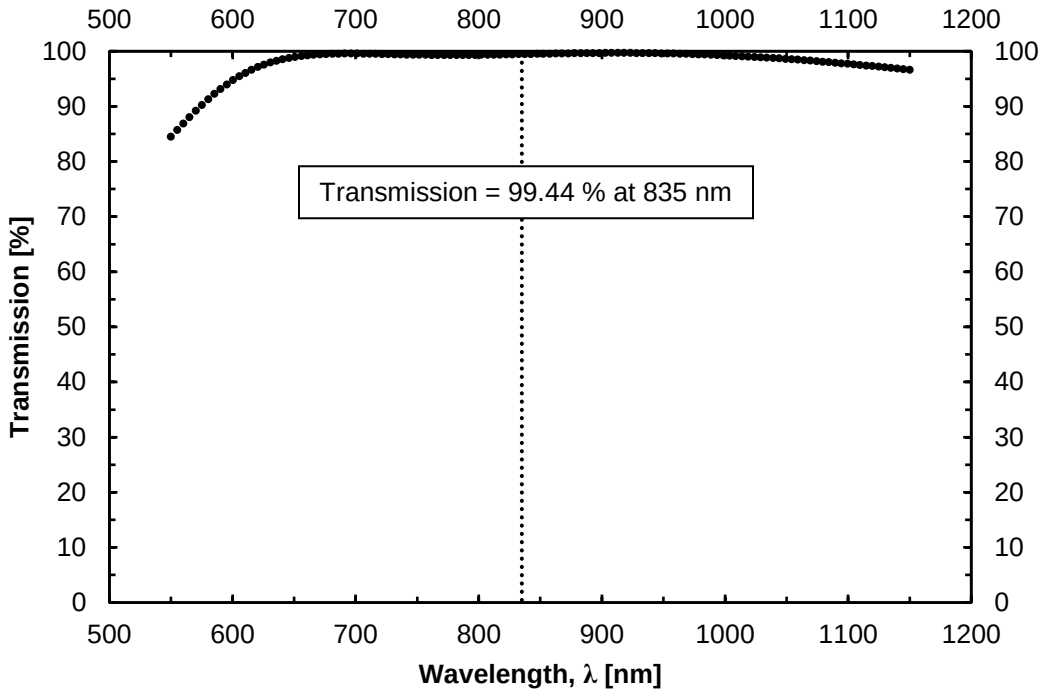

Figure A.19. Light transmission as a function of wavelength for near-infrared coated AC080-010-B lens N-LAK22/N-SF6HT substrate (raw data from Thorlabs).

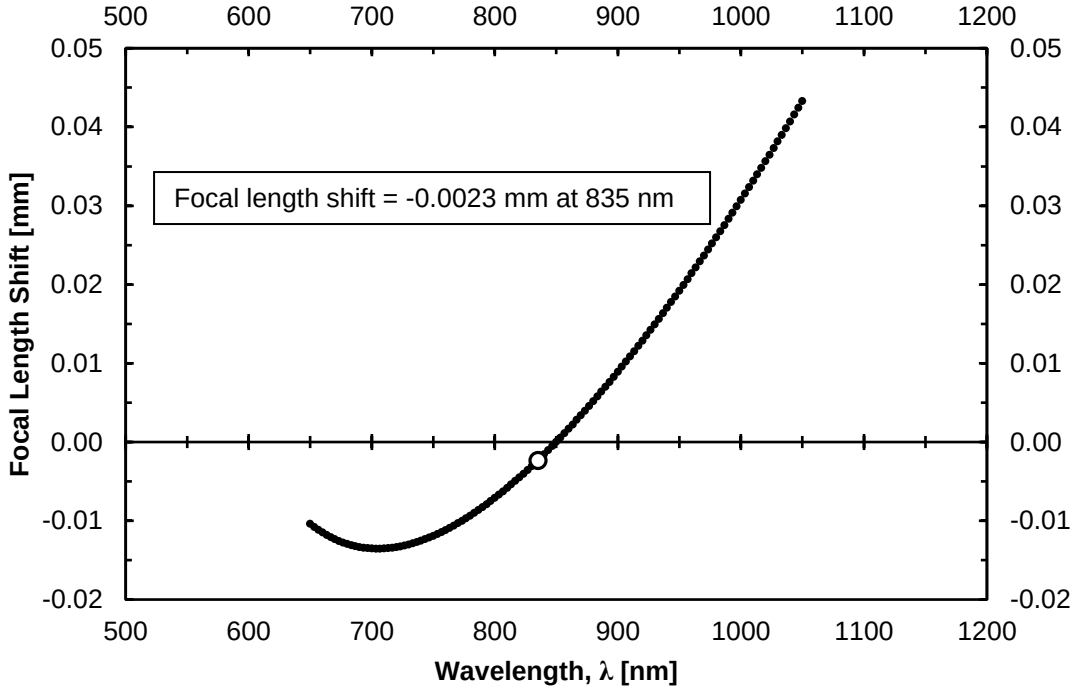

Figure A.20. Focal length shift as a function of wavelength for near-infrared coated AC127-025-B lens (raw data from Thorlabs).

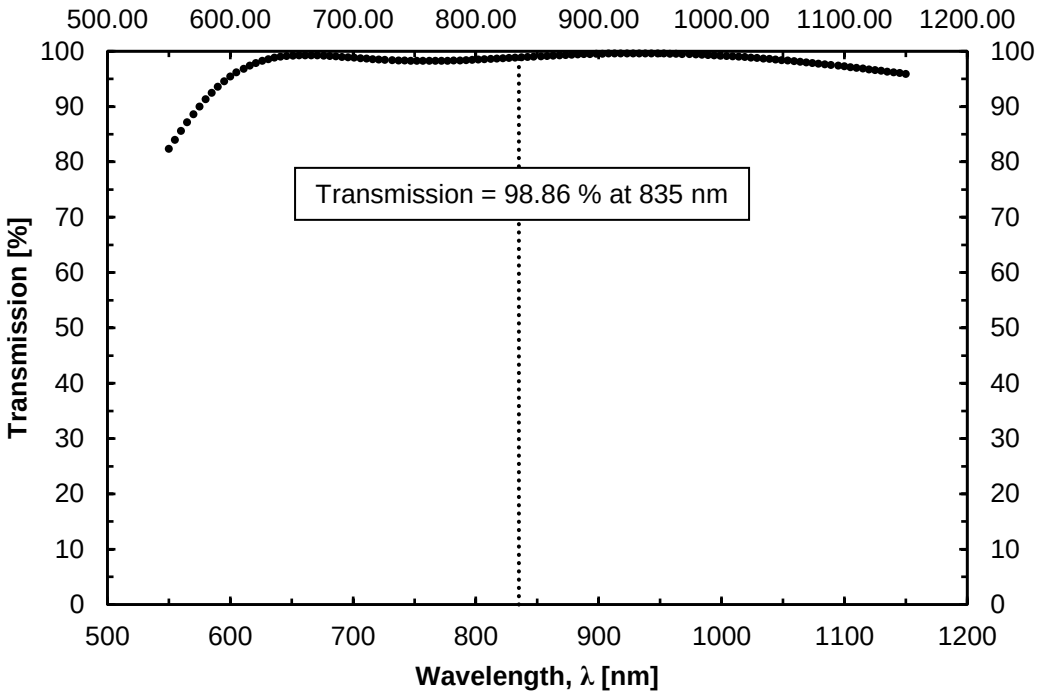

Figure A.21. Light transmission as a function of wavelength for near-infrared coated AC127-025-B lens N-LAK22/N-SF6HT substrate (raw data from Thorlabs).

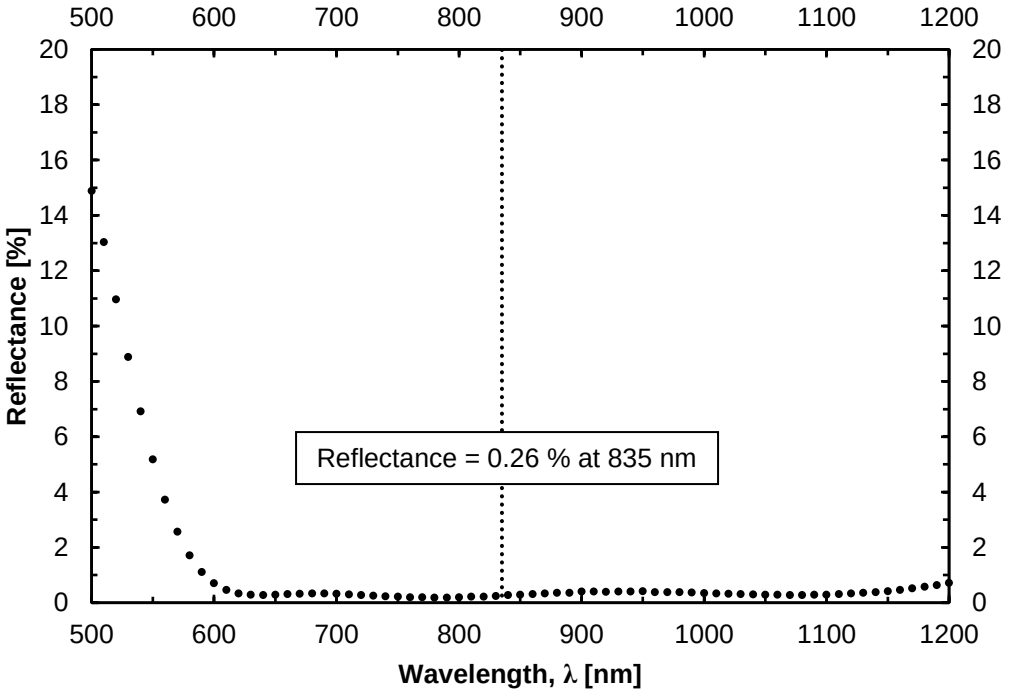

Figure A.22. Light reflectance as a function of wavelength for broadband near-infrared anti-reflective coating (raw data from Thorlabs).

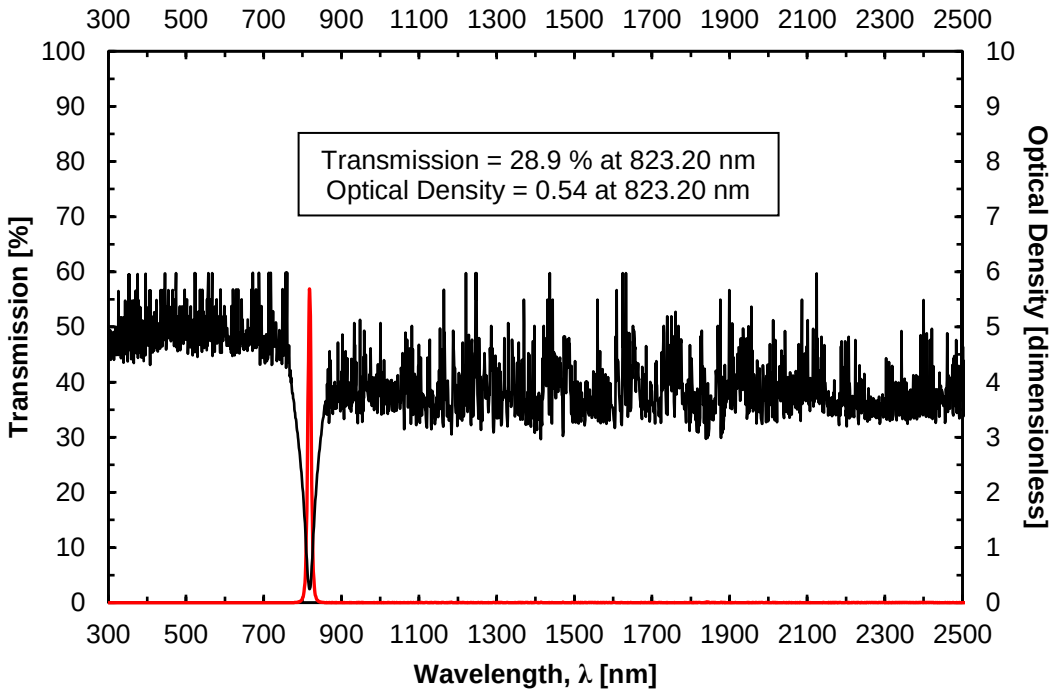

Figure A.23. Light transmission and optical density as functions of wavelength for FB820-10 narrow bandpass filter (raw data from Thorlabs).

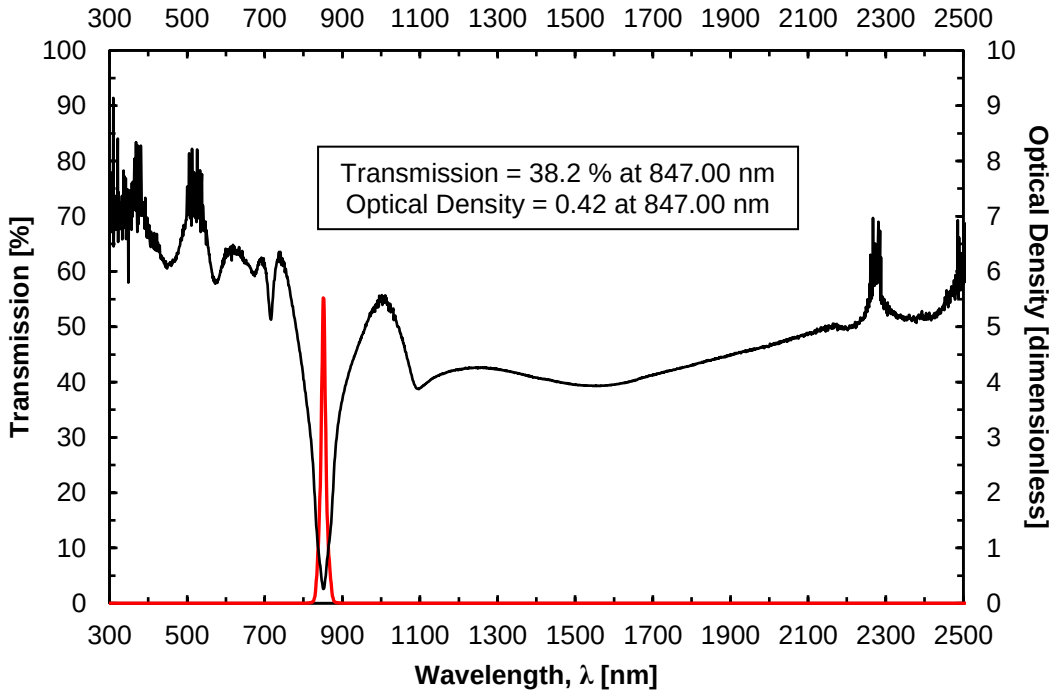

Figure A.24. Light transmission and optical density as functions of wavelength for FB850-10 narrow bandpass filter (raw data from Thorlabs).

A.4. References

Morgan, J., 1953, *Introduction to Geometrical and Physical Optics*, 1st ed., McGraw-Hill, New York, NY, USA.

New Focus, 2014, *TLB-6800 Vortex Plus™ Laser System User's Manual*, Rev. A, New Focus, Santa Clara, CA, USA.

Thorlabs, 2014, *IO-5-850-HP Free-Space Isolator User Guide*, Rev. A, Thorlabs, Inc., Newton, NJ, USA.

APPENDIX B: SENSITIVITY TESTING AND NOISE CHARACTERIZATION

B.1. Chapter Overview

Additional testing results and supplemental data, not presented in the preceding chapters, are provided herein. The SOLAS telescope-assisted hyperspectral receiver was tested in indoor and outdoor environments to observe the sensitivity of measurements to several factors, including the range to the target, spectra acquisition sample size, illumination and incidence angles, and long-path atmospheric absorption, as presented in Sections B.2 and B.3. The signal noise is also characterized for the aforementioned measurements and is described in Section B.4.

B.2. Sensitivity Testing of the SOLAS Hyperspectral Receiver

The SOLAS instrument receiver was tested indoors at the Engineering Research Center (ENRC) in an indoor hallway that was approximately 120 meters in length. To determine the effect of various factors on the measured spectra, each factors was controlled and independently studied for comparison. The factors included range, spectra sample size, target specimen orientation, observation and illumination incidence angles, and time periods between instrument recalibration to study the drift in collected data. The testing was performed primarily with the 25 cm by 25 cm (625 cm^2) square Spectralon® reference panel. Some of the tests were also performed with an air-dry Ottawa sand specimen that was 25 cm in diameter (491 cm^2), though for all of the tests, the diameter of the receiver field of view was less than the diameter of the target.

The factors that were studied are outlined in the matrices below and Table B.1 contains a summary of the tests that were performed. The data were processed according to the procedures outlined in Section 4.6 and Section 5.6. The resulting spectra were plotted in the reflectance as a function of wavelength domain and are included as Figures B.1 – B.12.

$Range(m)\begin{bmatrix}20\\50\\100\end{bmatrix}$ $Sample\ size(spectra)\begin{bmatrix}10\\25\end{bmatrix}$

$Specimen\ orientation(deg.)\begin{bmatrix}0\\90\end{bmatrix}$ $Instrument\ drift\ period(min.)\begin{bmatrix}0\\15\\30\end{bmatrix}$

$Observation\ incidence\ angle(deg.)\begin{bmatrix}35\\70\end{bmatrix}$ $Illumination\ incidence\ angle(deg.)\begin{bmatrix}20\\90\end{bmatrix}$

Table B.1. Summary of tests performed to study the influence of various factors on the data measured with the SOLAS instrument hyperspectral receiver.

Acquisition Number	Target	Range (m)	Incidence Angle (Degrees)	Illumination Angle (Degrees)	Field of View Diameter (cm)
1	Spectralon	20	35	90	0.64 (VNIR) 1.2 (SWIR)
2	Spectralon				
3	Spectralon				
4	Spectralon				
5	Ottawa Sand				
6	Ottawa Sand				
7	Spectralon			20	
8	Spectralon		70		
9	Spectralon			90	
10	Ottawa Sand				
11	Spectralon	50	35	90	1.6 (VNIR) 3.1 (SWIR)
12	Ottawa Sand				
13	Ottawa Sand				
14	Ottawa Sand				
15	Spectralon		70		
16	Spectralon	100	35	90	3.2 (VNIR) 6.1 (SWIR)
17	Spectralon		70		

Based on the collected spectra, the following preliminary conclusions were made. There was no significant difference in the spectral noise between a set of 10 averaged spectra and a set of 25 averaged spectra (the number of spectra collected is different than the number of averages collected – an adjustable parameter in the instrument settings accessible in the data acquisition software). The set of 10 and set of 25 averaged spectra contained similar noise, as illustrated by

the statistical metrics included in Figure B.1. It is recommended that future data collection campaigns continue to collect 10 spectra (to be averaged) to minimize collection time.

The illumination angle did not have a significant effect on the collected spectra. As presented by the metric in Figure B.2, the oblique illumination condition (approx. 20-degree incident angle) was similar in noise to the perpendicular illumination condition (approx. 90-degree incident angle). Although further study on soil specimens is required, it is recommended for future laboratory-based data collection that the specimens are illuminated directly (perpendicular) using a full-spectrum halogen lamp. For outdoor measurements and field campaigns, it is recommended that data be collected under high (noon) sun conditions, while careful attention must also be paid to any shadows cast by the terrain or clouds. Solar illumination conditions other than noon sun may also be considered, if reference calibrations are performed routinely and after any changes in atmospheric conditions occur.

As presented in Figure B.3, the (rotational) orientation of a specimen had no significant effect on the collected spectra. It is expected that specimens with a larger average grain size than the Ottawa sand that was tested, would have a greater surface roughness and may therefore be more affected by specimen orientation. An increase in the range (distance between target and receiver) resulted in an increase in the average amplitude of the reflectance measurements for the Ottawa sand specimen, as illustrated by Figure B.4. This finding is inconsistent with the results collected previously. It is hypothesized that the effect was caused by a difference in the focal spot on the specimen or a poorly calibrated measurement. Similarly, the spectra contained in Figures B.11 and B.12 appear to be affected by poor focusing on the target. The effect of range on measured spectra requires further study in both laboratory and field settings.

The drift in the data collected with the instrument over periods of 15 and 30 minutes (between reference calibrations) is presented in Figures B.5 and B.6. The drift was insignificant for the Spectralon panel but was significant for the Ottawa sand specimen. Further study is required. As presented in Figures B.7 and B.8, an increase in the observation angle incident on the target (reference panel) resulted in a slight increase in the magnitude of the reflectance spectrum. This was also observed for the Ottawa sand specimen, as presented in Figure B.10; however, the Spectralon panel measurements should not be considered significant alone, due to the intense scattering properties of the panel. The Ottawa sand specimen better represents the effect of target incidence angle. As demonstrated by Figure B.9, the reference panel spectrum, measured at a range of 100 meters, was heavily affected in the two SWIR channels (>1000 nm) of the receiver instrument by the change in incidence angle. It is hypothesized that the spot was not centered on the panel, causing the larger SWIR field of view to be affected while the VNIR field of view was largely unaffected. This hypothesis is further supported by the spectra contained in Figures B.11 and B.12.

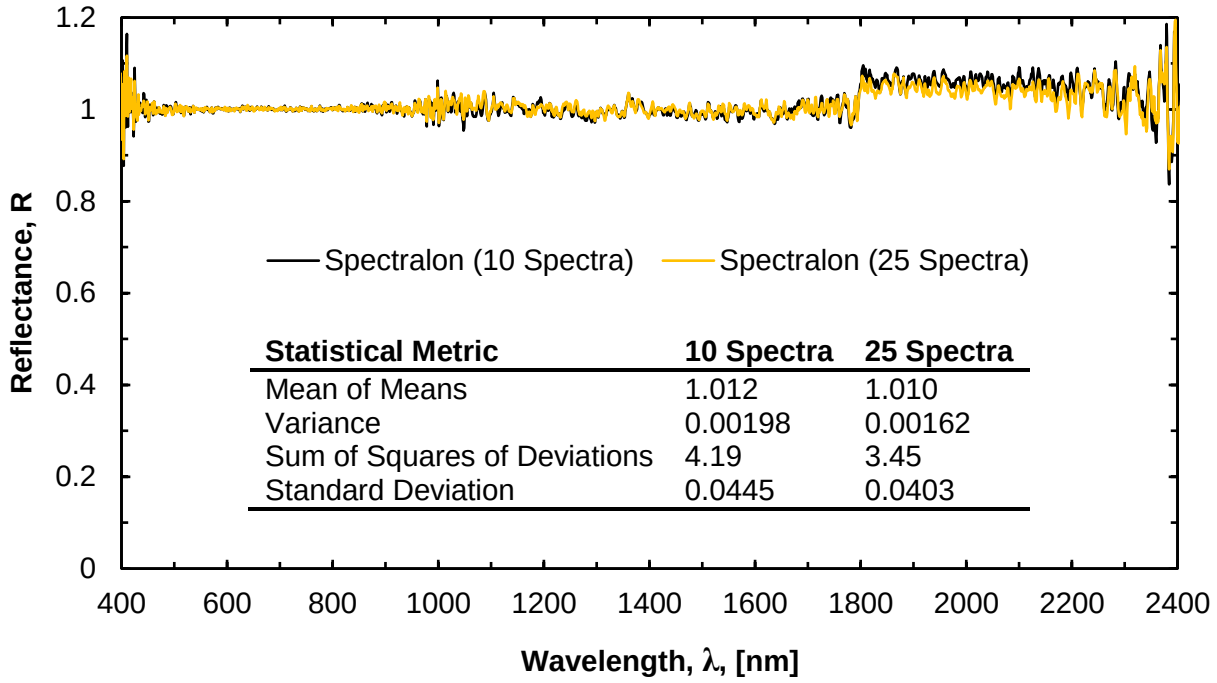

Statistical Metric	10 Spectra	25 Spectra
Mean of Means	1.012	1.010
Variance	0.00198	0.00162
Sum of Squares of Deviations	4.19	3.45
Standard Deviation	0.0445	0.0403

Figure B.1. Comparison of the effect of spectral sample size on the reflectance for the reference panel, measured at a range of 20 meters and an incidence angle of 35 degrees.

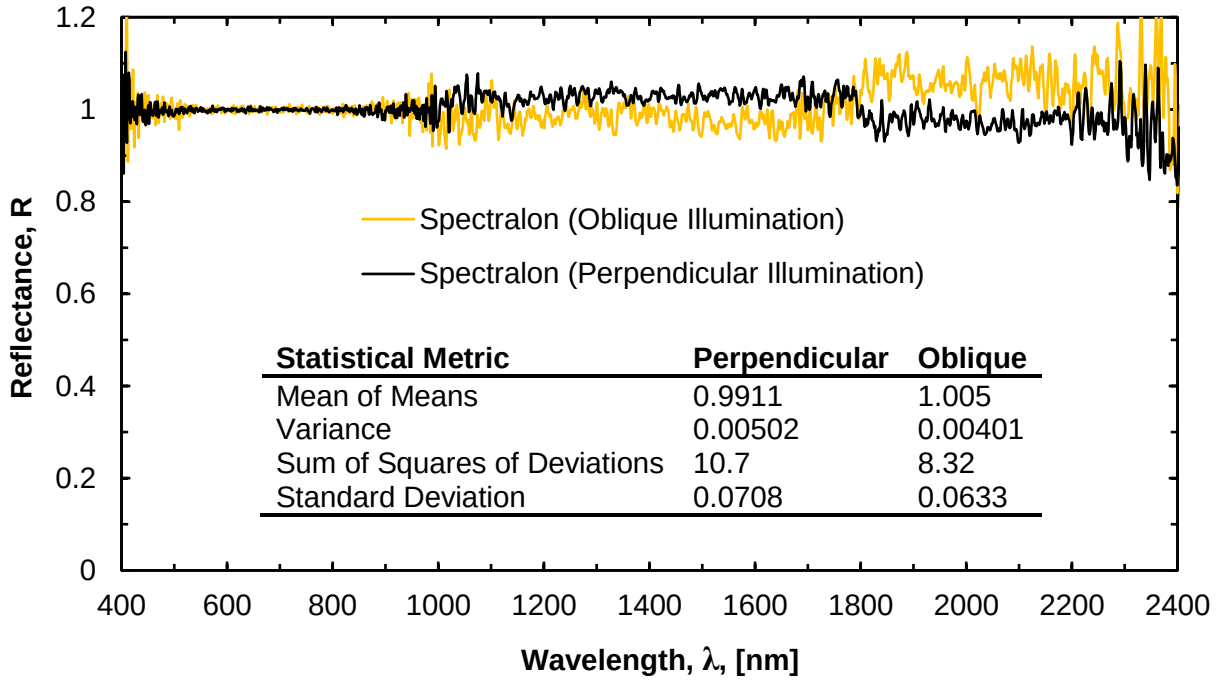

Statistical Metric	Perpendicular	Oblique
Mean of Means	0.9911	1.005
Variance	0.00502	0.00401
Sum of Squares of Deviations	10.7	8.32
Standard Deviation	0.0708	0.0633

Figure B.2. Comparison of the effect of illumination angle (oblique = 20 degrees) on the reflectance for the reference panel, measured at a range of 20 meters and an incidence angle of 70 degrees.

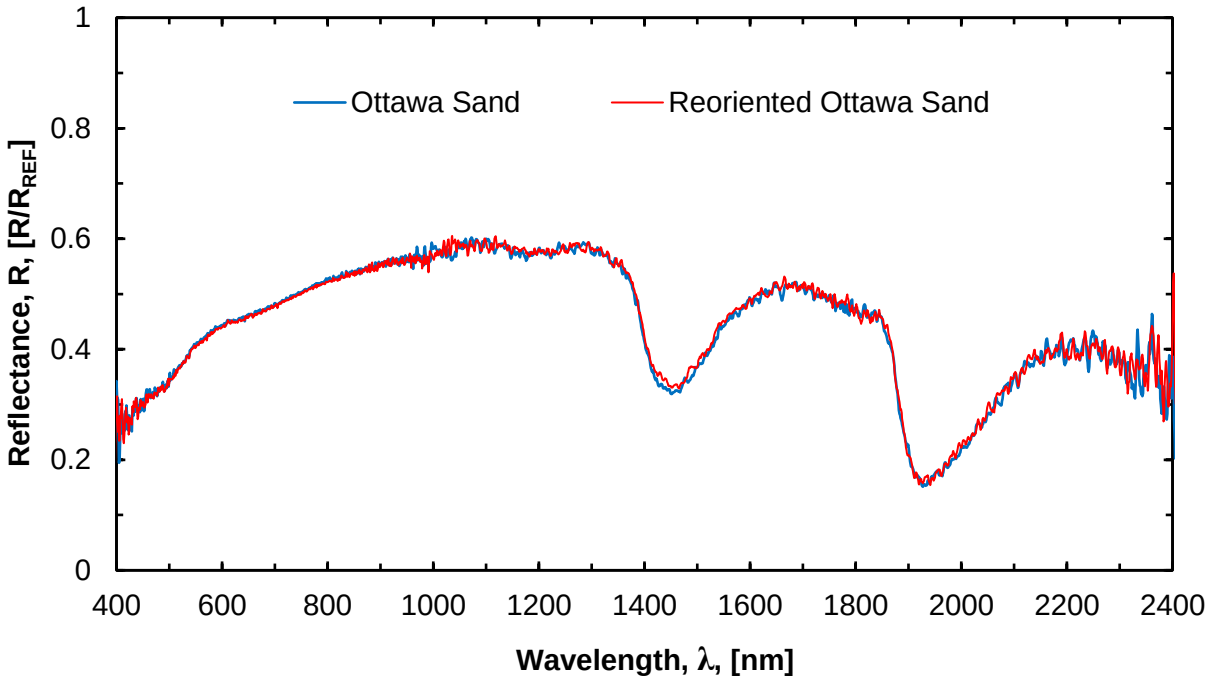

Figure B.3. Comparison of the effect of specimen orientation (in-plane rotation of 90 degrees) on the reflectance for an air-dry Ottawa sand specimen, measured at a range of 20 meters and an incidence angle of 35 degrees.

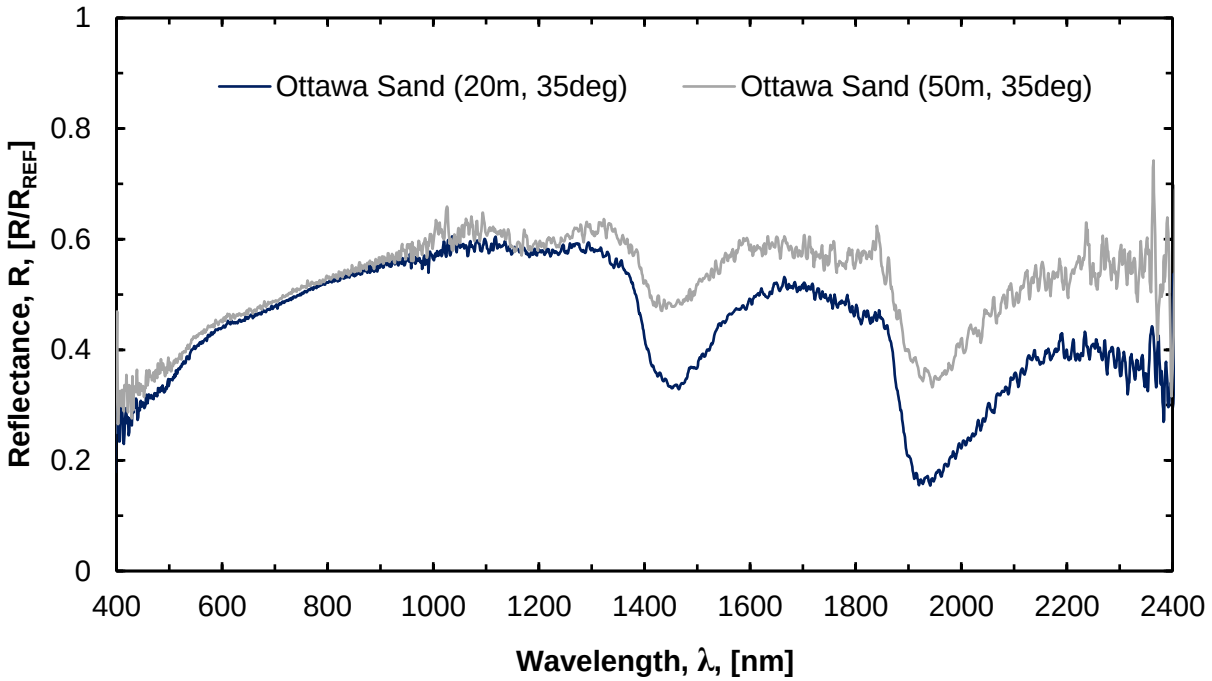

Figure B.4. Comparison of the effect of range on the reflectance for an air-dry Ottawa sand specimen, measured at an incidence angle of 35 degrees.

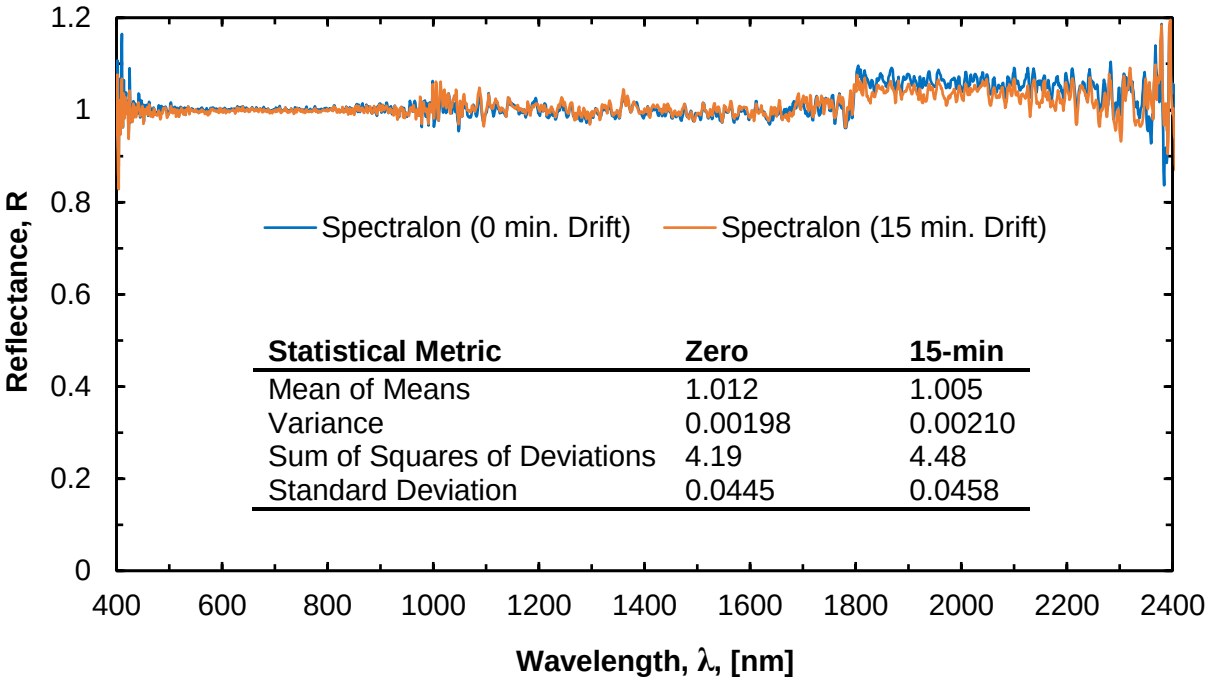

Figure B.5. Comparison of the effect of idle time after calibration on the drift in data, represented as reflectance over wavelength for the reference panel, measured at a range of 20 meters and an incidence angle of 35 degrees.

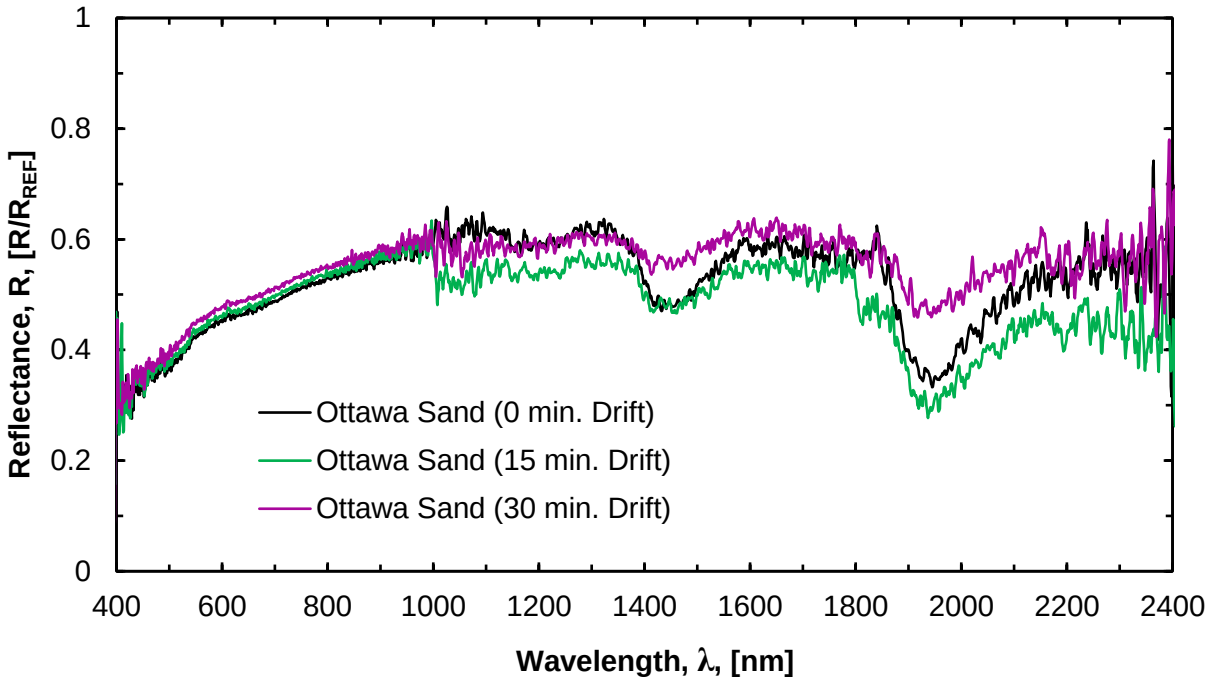

Figure B.6. Comparison of the effect of idle time after calibration on the drift in data, represented as reflectance over wavelength for an air-dry Ottawa sand specimen, measured at a range of 50 meters and an incidence angle of 35 degrees.

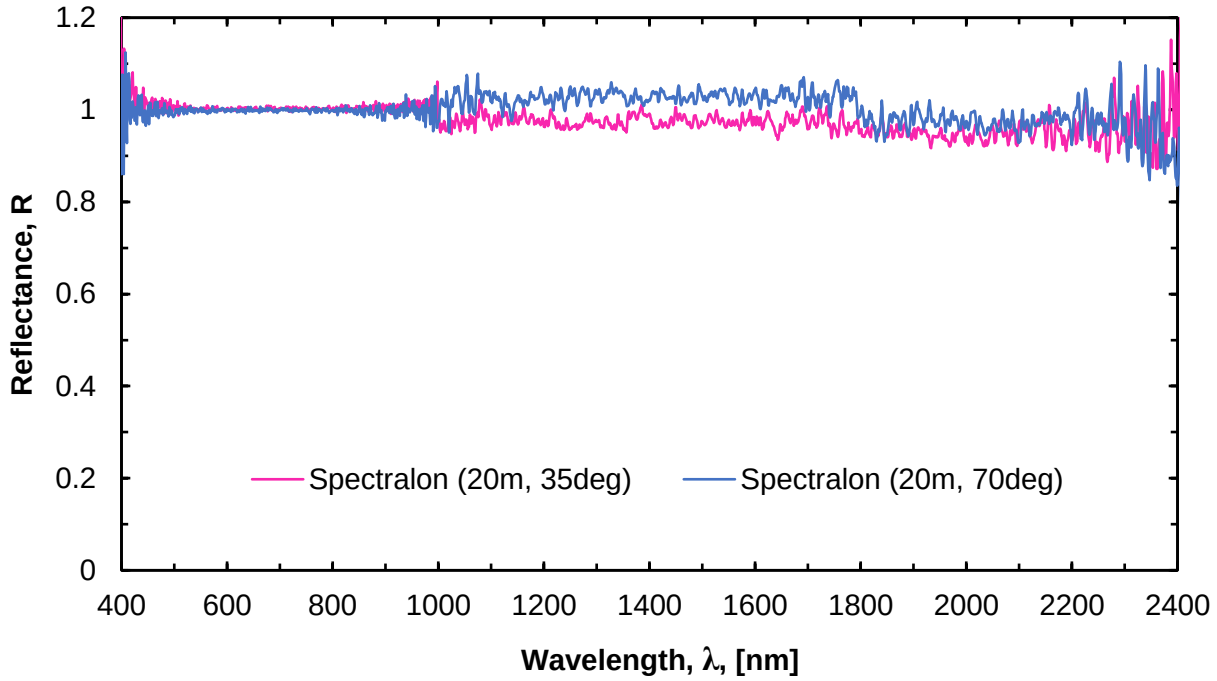

Figure B.7. Comparison of the effect of incidence angle on the reflectance as a function of wavelength for the reference panel, measured at a range of 20 meters and for incidence angles of 35 and 70 degrees.

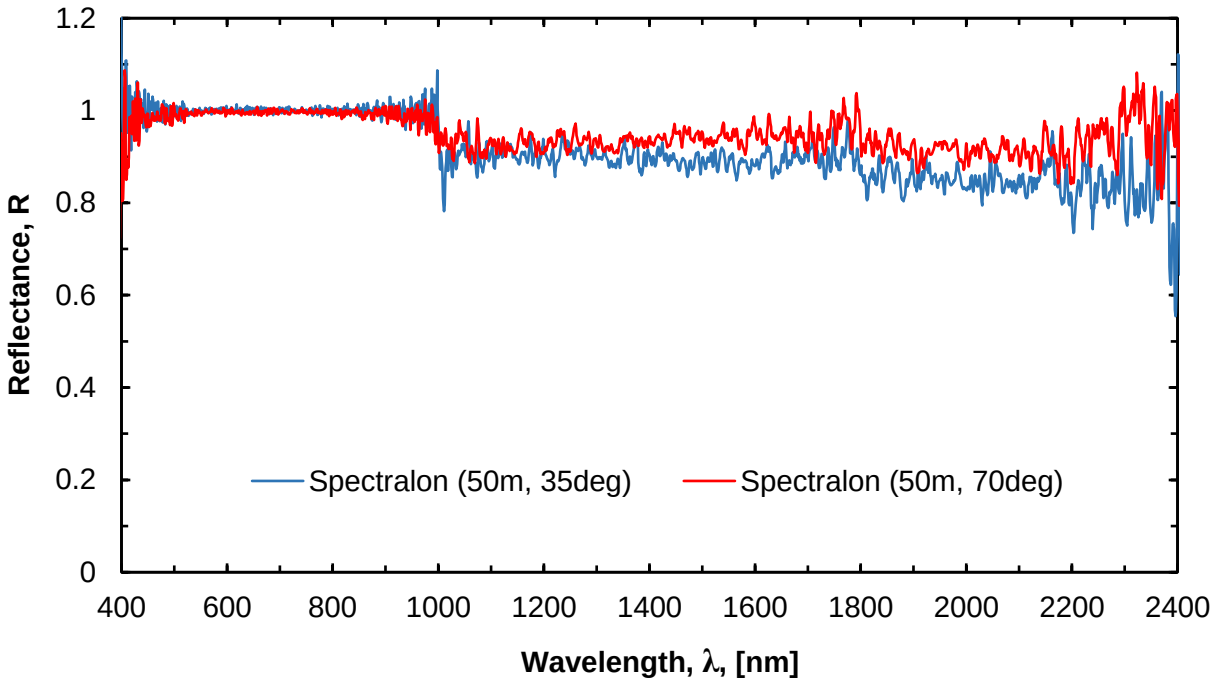

Figure B.8. Comparison of the effect of incidence angle on the reflectance as a function of wavelength for the reference panel, measured at a range of 50 meters and for incidence angles of 35 and 70 degrees.

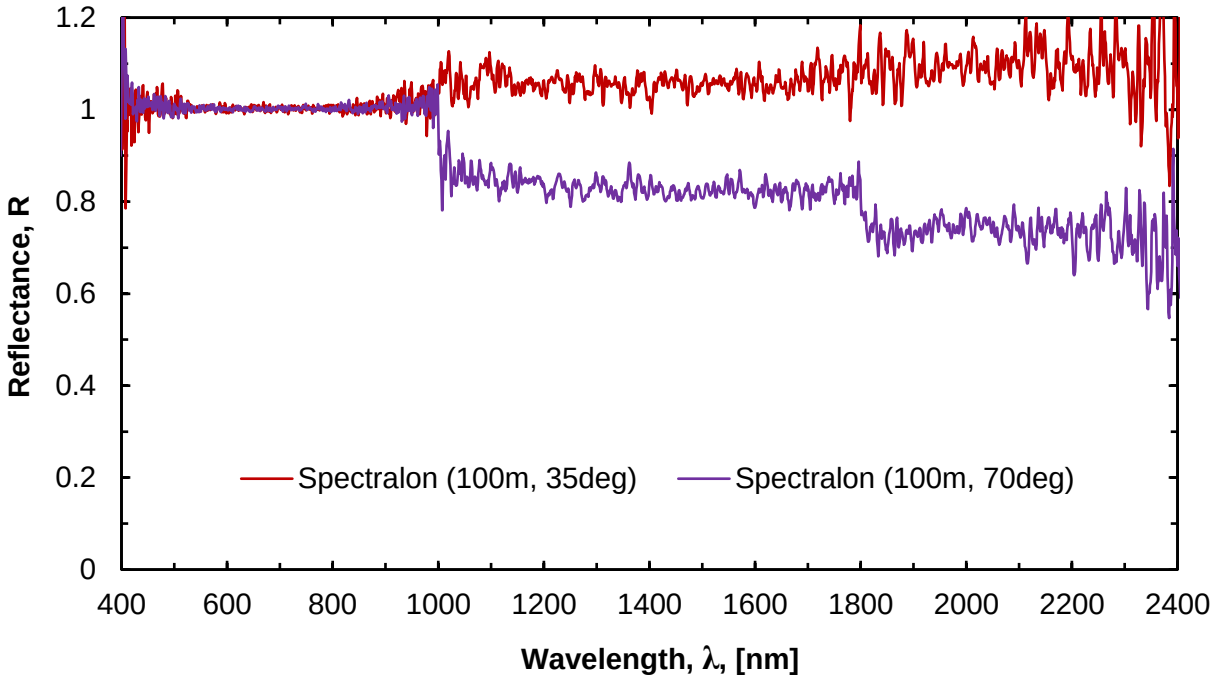

Figure B.9. Comparison of the effect of incidence angle on the reflectance as a function of wavelength for the reference panel, measured at a range of 100 meters and for incidence angles of 35 and 70 degrees.

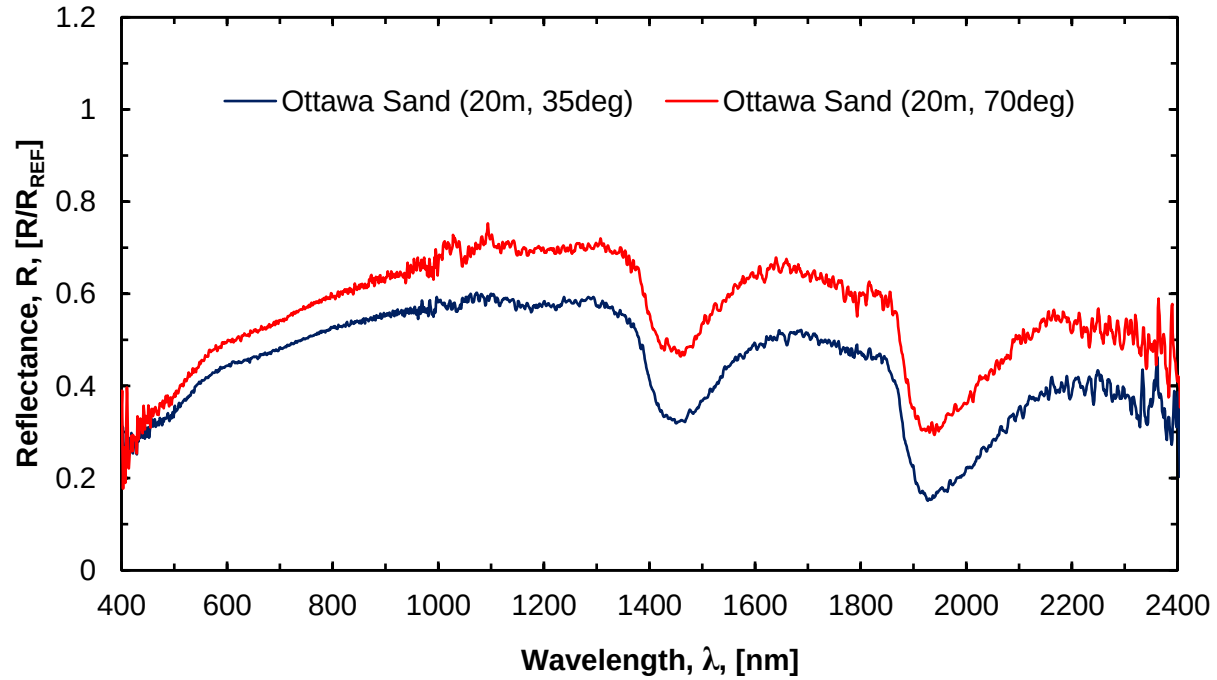

Figure B.10. Comparison of the effect of incidence angle on the reflectance as a function of wavelength for an air-dry Ottawa sand specimen, measured at a range of 20 meters and for incidence angles of 35 and 70 degrees.

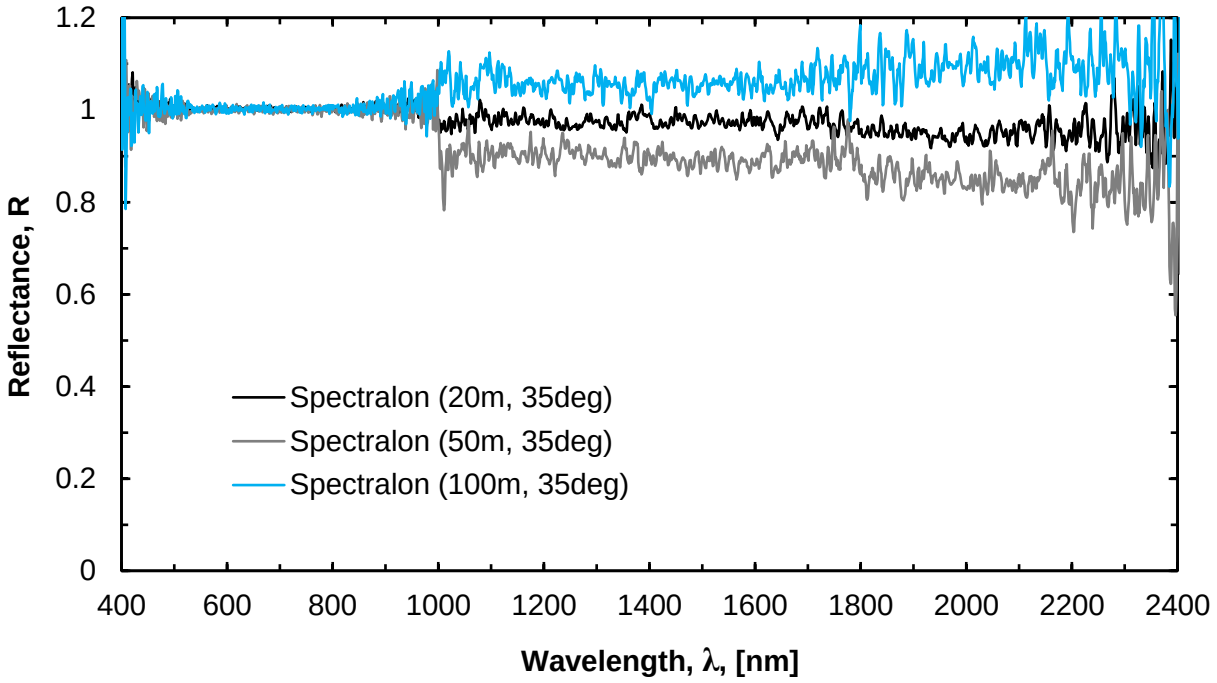

Figure B.11. Comparison of the effect of range on the reflectance as a function of wavelength for the reference panel, measured at an incidence angles of 35 degrees.

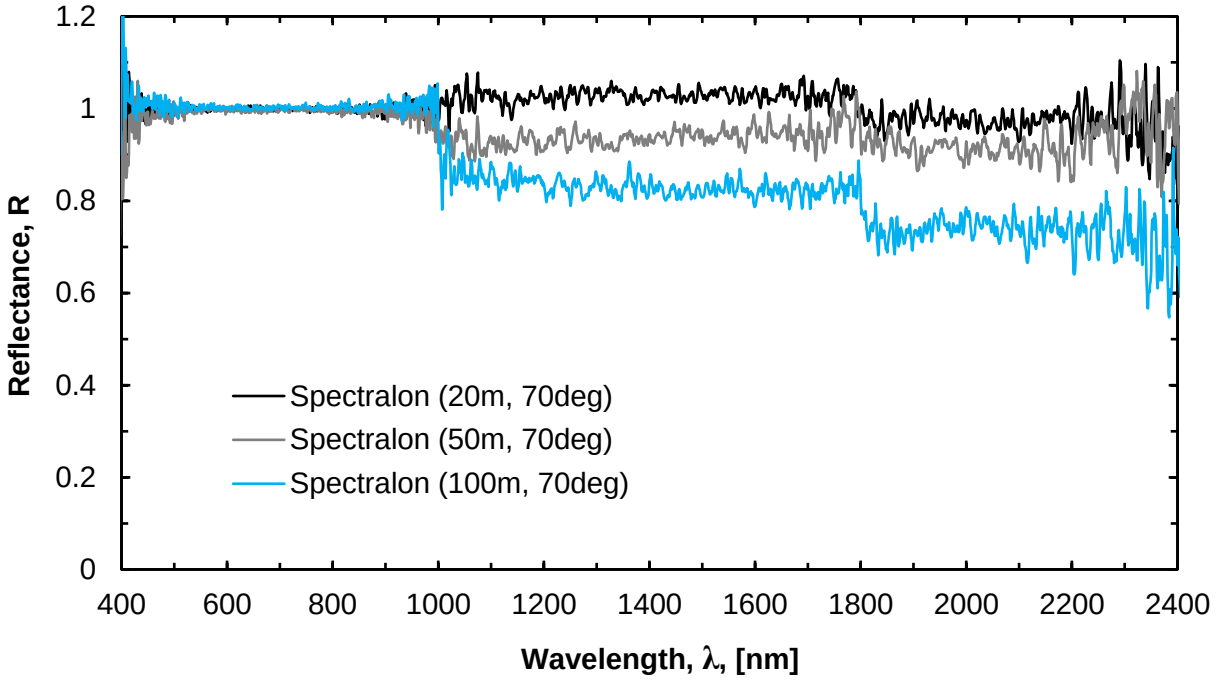

Figure B.12. Comparison of the effect of range on the reflectance as a function of wavelength for the reference panel, measured at an incidence angle of 70 degrees.

B.3. Field Testing of the SOLAS Hyperspectral Receiver

The SOLAS instrument receiver was tested outdoors at the ENRC parking lot to determine the influence of long-path atmospheric absorption and solar absorption features (Fraunhofer lines) on the measurements. The tests, summarized in Table B.2, were performed starting around 15:00 with a partially overcast sky, temperature of 10.5 °C (warming), an 11 $km \cdot h^{-1}$ WNW wind (slowing), humidity of 65%, and a dew point of 3.9 °C. The data were processed according to the procedures outlined in Section 4.6 and Section 5.6.

Table B.2. Summary of tests performed to study the influence of atmospheric effects on the data measured with the SOLAS instrument hyperspectral receiver.

Acquisition Number	Target	Range (m)	Incidence Angle (Degrees)	Illumination Angle (Degrees)*	Field of View Diameter
1	Spectralon	20	30	55	0.64 (VNIR) 1.2 (SWIR)
2	Ottawa Sand				
3	Spectralon				
4	Coarse River Sand				
5	Spectralon				
6	Donna Fill (Smooth)				
7	Spectralon				
8	Donna Fill (Rough)				
9	Spectralon				
10	Bentonite				
11	Spectralon				
12	Kaolinite (Smooth)				
13	Spectralon				
14	Kaolinite (Rough)				
15	Spectralon	20	30	50	0.64 (VNIR) 1.2 (SWIR)
16	Ottawa Sand				
17	Coarse River Sand				
18	Donna Fill (Smooth)				
19	Donna Fill (Rough)				
20	Bentonite				
21	Kaolinite (Smooth)				
22	Kaolinite (Rough)				

*Approximated using Equation 5.2 in Section 5.6.

The resulting spectra were plotted in the relative reflectance as a function of wavelength domain and are presented as Figures B.13 – B.19. Based on the collected spectra, the following preliminary conclusions were made. Long-path atmospheric absorption was observed, as illustrated by the water band noise around the 1400 nm and 1900 nm wavelength regions in Figures B.13 – B.19. The effect of range (horizontal atmospheric absorption and scattering) on the measurements was indistinguishable from the long-path atmospheric absorption effects on the reflectance without additional measurements.

As evidenced by Figures B.13 – B.17, each of the spectra that were referenced immediately before a measurement returned higher reflectance values across the range of wavelengths than the spectra that were referenced at an undefined time (1 – 10 minutes) before a measurement. However, the shape of each of the spectra was consistent. It is hypothesized that under more stable illumination conditions (high sun, clear skies), less frequent referencing is necessary. The referenced spectra in Figure B.16 exceeded the theoretical maximum reflectance of 1 for some wavelengths, indicating that a calibration error was present. It is also likely that the illumination conditions changed between the Spectralon® panel and soil specimen measurements, causing this error.

As illustrated in Figure B.18, the commonly accepted splice correction procedure (Danner et al. 2015) for wavelengths below and above the 1800 nm transition between SWIR channels may be affected by water band absorption noise, causing an erroneous offset in the data. An alternative splice correction procedure, such as discussed by Hueni and Bialek (2017) is recommended. Smoothing of the spectra using a Savitzky-Golay (1964) filter is recommended to reduce spectral noise and to ease interpretation (example in Figure B.19).

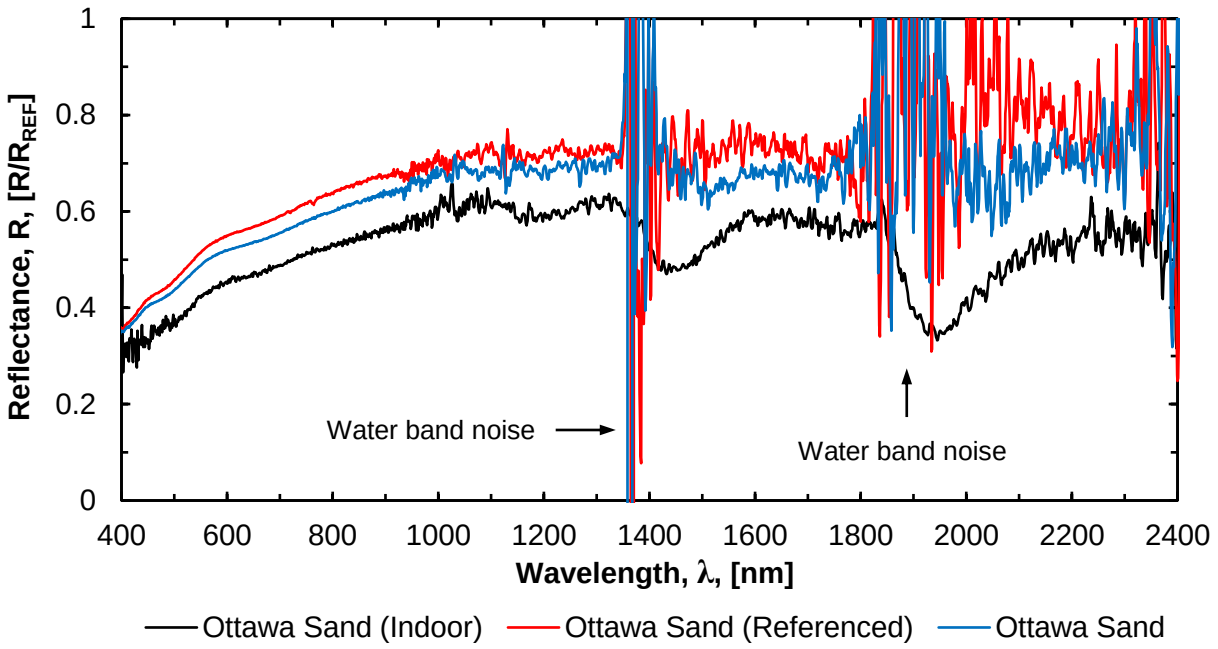

Figure B.13. Comparison of the effect of indoor and outdoor environments on the spectral reflectance of a dry Ottawa sand specimen, measured at a range of 20 meters and an incidence angle of 35 degrees under artificial illumination (indoors) and 30 degrees under solar illumination (outdoors).

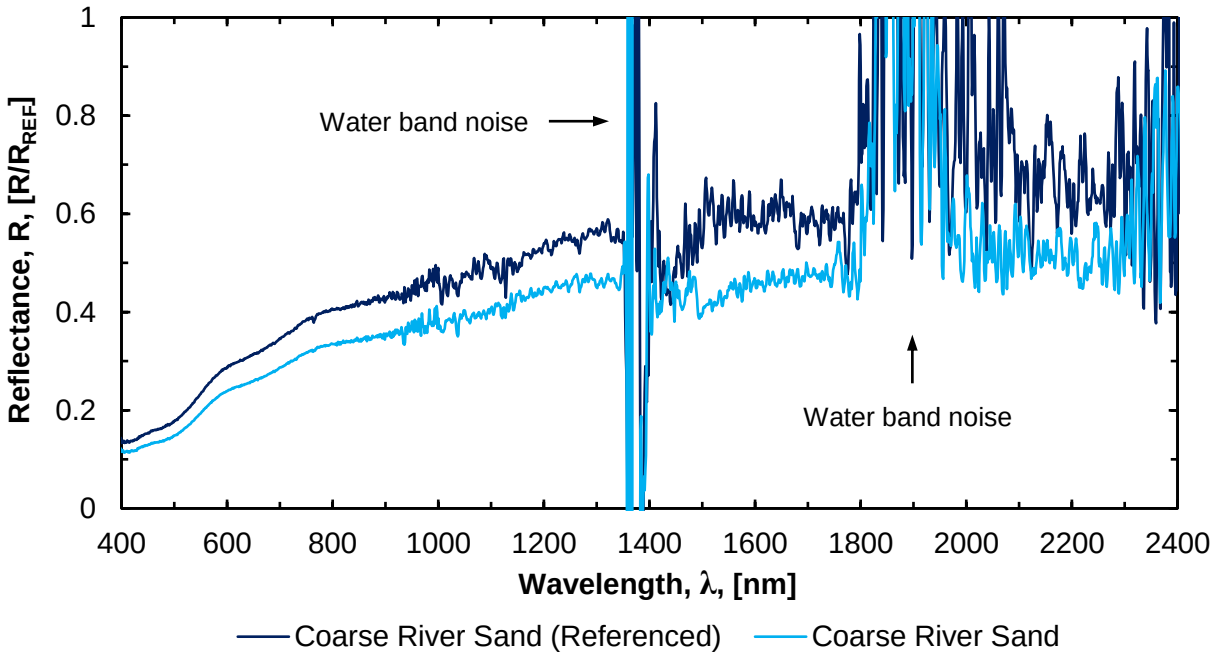

Figure B.14. Comparison of the effect of Spectralon panel referencing immediately before, or at an arbitrary time prior to measurement, on the reflectance of a dry Ottawa sand specimen, measured at a range of 20 meters and an incidence angle of 30 degrees under solar illumination.

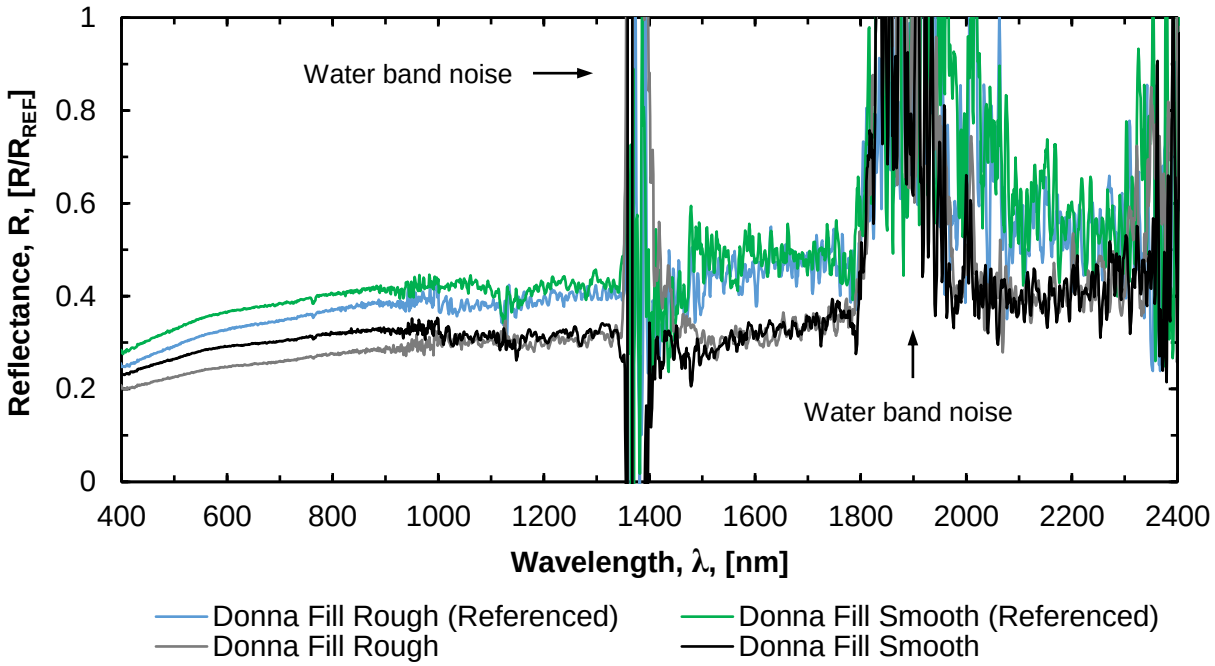

Figure B.15. Comparison of the effect of Spectralon® panel referencing immediately before, or at an arbitrary time prior to measurement, on the reflectance of a dry Donna Fill specimen (smooth and rough surface textures), measured at a range of 20 meters and an incidence angle of 30 degrees under solar illumination.

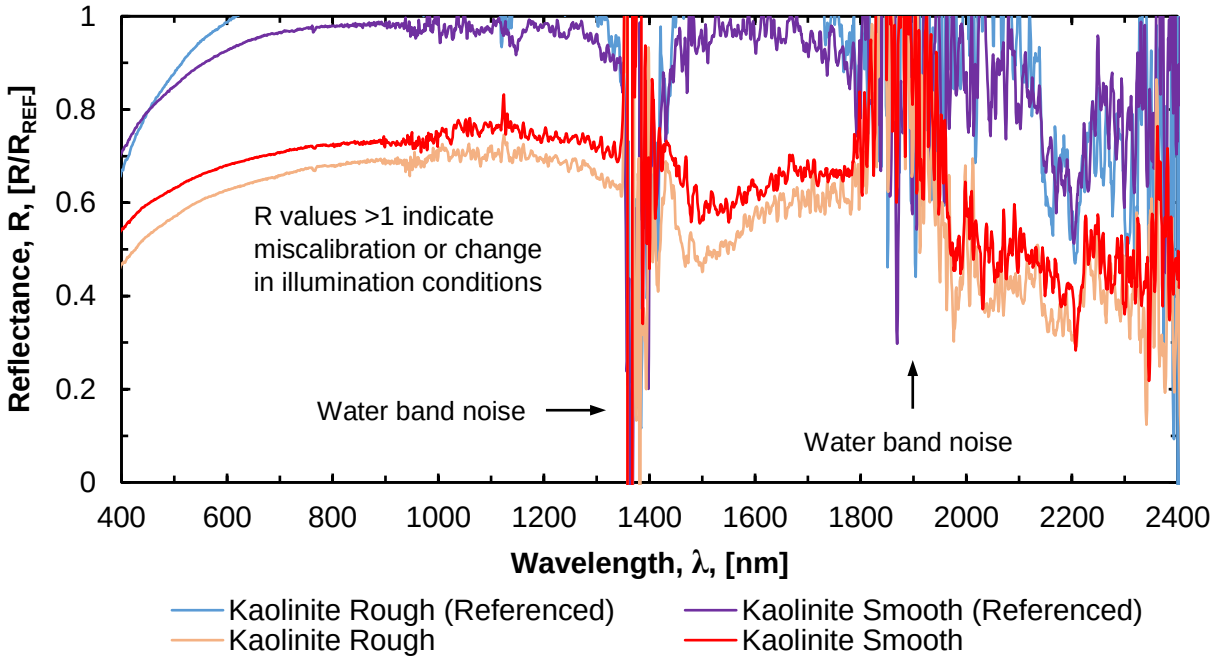

Figure B.16. Comparison of the effect of Spectralon® panel referencing immediately before, or at an arbitrary time prior to measurement, on the reflectance of a dry kaolinite soil specimen (smooth and rough surface textures), measured at a range of 20 meters and an incidence angle of 30 degrees under solar illumination.

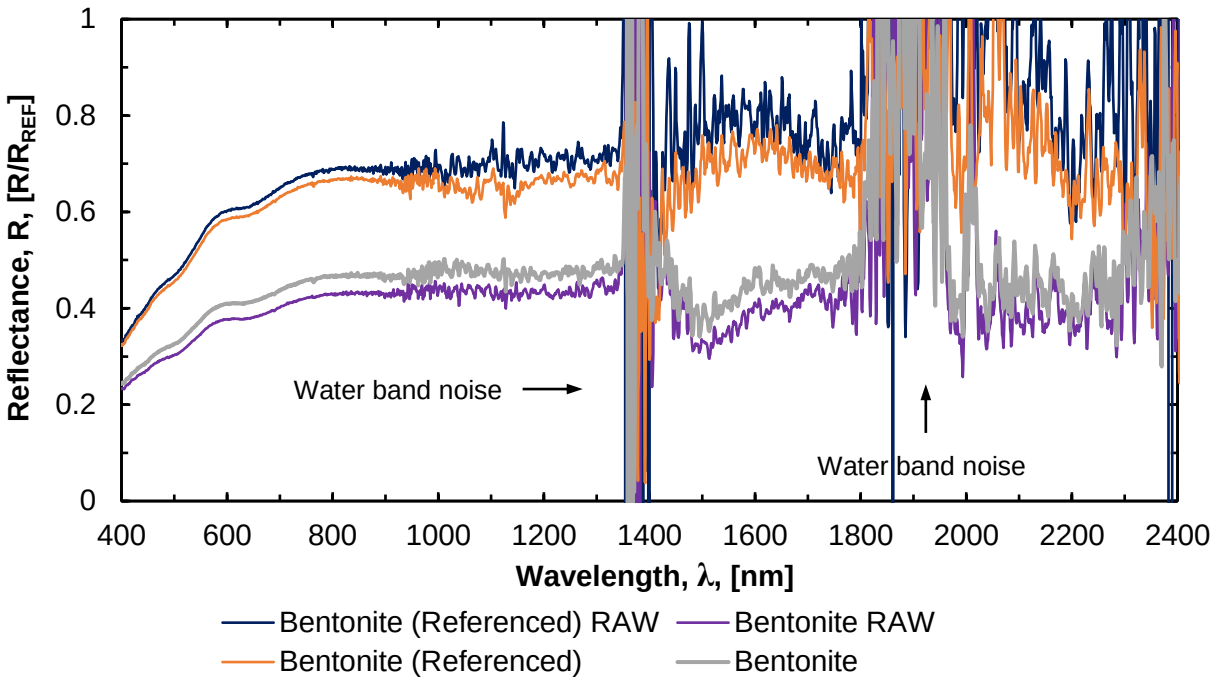

Figure B.17. Comparison of the effect of Spectralon® panel referencing immediately before, or at an arbitrary time prior to measurement, on the reflectance of a dry bentonite soil specimen, measured at a range of 20 meters and an incidence angle of 30 degrees under solar illumination (raw reflectance and relative reflectance values presented).

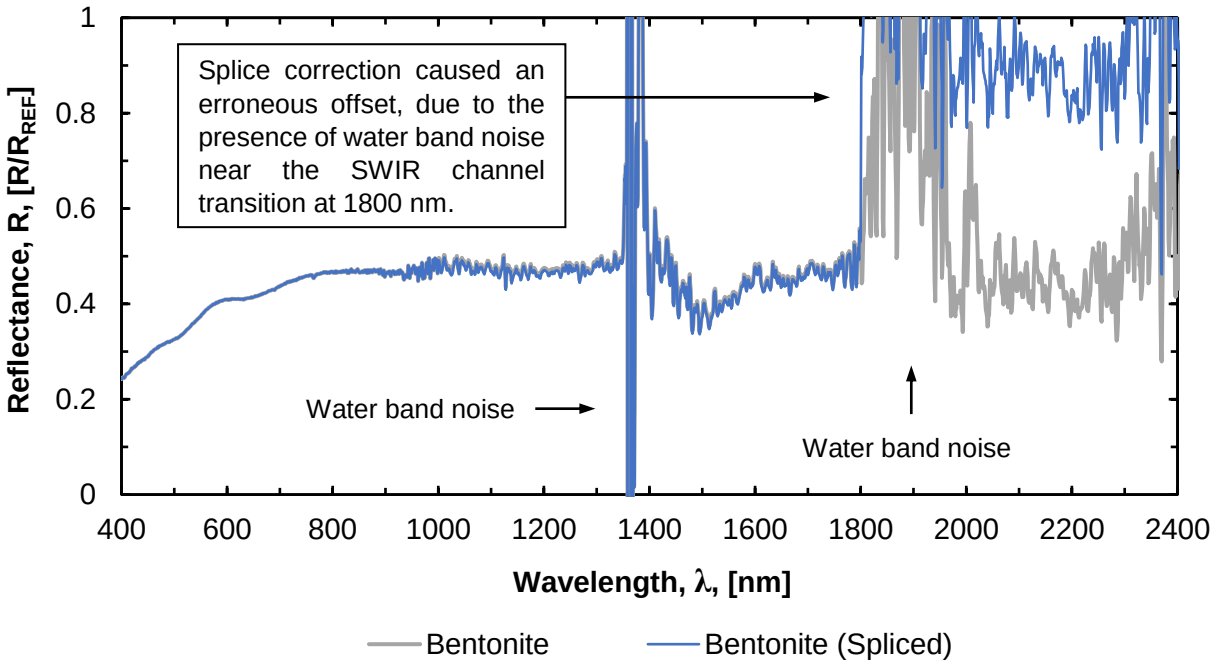

Figure B.18. Comparison of the spectra presented in Figure B.17 with the same spectra after a conventional splice correction procedure was applied.

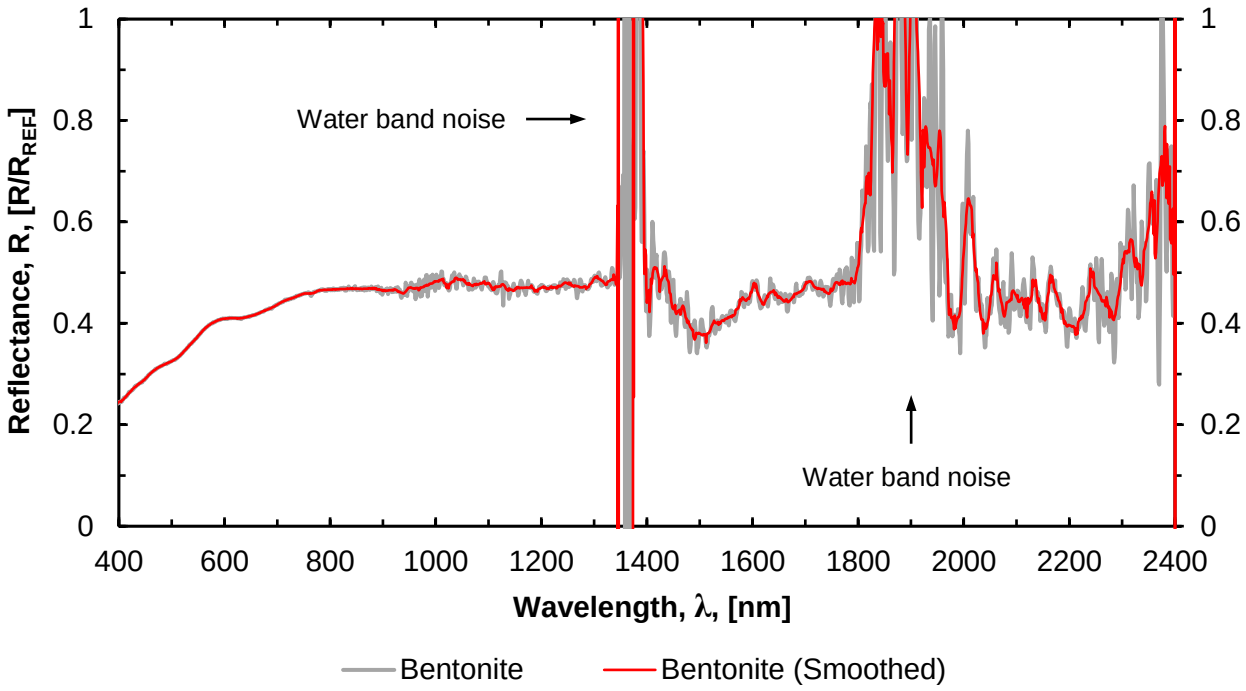

Figure B.19. Comparison of the bentonite spectrum presented in Figures 5 and 6 with the same spectrum after least-squares fit (Savitzky-Golay filter) smoothing.

B.4. Noise Characterization of the SOLAS Hyperspectral Receiver

The SOLAS instrument receiver was tested in laboratory and field settings to determine the characteristic noise. The Spectralon white reference panel was used as the target, because of the Lambertian properties (100% reflectance) of the panel across the entire 350 – 2500 nm spectrum. Table B.3 contains a typical summary of statistics comparing each of the three instrument detectors. The SWIR 1 range was the most stable, but also contained the greatest noise-equivalent-radiance (NEdL) value. In addition to the typical values provided in Table B.3, a plot of the NEdL, as a function of wavelength (after ASD 1999), is presented as Figure B.20. The NEdL was also used to derive the signal-to-noise ratio (SNR) across the range of wavelengths for typical, proximal laboratory measurements, as presented in Figure B.21, for remote measurements performed indoors, as presented in Figure B.22, and for remote

measurements performed outdoors, as presented in Figure B.23. A comparison between typical indoor and outdoor SNR is presented in Figure B.24.

According to Hueni and Bialek (2017), the observed noise for the FieldSpec 4 spectroradiometer is caused by changes in ambient temperature and at-sensor radiance levels. The noise is greatest at the edges of the detector ranges; often resulting in radiometric 'jumps' between the detectors. The noise is greatest at the far edges of the instrument range near 350 nm and 2500 nm. Fluctuations in ambient temperature of 5 °C typically require the instrument to reach internal thermal equilibrium. The noise induced by ambient temperature fluctuations is minimized after a 1-hour warmup period. Based on the conclusions of Hueni and Bialek (2017), radiance mode data collections allow for parabolic corrections in post-processing before calculating reflectance values. Corrections applied directly to the reflectance data, such as presented in Danner et al. (2015), do not fully address the thermal noise.

Table B.3. Statistical noise metrics for a typical hyperspectral baseline measurement (Salazar and Coffman 2019).

Statistical Metric (Reflectance Units)	VNIR Range* (350 – 1000 nm)	SWIR 1 Range (1001 – 1800 nm)	SWIR 2 Range* (1801 – 2500 nm)
Mean	1.00	1.01	0.976
Variance	1.11×10^{-3}	2.00×10^{-4}	4.10×10^{-3}
Sum of Squares of Deviations	7.07×10^{-1}	1.60×10^{-1}	2.83
Standard Deviation	3.34×10^{-2}	1.41×10^{-2}	6.40×10^{-2}
Noise-Equivalent-Radiance ($W \cdot cm^{-2} \cdot nm^{-1} \cdot sr^{-1}$) †	9.2×10^{-10}	1.7×10^{-9}	7.5×10^{-10}

*****Erroneous reflectance values greater than 1.2 at the near (350 nm) and far (2500 nm) edges of the wavelength range were excluded from the statistical summary (approximately 1% of the 2151 individual wavelength bands). †Values for the midpoint of each wavelength range.

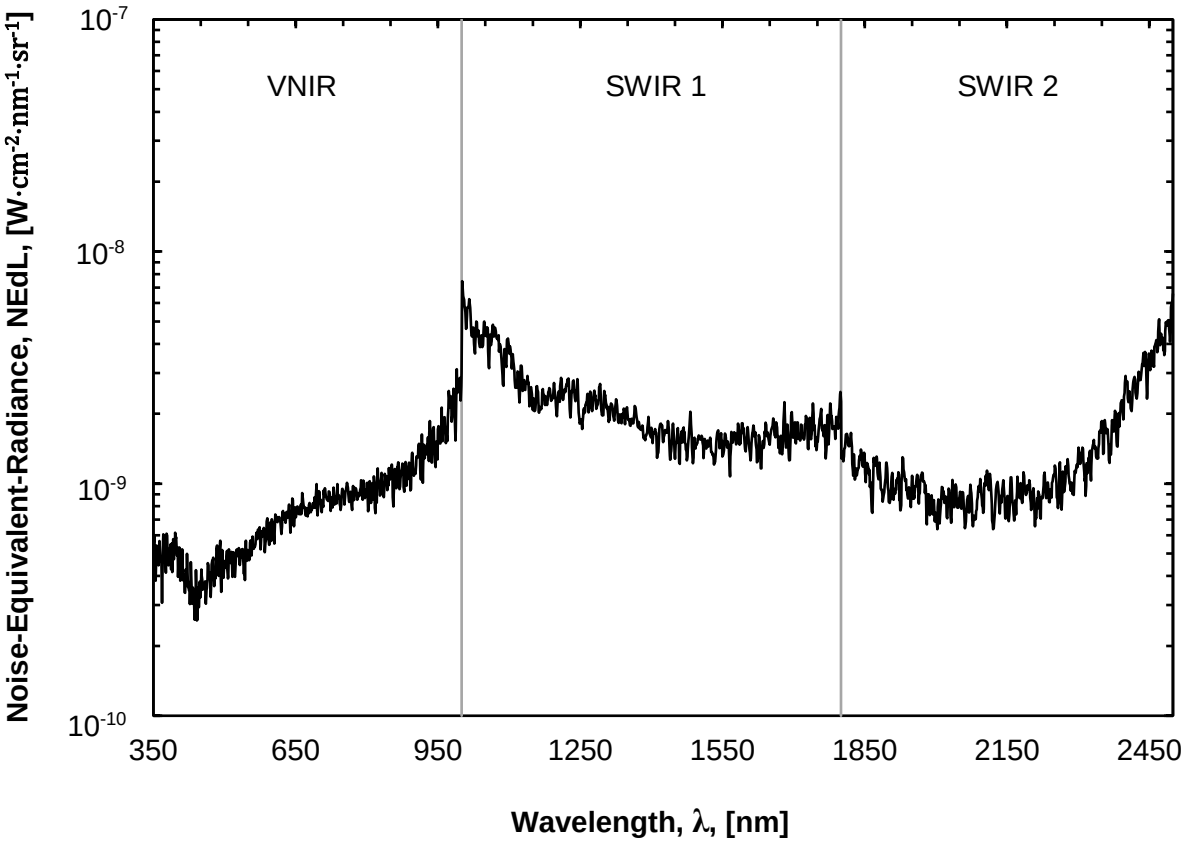

Figure B.20. Noise-equivalent-radiance as a function of wavelength across the three detector ranges of the ASD FieldSpec 4 Hi-Res spectroradiometer (SN 18304).

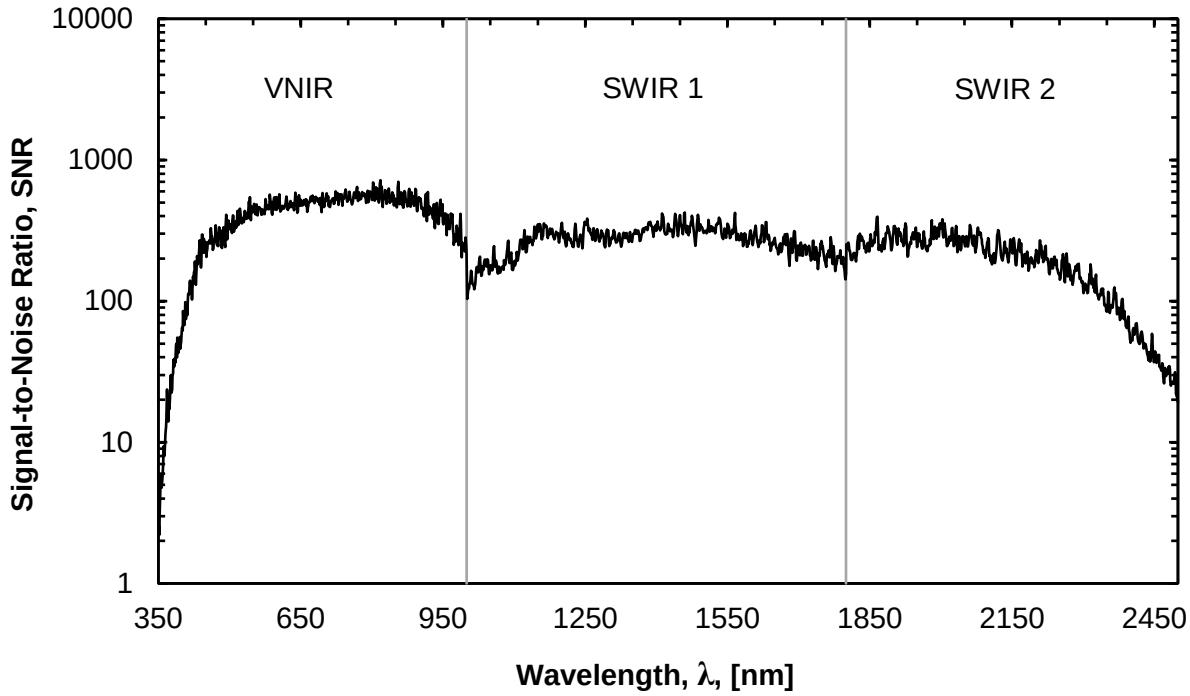

Figure B.21. Signal-to-noise ratio as a function of wavelength for proximal measurements performed in the laboratory.

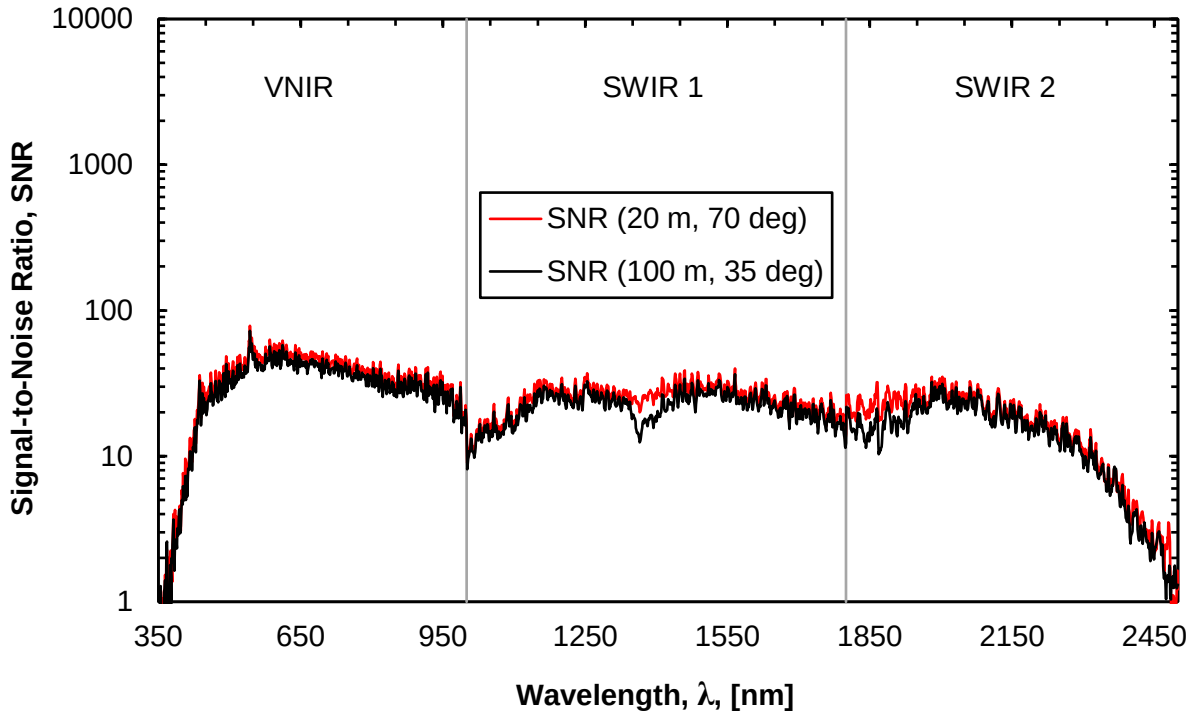

Figure B.22. Signal-to-noise ratio as a function of wavelength for telescope-assisted measurements performed in an indoor environment (20-m range and 35-degree incidence angle, compared with 100-m range and 70-degree incidence angle).

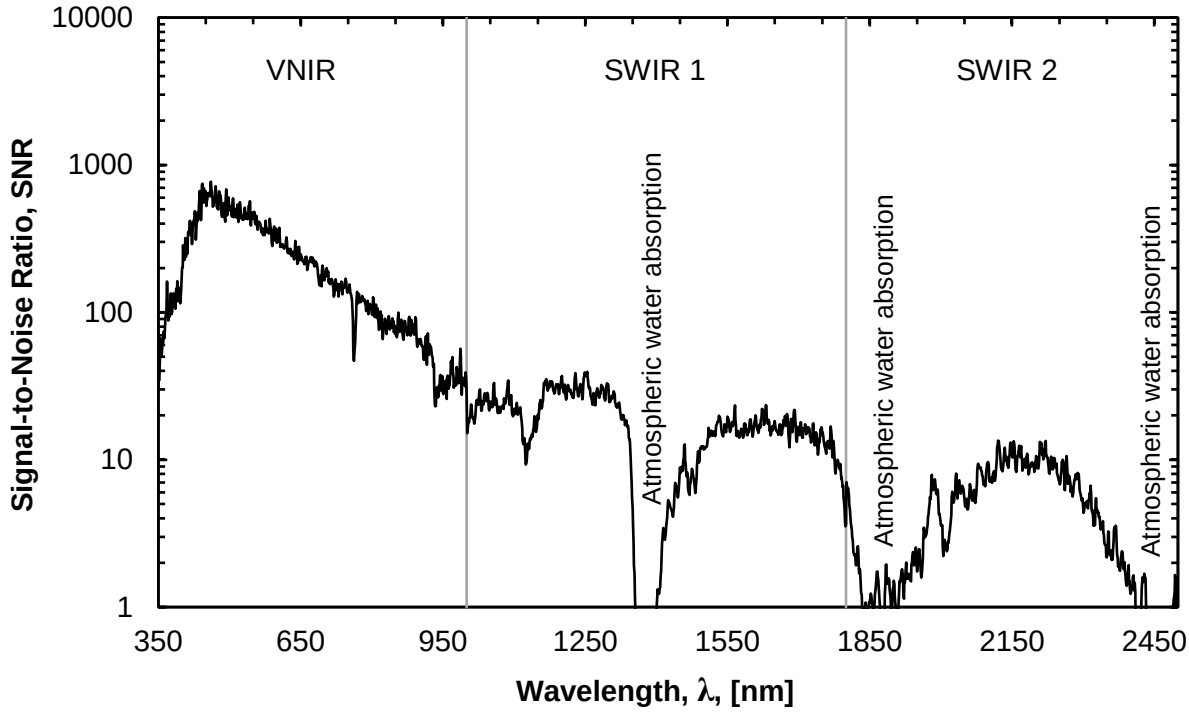

Figure B.23. Signal-to-noise ratio as a function of wavelength for telescope-assisted measurements performed in an outdoor environment (20-meter range, 30-degree incidence angle, partially overcast sky, 10.5 °C air temperature, 65% humidity).

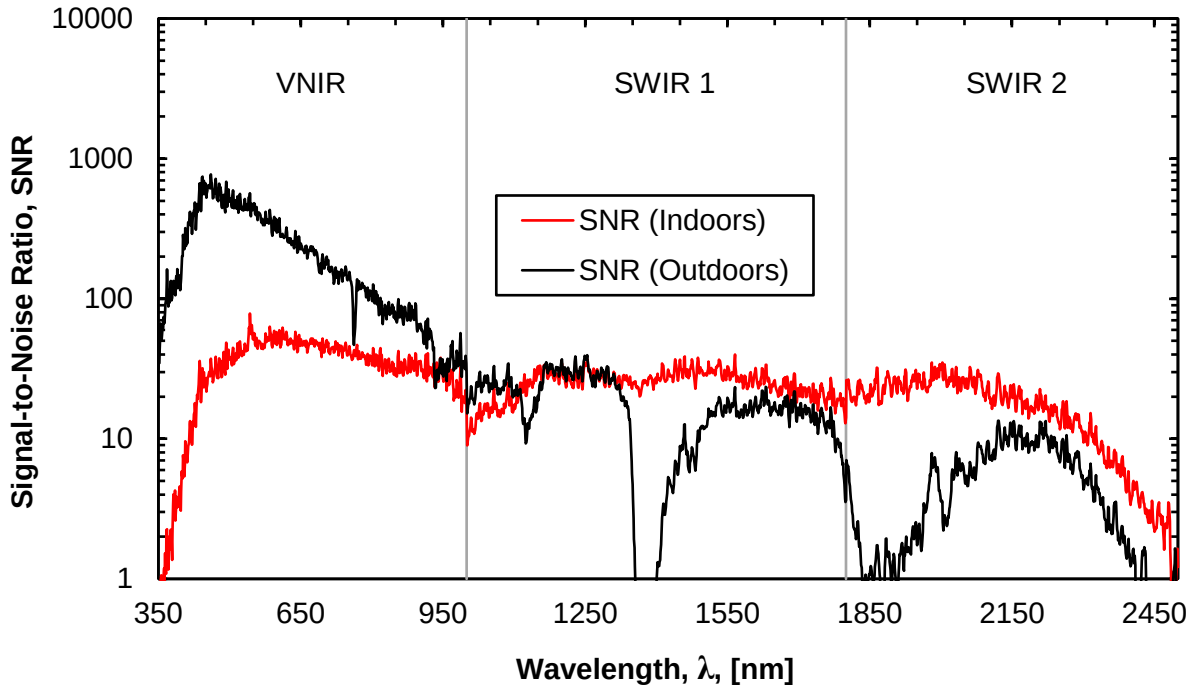

Figure B.24. Comparison of signal-to-noise ratios for telescope-assisted measurements performed in indoor and outdoor environments (data presented in Figures B.22 and B.23).

B.5. References

Analytical Spectral Devices, 1999, *ASD Technical Guide*, 3rd ed., Hatchell, D. C., Ed., Analytical Spectral Devices, Inc., Boulder, CO, USA.

Danner, M., Locherer, M., Hank, T., and Richter, K., 2015, "Spectral Sampling with the ASD FieldSpec 4—Theory, Measurement, Problems, Interpretation," EnMAP Field Guides Technical Report, GFZ Data Services, Potsdam, Germany.

Hueni, A. and Bialek, A., 2017, "Cause, Effect, and Correction of Field Spectroradiometer Interchannel Radiometric Steps," *IEEE J. Sel. Top. Appl. Earth Obs. Remote Sens.*, Vol. 10, pp. 1542–1551. doi:10.1109/JSTARS.2016.2625043.

Salazar, S. E. and Coffman, R. A., 2019, "Multi-Channel Optical Receiver for Ground-Based Topographic Hyperspectral Remote Sensing," *Remote Sens.*, Vol. 11, No. 5, 578. doi:10.3390/rs11050578.

Savitzky, A. and Golay, M. J. E., 1964, "Smoothing and Differentiation of Data by Simplified Least Squares Procedures," *Anal. Chem.*, Vol. 36, pp. 1627–1639. doi:10.1021/ac60214a047.